



School of Chemical, Environmental and Mining Engineering

**AN INVESTIGATION OF
GEOMETRICALLY INDUCED SWIRL APPLIED TO
LEAN PHASE PNEUMATIC FLOWS**

Smeeta Fokeer, BEng (Hons), MSc

Thesis submitted to the University of Nottingham for
the degree of Doctor of Philosophy

September 2006

ABSTRACT

This thesis provides unique insights into the application of a geometrically induced swirl by a three-lobed helix pipe on a lean phase of particulate suspension in air along a horizontal pipe section. A series of experimental and computational studies were applied to three flow conditions employing high speed photography, Particle Image Velocimetry (PIV) and Laser Doppler Anemometry (LDA), as well as Computational Fluid Dynamics (CFD) techniques. The CFD simulation predictions were validated both qualitatively and quantitatively against the experimental data and were then used to obtain further insights into the characteristics of the flow behaviour.

The LDA measurements of u , v and w velocities were shown to be in good agreement with the predicted CFD velocity components. Additional pressure loss caused by the swirl pipe was found to be proportional to the Reynolds number of the flow and increased further with an addition of particles to the swirling flow.

It was concluded that the swirl pipe imparts a wall jet type swirl to both an air-only flow and a lean pneumatic flow with velocity and momentum shifts from axial to tangential closer to the wall. The cusps and ridges of the twisted three lobe surfaces were shown to create a primary flow parallel to the flow axis, and secondary flows of a circulatory motion perpendicular to the primary flow. As a result, the trajectories followed by particles were observed to be affected by their size. The generated turbulence was shown to impart higher core axial velocity for both air and particles. The swirl was found to decay proportionally with the distance downstream of the swirl pipe and inversely to the flow's Reynolds number.

The major conclusions drawn from the study were that the swirl pipe locally increases the conveying velocity and produced an improved particle distribution across the downstream section of the pipe.

ACKNOWLEDGEMENTS

I would like to thank the International Office of the University of Nottingham for the scholarship awarded to me to make this PhD possible.

I owe a world of gratitude to my supervisors, Dr. Ian Lowndes and Dr. Sam Kingman for their financial help. I would like to particularly thank Dr. Ian Lowndes for his enduring trust in me and constant encouragement throughout my learning curve.

I extend my gratitude to:

Dr. David Hargreaves for his help and advice with CFD modelling

Dr. Aroussi, Phil Rogers and Jake Roberts for allowing the use of their experimental rig for initial testing

Dr. Matthew Crompton from Dantec for his invaluable help with the PIV and LDA experiments

Prof. Azzopardi and Dr. Stephen Silvester for their valued input and critical evaluation of my work.

Phil Bennet and his team for turning ideas into reality by making the experimental rig components

Tony Gospel for his help in various parts of the rig building

Dr. Rob Hart, Dr. Chanchala Ariyaratne and Xiyang Cai, my CFD lab mates, for their great friendship and most helpful discussions.

My friends, who make hard times easier and dull moments funnier: Thank you Bona, Conor, Gorgio, Kevin, Boki, Stacy, Andreas, Judy, Miguel, Mac and Andrew.

Dr. George Kuk for his endless patience, support and love when most required and for painstakingly reading through this thesis and suggesting valuable changes.

Finally, my parents, Dharam and Sheela, and sister, Danisha, whose support and understanding are precious to me and I am especially grateful for.

TABLE OF CONTENTS

Abstract.....	i
Acknowledgements.....	ii
Table of contents.....	iii
List of figures.....	x
List of tables.....	xvii
Nomenclature.....	xix
 Chapter 1: Introduction.....	 1
1.1 Motivation for present work.....	1
1.2 Aims and objectives.....	3
1.3 Methodology.....	3
1.3.1 Experimental Method.....	4
1.3.2 Computational Method.....	4
1.4 Thesis Outline.....	4
 Chapter 2: Literature review – Gas-solid flows in pipes.....	 8
2.1 Introduction.....	8
2.2 Stokes number.....	8
2.3 Pneumatic conveying classification	9
2.4 Energy minimum state and factors affecting it.....	11
2.4.1 Effect of particles parameters on minimum energy state.....	11
2.4.2 Effect of particle/wall interactions on minimum energy state.....	12
2.4.3 Effect of operational parameters on minimum energy state.....	12
2.5 Cross sectional particle distribution in dilute phase pneumatic conveying systems.....	12

2.5.1 Effect of Magnus force, shear stress and turbophoretic effect on cross sectional particle distribution.....	14
2.5.2 Effect of particle/wall collisions due to wall roughness and pipe diameter on cross sectional particle distribution.....	15
2.5.3 Effect of inter-particle collisions due to mass loading and particle size on particle cross sectional concentration distribution.....	17
2.5.4 Cross sectional particle distribution after bends.....	18
2.5.4.1 Rope formation and disintegration mechanism.....	19
2.5.4.2 Effect of particle size.....	20
2.5.4.3 Combinations of bends.....	20
2.5.4.4 Effect of bend radius to pipe diameter ratio.....	21
2.5.5 Equipment wear and particle attrition.....	22
2.6 Visualisation tools for the cross sectional particle distribution.....	24
2.6.1 Tomography.....	24
2.7 Summary.....	26

Chapter 3: Literature review – Modelling of gas-solid flows in pipes.....30

3.1 Introduction.....	30
3.2 Turbulence modelling approaches.....	31
3.3 Eulerian v/s Lagrangian modelling approaches.....	33
3.4 One-way v/s two-way coupling.....	39
3.5 Turbulence modulation.....	39
3.5.1 Particle size.....	40
3.5.2 Particle loading.....	42
3.5.3 Distance from wall.....	43
3.5.4 Relative velocity between particle and conveying gas.....	44
3.5.5 Physical balance model for turbulence generation and dissipation by the particles.....	44
3.6 Summary.....	45

Chapter 4: Literature review – Swirling flows in pipes.....48

4.1 Introduction.....	48
4.2 Swirl flow generation.....	48

4.3 Swirl flow anatomy for air only flows.....	50
4.4 Swirl flow characterisation for air only flows.....	52
4.5 Swirl flow experiments for air only flows	54
4.5.1 Swirl decay experiments for air only flows.....	56
4.5.2 Experiments in swirl flow pneumatic conveying.....	58
4.6 Swirl modelling.....	59
4.6.1 Swirl decay modelling.....	61
4.6.2 Modelling of swirl flow pneumatic conveying.....	62
4.7 Summary.....	64
 Chapter 5: Experimental rig design.....	67
5.1 Introduction.....	67
5.2 Experimental facility at the University of Manchester.....	67
5.3 Preliminary work.....	68
5.3.1 Choice of pressure system.....	70
5.4 Final experimental rig layout & specification.....	71
5.5 Rig components.....	73
5.5.1 Conveyed material.....	73
5.5.2 Pipework.....	76
5.5.3 Pressure monitoring.....	77
5.5.4 Air flow rate evaluation.....	79
5.5.5 Swirl inducing helix pipe.....	81
5.5.6 Solids mass flow rate/ Particles feeder.....	85
5.5.7 Gas-solid separation device.....	91
5.5.7.1 Principle of operation of a cyclone.....	92
5.5.8 Air mover.....	95
5.6 Conclusions.....	103
 Chapter 6: Experimental investigation.....	105
6.1 Introduction.....	105
6.2 Experimental conditions.....	105
6.3 Pressure measurement.....	107
6.4 High speed video imaging & laser sheet.....	110

6.4.1 Objectives and scope of the high speed video experimental programme.....	110
6.4.2 Experimental apparatus and instrumentation.....	111
6.4.2.1 High speed camera.....	111
6.4.2.2 Laser.....	112
6.4.3 Set-up and procedures.....	112
6.4.4 High speed video imaging results.....	114
6.4.4.1 Flow visualisation using white light.....	115
6.4.4.2 Flow visualisation using laser sheeting.....	119
6.4.5 Conclusions from speed video experiments.....	124
6.5 Particle Image Velocimetry (PIV).....	125
6.5.1 Objectives and scope of the PIV experimental programme.....	125
6.5.2 Experimental apparatus and instrumentation.....	126
6.5.3 Set-up and procedures.....	128
6.5.4 Presentation of the PIV measurements results.....	131
6.5.4.1 PIV results downstream of a swirl inducing pipe	131
6.5.5 Conclusions from PIV experiments.....	135
6.6 Laser Doppler Anemometry (LDA).....	136
6.6.1 Objectives and scope of the LDA experimental programme.....	138
6.6.2 Experimental apparatus and instrumentation.....	138
6.6.3 Set-up and procedures.....	143
6.6.4 LDA measurements results.....	148
6.6.4.1 LDA results on a horizontal circular pipe section (no swirl)...	152
6.6.4.2 LDA results downstream of a swirl-inducing pipe.....	154
6.6.5 Conclusions from LDA experiments.....	165
6.7 Experimental errors and uncertainties.....	166
6.8 Conclusions.....	173
 Chapter 7: CFD modelling and solution methodology.....	175
7.1 Introduction.....	175
7.2 Basic principles of CFD.....	175
7.3 Numerical conceptualisation for CFD modelling.....	176
7.3.1 Numerical schemes.....	176

7.3.2 Discretisation process.....	178
7.3.2.1 Spatial discretisation.....	179
7.3.2.2 Equation discretisation.....	179
Upwind advection schemes.....	180
Pressure Interpolation Schemes.....	180
Pressure-Velocity Coupling.....	181
7.3.3 Performance and monitoring criteria.....	182
7.4 Governing equations for turbulent flow.....	182
7.4.1 Continuity equation for mass conservation.....	183
7.4.2 Navier-Stokes equations for momentum conservation.....	183
7.5 Turbulence modelling - Reynolds averaged Navier-Stokes equations.....	184
7.5.1 Standard k- ϵ model.....	185
7.5.2 RNG k- ϵ model.....	187
7.5.3 Reynolds stress model (second order closure model).....	187
7.6 Near-wall treatment for wall-bounded turbulent flows.....	189
7.6.1 Wall functions.....	190
7.6.1.1 Standard wall functions.....	191
7.6.1.2 Non-equilibrium wall functions.....	192
7.6.2 Near wall modelling.....	192
7.6.2.1 Enhanced wall treatment.....	193
7.7 Model formulation for CFD.....	194
7.7.1 CFD software package.....	194
7.7.2 Construction of pipe geometry.....	194
7.7.3 Mesh generation.....	197
7.7.3.1 Boundary layer mesh.....	198
7.7.3.2 Face and volume meshing.....	199
7.7.3.3 Mesh quality.....	201
7.7.3.4 Grid adaptation for y^+	203
7.7.3.5 Grid independence tests.....	204
7.7.4 Solution methodology.....	206
7.7.4.1 Enabling assumptions.....	206
7.7.4.2 Solver parameters.....	206
7.7.4.3 Turbulence model.....	207

7.7.4.4 Wall treatment.....	208
7.7.4.5 Advection scheme for viscous terms.....	209
7.7.4.6 Pressure discretisation scheme.....	210
7.7.4.7 Pressure-velocity coupling scheme.....	211
7.7.5 Boundary conditions.....	212
7.7.5.1 Operating conditions.....	212
7.7.5.2 Inlet boundary conditions.....	213
7.7.5.3 Outlet boundary conditions.....	213
7.7.5.4 Wall boundary conditions.....	213
7.7.5.5 Grid interface.....	214
7.7.6 Convergence.....	214
7.7.6.1 Residual convergence.....	215
7.7.6.2 Outlet pressure convergence.....	216
7.7.6.3 Mass imbalance.....	216
7.8 Conclusions.....	217

Chapter 8: CFD modelling validation and further studies performed using the validated CFD models..... 220

8.1 Introduction.....	220
8.2 Verification v/s Validation.....	221
8.3 The CFD model.....	223
8.4 Pressure loss validation for air only flows	225
8.4.1 Control pipe.....	225
8.4.2 Swirl pipe.....	227
8.5 Laser Doppler Anemometry (LDA) velocity measurement validation for air only flows.....	228
8.5.1 Control pipe validation results and discussion.....	228
8.5.2 Swirl pipe validation results and discussion.....	234
8.5.2.1 Validation of tangential velocity distribution of induced swirling flow.....	244
8.5.2.2 Validation of rate of decay of induced swirling flow.....	248
8.6 Further studies performed using the validated CFD models.....	251
8.6.1 Pressure variables.....	252

8.6.2 Air velocity variables.....	258
8.6.3 Turbulence dissipation.....	264
8.6.4 Particles flow simulation.....	268
8.6.4.1 Equations of motion for particles.....	268
8.6.4.2 Stochastic particle tracking in turbulent flow.....	269
8.6.4.3 Boundary and initial conditions for discrete phase.....	270
8.6.5 Particles flow simulation results.....	272
8.6.5.1 Pressure drop.....	272
8.6.5.2 Particle tracks.....	273
Effect of particle diameter on particle tracks.....	276
Effect of air velocity on particle tracks.....	280
8.7 Conclusions.....	283
Chapter 9: Conclusions and recommendations for future work.....	287
9.1 Conclusions.....	289
9.1.1 Contribution to knowledge.....	292
9.1.2 Possible application of swirl induction.....	293
9.2 Recommendations for future work.....	294
9.2.1 CFD modelling.....	294
9.2.2 Experimental work.....	297
Bibliography.....	299
Appendices.....	313

LIST OF FIGURES

Figure 2.1: Zenz Diagram demarking pneumatic flow patterns (Adapted from Pan, 1999).....	10
Figure 2.2: Typical examples of solid deposition in a horizontal pneumatic conveying pipeline: (a) annular deposition; (b) gravitational deposition. (From Yan and Bryne, 1997).....	13
Figure 2.3: Velocity profile in the near wall region.....	16
Figure 2.4: Roping phenomenon after a horizontal to vertical bend (from Bilirgen and Levy, 1999).....	19
Figure 2.5: CFD simulation of secondary flows pattern for particle laden gas after a horizontal to vertical pipe bend (from Schallert and Levy, 2000).....	22
Figure 2.6: Schematic diagram of an ERT system (from Dyakowski et al, 2000)...	25
Figure 3.1: Model illustration for physical balance of turbulence generation and dissipation in 2-phase flows.....	45
Figure 4.1: Examples of swirl generators: (a) Propeller type (b) Fixed vanes (c) Twisted tape (d) Rotating pipe.....	49
Figure 4.2: Distribution of the axial vorticity in swirl pipe flows generated by (a) radial guide vanes, (b) tangential swirler, (c) axial–tangential inlet, (d) rotation of honeycomb section.....	51
Figure 4.3: Radial distribution of typical mean tangential velocity component of swirl pipe flow.....	52
Figure 4.4: Classification of swirl types.....	55
Figure 5.1: Experimental Facility at the University of Manchester.....	68
Figure 5.2: Initial experimental rig.....	69
Figure 5.3: Schematic illustration of pneumatic conveying rig.....	72
Figure 5.4: The final pneumatic conveying rig for the present study.....	72
Figure 5.5: a) PFA particles; b) Filllite particles.....	73
Figure 5.6: Filllite size distribution by weight.....	74
Figure 5.7: Filllite size distribution by volume.....	75
Figure 5.8: Construction of wall tapplings in cm (from BS 848).....	78
Figure 5.9: Resulting pressure tapplings.....	79
Figure 5.10: Manometers.....	79
Figure 5.11: Geometry of conical inlet (BS 848).....	80
Figure 5.12: Compound flowrate coefficients of conical inlets (BS 848).....	81
Figure 5.13: Patented design of a 3-lobed boiler tube by Spanner (1945).....	82

Figure 5.14: Helical turbulence inducing test pipe geometry (in mm).....	85
Figure 5.15: Venturi feeder.....	86
Figure 5.16: Simplest feeding device for negative pressure systems.....	86
Figure 5.17: Inclined screw feeder with venturi.....	87
Figure 5.18: Vibratory feeder with venturi (Mills, 2004).....	88
Figure 5.19: Pre- and post- screw feeder fillite particles size analysis.....	89
Figure 5.20: Solids feeding mechanism.....	90
Figure 5.21: Orifice plate performance curve.....	91
Figure 5.22: a) Operation principle of cyclones; b) standard Lapple cyclone measurements.....	93
Figure 5.23: Finding the optimum cyclone diameter.....	95
Figure 5.24: Classification of air movers.....	96
Figure 5.25: Air Movers: (a) Centrifugal fan; (b) axial fan; (c) roots type blower; (d) sliding vane compressor; (e) liquid ring compressor; (f) rotary screw compressor.....	98
Figure 5.26: Experimental setup for fan tests.....	102
Figure 5.27: Experimental fan characteristic curves.....	103
Figure 6.1: Pressure measurement locations on the experimental rig.....	107
Figure 6.2: Pressure drop distribution (Standard error ± 0.00981 kPa).....	108
Figure 6.3: Pressure drop per unit length of pipe.....	109
Figure 6.4: Sudden change in geometry at swirl/circular pipe intersection (scaled up).....	109
Figure 6.5: Kodak motion corder SR ultra.....	111
Figure 6.6: High speed camera recording arrangement (modified from Sommerfeld, 1994).....	113
Figure 6.7: Measurement location.....	113
Figure 6.8: Experimental setup.....	114
Figure 6.9: Flow pattern 0-10D downstream of control pipe section (with white light).....	117
Figure 6.10: Flow pattern 0-10D downstream of swirl pipe section (with white light).....	118
Figure 6.11: Flow pattern 0-10D downstream of control pipe section (with laser sheet).....	122
Figure 6.12: Flow pattern at 2, 3, 4, 5, 8 and 10 pipe diameters downstream of control pipe section (with laser sheet).....	122

Figure 6.13: Flow pattern 0-10D downstream of swirl pipe section (with laser sheet).....	123
Figure 6.14: Flow pattern at 2, 3, 4, 5, 8 and 10 pipe diameters downstream of swirl pipe section (with laser sheet).....	123
Figure 6.15: DANTEC PIV system.....	126
Figure 6.16: The configuration of the measurement optics.....	128
Figure 6.17: Calibration of PIV system.....	129
Figure 6.18: Typical image pairs as captured by PIV system, showing seeding dropouts (circled in red).....	131
Figure 6.19: Vortices observed on velocity vector map from single image pair.....	132
Figure 6.20: Clouded image.....	132
Figure 6.21: Image from sieved Fillite particles as seeder.....	133
Figure 6.22: Velocity vector map resulting from averaging 100 image pairs when -100mm Fillite seeding particles was used.....	134
Figure 6.23: Number of -100mm Fillite seeding particles per interrogation area.....	135
Figure 6.24: Main components of the LDA system.....	139
Figure 6.25: Laser optics probe orientation for x, y and z velocity component measurement.....	142
Figure 6.26: SPT smoke generator (model 90).....	143
Figure 6.27: Illustration of procedure used to align the horizontal laser beams with the midplane of the pipe.....	144
Figure 6.28: Matrix of measurement points in any y-z plane.....	145
Figure 6.29: Location of measurement planes.....	146
Figure 6.30: Illustration of a measurement point in Cartesian coordinates system.....	150
Figure 6.31: Axial air velocity contours at 2D, 6D, 10D and 14D planes downstream of the outlet of the control pipe section.....	152
Figure 6.32: (a) Axial air velocity along the horizontal centreline of the pipe at plane 2D downstream of the control pipe at low, medium and high Reynolds number flows and (b) Axial air velocity along the horizontal centreline of the pipe at planes 2, 6, 10 and 14D downstream of the control pipe for the high Reynolds number flow.....	153
Figure 6.33: Axial air velocity contours at planes 2, 6, 10 and 14 diameters downstream of swirl pipe.....	154
Figure 6.34: (a) Axial air velocity along the horizontal centreline of the pipe at plane 2D downstream of the swirl pipe at low, medium and high Reynolds number flows and (b) Axial air velocity along the horizontal centreline	

of the pipe at planes 2, 6, 10 and 14D downstream of the swirl pipe for the high Reynolds number flow.....	156
Figure 6.35: Comparison of axial air velocity contours downstream of the swirl and control pipe for low, medium and high Reynolds number flows.....	157
Figure 6.36: Radial and tangential air velocity contours at planes 6 and 10 diameters downstream of swirl pipe.....	158
Figure 6.37: (a) w-air velocity (b) Tangential air velocity profiles downstream of the swirl and control pipe sections for all three Reynolds number flows.....	159
Figure 6.38: Comparison of axial and tangential air velocity at the cross sectional horizontal line at a distance of two diameters downstream of the swirl and control pipe sections.....	160
Figure 6.39: (a) The original points, (b) The original points post the deletion of 18 of the original points, (c) The final points including the 30 new points.....	162
Figure 6.40: Swirl numbers at planes 2, 6 and 10D downstream of swirl pipe for the low, medium and high Reynolds number flows.....	163
Figure 6.41: Trendline for estimating swirl decay rates.....	164
Figure 6.42: Time series measurement of axial velocities for low, medium and high Reynolds number flows.....	169
Figure 7.1: Overview of the (a) Segregated Solution Method (b) Coupled Solution Method (Fluent Inc, 2004).....	177
Figure 7.2: The near-wall regions of turbulent flows (Fluent Inc, 2003).....	190
Figure 7.3: Dimensions of computational model geometry (units = mm).....	195
Figure 7.4: Complete model geometry.....	196
Figure 7.5: Geometries of rig components.....	196
Figure 7.6: Boundary layer mesh for the (a) circular cross-section rig components and (b) swirl pipe.....	199
Figure 7.7: 2D unstructured mesh for (a) circular cross-section rig components (b) swirl pipe.....	200
Figure 7.8: 3D hexahedral mesh for (a) circular cross-section rig components (b) swirl pipe.....	200
Figure 7.9: QEAS quality for the different rig components.....	202
Figure 7.10: y^+ contours for rig model.....	203
Figure 7.11: Performance monitors for turbulence models.....	208
Figure 7.12: Performance monitors for wall functions.....	209
Figure 7.13: Performance monitors for viscous terms advection schemes.....	210
Figure 7.14: Performance monitors for pressure-velocity coupling schemes.....	212

Figure 7.15: Non-conformal interface at swirl/circular intersection.....	214
Figure 7.16: Scaled residuals for a baseline case for the rig model.....	215
Figure 7.17: Variation of static pressure at inlet with iteration number for a baseline case.....	216
Figure 7.18: Variation of static pressure at inlet with iteration number for a baseline case (last 100 iterations).....	216
Figure 7.19: Histogram of mass imbalance for a baseline case.....	217
Figure 7.20: Variation of mass imbalance between the inlet and the outlet with iteration number for a baseline case.....	217
Figure 8.1: Rig model geometry.....	223
Figure 8.2: Pressure planes for rig model with (a) control pipe section; (b) swirl pipe section.....	225
Figure 8.3: Gauge static pressure for the low, medium and high Reynolds number flow cases post control pipe section.....	226
Figure 8.4: Gauge static pressure for the low, medium and high Reynolds number flow cases post swirl pipe section.....	228
Figure 8.5: Comparison of axial air velocity contours from experimental and computational results (units = m/s).....	230
Figure 8.6: Computational horizontal centreline axial air velocity profiles post the control pipe.....	232
Figure 8.7: Comparison of horizontal centreline axial air velocity profiles post the control pipe section at plane 2D from experimental and computational results.....	233
Figure 8.8: Comparison of horizontal centreline axial air velocity profiles post the control pipe section at planes 2,6,10 and 14D from experimental and computational results for the high Reynolds number flow.....	234
Figure 8.9: Comparison of axial air velocity contours post the swirl pipe from experimental and computational results (units = m/s).....	236
Figure 8.10: Comparison of axial air velocity contours post the swirl pipe from experimental and computational results for the high Reynolds number flow (units = m/s).....	237
Figure 8.11: Comparison of axial air velocity contours post the swirl pipe from experimental and computational results for the medium Reynolds number flow (units = m/s).....	238
Figure 8.12: Comparison of axial air velocity contours post the swirl pipe from experimental and computational results for the low Reynolds number flow (units = m/s).....	239
Figure 8.13: Computational horizontal centreline axial air velocity profiles post the swirl pipe.....	240

Figure 8.14: Comparison of horizontal centreline axial air velocity profiles post the swirl pipe section from experimental and computational results.....	242
Figure 8.15: Comparison of horizontal centreline axial air velocity profiles from computational results post the swirl pipe and post the control pipe section.....	243
Figure 8.16: Comparison of experimental and computational tangential air velocity contours at planes 2 and 10D post the swirl pipe (units=m/s).....	244
Figure 8.17: Comparison between computational and experimental horizontal centreline tangential air velocity profiles post the swirl pipe at plane 2 and 10D.....	245
Figure 8.18: Comparison between computational horizontal centreline w-air velocity profiles post the swirl pipe and control.....	247
Figure 8.19: Comparison between computational horizontal centreline tangential air velocity profiles post the swirl pipe and control.....	248
Figure 8.20: Swirl numbers at planes 2, 6, 10, 14, 18, 22 and 26D downstream of swirl pipe for the low, medium and high Reynolds number flows....	249
Figure 8.21: Comparison between computational and experimental Swirl number values for the low, medium and high Reynolds number flows.....	250
Figure 8.22: Trendline for estimating swirl decay rates.....	250
Figure 8.23: Computational pressure profile in horizontal section of rig model for (a) control pipe; (b) swirl pipe.....	254
Figure 8.24: Static pressure distribution within model geometry for control and swirl pipe.....	256
Figure 8.25: Dynamic pressure distribution within model geometry for control and swirl pipe.....	257
Figure 8.26: Axial air velocity distribution within model geometry for control and swirl pipe.....	259
Figure 8.27: Axial air velocity profile within model geometry for control and swirl pipe.....	260
Figure 8.28: Tangential air velocity distribution within model geometry for control and swirl pipe.....	262
Figure 8.29: Axial and tangential air velocity profile within model geometry for control and swirl pipe for the three Reynolds number flows.....	263
Figure 8.30: Turbulence dissipation rate distribution within model geometry for control and swirl pipe.....	265
Figure 8.31: Turbulence dissipation rate distribution at (a) swirl pipe inlet plane and (b) swirl pipe outlet plane.....	266
Figure 8.32: Turbulence kinetic energy distribution within model geometry for control and swirl pipe.....	267

Figure 8.33: Location of injection plane in reference to rig inlet and swirl pipe inlet.....	271
Figure 8.34: Pressure drop due to addition of particles.....	273
Figure 8.35: Particle tracks coloured by particles' velocity magnitude for high Reynolds flow in control and swirl pipe.....	275
Figure 8.36: Particle tracks coloured by particle's velocity magnitude for high Reynolds flow in swirl pipe.....	276
Figure 8.37: Particle tracks coloured by particle diameter for high Reynolds flow in swirl pipe.....	279
Figure 8.38: Velocity vectors showing localised eddies inside the swirl pipe (circled in white) due to the non-conformal cross-sectional geometries of the swirl and circular pipes.....	280
Figure 8.39: Particle tracks coloured by particles' velocity magnitude for low, medium and high Reynolds flow in swirl pipe.....	282

LIST OF TABLES

Table 3.1: Computational studies of lean phase pneumatic conveying and turbulent swirling gas-solid flows.....	34
Table 4.1: General characteristics of vortices.....	50
Table 4.2: k- ϵ model constants.....	61
Table 5.1: Chemical properties of fillite.....	75
Table 5.2: Physical properties of fillite.....	76
Table 5.3: Refractive indices (from Duran/Schott Lab glassware catalogue, 1994).....	77
Table 5.4: Orifice plate calibration data.....	91
Table 6.1: Phase density conditions for experiments.....	106
Table 6.2: Inlet conditions used in experiments.....	107
Table 6.3: High speed recording specification (from Kodak Motion Corder Analyser User's Manual, Kodak Company, 1998).....	111
Table 6.4: Main operating parameters of LDA system.....	141
Table 6.5: Summary of measurement method.....	148
Table 6.6: Swirl decay rates for the three Reynolds number flows.....	164
Table 6.7: Error in Reynolds number calculation.....	169
Table 6.8: Error in LDA velocity measurements.....	171
Table 6.9: Error in calculation of cylindrical velocity components.....	173
Table 7.1: Breakdown of mesh quality with respect to Q_{EAS}	201
Table 7.2: Mesh quality analysis.....	202
Table 7.3: y^+ values for different rig components.....	203
Table 7.4: Mesh independence results for circular pipe.....	205
Table 7.5: Mesh independence results for swirl pipe.....	205
Table 7.6: Inlet boundary condition – mass flowrate.....	213
Table 8.1: Inlet conditions for CFD models of low, medium and high Reynolds number flows.....	224
Table 8.2: Percentage difference between computational and experimental gauge static pressure for low, medium and high Reynolds number flows post control pipe.....	227
Table 8.3: Percentage difference between computational and experimental gauge static pressure for low, medium and high Reynolds number flows post swirl pipe.....	228

Table 8.4: Percentage difference between computational and experimental axial air velocity values for low, medium and high Reynolds number flows post control pipe.....	233
Table 8.5: Percentage difference between computational and experimental axial air velocity values for low, medium and high Reynolds number flows post swirl pipe.....	242
Table 8.6: Percentage difference between computational and experimental tangential velocity air values at 2 and 10D for the low, medium and high Reynolds number flows.....	246
Table 8.7: Percentage difference between computational and experimental Swirl number values for the low, medium and high Reynolds number flows...	249
Table 8.8: Swirl decay rates for the three Reynolds number flows.....	251
Table 8.9: Planes locations.....	252
Table 9.1: Experimental and computational inlet flow conditions.....	288

NOMENCLATURE

General and Roman Symbols

C	-	log layer constant depending on wall roughness
d _e	m	laser beam diameter at focal waist
d _f	m	fringe spacing
d _m	m	measurement volume length in y-direction
d _p	m	diameter of solid particles
d _{pc}	m	diameter of particles that cyclone collects with 50% efficiency
d _{pj}	m	characteristic diameter of the j th particle size range
D	m	pipe diameter
D _b	m	laser beam spacing
D _e	m	width of cyclone vortex finder
D _l	m	laser beam diameter at converging lens
D _m	m	mean particle diameter
G _θ	Nsm ⁻² s ⁻¹	swirl/angular momentum flux
G _x	Nsm ⁻² s ⁻¹	axial momentum flux
f	m	lens focal length
f _D	Hz	frequency of Doppler shift
F _D	N	drag force
h _m	m	measurement volume length in z-direction
H	m	cyclone inlet height
I	cd	light intensity
k	-	Von Karman's constant
l _m	m	measurement volume length in x-direction
L	m	characteristic length of pipe
L _b	m	length of cyclone body
L _c	m	length of cyclone cone
L _e	m	development length for turbulent flow
m _j	%	mass percent of particles in the j th range
n	-	spread parameter of particle distribution
N _e	-	number of revolutions of gas through the outer vortex of a cyclone

Q_{EAS}	0	EquiAngle Skew
Q_M	kgs^{-s}	mass flow rate
Q_V	m^3s^{-1}	volumetric flow rate
r	m	radial distance from pipe centre
R	m	pipe radius
Re	-	Reynolds number
S	-	swirl number or swirl intensity
S_0	-	initial swirl number or intensity
S_{ref}	-	swirl number defined using the reference velocity
St	-	Stokes number
u	ms^{-1}	mean velocity in the x-direction
u_f	ms^{-1}	friction velocity
u_x	ms^{-1}	mean axial velocity
u'	ms^{-1}	root-mean-squared of velocity fluctuations in the x-direction
u'_x	ms^{-1}	root-mean-squared of axial velocity fluctuations
u_{ref}	ms^{-1}	reference velocity = the ratio of the average of the axial mean velocity over the radial span of the pipe
u_r	ms^{-1}	mean radial velocity
u'_r	ms^{-1}	root-mean-squared of radial velocity fluctuations
u_θ	ms^{-1}	mean tangential velocity
u'_θ	ms^{-1}	root-mean-squared of tangential velocity fluctuations
U	ms^{-1}	characteristic flow velocity (free mean stream velocity)
U^+	ms^{-1}	near wall velocity
U_t	ms^{-1}	velocity tangent to wall at a distance y from wall
v	ms^{-1}	mean velocity in the y-direction
v'	ms^{-1}	root-mean-squared of velocity fluctuations in the y-direction
V_d	m^3	volume of measurement volume
w	ms^{-1}	mean velocity in the z-direction
w'	ms^{-1}	root-mean-squared of velocity fluctuations in the x-direction
W	m	cyclone inlet width
x	m	distance in x-direction
y	m	distance in y-direction

y^+	-	dimensionless distance from the wall which defines where the log-law region of the velocity profile starts
Y_d	%	mass fraction with diameter greater than d_p
z	m	distance in z-direction
Δp	Pa	pressure drop
Δt	s	time interval

Greek Symbols

α	$^\circ$	half-angle between laser beams
β	-	decay rate of swirl intensity
δ	-	uncertainty or error
ϕ	-	phase density
γ	m	wavelength of the laser illumination
η_0	%	overall cyclone collection efficiency
η_j	%	cyclone collection efficiency of the j^{th} range
φ	$^\circ$	angle between edges of an element
λ	-	friction coefficient for fully developed flow
μ	$\text{kgm}^{-1}\text{s}^{-1}$	dynamic viscosity
ν	m^2s^{-1}	kinematic viscosity
θ	$^\circ$	angle with positive x-axis
ρ	kgm^{-3}	density
σ	-	standard deviation
τ_r	s	aerodynamic response time of particles
τ_f	s	characteristic time of the fluid motion
ω	s^{-1}	vorticity
Γ	m^2s^{-1}	circulation
Ω	rads^{-1}	angular velocity

Subscripts

solids	conveyed solid particles
p	conveyed solid particles
air	conveying air medium
g	conveying air medium
f	conveying air medium
c	concentration
in	at inlet
out	at outlet
hi	high (light intensity)
low	low (light intensity)

CHAPTER 1

INTRODUCTION

1.1 MOTIVATION FOR PRESENT WORK

The process of moving suspended solids in a gas stream through horizontal and/or vertical pipes is commonly referred as pneumatic conveying. Ever since the early twentieth century, bulk solid materials have been pneumatically conveyed on an industrial scale (Pacific Pneumatics Inc., 2005). The process of pneumatic conveying is applicable to many solid particulate materials with particle sizes ranging from tens of microns to tens of centimetres. Because of this versatility, the applications of pneumatic conveying have been extended widely across the process industries including chemical, pharmaceutical, food, mineral processing, steel, plastic, rubber and electric power generation.

One of the main concerns related to lean phase pneumatic conveying, where the particles are transported in suspended flow, is finding the right velocity to keep the particles in suspension, without escalating the costs associated with generating high conveying energy (see for e.g. Tashiro et al, 1997, Jama et al., 1999 and Herbreteau and Bouard, 2000). Achieving this condition has been difficult to achieve in industry, resulting in poor transportation of solids and blockage when too low conveying velocity is used; and high costs due to high pressure drops and pipe wear when the conveying velocity is too high.

The challenge of optimising pneumatic systems has resulted in a growing body of research. Preliminary evidence suggests that effective way to solve the velocity related problems of pneumatic conveying is to intervene locally (see for example Li and Tomita, 2000 and Ganeshalingam 2002). For example, when settlement occurs in a specific region such as after an enlargement in the pipeline cross section or around bends, the conveying velocity should not be increased indiscriminately for the whole pipeline but applied to those regions where it is needed. This localised application should prove to be more cost effective. One of the suggested ways is to locally increase the turbulence and conveying velocity of the fluid by imparting a swirling motion to the flow (Li and Tomita, 2000 and Ganeshalingam 2002).

Swirl flows have been used for a wide range of engineering applications such as chemical and mechanical mixing devices, separation devices, turbo machinery, etc. The common contraptions used to generate swirl flows include: propeller type swirl generators (Zaherzadeh and Jagadish, 1975; Bali and Ayhan, 1999), tangential slots (Hay and West, 1975), honeycomb structures (Nishibori et al., 1987), and inserts of twisted tapes, wires or tubes mounted at the inlet of the pipe (Narezhny and Sudarev, 1975; Algiffi and Bhardwaj, 1985). At the downstream end of these swirl generators the previously non-swirling flow acquires a decaying swirl flow pattern. These devices have proved popular as they are easy to install in a circular pipe. Regular maintenance is however required as the devices are prone to erosion and often detach themselves from the pipe wall.

At the University of Nottingham, research on designing swirl inducing pipes for slurry transport began in 1993. Based on experimental work and Computational Fluid Dynamics (CFD) modelling, Nottingham researchers have showed that a near-optimum design for such a device comprises of a lobed geometry of fixed cross-section and constant helix (Ganeshalingam, 2002; Ariyaratne, 2005). The helical swirl inducing pipe was found to reduce the pressure loss across bends for hydraulic flows and provide better particle distribution, thus potentially reducing localised wear. It was also shown that in the case of hydro-transport, blockage can be minimised even at comparatively higher concentration of conveyed solids.

The advantage of the swirl pipe over other swirl generation devices is that the swirl pipe is minimally intrusive to the flow compared to propellers, tangential slots, honeycomb structures and other inserts. It avoids blockage which would otherwise occur as the particles collect into and around these devices. The swirling motion generated from a swirl pipe is geometrically induced due to the lobed cross-section of the pipe and the twist of this cross section. This swirling motion can be used to locally provide the adequate turbulent motion for keeping the particles in suspension. The swirl pipe is believed to be perfectly suited as the twist and lobes of the swirl pipe produce centrifugal force which in turn increases average flow turbulence and promotes local secondary flows that prevent particle settlement.

Previous research by Ganeshalingam (2002) and Ariyaratne (2005) provided encouraging and positive results where the swirl pipe was applied to hydraulic flows. Against this, the present study extends the application of the swirl pipe to pneumatic flows.

Despite the large body of literature on the development and optimisation of pneumatic conveying systems, there is still a lack of understanding of the fluid dynamics involved in swirl-flow pneumatic conveying and its resultant particle distributions. This knowledge is essential to any of further developments and improvements of these systems, particularly so if swirling flow pneumatic conveying is to be subjected to an in-process application involving heat and/or mass transfer, reactions and/or comminution.

The unique contribution of this thesis to the literature is the application of a geometrically induced swirl to pneumatic flows to increase conveying velocities at a local level. In doing so, this study provides a better understanding of the fluid dynamics involved in swirl-flow pneumatic conveying and its resultant particle distributions.

1.2 AIMS AND OBJECTIVES

Taken together, the primary focus of this present study is to investigate the impact of a geometrically induced swirl on suspended particles in air, specifically the swirl flow induced by a twisted three-lobed helix pipe, placed in a horizontal pipe section and applied to a lean phase of particulate suspension in air. To provide an accurate picture, the swirling flowfield is characterised by the quantification of the velocity distribution, pressure drop, vortex formation and the decay of the swirl. This approach is to be extended to infer the influence of such a swirling flow on the cross sectional distributions of particles during lean phase pneumatic conveying.

1.3 METHODOLOGY

Two specific approaches are commonly deployed in research on pneumatic conveying: experimental and computational. Prior to 1990s, most of the research was based on an experimental approach. However, since significant progress has been made in the field

of Computational Fluid Dynamics (CFD) and the computational power to support it is widely accessible, researchers have increasingly deployed CFD in their work and used previous published experimental work to ensure the accuracy of their CFD models. This deployment of CFD models is motivated by the higher cost involved in carrying out experimental work and the limitations of available experimental techniques to investigate complex flows.

Hence, this present research deployed a more systematic research design which combined both experimental and computational approach to achieve the aforementioned objectives. The experiments allowed the collection of in-situ data for validation of the numerical models, which were then used to further investigate the swirl flow.

1.3.1. Experimental method

The experimental study was carried out on an experimental Perspex rig, using the helical turbulence-inducing pipe placed in a fully developed horizontal flow. High speed video visualisation techniques were used to examine the dispersion of the solid particles within the lean phase particulate flow downstream of the helical turbulence-inducing pipe. Particle Image Velocimetry (PIV) and Laser Doppler Anemometry (LDA) were also employed for measuring the instantaneous velocities of the flowfield downstream of the swirl-inducing pipe.

1.3.2. Computational method

The modelling was carried out using FLUENT version 6.2.16, which is commercially available, for developing computational models of the swirling flow conditions experienced in the experimental rig. In addition, the trajectories of the solid particles were modelled by the use of one way coupled Lagrangian particle tracking models.

1.4 THESIS OUTLINE

This thesis consists of 9 chapters. The first chapter sets out the context against which this research was carried out, the aims and objectives of the present research, a brief outline of the methodology, and an outline structure of the thesis.

Since this research work required a current working knowledge of two different topics, namely pneumatic conveying and turbulence modelling, their relevant literature were reviewed respectively in Chapters 2 and 3. Pneumatic conveying and turbulence modelling were then brought together in a logical way in an additional literature review in Chapter 4. The following four chapters (Chapters 5, 6, 7 and 8) form the empirical and the core elements of this thesis.

In chapter 2, a summary of the theoretical background to gas-solid flows in pipes and the factors affecting its optimisation are presented. This is followed by a review of a growing body of research on particle cross sectional concentration distribution and the underlying factors affecting it. A general description of the tools for visualizing the distribution of particle cross sectional concentration is also included.

The modelling of gas-solid flows in pipes is introduced in Chapter 3 and will be further expanded in Chapter 7. The main concepts examined include turbulence modelling, Eulerian and Lagrangian modelling approaches, 1-way and 2-way coupling, and the modulation of turbulence.

The swirling flows in pipes and its modelling are presented in Chapter 4. A brief description of swirl generation methods, types of swirling flows, their anatomies and parameterisation is provided. A summary of recent experimental and modelling work that has been done in the field of swirl flows and swirling flow pneumatic conveying is also presented. This covers a number of special topics of interest in the general context such as swirl decay rate.

In order to carry out the experiments, it was necessary to build an experimental rig. The selection and modification or design of each rig component, including the pipework, the pressure monitoring system, the air flowrate evaluation system, the particle feeding system, the gas-solid separation device, the air mover and the conveyed material. All these components are detailed in Chapter 5, along with an assessment of alternatives. A historical background of the design and applications of the swirl pipe is also outlined, along with the preliminary experimental work that was carried out on an initial test rig.

Chapter 6 is an experimental investigation of the use of swirl-inducing pipe for the gas-solid flow in pipes. It details the experimental investigations carried out using high speed camera, Particle Image Velocimetry (PIV) and Laser Doppler Anemometry (LDA). The experimental conditions are presented after a brief description of the basic principles behind each experimental technique. Finally, the present findings are presented, analysed and discussed. Each experimental method employed was treated as separate experimental programmes, with their individual aims and scopes. At the end of each experimental programme, conclusions were drawn, the aims and objectives reassessed and decisions made on the best way forward. The pressure gradient-flow velocity relationships and flow visualisation of particle distributions using high speed camera are given. The core of Chapter 6 presents the application of Laser Doppler Anemometry for velocity measurements of the flowfield with and without swirl-induction. A qualitative and quantitative comparison of the observed type of swirl is given and the swirl decay is critically analysed and compared to theoretical and empirical findings of other researchers. An assessment of experimental errors and uncertainties is also considered.

Chapter 7 highlights the features of turbulence models, modelling techniques and the solution methodology of Computational Fluid Dynamics (CFD). The numerical conceptualisation for CFD modelling including the Navier-Stokes equations, the numerical and discretisation schemes are introduced. This is then followed by an outline of the standard k - ϵ , RNG k - ϵ and the Reynolds stress turbulence models. The importance of near-wall treatment for wall-bounded turbulent flows and its implementation in the FLUENT CFD software is also highlighted. The second half of Chapter 7 describes the CFD model formulation for the simulation of the 3-lobed swirl-inducing pipe flow. This chapter builds on Chapter 4 and the first section of Chapter 7 to justify the choice of the meshing techniques, enabling assumptions and the solver parameters, including the turbulence model, discretisation schemes, and wall functions. This chapter also presents the performance and monitoring tests carried out to ensure that the numerical procedure employed is stable, consistent and robust; and that the errors associated with programming, spatial and temporal discretisation, convergence, iterative procedures and computer round-off have been fully resolved, and the model verified.

In Chapter 8, the CFD predictions are compared to pressure and velocity results measured on the flow rig. First, the difference between validation and verification was clarified and the comparison results of static gauge pressure as the first validation parameter is presented. Velocity data and the rate of decay from the experimental findings with and without the swirl pipe at three different Reynolds numbers formed the next sets of validation parameters. Additional CFD results, including the addition of particles into the flowfield, are also presented in the second part of Chapter 8 to obtain a better understanding of the induced swirling flow. The effects of adding particles on the static gauge pressure are also investigated and also the effect of particle diameter and conveying air velocity on the trajectories followed by the particles.

Finally, Chapter 9 provides a synthesis of all the present experimental and computational research and discusses the implications of the present findings for research and practice.

CHAPTER 2

LITERATURE REVIEW – GAS-SOLID FLOWS IN PIPES

2.1 INTRODUCTION

Researchers are constantly trying to optimise pneumatic conveying systems by finding new ways to keep energy losses to a minimum. Ideally the momentum of the particles should be high enough to avoid settlement and flow instability, but low enough to minimise particle attrition, equipment wear and to keep pressure drop and conveying velocity to a minimum. It is believed that these can be achieved by inducing swirl to the flow from the use of the swirl pipe within the pneumatic pipeline. A detailed understanding of particle behaviour within the pipe is also crucial for the proposed development of a physically based model for the numerical prediction of the wall-bounded particulate flows. A theoretical background to the gas-solid flows in pipes is presented in this chapter to provide a better understanding of the physics of the flow.

2.2 STOKES NUMBER

The response of a particle in an airflow is often characterised by the dimensionless number called Stokes Number, which is defined as the ratio of the aerodynamic response time of particles τ_r to a characteristic time of the fluid motion τ_f (Crowe, 1991). The latter can be a nominal length divided by a characteristic gas phase velocity.

$$St = \frac{\tau_r}{\tau_f} = \frac{\rho_p d_p^2 U}{18 \mu_g L} \quad (2.1)$$

As defined by Crowe (1991), for a given flow regime, a small Stokes number ($St \ll 1$) implies that the inertial effects are small, such that the time scale associated with particle inertia is much smaller than the time scale associated with the background fluid flow. The particles therefore respond rapidly to changes in the fluid motion and a near velocity equilibrium exists between the discrete particle phase and the continuous gaseous phase. A large Stokes number ($St \gg 1$) indicates that the particle motion is independent of the carrier gas flow as they are not able to respond to its changes. This

is typically associated with dense phase pneumatic conveying (discussed in Section 2.3), where the particle motion and colliding particles are highly de-correlated with the fluid motion.

2.3 PNEUMATIC CONVEYING CLASSIFICATION

Pneumatic conveying is usually classified into different phases according to the conveying air velocity and how much solids are being conveyed in relation to the conveying air, i.e. the mass concentration of solids to air ratio, also known as the phase density of the system. The volume concentration can also be used.

$$\phi = Q_{mc} = \frac{\dot{Q}_{m \text{ solids}}}{\dot{Q}_{m \text{ air}}} \quad \text{or} \quad V_c = \frac{\dot{V}_{\text{solids}}}{\dot{V}_{\text{air}}} \quad (2.2)$$

At a low end of the phase density scale is dilute (or lean) phase pneumatic conveying with a solids-to-air volume fraction typically less than 1% (Mills, 2004) and high enough conveying velocities (to keep the particles in full suspension in the gas. Under these flow conditions, the particles have individual behaviour with their motion being mostly governed by local aerodynamic forces. Particle/wall collisions rather than particle/particle collisions are predominant. At the high end of the scale is dense phase pneumatic conveying with solids-to-air volume fraction typically greater than 30 (Mills, 2004). Due to this combination of low velocity and high concentration, the particles are not fully suspended and particle-particle collisions dominate the motion of the particles.

Figure 2.1 depicts the Zenz diagram, which shows the transitions from dilute to dense phase. The boundary between these two flows is not well defined. For a fixed solids loading ratio, as the air mass flow rate is reduced for the same solids loading, the flow condition shifts from a steady phase (dilute or lean) to an unsteady phase (slug or plug) and finally to another steady phase (dense) (Pan, 1999), as shown in Figure 2.1.

In the unsteady flow region, a number of different flow patterns occur although many consider them to be a subset of dense phase pneumatic conveying. Some of the most distinguishable include the dune flow, slug or plug flow, discrete plug flow and saltation flow. Discrete plug flows are said to occur when discrete plugs of solids

occupy the full pipe cross section. Dune flow is characterised by a layer of solids settled at the bottom of the pipe and moving along in the form of rolling dunes. Plug or Slug flow is a hybrid of these two flow patterns. Saltation flow is characterised by conveying velocities which are slightly insufficient to keep the particles in suspension. The particles are therefore conveyed in suspension above a layer of settled solids, where the particles may be deposited onto and re-entrained from this layer.

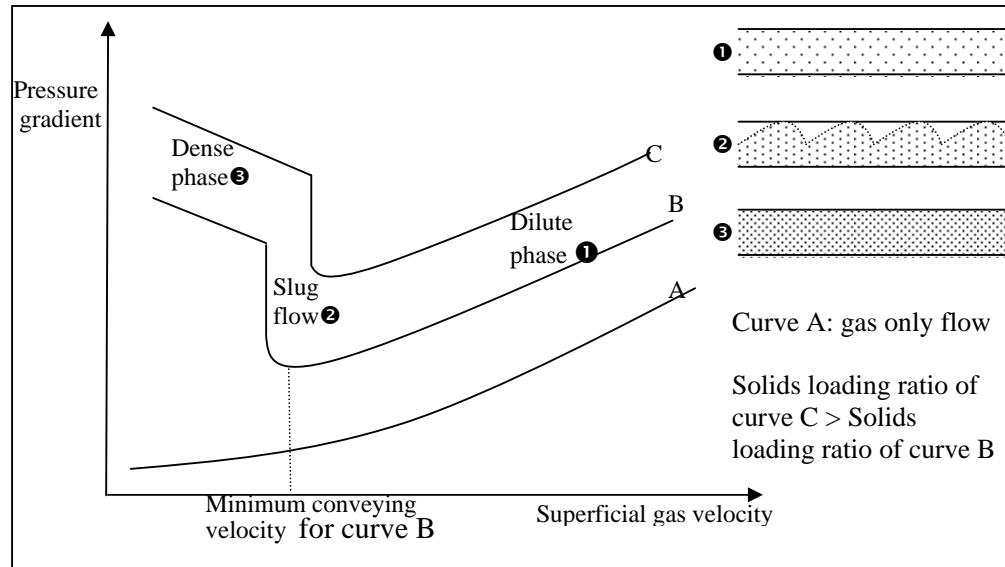


Figure 2.1: Zenz Diagram demarking pneumatic flow patterns (Adapted from Pan, 1999)

It was decided to study lean rather than dense phase pneumatic conveying. The reasons include that the particles are fully suspended and therefore more susceptible to the effect of swirl flows; that lean phase flows are used in 95% of pneumatic conveying applications; that the motion of the particles are governed by local aerodynamic forces of the surrounding flowfield; the absence of particle/particle collisions; and that the physics of the flow is simpler and easier to simulate than dense flow pneumatic conveying; . Hence the literature review will concentrate on lean phase pneumatic conveying. Dune flow, slug or plug flow, discrete plug flow and saltation flow will be considered as a subset of the dense phase pneumatic conveying.

The different flow characteristics render dilute (or lean) phase and dense phase conveying suitable for diverse applications. Dilute phase conveying is suited for transporting powders and non-friable products such as flour and starches. It is

frequently the most cost effective solution for the transport of chemicals, granular and pelletised products. In contrast, dense phase pneumatic conveying is suitable for high rate transfer of granular products, fine powders exhibiting good air retention capabilities (Jones and Williams, 2003), abrasive materials (e.g. cement, sand and metals), friable materials (e.g. sugar), and materials that are homogeneously blended and where segregation has to be avoided.

2.4 ENERGY MINIMUM STATE AND FACTORS AFFECTING IT

The shift from stable to unstable transport is marked by a characteristic point called the critical velocity, which has been defined as the transition from a temporally constant pressure behaviour of stand pipe transport to a strongly fluctuating pressure drop of slug flow or plug flow transport (Pan, 2000).

Another similar characteristic point is the saltation velocity. Although the two terms have been used interchangeably; recently, saltation velocity has been defined as the superficial gas velocity at which particles begin to separate from the gas phase and slide or roll along the bottom of the pipe (see for example Roco, 1993; Tashiro et al, 1997; Jama et al., 1999 and Herbreteau and Bouard, 2000).

One of the main factors when optimising pneumatic conveying systems is to keep energy losses to a minimum. Ideally the velocity of the particles should be high enough to avoid settlement and flow instability, but low enough to minimise particle attrition and equipment wear, and to keep pressure drop to a working minimum. The velocity which would enable steady and continuous flow whilst minimising energy losses is termed the pressure minimum velocity and is slightly above saltation velocity (Hong et al., 1995). It is believed that one way of achieving these conditions is by inducing swirl to the flow from the use of the swirl pipe within the pneumatic pipeline.

2.4.1 Effect of particle parameters on minimum energy state

Quantitative studies by Hong et al. (1995) and Yan and Byrne (1997) found that the magnitude of the saltation velocity was dependent on particle size. Huber and Sommerfeld (1994) and Hyder et al. (2000) observed that for the same conveying conditions the energy required to convey particles is dependent on the particle size.

These authors postulated that this may be due to the increased drag forces associated with an increase in particle sizes. Herbreteau and Bouard (2000) later confirmed that although the saltation velocity did depend on the particle size, shape and density, the particle diameter was the major factor.

2.4.2 Effect of particle/wall interactions on minimum energy state

Particle/wall interactions generate large drag forces that can result in large pressure drops being experienced in lean phase pneumatic conveying systems. Marcus (1984) concluded that the pressure drop experienced along a section of pipe can be reduced by employing an outer steel pipe that supplies bleed air into an inner porous pipe, to create an air envelope to the flow of materials.

2.4.3 Effect of operational factors on minimum energy state

Marcus (1984) also found that a reduction in drag could be effected by the introduction of high frequency reverse flow pulsations, e.g. by the use of a roots type blower. This effect was however attenuated after bends and localised drag reduction was experienced within long test sections. It was also concluded that to promote a smooth flow and therefore keep energy requirements to a minimum, a minimum fluctuation in the solids feed is crucial. This is usually achieved by the use of a volumetric feeder.

2.5 CROSS SECTIONAL PARTICLE DISTRIBUTION IN DILUTE PHASE PNEUMATIC CONVEYING SYSTEMS

A study of the cross sectional particle concentration distribution within pipe sections requires the resolution of forces which act on the suspended particles and the behaviour of these particles under these forces. In particular, this entails the identification of the prevailing conditions which are responsible for:

- Particle settlement
- Particle re-suspension
- Segregation of particle size.

It is generally accepted that the particle transport mechanism is governed by particle/wall and particle/particle collisions (related to the particle sizes), turbulent diffusion (the tendency for particles to move down particle concentration gradients) and turbophoresis (the tendency for particles to migrate in the direction of decreasing turbulence level) (Young and Leeming, 1997).

The quantification of solids deposition is particularly important in lean-phase conveying, as the amount of accumulated material is often comparable with or even greater than the amount of solids in suspension within a pipe cross-section. Young and Leeming (1997) developed an Eulerian Reynolds averaged turbulence model and found that turbulent diffusion flux and turbophoresis were mechanisms of highest importance that caused solids to deposit.

Yan and Byrne (1997) classified solids deposition within a horizontal pipe as either annular deposition or gravitational deposition, as illustrated in Figure 2.2. Annular deposition is expected at velocities greater than 15 ms^{-1} and low solid to gas mass flow rates ratio, as found especially in lean-phase conveying. Gravitational deposition is more likely at lower velocities and higher mass flow ratios in either lean or dense phase conveying. From the study, the authors found that the degree of solids deposition was directly proportional to particle size, solid adhesiveness and ratios of mass flowrates, but indirectly proportional to the particle velocity.

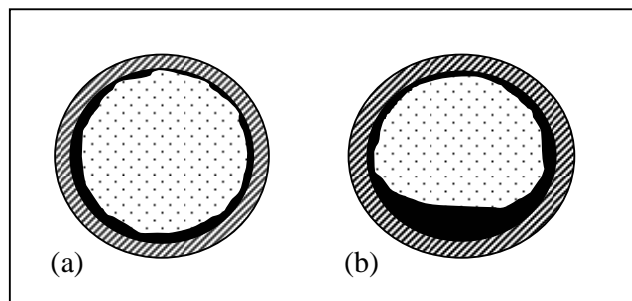


Figure 2.2: Typical examples of solid deposition in a horizontal pneumatic conveying pipeline: (a) annular deposition; (b) gravitational deposition. (From Yan and Bryne, 1997)

A physically based model for the numerical prediction of wall-bounded particulate flows to support process development and optimisation is of great interest for the

powder processing industries. However, this is not possible without a detailed understanding of particle behaviour within the pipe.

To study the cross-sectional particle distribution within pipe sections, it is important to understand the physics of particle motion, specifically the physical effects that cause settling or re-suspension of particles into a flow. They have been summarised by Huber and Sommerfield (1994) into the following factors:

- gravitational effects in horizontal pipes,
- inertial effects in pipe bends,
- turbulent transport of particles,
- Magnus effect (induced by particle-wall collision)
- Saffman lift force (transverse lift of forces due to particle rotation)
- particle-particle collisions
- modulation of the fluid flow and turbulence

Among these factors, Triesch (2001) established that for dilute phase pneumatic conveying, the most important features that dictate the particle concentration distribution include irregular particle-wall collisions, the effect of Saffman lift forces on particles close to the wall and the turbulent dispersion of fine particles.

2.5.1 Effect of Magnus force, shear stress and turbophoretic effect on cross sectional particle distribution

In most of the numerical simulation studies of the interaction of individual particles with the turbulent flow eddies, only the drag and gravity forces have been considered. However, lift forces are important when strong shear layers are present in the flow. For example, in the near wall region, the Magnus force (slip/rotation lift force) may have a significant influence on the particle motion for particles which are not freely rotating, or where particle-wall collision is significant. Sommerfeld (1990) showed that considerable improvements in the numerical simulation of turbulent gas/particle flows with a Lagrangian treatment of the particle phase can be achieved by including the lift forces resulting from shear flows and particle rotation. Ziskind and Gutfinger

(2002) suggest that shear is a causal factor to noticeable particle motion normal to the surface, and that is not predicted by consideration of purely turbulent effects. Louge et al. (1991) concluded that shear stress in the particle phase causes particles further from the wall to be lifted by the gas and through collisions, transfer momentum to particles closer to the wall. It was also concluded that the mean velocity profiles and the gas velocity fluctuations were rather insensitive to the actual values of the restitution coefficients, but were strongly influenced by the coefficient of friction, which governs the magnitude of the shear stress at the wall.

Portela et al. (2002) studied the near-wall behaviour of small, elastic-bouncing and heavy spherical particles in fully developed turbulent pipe flows without gravity, using direct numerical simulations (DNS). Close to the wall, the absence of a mean drag force was observed. Hence it was postulated that the turbophoretic effect, due to the gradient in the particle-velocity fluctuation in the radial direction, can only be balanced by a drift-velocity, caused by a gradient in the particle-concentration. It was concluded that for the region of $y^+ < 20$, local-equilibrium models are not adequate due to the fact that the reduction in the radial fluid-velocity fluctuation is not accompanied by an equivalent reduction in the radial particle-velocity fluctuation.

2.5.2 Effect of particle/wall collisions due to wall roughness and pipe diameter on cross sectional particle distribution

For small particles, the wall roughness considerably influences the wall collision process (Sommerfeld, 1995, 1998). When a hydrodynamically smooth wall is used, the assumption is that the viscous sub-layer is not pierced, whilst a rough wall will pierce the viscous sub-layer and cause a transfer of momentum from the flow direction to that normal to the wall.

In the near wall region, the velocity profile is given by (Schlichting and Gersten 2000)

$$U^+ = \frac{U_t}{u_f} = \frac{1}{k} \ln(y^+) + C \quad (2.4)$$

where

C is a log layer constant depending on wall roughness and

y^+ is a dimensionless distance from the wall which defines where the log-law region of the velocity profile starts.

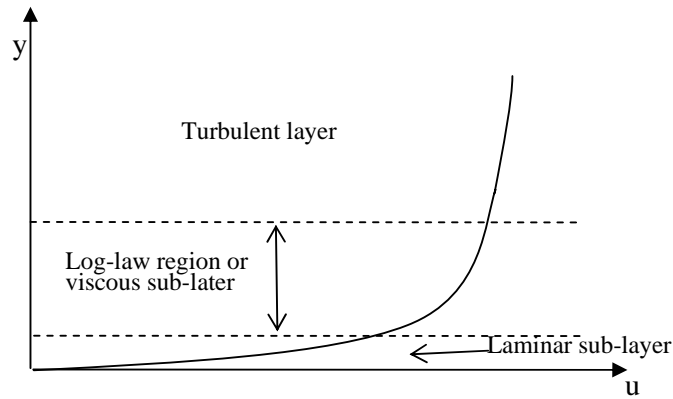


Figure 2.3: Velocity profile in the near wall region

Huber and Sommerfeld (1994) developed an Euler/Lagrange model for the calculation of dispersed gas-solid flows in pipe systems. The model addressed the significance of the effects like turbulence, two-way coupling, particle transverse lift forces, particle-wall collisions including wall roughness, and inter-particle collisions on the development of the two-phase flow in different pipe elements. The authors found that for rough walls, gravitational settling is reduced and particles are re-suspended due to the average increase of the rebound angle compared to impact angle. This also means that the particles require more energy to reaccelerate in the streamwise direction. It was concluded that wall roughness reduces the effect of gravitational settling, but increases the pressure loss in pneumatic conveying systems. These findings were confirmed in another study (Sommerfeld, 1998) in which a secondary gas flow was found to develop in the rough pipe cross-section due to a locally higher momentum transfer to the gas phase in the bottom section of the pipe induced by the wall roughness and particle-wall collision process. In smooth pipes, the turbulence is not sufficiently developed to disperse the particles and segregation of the two phases is evident. The higher particle mass flux at the bottom of smooth pipes causes a stronger coupling that in turn results in a pronounced deformation of the streamwise gas velocity profile.

Sommerfeld and Huber (1999) found that wall roughness considerably alters the rebound behaviour of the particles upon hitting the wall and causes a re-dispersion of the particles by reducing the effect of gravitational settling. In another study, Kussin and Sommerfeld (2002) confirmed that wall roughness decreases particle mean velocity and enhances fluctuating velocities due to irregular wall bouncing and an increase in wall collision frequency, i.e. a reduction in mean free path. Thereby larger particles are more uniformly distributed in the channel and gravitational settling is reduced. Particle velocity fluctuations were reduced with increasing mass loading due to inter-particle collisions and the momentum loss involved. Increasing wall roughness results in stronger turbulence dissipation due to two way coupling.

The effect of wall collisions was shown to be less significant for small particles. In 1990, Sommerfeld (1990) concluded from a numerical study that for the case of small particles ($d_p/D = 0.002$), the effect of the realistically modelled wall collision was found to have no considerable influence on the particle motion since they follow the mean fluid flow soon after the wall collision. Depending on the relative velocity between the particle and wall surface, the author observed sliding and non-sliding collisions and very high particle rotations after particle bounce. Sommerfeld (2003) also demonstrated that for small particles wall roughness causes a considerable reduction in wall collision frequency (i.e. increase of wall collision mean free path), while the opposite was true for particles with response times larger than about 50 ms. Sommerfeld and Kussin (2003) showed that the importance of wall collisions and hence wall roughness decreases with higher stream-wise mean particle velocities. This was particularly true for smaller particles.

Kussin and Sommerfeld (2002) also found that with an increase in pipe diameter, turbulent length scales increase but particle-wall collision frequency decreases and particles are better dispersed.

2.5.3 Effect of inter-particle collisions due to mass loading and particle size on cross sectional particle distribution

Elghobashi (1994) showed that the increased particle/particle collisions for pneumatic systems with a volume fraction greater than 10^{-3} affect the turbulence of the carrier phase. More recently, Sommerfeld (2001) introduced a stochastic inter-particle

collision model in an Euler/Lagrange frame that relies on the generation of a fictitious collision partner, which is representative of the local particle phase properties. Large Eddy Simulation (LES – an overview of which is given in Chapter 3) was used to validate the results and good agreement was reported. The model proved to be very computationally economic, since it does not require the search for possible collision partners in the vicinity of the considered particle. Collision frequency was found to increase with increasing Stokes number, peaking at Stokes numbers of about 0.4 thereafter decreasing for greater values. This was associated with the increasing velocity correlation of colliding particles and the fact that the kinetic theory limit is approached for particles following the turbulence. The simulations produced by models that did not consider the correlated particle motion in a homogeneous turbulence field, yielded a considerable over-prediction of the collision frequencies at particle Stokes numbers below 10. For the smallest Stokes numbers considered the difference was about one order of magnitude.

Sommerfeld (2003) proved that for particle volumetric fractions greater than 0.1, neglecting of inter-particle collisions gives completely erroneous results. Inter-particle collisions was found to cause a redistribution of the particle momentum from the streamwise to the lateral component until an equilibrium was reached. This resulted in an enhancement of lateral particle dispersion whereby gravitational settling is reduced. This was also found to be responsible for the components of the particle fluctuation velocities becoming more isotropic. In 2003, Sommerfeld and Kussin postulated that this was because of the dissipation of energy associated with inter-particle collisions.

2.5.4 Cross sectional particle distribution after bends

The flow of particle laden gas around bends produce variations in cross sectional particle concentrations. The forces acting on the conveyed particles at bends therefore differ from those experienced along horizontal and/or vertical conveying pipe sections. Consequently there have been many research studies to investigate the cross-sectional distribution of particle concentration at bends. The following section summarises the findings of recent research work.

2.5.4.1 Rope formation and disintegration mechanism

The results of the research work of Akilli et al (2001) provided an outline of the particle segregation process in pipe elbows due to the action of centripetal forces, whereby solid particles impinging on the outer wall of the elbow form a relatively dense phase structure in a small portion of the pipe cross-section close to the outer wall that is termed as a rope. Figure 2.4 diagrammatically illustrates the roping phenomenon. Just after an elbow, transport of particles is mainly due to the roping effect. The region of the rope has a much higher solid concentration than the remainder of the pipe. This high concentration increases the particle-particle collisions and causes the particles to decelerate. The ropes were dispersed further down the elbow where the particles accelerate and a secondary flow carries them around the pipe circumference and eventually to the middle of the pipe where turbulence causes them to spread over the entire cross-section. These observations were confirmed independently in other studies (Al-Rafai et al.,1990; Levy and Mason, 1998; Bilirgen and Levy, 2001).

The formation and disintegration of ropes are reported to be governed by centripetal forces, secondary flows, conveying gas velocity, elbow radius, solids loading, pipe orientation, particle size and diameter.

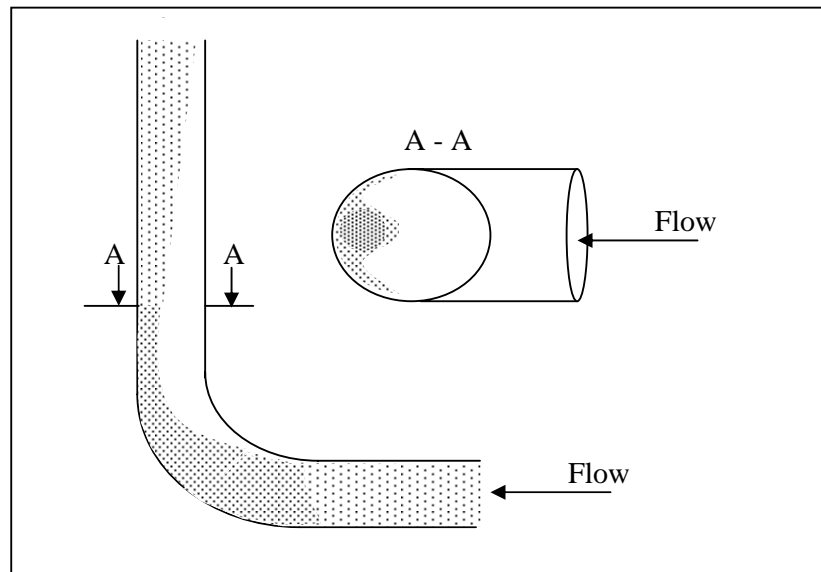


Figure 2.4: Roping phenomenon after a horizontal to vertical bend, (not to scale) (from Bilirgen and Levy, 1999)

The numerical model of Levy and Mason (1998), explained the dispersion of ropes by the formation of two vortices downstream of a bend for small particles, with the upper vortex being larger due to the influence of gravity and of higher particle concentration in the lower half of the pipe. For large particles however, a very, large vortex was predicted that engulfs the bottom vortex downstream.

For vertical to horizontal elbow sections, McCluskey et al. (1989) showed that the particles in the rope at the bend exit have a velocity one third of that of the average gas velocity. They observed formation of particle deposits near the elbow exit and concluded the deposit was created as the rope, travelling along the bottom of the pipe and was slowed by frictional forces to a velocity of zero.

2.5.4.2 Effect of particle size

Levy and Mason (1998) predicted that the maximum concentration is observed just downstream of a bend for small particles and further downstream for larger particles. The authors concluded that the paths taken by the particles after the elbow are strongly dependent upon particle size. Also the flow became fully developed sooner for larger particles. Because real particulate phases have a particle size distribution, segregation of particles in the pipe downstream of a bend is expected.

Huber and Sommerfeld (1994) inferred that bends cause a particle concentration segregation as well as a particle size segregation, both of which are more pronounced at lower gas velocity and higher particle loading. Contours of the average particle diameter by Akilli et al. (2001) confirmed these findings by indicating that the particles in the rope are much coarser than particles elsewhere in the pipe cross-section. Akilli et al. (2001) also predicted that higher conveying air velocities and solids loading ratios resulted in a denser rope, which required a longer distance over which to disintegrate. Whilst the two parameters affected the magnitude of the concentration values, they exerted little influence on the general shape of the fully developed profiles.

2.5.4.3 Combinations of bends

Schallert and Levy (2000) reported the results obtained from laboratory experiments and numerical simulations performed to determine the effect of two closely spaced

elbows on roping behaviour in a vertical pipe downstream of the second elbow. They confirmed that the rope that forms in the horizontal to vertical elbow is symmetrically positioned within the pipe cross-section, with its symmetry plane aligned with the axis of the pipe. However, the combination of elbows results in a more persistent and stationary rope, which spirals around the inside of the vertical pipe, adjacent to the pipe wall. They also inferred that two elbows resulted in significantly lower particle velocities in the rope than does a single elbow. The roping characteristics were found to depend strongly on the length of pipe connecting the two elbows, with an increase in the peak particle concentration being observed as the connecting pipes were made shorter. The angular position of the rope, peak particle concentration, and particle velocity in the rope were shown to depend strongly on the length of the pipe connecting the two elbows. The numerical simulations predicted that the gas phase secondary flow fields generated in the elbows were responsible for the spiralling motion observed with the double-elbow case. The double-elbow geometry produces a secondary flow field dominated by a single vortex that causes large-scale rotation over the pipe cross-section. The single-elbow configuration produces a double vortex that is symmetrically positioned within the pipe cross-section and is aligned with the axis of the inlet pipe.

2.5.4.4 Effect of bend radius to pipe diameter ratio

Huber and Sommerfield (1994) concluded that within a vertical pipe section located after a bend of radius to diameter ratio 2.54, the ropes that are formed disintegrate after a distance to diameter ratio of 12.5 and that a symmetric particle distribution is established after about twice that length. The use of a large bend radius results in a low particle concentration rope that disintegrates faster. Levy and Mason (1998) came to the same conclusion of a more uniform distribution of particles concentration downstream of a large bend from a computer simulations study. The authors also found that the maximum particle concentration in the rope depends on elbow radius-to-pipe diameter ratio, with a smaller ratio causing a smaller and higher concentrated rope region and a smaller variation in pressure across the pipe section.

Yilmaz and Levy (2001) concurred from their experimental and numerical results that formation and dispersion of a particle rope flow after a bend was strongly dependent on the pipe bend radius and to a lesser extent on the conveying air velocity and solids

loading. The experiments showed that ropes formed within the elbow with smaller pipe bend radius to inside pipe diameter ratio moved towards the centre of the pipe and dispersed at a faster rate, while the Computational Fluid Dynamics (CFD) models predicted that the rope flow stayed close to the outer wall and that its rate of dispersion was relatively slow. This discrepancy was attributed to the absence of particle-particle interactions in the CFD model. The CFD simulation results also indicated that secondary flows disperse the rope by carrying particles around the pipe circumference, as illustrated in Figure 2.5, whilst turbulence disperses the rope by localized mixing of particles.

Kussin and Sommerfeld (2002) advanced a new idea that inter-particle collisions within the regions of high particle concentration of the rope supported the dispersion and disintegration dust ropes formed after pipe bends.

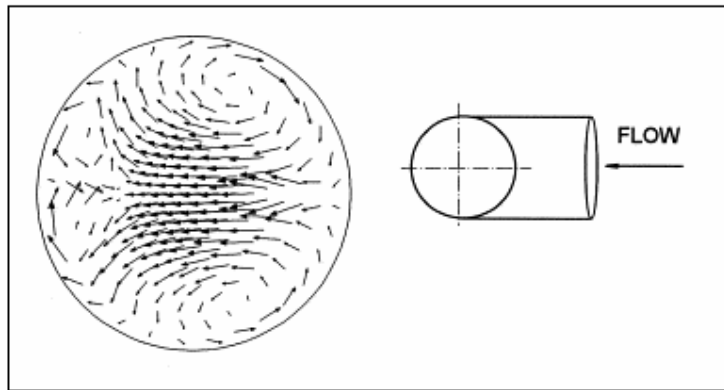


Figure 2.5: CFD simulation of secondary flows pattern for particle laden gas after a horizontal to vertical pipe bend (from Schallert and Levy, 2000)

2.5.5 Equipment wear and particle attrition

After operating for a period of time, industrial pneumatic conveyor rigs, the pipe components, especially at bends, suffer from wear due to the repeated erosive damage by particulate impact. Components of pneumatic conveying systems therefore have to undergo unplanned maintenance, thereby increasing production costs. Bridle and Woodhead (2002) presented an economic model prediction for the degradation level likely to occur in an industrial conveyor which can be used at the design stage of the pneumatic conveying system. Nonetheless, understanding particle concentrations in various pipe bends can help to reduce equipment wear (Burnett et al, 1998 and Burnett,

2001) and also particle attrition, which is usually considered as an undesired process in pneumatic conveying because it causes particle degradation. Parameters affecting particle attrition and equipment wear can be categorised as relating to particle strength (material, size and shape), to operational parameters (particle and air velocity and loading ratio) and pipeline design (number of bends and construction material).

Burnett et al (1998) investigated the wear that occurs at long radius bends. The authors concluded that the distribution of the particles at the bend is accountable for an intensification of particle impacts. This would result in pipe wear as the accumulated particles against the outside bend wall cause the particles to rebound back towards the pipe bore centre-line after primary impact.

In 1984 Hilbert found that a blinded-tee bend caused least particle attrition/equipment wear, closely followed by short radius elbow bends and the long radius bend caused the most equipment and particle damage. This is believed to be the result of the conveyed materials filling out the pocket of blinded tee bends, dampening the impact of the particle/wall collisions. In 1999, Kalman also investigated the effect of bend radius on particle attrition. The author subdivided the impact of collision into two components: a tangential one that causes a slight slide and shear loads and a normal component. The results show that most damage to particles was being caused by the normal component. The author therefore concluded that increasing the bend radius would increase the angle of collision and thus reduce particle attrition.

McKee et al. (1995), Bell et al (1996) and Papadopoulos (1998) showed that the air velocity was a prime effect on the attrition rate, although the effect of loading ratio and the bend structure could not be ignored. In 2000, Kalman also came to the same conclusions that a high air velocity that is typical to lean phase pneumatic conveying imparts high momentum to the particles and this turns into high impact load during collision. It was also concluded that lower attrition is achieved by operating at high loading ratio as this keeps the particle velocity low. Experimental results of Deng et al. (2005) also showed similar reduction of erosion rate for high particle concentrations and considered it to be a result of the shielding effect by the particles during the particle impacts. In the case of lower loading ratios, Kalman (2000) recommended the use of a flexible material for pipe-walls to absorb some of this collision energy.

2.6 VISUALISATION TOOLS FOR THE CROSS SECTIONAL PARTICLE DISTRIBUTION

The characterisation of flows, particle concentration distribution and the development and verification of models rely heavily upon the ability to observe and measure flow characteristics in working pneumatic conveying systems. It is therefore necessary to have reliable measurement tools, which can determine particle concentration and velocity at the pipe cross-section. Various measuring devices for measuring particle velocity (Laser-Doppler Velocimetry, LDV), solid mass flux (electrostatic and isokinetic probes) and density (phase-Doppler anemometry) have been used over the last decade (see for example Levy and Mason, 1998, Huber and Sommerfeld, 1994). Fibre-optic probes have also been used for measuring both particle velocity and concentration (see for example Yilmaz and Levy, 2001, Schallert and Levy, 2000, Alkilli et al, 2001 and Yilmaz and al., 1996) and various tomography systems have recently been developed for similar applications (see for example McKee et al, 1995, Dyakowski et al, 2000, Brown et al, 1996, and Deloughry et al, 2001).

The measurement techniques outlined above, may be divided into two broad categories: invasive and non-invasive techniques. Invasive techniques refer to methods where probes present within the flow are used for data capture. Local disturbances and changes in the solids concentration in the probe area, resulting in poor measurement quality have been observed (Dyakowski et al, 2000). Examples include electrokinetic and electrostatic probes and fibre optic probes. On the other hand, non-invasive measurement techniques have no physical parts within the flow and therefore do not cause any flow disturbances. Examples include LDV, PDA and all tomography methods.

2.6.1 Tomography

Very often in practice, the measurements made using a single probe are based on certain assumptions regarding the nature of the flow under investigation. Tomography, on the other hand, does not rely on such assumptions, but it can be used to verify their validity. Tomographic imaging techniques produce cross-sectional images of high temporal and spatial resolution of the distribution of flow components in a pipeline.

Tomographic techniques that are currently available include X-ray, γ -ray and positron emission tomography (PET) systems, magnetic resonance imaging (MRI), ultrasonic systems, electrical capacitance tomography (ECT), electrical resistance (or resistivity) tomography (ERT), optical and infrared tomography. There are advantages, disadvantages and limitations associated with the use of each of these techniques. In most cases, operational factors, such as physical properties of the constituents of multiphase flow, the desired spatial and temporal resolution of imaging, cost of the equipment, its physical dimensions, etc dictate the choice for a particular technique. A comprehensive review paper of electrical tomography methods for investigating, monitoring and controlling gas-solids systems was presented by Dyakowski et al (2000).

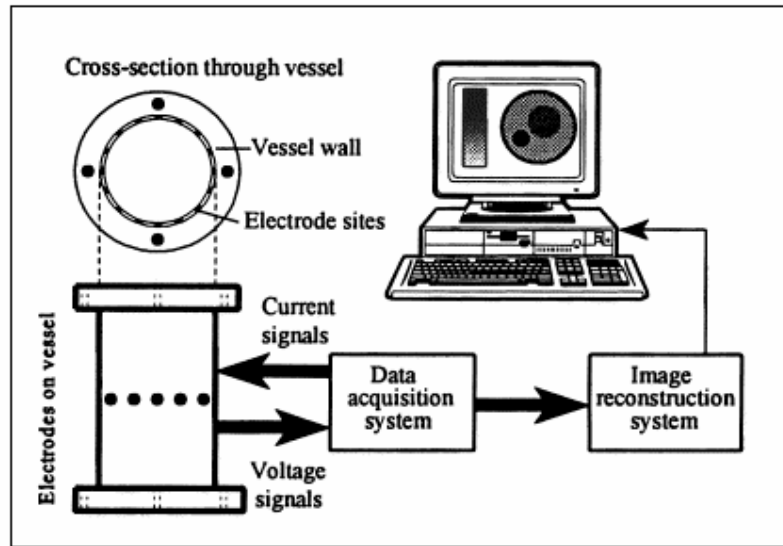


Figure 2.6: Schematic diagram of an ERT system (from Dyakowski et al, 2000)

McKee et al. in 1993 presented a discussion paper about the experimental application of capacitance tomography to the dilute phase pneumatic conveying of granular products. Capacitance tomography provides 2D imaging of the dielectric distribution of a contained medium. Images of materials with different permittivities are mathematically reconstructed and therefore different phases can be discerned. McKee et al. showed how the use of tomograms reflected dynamic events in real time and also represent an accurate portrait of the extent of solids homogeneity across a pipe cross-section within a conveying line. Subsequently, McKee et al. (1995) presented the

application of non-invasive capacitance tomographic technique to monitoring the behaviour of industrial scale pneumatic conveyors and analysing air conveying velocity and loading factor in relation to particle attrition. The images obtained allowed a better understanding of the mechanics of conveying and thus enabled the identification of an appropriate location for the sampling of a material stream. Deloughry, R.P. (2001) has shown that tomographic imaging could be used for closed loop control of a pneumatic conveying system.

Ultrasonic tomography techniques offer potentially higher resolution than capacitance techniques at comparable frame capture rates. However, as Brown et al. (1996) showed, it requires the use of frequencies in excess of 1MHz and can only be applied to particles of sizes greater than 1mm. Bearing in mind that the frequency used is size specific, a large particle size distribution is problematic. Hence an exact knowledge of the acoustic properties of the substances is necessary. Moreover, only a moderate resolution of both dense and dilute gas-solid distributions can be reconstructed when using an efficient back-projection method implemented with standard graphics algorithms. The measurement system is also vulnerable to electronic noise. Ultrasonic tomography is a technology that is still in the developing process but which holds great hope for its potentially unique ability for dilute flow visualisation. Further comprehensive review of ultrasonic tomography is provided by Hauptmann et al. (2002).

2.7 SUMMARY

The flow of gas and solids in pipes can be classified according to its phase density. Two main phases of pneumatic conveying were identified as being lean and dense. Lean phase pneumatic conveying is characterised by particles being in full suspension, the motion of the particles being governed by local aerodynamic forces of the surrounding flowfield, and the relatively low prevalence of particle/particle collisions. As a result, the physics of the flow is simpler and easier to simulate than dense flow pneumatic conveying. It was decided to employ a lean pneumatic phase in this study due to its susceptibility to swirl.

A minimum fluctuation in the solids feed was identified as crucial for a smooth flow and therefore keep energy requirements to a minimum. This was an important

parameter when the solids feeder system was designed for the pneumatic rig, as detailed in Chapter 5.

Solids deposition within a horizontal pipe was classified as either annular deposition or gravitational deposition. Particle/wall interactions were reported to generate large drag forces that can result in large pressure drops being experienced in lean phase pneumatic conveying systems. It was shown that after rebounding from the wall, particles require more energy to reaccelerate in the streamwise direction, creating further energy demands and pressure drops. This was identified to be potentially an important factor within the swirl pipe as the surface geometry of the swirl pipe lies on the streamline of the flow at the swirl pipe inlet.

It was also reported that for small particles ($d_p/D = 0.002$), the effect of the realistically modelled wall collision was found to have no considerable influence on the particle motion since they follow the mean fluid flow soon after the wall collision.

It was also identified that for flows where strong shear layers are present, for e.g. close to the boundary layers, Saffman lift forces and the Magnus force significantly influence on the particle motion and that considerable improvements in a numerical simulation of turbulent gas/particle flows with a Lagrangian treatment of the particle phase was achieved by accounting for these forces. These will be implemented in the subsequent computational simulation of a lean pneumatic phase within the swirl inducing pipe.

The physical factors which dictate the behaviour of solid particles in dilute phase pneumatic conveying are reported in the literature as:

- inertial effects (Akilli et al, 2001; Mason, 1998; Bilirgen and Levy, 2001)
- gravitational effects (Yan and Byrne, 1997; Levy and Mason, 1998)
- turbulent diffusion which is the tendency for particles to move down particle concentration gradients (Huber and Sommerfeld, 1994; Huber and Sommerfeld, 1995; Young and Leeming, 1997; Levy and Mason, 1998)

- particle size (Hong et al., 1995; Huber and Sommerfeld, 1994; Sommerfeld, 1995, 1998; Yan and Byrne, 1997; Levy and Mason, 1998; Herbreteau and Bouard, 2000; Hyder et al., 2000; Akilli et al., 2001; Sommerfeld, 2001; Kussin and Sommerfeld, 2002; Sommerfeld, 2003; Sommerfeld and Kussin, 2003)
- particle mass flow rate (Yan and Byrne, 1997; Sommerfeld, 2003)
- particle/wall collisions (Marcus, 1984; Huber and Sommerfeld, 1994; Sommerfeld, 1995, 1998; Sommerfeld and Huber, 1999; Triesch, 2001; Kussin and Sommerfeld, 2002; Sommerfeld, 2003; Sommerfeld and Kussin, 2003)
- inter-particle collisions (Elghobashi, 1994; Huber and Sommerfeld, 1994; Sommerfeld, 2001; Sommerfeld and Kussin, 2003)
- particle velocity (Yan and Byrne, 1997; Akilli et al., 2001)
- Turbulent modulation (Huber and Sommerfeld, 1994; Huber and Sommerfeld, 1995). This topic is discussed further in Chapter 3.
- Turbophoresis, which is the tendency of particles to migrate in the direction of decreasing turbulence level (Young and Leeming, 1997; Portela et al., 2002)
- Saffman lift forces, which is a transverse lift forces due to shear (Marcus, 1984; Sommerfeld, 1990; Loungue et al., 1991; Huber and Sommerfeld, 1994; Huber and Sommerfeld, 1995; Triesch, 2001; Ziskind and Gutfinger, 2002)
- Magnus effect which is due to particle rotation induced by particle-wall collision (Sommerfeld, 1990; Huber and Sommerfeld, 1994)

Ropes formation and disintegration post bends was described and reported to be governed by centripetal forces, secondary flows, conveying gas velocity, bend radius to pipe diameter ratio, solids loading, pipe orientation, particle size and diameter. Pipe wear and particle attrition were identified to be problematic in some pneumatic conveying systems. Parameters affecting particle attrition and equipment wear were categorised as relating to particle strength, material size and shape, to operational parameters (loading ratio, particle and air velocity) and pipeline design (number of bends and construction material).

The measurement techniques for flow characteristics in working pneumatic conveying systems, were divided into two broad categories: invasive and non-invasive techniques. Non-invasive techniques were the preferred choice for the subsequent experiments.

The use of these measurement techniques are only restricted to some flow conditions and properties. Hence researchers have recourse to computational fluid dynamics to investigate flow conditions and optimisations. Different approaches to the numerical modelling of turbulent pneumatic flows are presented in the next chapter.

CHAPTER 3

LITERATURE REVIEW – MODELLING OF GAS-SOLID FLOWS IN PIPES

3.1 INTRODUCTION

The previous chapter provided a review of the experimental findings of pneumatic conveying. This chapter reviews the literature pertaining to the application of computational models in examining the complex fluid dynamics associated with turbulent pneumatic flows. Due to the great diversity and complexity of the physical phenomena present in gas-solid flows, most of the previous study has been principally empirical. The employment of computational models has been driven by the cost of carrying out experimental research and the physical limitations imposed by the measurement techniques. Meanwhile, the rapid growth of computational power, allied to more efficient numerical methods, has allowed problems of flow modelling and visualisation to be tackled more precisely. Increasingly, researchers are using computational models to extrapolate experimental findings to other sets of conditions and to assist process development and optimisation of pneumatic systems:

- by predicting velocity and concentration profiles
- by predicting effects of bends and enlargements
- by understanding effect of inter-particle, particle/wall collision
- for attrition studies
- by predicting saltation velocity
- by simulating swirl flows

This chapter introduces three main concepts involved in computationally simulating turbulent pneumatic flows. They comprise of the different numerical models, representative model for the particulate phase, and the interaction of the particulate phase with the fluid phase. These are further expanded in Chapter 7. A summary of the modelling attempts of turbulent gas-solid flows is also presented to underline how numerous factors (such as particle size, particle loading, distance from the wall and the

relative velocity between particle and conveying gas) affect local particle concentration and the level of turbulence in the carrier phase during turbulence modulation.

3.2 TURBULENCE MODELLING APPROACHES

Navier-Stokes equations with additional terms that take into account the flows and generation of energy and momentum from the particulate phase can be used to describe gas-solid flows (see for example Tashiro et al, 1997). Alternative techniques are also given in the literature by stochastic models of particle trajectory (e.g. object oriented simulation, see for example Cartaxo and Rocha, 2001) or statistical models, which are based on a modified Boltzmann equation, associated most often with the Monte Carlo method (see for example Huber and Sommerfeld, 1998, Zhou et al, 2001, Triesch and Bohnet, 2001).

The numerical models commonly used for two-phase turbulent flows are:

- Two-equations model, of which the k- ϵ model is the most common. Here partial differential equations representing the conservation of mass, momentum and turbulence energy are incorporated into the numerical codes, and the effective eddy viscosity is related to the energy and dissipation rate. Computational Fluid Dynamics (CFD) techniques are derived from two-equations models. The partial differential equations are reduced to an approximate and equivalent set of algebraic equations, which are solved numerically to give the flow field at discrete points in the calculation domain. Most models reported in the literature are based on a two-phase description, one gas and one solid phase, where all the particles are assumed to have identical diameter, density and restitution coefficient.
- Direct Numerical Simulations (DNS): This method provides a direct three-dimensional, time independent solution to the non-linear Navier Stokes equations with no empirical closure assumptions (averaging or turbulence modelling). This numerical scheme must be able of resolving the smallest eddies in the turbulent flow. It therefore requires a large number of grid points that are sufficiently fine to resolve all flow eddies down to the very smallest scales; and a large number of time steps to reach a statistically steady state. DNS is therefore the most accurate way to numerically study

turbulent flows. In DNS, all the scales of motions, from the energy containing eddies (l) to the Kolmogorov length scales (η), are captured. The number of grid points (N) and timesteps (t) required are both functions of the Reynolds number. They are given respectively by $N = Re^{9/4}$ and $t = Re^2$ where $Re = (\eta/l)^{4/3}$. DNS is therefore restricted in application to modest flows with modest Reynold numbers.

- Large eddy simulation (LES). The large scale eddies are computed by direct numerical simulation while the small eddies are modelled. It involves both direct simulation and Reynolds averaging techniques. Because large scales are typically assumed to be the most important with respect to momentum and energy transport in turbulent flows, LES offers the advantage of being able to accurately incorporate these structures into the calculation. The smaller scales are generally assumed to be homogeneous and isotropic on average over space and time as well as relatively independent of the overall flow geometry. For these smaller scales, LES approaches therefore assume that a time average type model should be able to give reasonably accurate results. LES offers the practical computational potential to simulate much higher Reynolds number and geometrically more complex flows than are possible with DNS.

The equations most commonly used to model the carrier phase are based on volume averaging because the property values at nodal points are regarded as the average properties over a computational cell. If the particles are significantly smaller than the Kolmogorov length scale, then the effects of the particles are treated as point sources in the turbulent fluid. However, if the particles are comparable to, or larger than, the smallest scales of turbulence, the contribution of the boundary layers on these particle surfaces to the dynamics of the turbulent flow have to be included. Volume averaging requires that the volume dimension be much larger than the particle size. Thus the spatial resolution achievable must be larger than the smallest length scale of turbulence, so volume averaged equations tend not to result in a detailed turbulence model of the carrier phase.

3.3 EULERIAN V/S LAGRANGIAN MODELLING

Computational modelling efforts on gas-particle flows have developed into two parallel categories: Lagrangian and Eulerian models (Durst, 1984). Both approaches usually make use of turbulence closure schemes to obtain gas phase solutions. However, the Lagrangian approach treats the particles as discrete entities interacting with turbulent eddies in a Lagrangian coordinate frame while the Eulerian approach treats the particulate phase as a continuum having conservation equations similar to those of the continuous gas phase. Comparative studies of the two modelling approaches performed in fully accelerated gas-solids flow in vertical tubes resulted in close agreement on the predictions of average gas and particle velocity profiles (see for example Adeniji-Fashola and Chen, 1990). However, the Lagrangian particle tracking approach is better suited for modelling dilute phase pneumatic conveying (see for example Crowe 1982, 1986, 1996).

The two common particle dispersion models used are the Lagrangian approach and the two-fluid approach:

- Lagrangian (or Euler- Lagrange or trajectory) approach: Here the particle field is represented by particle trajectories obtained from integrating the particle motion equation. The particle mass, velocity, and temperature are simultaneously, calculated along the trajectories. Current Lagrangian models identify a packet of particles as a single computational particle with the same properties as the physical particle.
- Two-fluid approach (or Euler-Euler): This method uses volume averages of the particulate phase by summing the mass of each particle in the measuring volume and dividing by the volume. This approach requires that the averaging volume is large enough to yield a stationary value for the averaged property. Conservation equations are developed for mass, momentum and energy of the particle cloud, and these are integrated to predict the volume averaged particle properties throughout the field.

Crowe (1982) reviewed these two main numerical models available for modelling the dispersed phase in gas-particle flows that consider both the coupling effects between the phases and the mechanism of information transfer between the elements of the particulate phase. The author concluded that the two-fluid model can easily incorporate particle diffusion effects and can also be easily extended to multi-

dimensional flows. However, the large computational storage required for multiple particle sizes, numerical instabilities and numerical diffusion are major disadvantages. On the other hand, Lagrangian models gave the 'natural' solution schemes for each phase, required non-excessive storage for multiple particle sizes and the particulate phase exhibited no numerical diffusion. The drawback is the need to incorporate particle dispersion through an empirical diffusion velocity or expensive Monte Carlo methods.

Object-oriented simulation methods provide a deterministic treatment of the particles and fluid within the model's abstraction. In other words, the relevant dynamic phenomena and the several interactions with the neighbourhood are incorporated into each particle model. The immediate result is that, during the simulation, the dynamic state of the particles is updated along the time as a direct consequence of its interactions. As the particle dynamics are treated in an individual basis, detailed information about their positions, velocities and accelerations can be captured instantly.

Table 3.1 summarises the work done in the modelling of lean phase pneumatic conveying and the simulation of turbulent swirling gas-solid flows.

Author/ Year	Subject of Investigation	Modelling Approach	Factors accounted for	Validation method	Results and conclusions
Tashiro et al. (1997)	Saltation velocity Flow patterns around the saltation velocity	Lagrangian model	Fluid drag, gravity forces, Magnus force and Saffman force were superimposed to model the forced acting on the particles A particle source term was introduced in the Reynolds gas flow equation to account for the effect of particles on the gas flow The particles were assumed to be spherical and a regular bouncing model for particle-particle and particle-wall collision was used.	Comparison with experimental data	Despite some degree of accuracy in the model for the prediction of saltation velocity and total pressure drop in horizontal pneumatic conveying systems, comparison with experimental correlations showed considerable differences.
Huber and Sommerfeld (1998)	Evolution of cross sectional particle concentration distribution in a horizontal and vertical pipe of different diameters and pipe bends Conveying velocity Solids loading	3-D numerical predictions based on Euler/ Lagrange approach	Two-way coupling Turbulence Turbulence particle dispersion Rough walls/particle interactions Particle/Particle collisions	Comparison with experimental measurements using a PDA technique.	Rough walls increase particle-particle collision Secondary gas flows disperse regions of high particle concentration and reduce gravitational settling, thereby increasing the pressure drop. Accounting for particle-particle collision in the model is of importance for a proper prediction of the particle mass flux profiles, even for relatively low solid loading ratios. The model could not predict the formation and disintegration of dust ropes accurately.
Marjanovic et al (1999)	Simulate the flow structure which develops when gas- solids mixture flows through an	1-D analytical model	1-D model was solved for both isothermal and adiabatic conditions Pressure force by the fluid on the annular area of the pipe was used to model the	Comparison of 1-D analytical model to 3-D numerical model	The results from the 1-D model indicate possible influences of gas flow rate and solids loading ratio on the pressure recovery after an abrupt enlargement. Very good agreement was found when the

	abrupt enlargement	3-D numerical model	reaction force The 3-D model was based on the concept of interdispersal continua.		results were compared with the 3-D numerical model.
Zhou and Li (2000)	Simulation of the swirling gas-particle flows with swirl number of 0.47	A DSM-PDF 2-phase turbulence model and k- ϵ -kp model	Boundary conditions for gas phase were: measured inlet velocities and Reynolds stresses; fully developed flow exit conditions; axi-symmetric conditions at the axis, no-slip conditions at the walls. Particle-phase boundary conditions were: measured inlet velocities and stresses and assumed three-peak inlet PDF as fully developed flow exit conditions; symmetrical conditions at the axis and zero normal velocities and zero fluxes of other quantities at the walls.	Verification against experimental data reported in the literature.	For weakly swirling flows both models can reasonably predict the mean-flow behaviour, but the DSM-PDF model can better predict the anisotropy of two-phase turbulence and turbulence interaction between two phases, and hence may have the potential superiority in predicting strongly swirling flows.
Triesch and Bohnet (2001)	Simulation of a gas-solids flow in pipes to predict its axial particle velocity and solids concentration	CFD program (Fluent v. 4.4.8) using the Lagrangian approach for calculating the dispersed phase	the influence of surface roughness on the particle-wall collision; the laws of impact, distinguishing between sliding and adhesive friction; the angular velocity of the particles that is initiated by wall collisions; the Magnus and Saffman lift forces; particle-particle collisions.	Comparison with experimental measurements using a PDA technique	Good agreement was obtained between measurement and calculations only when factors describing particles motion were added via subroutines to the original version of the program.

Yilmaz and Levy (2001)	Flow non-uniformities that develop after a horizontal-to-vertical elbow bend	CFD model based on the Lagrangian particle-source-in-cell method	<p>2-way coupling was used to model the mutual interphase coupling.</p> <p>Particle/wall interactions were modelled using a coefficient of restitution with constant tangential particle velocity. Particle/particle collisions was not modelled.</p> <p>Renormalisation group κ-ϵ model was used to predict turbulent quantities within the flow field</p>	Comparison with time averaged experimental measurements.	<p>The model overpredicted the peak particle concentrations within the rope at the elbow exit as it did not account for particle-particle interactions.</p> <p>Secondary flows and turbulence on rope dispersion were identified</p>
Cartaxo and Rocha (2001)	Particle segregation Particle-particle interactions	Object-oriented model	<p>Newton's second law was used to describe the particle movements, giving realistic translational particles movement, with tridimensional characteristics and centrifugal force action along any axis</p> <p>The whole fluid inside the pipe was considered to be made up of several fluid volumes elements flowing in the axial direction. Each fluid element was submitted to tangential forces in the axial, gravity force and normal forces produced by pressure gradients.</p> <p>The modified κ-ϵ turbulence model for low Reynolds numbers was used to account for turbulence effects</p> <p>Frontal and oblique particle-particle collisions were accounted for but disregarded whenever the particles and fluid density ratio is much higher than</p>	Comparison of the model results with experimental data on two-phase flow	<p>Detailed information about the pattern of the flow such as particle, fluid velocities and local voidage was obtained</p> <p>The existence of a low concentration solid region by the pipe wall was observed.</p> <p>A crown-shaped fluid velocity profile, together with an increase in the solid hold-up inside the pipe was revealed with the addition of bidirectional coupling to the model.</p> <p>Satisfactory qualitative and quantitative agreement was demonstrated when comparing the model results with experimental data on two-phase flow</p>

			unity.		
Zhou and Chen (2001)	Effect of different swirl numbers 0.47 and 1.5 on the behaviour of turbulent swirling gas particle flows	Unified second order momentum (USM) two phase turbulence model	<p>Eddy-viscosity was assumed for the shear Reynolds stress component while the normal component was found by experiment</p> <p>Zero normal velocity, zero mass flux, zero gradients of longitudinal and tangential velocity were used for the particle phase.</p> <p>At the axis, symmetric conditions were adopted for both two phases.</p>	Comparison with k- ϵ -kp model and experimental data	<p>Model can predict well the axial time-averaged 2 phase velocities</p> <p>USM model is better at predicting tangential time-averaged 2 phase velocities of strongly swirling flows.</p> <p>Anisotropic 2-phase turbulence can be described only by USM model.</p> <p>Increasing swirl numbers increases tangential slip velocity and anisotropy.</p>
Zhou et al. (2001)	Simulation of swirling gas-particle flows in a co-axial sudden-expansion chamber with swirl numbers of s=0, s=0.47 and s=0.94	USM turbulence model based on a Lagrangian analysis	Crossing-trajectory effect, inertial effect and continuity effect are accounted for by the Lagrangian Analysis.	Comparison with PDPA measurement from experimental data	<p>Mean and fluctuation velocities of single-phase swirling flows and two-phase mean velocities of swirling gas-particle flows agreed with PDPA measurements</p> <p>Normal components of Reynolds stresses or the fluctuation velocities of two phases for swirling gas-particle flows could not be underpredicted</p> <p>Increasing swirl number changes the shape and sizes of re-circulation zones, the size of the solid-body rotation zone, reduces the turbulent fluctuation of two phases in the upstream region and enhances it in the downstream region.</p>

Table 3.1: Computational studies of lean phase pneumatic conveying and turbulent swirling gas-solid flows

3.4 ONE-WAY V/S TWO-WAY COUPLING

Numerical models for particle/gas flows are founded on one-way or two-way coupling. The leading assumption of the former is that the particulate phase has a negligible effect on the fluid phase. It is therefore applicable to dilute phase conveying with solids volume fraction less than 10% and Stokes number being characteristically lower than 1 (Crowe, 1991). In contrast, two-way coupling accounts for the interactive coupling and the mutual effects of the particles and the carrier gas, or turbulence modulation (discussed in section 3.5).

However, Sommerfeld (1995, 1998) showed that even at mass loading as low as 0.1, particle-particle collisions have strong influences on the profiles of the particle mass flux, particle velocities and the fluctuating motions of the particles. In 1995, the author used an Eulerian-Lagrangian approach to model the inter-particle collisions in the pneumatic flow. Collision probability, analogous to kinetic theory, was calculated at each time step along the particle trajectory. A stochastic method was then used to calculate the collision process and the resulting change of translational and rotational velocities of the particle. For large particles, an almost uniform particle concentration distribution was achieved when wall roughness was also considered. In 1998, Sommerfeld also used LES for a homogeneous isotropic turbulence flow to refine and validate the stochastic inter-particle collision model. It confirmed the importance of two-way coupling effects even in moderate mass loading as the inter-particle collisions caused the fluctuations of the particle phase to become more isotropic. These conclusions are supported by Zhang and Reese (2001).

3.5 TURBULENCE MODULATION

Modern viewpoint of turbulence classifies it as neither completely ordered nor completely random, but somewhere in between because of the existence of the coherent structures (persistent eddying motions) (Kline et al., 1967). The assumption that the effect of turbulence on the particles is purely that of a dispersive random nature is therefore no longer valid.

The level of turbulence of the carrier phase affects particle dispersion, the effective viscosity of the fluid, and the particle-fluid transfer coefficients. In turn the resulting local particle concentration affects the level of turbulence in the carrier phase. This is

known as turbulence modulation. According to Adeniji-Fashola and Chen (1990), almost all modelling efforts have failed to address the carrier fluid turbulence modulation due to particles because of a lack of understanding of the mutual couplings between the gas and particulate phase.

Elghobashi (1994) suggested that the degree of modulation of fluid turbulence in a fully developed channel flow by the solid phase is dependent on:

- particle size,
- particle loading,
- distance from the wall,
- relative velocity between particle and conveying gas.

3.5.1 Particle size

It has been found that small particles attenuate turbulence because they follow the turbulent fluctuations and add mass to the fluid while large particles generate turbulence as a result of the instantaneous relative velocity between the particles and the gas (Gore and Crowe, 1989, 1991; Elghobashi, 1994; Cao and Ahmadi, 1995; Stock, 1996).

In 1989, Gore and Crowe observed that a critical parameter determining the effect of addition of a dispersed phase on the turbulent intensity of the carrier phase was the ratio of particle diameter to a turbulent length scale. It was found that for values greater than a critical length scale ratio, $d_p/l_e > 0.1$, the addition of particles will increase the carrier phase turbulent intensity (where d_p is the particle diameter and l_e is the characteristic length of the most energetic eddy). Similarly for lower values of the critical length scale ratio, a decrease in the turbulent intensity of the carrier phase was observed. The results were interpreted as follows: small particles, which are smaller than the most energetic eddy, will follow the eddy for at least part of its lifetime. Part of the eddy's energy was imparted to the particle, since the eddy, through the drag force, was moving the particle. The turbulent energy of the eddy was therefore transformed into the kinetic energy of the particle and the turbulent intensity of the carrier phase was reduced. The larger particles tended to create turbulence (in its

wake) near the scale of the most energetic eddy, thus increasing the turbulent intensity of the fluid. In this case, energy was transformed from the mean flow, which was moving the particles, to the turbulent kinetic energy of the fluid.

The change in turbulence intensity with the addition of a second phase was later reported by Gore and Crowe (1991) to be a function of particle size, particle density, concentration, relative viscosity between the dispersed and continuous phases, fluid phase velocity, fluid density, fluid viscosity, fluid turbulent velocity scale and fluid turbulent length scale. In examining the effect of the other non-dimensional parameters, it was shown that they do not correlate the data as well as the critical length scale ratio. However, this ratio could not compute the magnitude of the increase or decrease in the turbulence level.

Stock (1996) showed that in fully developed flow, particles are spread by the stochastic interaction of turbulence with the particles, whereby groups of particles that started in the same area would eventually have the distance between them increase with time due to the random action of the fluid turbulence. The author concluded that this dispersion was controlled by the particle rms velocity and the particle Lagrangian integral time scale. The diffusivity decreased in all three directions and became more anisotropic as the particle diameter increased. For a fixed particle size, the diffusivity decreased as the fluid rms fluctuating velocity decreased. For all Stokes numbers particle diffusivity was found to be inversely proportional to the free-fall velocity of the particle.

The dispersion of heavy particles in an isotropic, stationary turbulence was found to be governed by Stokes number, drift parameter and the structure of the turbulence, which all in turn depend on the particle size, density, drift velocity and turbulence scales. The velocity at which the particle moves was always less than that of the fluid and was dependent on inertia and free-fall velocity. The velocity scale was a strong function of Stokes number for $St < 1$. As the Stokes number increased, the particle velocity scale became a stronger function of the drift parameter. The time scale of the particle was larger than that of the fluid time scale except for $St < 1$, when it became mainly a function of the Stokes number.

Small particles were found to have a tendency to decrease the gas phase turbulence because they follow the turbulent fluctuations and add mass to the fluid. Large particles, on the other hand, do not follow the gas phase turbulent fluctuations and generate turbulence in the gas phase as a result of the instantaneous relative velocity between the particles and the gas.

For large particles, the ratio of particle relaxation time to a typical large eddy turbulent timescale is large. Hence the gas influences the mean velocity of the particles but it has a smaller effect on their random motion. By analogy with molecular dynamics, the particle velocity distribution function can be determined as a solution of the Boltzmann transport equation by particle collision, rather than by the gas turbulence.

The author also reported that most of the Lagrangian models failed to give accurate trajectory predictions as they do not take into account the directional difference between the motion of the eddy containing the particle and the motion of the particle. If the particle and eddy are moving in the same or opposite directions and relative motion is large enough that the particle travels through the eddy before it decays, then the length scale that governs the motion was found to be the longitudinal spatial integral length scale. However if the particle and the eddies are moving perpendicular to one another and the particle moves through the eddy before it decays, then the motion was found to be governed by the transverse spatial integral length scale. When the drift velocity is large, diffusivity was controlled by the turbulence length because the particle moves through an eddy before the eddy decays. Therefore it was concluded that the length scale of turbulence limits the interaction time, instead of the time scale of the eddy.

Results of a turbulence modulation investigation carried out by Hussainov et al. (2000) showed that coarse particles attenuated the grid-generated turbulence resulting in an increase of the dissipation rate of turbulence and a decrease of the turbulent energy in the sub-range of the energy containing eddies.

3.5.2 Particle loading

Elghobashi (1994) proposed that for volume fractions less than 10^{-6} , the presence of particles have no effect on turbulence. For volume fractions between 10^{-6} and 10^{-3} , the

particles were found to augment turbulence, if the ratio of particle response time to turn-over time of a large eddy is greater than unity, or attenuate turbulence otherwise. For volume fractions greater than 10^{-3} , particle-particle collisions became important and the turbulence of the carrier phase was affected by the oscillatory motion due to particle collisions.

Cao and Ahmadi (1995) also found that that particle loading affected how the particulate phase interacted with the gaseous phase. It was found that for a mass-loading ratio of 0.6 or larger, the particulate fluctuation energy and its collisional production were important and affected the dynamic behaviour of two-phase flows. In many cases, production of particulate fluctuation energy exceeded its dissipation rate. As a result, the presence of particles promoted turbulence in the gas phase. The gas phase velocity profile was also found to become more flat due to the presence of particles. The larger the mass loading ratio, the flatter the mean air velocity profile became. The energy production of particulate and fluid phases was also found to be larger than their energy dissipations in most parts of the flow region except near the wall and the channel centreline regions for both dilute and dense flows. There was significant energy dissipation because of fluid-particle interactions.

Lun (2000) also concluded that even if suspension are dilute with the solid volume fraction of the order 10^{-3} , the interfacial coupling effects are still significant and should not be ignored. The interfacial force is responsible for modulating the fluid and particle velocity distributions but is not the only factor to do so. The interfacial kinetic energy interactions were found to not only influence the turbulence kinetic energy distribution but also the fluid and particle velocity distributions.

3.5.3 Distance from the wall

In 1991, Gore and Crowe extended their investigation to radial locations other than the centreline. They found that the critical value of d_p/l_e is increased closer to the pipe wall ($d_p/l_{e \text{ crit}} = 0.3$ at $r/R = 0.9$). It was hypothesized that this was due to the anisotropic nature of turbulence in the vicinity of the pipe wall.

3.5.4 Relative velocity between particle and conveying gas

Lun (2000) confirmed that turbulence modulation in fluid-solid two-phase flow system depends crucially on the particle Reynolds number, Re_p . The onset of flow separation around a smooth sphere in a laminar environment was reported to occur at a critical particle Reynolds number, Re_{pc} of 24 (Taneda, 1956). If $Re_c > Re_p$, then the particle was found to cause no turbulence modulation. For $Re_c < Re_p < 310$, only the ‘streamwise’ component was effective in augmenting the turbulence fluctuations. The turbulence modulation imparted in the fluid phase by the solid phase was assumed to decay in the same manner as the regular eddies, since the wakes were carried downstream by the surrounding fluid. Turbulence enhancement resulted for $Re_p > 310$.

3.5.5 Physical balance model for turbulence generation and dissipation by the particles

Following these findings, Kenning and Crowe (1997), presented a new model for modulation of carrier phase turbulence based on a simple physical balance model for turbulence generation and dissipation by the particles and which would predict the turbulence level in a gas-solid flow.

The authors found it necessary to introduce additional length scales due to the additional complexities that arise when particles are introduced into a flow. One such length scale is the diameter of the particles as the wakes produced by particles yield a length scale on the order of the particle size, and assuming that if the particle size is smaller than the Kolmogorov scale, it will not affect dissipation. Secondly there is the average inter-particle spacing. If the concentration of particles introduced into a flow results in an average inter-particle spacing smaller than the inherent dissipation length scale, the particles may interfere with the existing eddies breaking them up so that the new dissipation length scale is proportional to the average inter-particle spacing rather than the geometry of the pipe. Inter-particle spacing is usually normalised by the particle diameter (λ/d). Elghobashi (1991) showed that for $\lambda/d > 100$, two-way coupling regime is of considerable importance.

A hybrid length scale $L_h = \frac{2L_i\lambda}{L_i + \lambda}$, dependent on both the inherent dissipation length scale, L_i , and the average inter-particle spacing, λ/D was used in the analysis. The importance of inter-particle spacing as a turbulent length scale in particle-laden flows was highlighted as the model compared well with the available data.

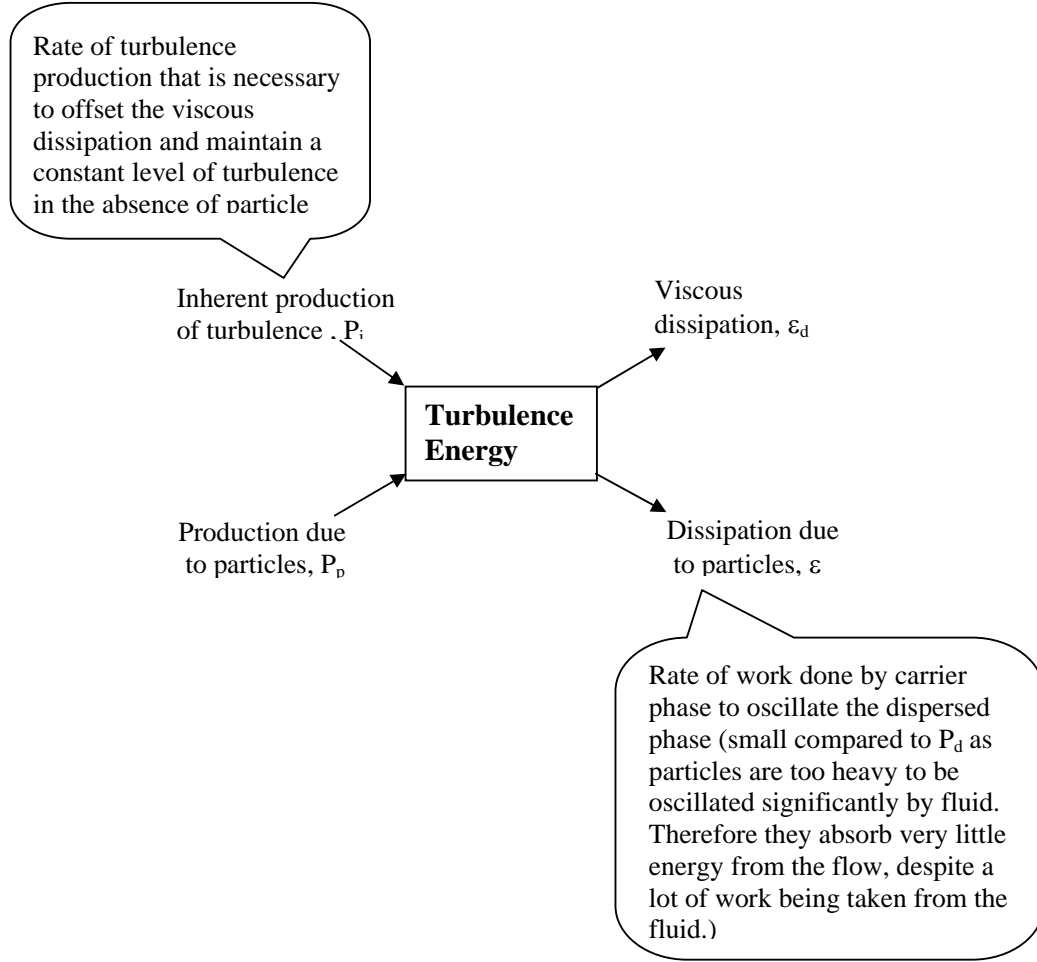


Figure 3.1: Model illustration for physical balance of turbulence generation and dissipation in 2-phase flows

3.6 SUMMARY

Gas-solid flows are commonly modelled using the Navier-Stokes equations with additional terms that take into account the flows and generation of energy and momentum from the particulate phase. Depending on the level of accuracy and the computational resources available, different modelling approaches can be employed, including two-equations models (as employed by most Computational Fluid Dynamics

techniques); Direct Numerical Simulation (the most accurate as even the smallest eddies are resolved and no empirical closure assumptions are made and therefore also the most expensive computationally) and Large Scale Simulation (a combination of both direct simulation and Reynolds averaging techniques).

When modelling gas-solid flows using 2-equations models, the gaseous phase is always modelled using the Eulerian approach. Modelling efforts of the particulate phase on the other hand have developed into two parallel categories: Lagrangian and Eulerian models. Lagrangian approach treats the particles as discrete entities interacting with turbulent eddies in a Lagrangian coordinate frame. The particle field is represented by particle trajectories. On the other hand, the Eulerian approach treats the particulate phase as a continuum having conservation equations similar to those of the continuous gas phase. The particles variables are calculated from resolving conservation equations similar to that of the gaseous phase. It has been reported that the Lagrangian particle tracking approach is better suited for modelling dilute phase pneumatic conveying.

Turbulence modulation in a gas-solid flow is said to occur when the resulting local particle concentration affects the level of turbulence in the carrier phase. It has been reported that most modelling efforts have failed to address the carrier fluid turbulence modulation due to particles. It was shown that the degree of modulation of fluid turbulence in a fully developed channel flow by the solid phase is dependent on particle size, particle loading, distance from the wall and the relative velocity between particle and conveying gas.

Small particles are reported to attenuate turbulence because they follow the turbulent fluctuations and add mass to the fluid while large particles generate turbulence as a result of the instantaneous relative velocity between the particles and the gas. Hence for small particles, turbulence energy of the eddies is transformed to heat and kinetic energy of the particle, thereby reducing the turbulent intensity of the carrier phase. Closer to the wall, due to the anisotropic nature of turbulence in this region, turbulence modulation is less sensitive to the presence of particles.

At solids volume fractions less than 10%, the presence of particles was reported to have no effect on turbulence (Crowe, 1986). At high volume fractions however,

particle-particle collisions becomes important and the turbulence of the carrier phase is affected by the oscillatory motion due to particle collisions. Sommerfeld (1995) later predicted that turbulence modulation is significant even at solids mass loading as low as 0.1. The work presented later on will show that this is not the case.

Turbulence modulation in fluid phase depends on the particle Reynolds number, Re_p . Turbulence modulation was shown to be insignificant if $Re_p < 24$, but for $Re_p > 310$, turbulence enhancement was reported.

Numerical models for particle/gas flows are founded on one-way or two-way coupling. Two-way coupling accounts for the interactive coupling and the mutual effects of the particles and the carrier gas, or turbulence modulation. On the other hand, the leading assumption of one-way coupling is that the particulate phase has a negligible effect on the fluid phase. It is therefore applicable to dilute phase conveying with solids volume fractions less than 10% and Stokes number being characteristically lower than 1.

This chapter highlighted the important factors to consider during the numerical simulations of pneumatic flows. The next chapter draws upon this knowledge and that of Chapter 2 to provide the backdrop for reviewing the work that has been carried out, both experimentally and numerically in the field of swirl flow pneumatic conveying.

CHAPTER 4

LITERATURE REVIEW – SWIRLING FLOWS IN PIPES

4.1 INTRODUCTION

Swirl flows are a common occurrence both in nature and engineering equipments. Over the centuries, engineers have invested heavily to strive for reproducing and controlling swirl flows where they are favourable to their applications; and suppressing, with great difficulty, the occurrence of swirl flows where they are undesirable. As swirl flows offer good fluid mixing and long residence times for complete reactions to take place, they are widely adapted in applications of various engineering areas such as mechanical mixing, separation, in combustion chambers, turbo machinery, and pollution control devices.

Recently it has been suggested that a localised application of swirl to a low velocity conveying fluid stream can increase velocity and improve the conveying process in both hydraulic or pneumatic transport (Li and Tomita, 2000; Ganeshalingham, 2002). Hence, it is important to understand how it is generated, develops and eventually dies out in order for swirling flows to be applied to a pneumatic system, as proposed by this present research. This chapter presents a theoretical background of swirl flows, including swirl generation methods in section 4.2, its nature and characteristics in section 4.3, a method of quantifying swirl in section 4.4 and a survey of experimental and numerical research into swirl flows and swirl flow pneumatic conveying in sections 4.5 and 4.6.

4.2 SWIRL FLOW GENERATION

Swirl flows can be generated from the application of a spiral motion to a laminar flow by the use of various swirl-generating methods. A swirl velocity component, also known as the ‘azimuthal’, ‘transverse’ or ‘tangential’ velocity component, is thereby imparted to the flow, resulting in a helical winding of the streamlines. Swirl flows are typically accompanied by an increase in velocity fluctuations.

All the methods used to induce swirl can be classified into 3 principal categories (Gupta et al, 1984):

- tangential entry such as axial-plus-tangential entry swirl generators, tangential slots (Hay & West, 1975), propeller type swirl generators (see Figure 4.1a) (Zaherzadeh and Jagadish, 1975; Bali and Ayhan, 1999)
- guided vanes such as swirl vane packs (Figure 4.1b), swirlers, honeycomb structures (Nishibori et al., 1987), inserts of twisted tapes (Figure 4.1c), wires or tubes mounted at the inlet of the pipe (Narezhny and Sudarev, 1971; Algiffi and Bhardwaj, 1985)
- direct rotation such as rotating pipes (Figure 4.1d)

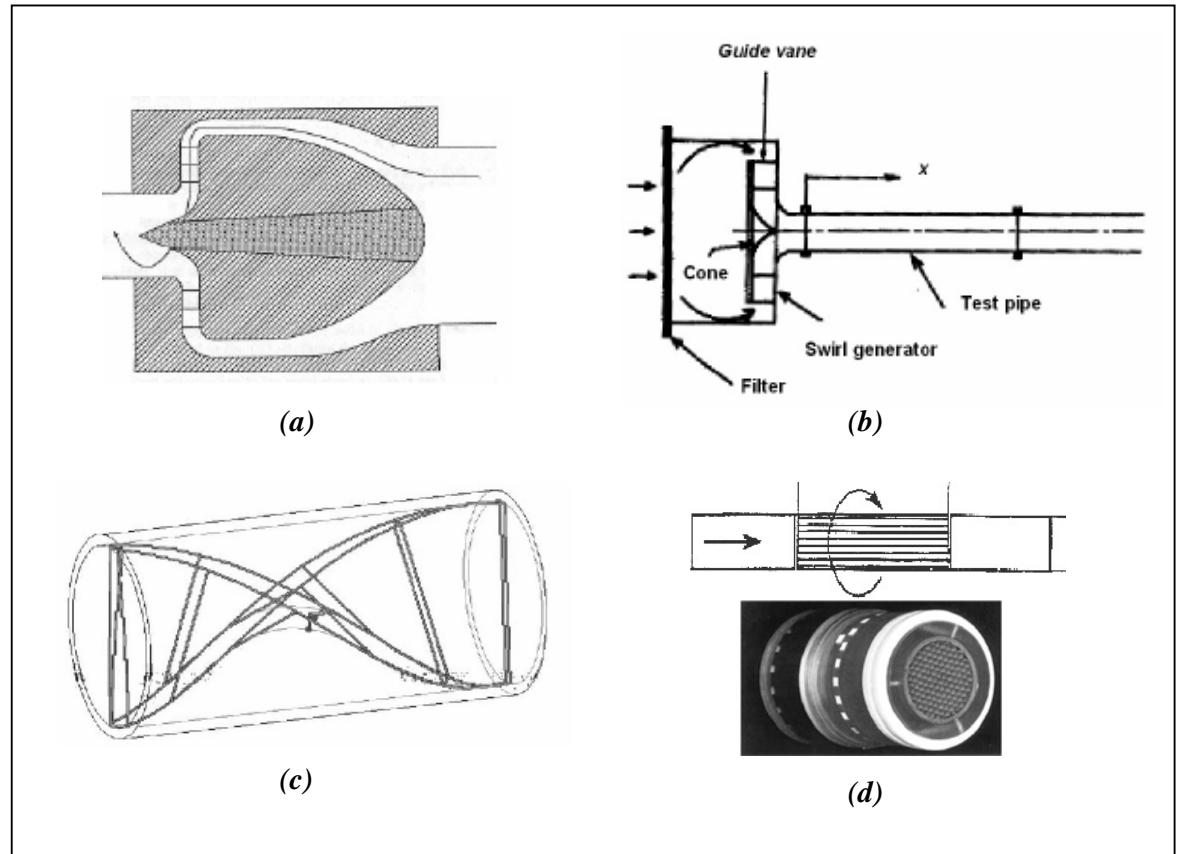


Figure 4.1: Examples of swirl generators: (a) Propeller type (b) Fixed vanes (c) Twisted tape (d) Rotating pipe

These devices have proved popular, as they are easy to install in a circular pipe. The main drawback however is the high pressure drop associated with them, causing the

total pressure requirements for the systems to be considerably higher. Also it is only possible to generate weak swirl to air flows by the above methods because of the relatively low viscosity of air.

Swirl flows are usually used in gas turbine engines, furnaces, burners and cyclones. In heat exchangers, swirl is usually induced to a flow to increase the turbulence of fluids in a pipe section so as to enhance convective heat transfer between fluids and pipe walls in heat exchangers. The induced turbulence also allows good mixing of fluids.

4.3 SWIRL FLOW ANATOMY FOR AIR-ONLY FLOWS

Downstream of the swirl generators, the previously non-swirling flow acquires helical streamlines, a characteristic of swirling flows. The flow tends to fade away until it eventually reverts back to a turbulent non-swirling flow a few pipe diameters downstream.

According to Baker and Sayre (1974) “A swirling flow in a pipe may be considered to combine the characteristics of vortex motion with axial motion along the pipe axis”. The fluid moves in helical paths and may be considered as a combination of primary and secondary flows (Chiu and Seman, 1971). The primary flow is parallel to the longitudinal axis whereas the secondary flow is a circulatory fluid motion about the axes parallel to the primary flow.

Kitoh (1991) and Martemianov and Okulov (2004) suggested that the method of swirl generation played an important role in the production of different types of swirl and the axial vorticity (spin) profiles. The results of Martemianov and Okulov (2004) showed that for guide vane swirlers the vorticity distribution is concentrated near the flow axis as shown in Figure 4.2(a). For tangential swirlers (Figure 4.2(b)) and swirlers with combination of axial and tangential entry (Figure 4.2(c)), the vorticity distribution is smoother. The last type of swirlers with rotating honeycomb section (Figure 4.2(d)) generates quasi-uniform vorticity distribution.

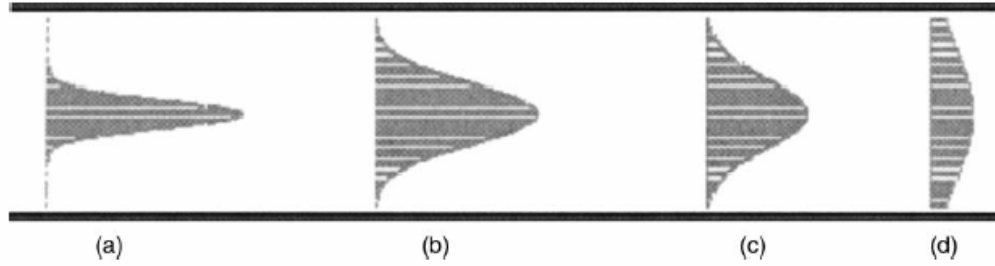


Figure 4.2: Distribution of the axial vorticity in swirl pipe flows generated by (a) radial guide vanes, (b) tangential swirler, (c) axial–tangential inlet, (d) rotation of honeycomb section

Gupta et al (1984) identified three categories of swirl flows: forced vortex, free vortex or Rankine vortex flows. Their general characteristics of vortices are summarized in Table 4.1.

	Forced vortex	Free vortex	Rankine Vortex
Tangential velocity distribution w	$c' r$	$\frac{c}{r}$	$\frac{c'}{r} \left[1 - e^{-\frac{r^2}{R^2}} \right]$
Angular velocity $\Omega = w/r$	$c' \text{ (constant)}$	$\frac{c}{r^2}$	function of radius
Circulation along one of the concentric paths of rotating motion $\Gamma = 2\pi r w$	$2\pi \Omega r^2$	$2\pi c$	$2\pi c' \left[1 - e^{-\frac{r^2}{R^2}} \right]$
Vorticity ϖ	$4\pi \Omega \text{ (constant)}$	0	$\frac{4\pi c'}{R^2} \left[1 - e^{-\frac{r^2}{R^2}} \right]$

Table 4.1: General characteristics of vortices

A forced vortex flow, also known as solid body vortex or rotational flow, is characterised by a sustained vorticity, while in the free vortex flow, also known as irrotational flow, the vorticity is not sustained and it eventually disappears. In real fluids, a combination of the forced and free vortices occur. Hence the Rankine vortex characterised by a central vortex core in which the vorticity is non-zero, and an outer region where the vorticity decreases to zero. This occurs because the tangential velocity component, which is zero at the centre, first increases with the radial distance to a maximum value and then decreases again with the radial distance. The vorticity therefore also varies with radial distance, resulting in a forced vortex closer to the axis

of symmetry and a free vortex further from it. Figure 4.3 shows a typical mean tangential velocity component profile from the centre to the wall of a swirl flow in a pipe.

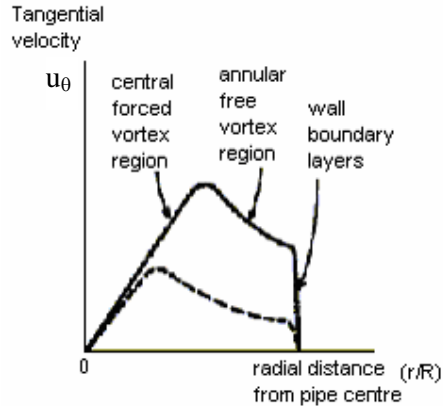


Figure 4.3: Radial distribution of typical mean tangential velocity component of swirl pipe flow.

This profile can be used to classify the cross-section of the swirling stream into three distinct flow regimes, which are characterised by the variation of the tangential velocity and Reynolds stresses (Kitoh, 1991; Algifri et al., 1988):

- Near the centre, in the “core region,” the flow is in rigid-body rotation, corresponding to a forced vortex. Here the flow is unstable and more turbulence is generated.
- Near the wall in the “wall boundary layers,” there are very high velocity gradients.
- Between the core region and the wall layers in the “annular region,” the flow is essentially a free vortex, with tangential velocity \approx constant. The flow is stabilized.

4.4 SWIRL FLOW CHARACTERISATION FOR AIR ONLY FLOWS

One of the outstanding characteristic of swirl flows is its topology as a helical winding of the streamlines. The pitch of the helix, given by the ratio of the tangential to the axial velocity, is an important quantity influencing the dynamics of the flow when swirl is present.

Although there is no standard for quantifying the degree or the strength of a swirl inside a pipe, the swirl intensity or number S , is commonly used. The definition of the swirl number varies from author to author. The complete form of its definition for pipe flow was given by Gupta et al. (1984) as Eq. 4.1 to 4.3. It is defined as a non-dimensional number representing the swirl/angular momentum flux divided by axial momentum flux and multiplied by the hydraulic radius. Thus,

$$S = \frac{G_\theta}{G_x R} \quad (4.1)$$

where

$$G_\theta = \int \left(\rho u_x u_\theta + \overline{\rho u'_x u'_\theta} \right) r^2 dr \quad (4.2)$$

and

$$G_x = \int_0^R \left(\rho u_x^2 + \overline{\rho u_x'^2} + (p - p_\infty) \right) r dr \quad (4.3)$$

The turbulent fluctuations are generally neglected, therefore the pressure and velocities are considered to be time-averaged. An exact calculation of the swirl number by means of Eqs. 4.1 to 4.3 is practically impossible since the velocity and the pressure fields are difficult to experimentally measure with a high accuracy. Simplifications to the definition are abundant in literature, and Gupta et al. (1984) have discussed a number of them.

The widespread simplification of the definition of the swirl number is given by the following formula (eg. from Rocklage Marliani et al, 2003):

$$S = \frac{\int_0^R u_x u_\theta r^2 dr}{R \int_0^R u_x^2 r dr} \quad (4.4)$$

Typically, the velocity profiles would be generated using a hotwire anemometer or LDV, and the swirl number obtained by using the experimentally generated velocity profiles and equation 4.4. However, this procedure requires the knowledge of the velocity profiles at every condition where the swirl number needs to be known.

Rocklage-Marliani et al (2003) further simplified equation 4.4 by replacing the axial momentum flux with a reference velocity u_{ref} , which is described as the average of the axial mean velocity over the radial span of the pipe, to define the swirl number as:

$$S_{ref} = \frac{2 \int_0^R u_x u_\theta r^2 dr}{R^3 u_{ref}^2} \quad (4.5)$$

Parchen and Steenbergen (1998) showed that swirl intensity, defined by Eq. 4.5, decays exponentially as:

$$S = S_0 e^{-\frac{\beta x}{D}} \quad (4.6)$$

where β is the decay rate and S_0 is the initial swirl intensity. The relationship between the swirl intensity, the decay rate and Reynolds number has been thoroughly investigated by researchers and will be discussed in sections 4.5 and 4.6.

Efficiency is a practical consideration since only part of the pressure drop across the swirler gets converted into kinetic energy of the subsequent swirl flow. The remainder is lost via thermal energy. The efficiency of swirl generation ε for a given swirl intensity is defined as the ratio of the kinetic energy of the swirl flow through the swirler to the drop in static pressure energy across the swirler.

4.5 SWIRL FLOW EXPERIMENTS FOR AIR-ONLY FLOWS

In order to further understand the physics of swirl flows, Kitoh (1991) introduced a free-vortex-type swirling flow in a long straight circular pipe and measured the velocity distributions and all Reynolds stress components at various axial positions in the pipe. From this study, the author classified the tangential velocity profile into three regions: core, annular and wall regions. The core region was described as being

characterised by a forced vortex motion and the flow in this region was found to be more dependent upon the upstream conditions than in the annular region. Here, the skewness of the velocity vector was reported to be noticeable and highly anisotropic. This contradicted the study by Backshall and Landis (1969), which showed that the universal logarithmic velocity profile is valid in the swirl flow after carrying out boundary-layer velocity measurements downstream of a twisted tape swirl generator. Kitoh (1991) also found that in the wall region the skewness of the flow was reported to become weak. For low swirl numbers ($S < 0.2$), the author reported difficulty in distinguishing between the core and the annular regions.

These findings were consolidated by Steenbergen and Voskamp (1998) who experimentally investigated the velocity components of swirling flows in smooth circular pipes for different Reynolds numbers and initial flow conditions. They identified three different types of swirl based on the radial distribution of tangential velocity components: a “concentrated vortex” (CV) with a rotation concentrated near the pipe centre, a “solid body rotation” (SB) with an almost uniform rotation, and a “wall jet” (WJ) with the angular momentum concentrated near the wall.

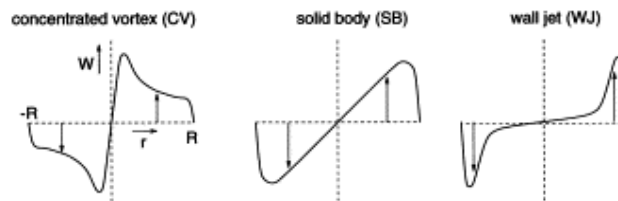


Figure 4.4: Classification of swirl types

Nishibori, K. et al. (1987) found that for a turbulent flow in an axially rotating pipe resulting from a honeycomb structure at the inlet, the axial velocity component was similar to that in a fully developed turbulent flow, while the tangential component of velocities exhibited a forced vortex type profile. This was later supported by Kitoh's (1991) indication that turbulence intensities gradually increases in the core region before decreasing in the annular. Algifri et al. (1988) and Parchen and Steenbergen (1998), among others, also report that Reynolds normal stresses reach their maximum values close to the pipe centreline.

The experimental results of Algifri et al. (1988) showed that the radial location of the maximum tangential velocity moves towards the pipe centreline as the distance downstream of the swirler increases, as predicted by the Rankine vortex-based model. As the flow proceeded downstream, Nishibori, K. et al. (1987) showed that the straight velocity gradient of the tangential velocity component gradually deformed into a concave profile.

Most of the research work that has been carried out in swirl flows, has been related to heating and cooling applications as the high turbulence resulting from the secondary flows created by swirling flows greatly improves the heat transfer coefficient of the fluids. Narezhny and Sudarev (1971), Hay and West (1975), Zaherzadeh and Jagadish (1975) and Algiffi and Bhardwaj (1985) among others showed the heat transfer coefficient was dependent on the initial flow swirl angle, swirl number and Reynolds number. We can infer from their conclusions that turbulence is also affected by these three factors.

Algifri et al. (1988) experimentally showed the three mean velocities and stress tensor were strongly dependent on the initial swirl but to be almost not influenced by the Reynolds number. They therefore suggested that swirling flows are “self modelling” with respect to Reynolds number. This finding was however disputed by Kitoh (1991) who maintains that the wall shear stresses are a function of both the swirl intensity and the Reynolds number, except in a short inlet region.

4.4.1 Swirl decay experiments for air-only flows

The presence of swirl is known to significantly promote turbulence level further downstream of the swirler. Baker and Sayre (1974) and Chang and Dhir (1995) attributed the phenomenon to energy conversion due to the existence of a destabilizing free vortex zone and a large shear stress at the boundary of the swirl flow. Wall shear stresses due to the pipe wall friction produce dissipating forces to reduce the high tangential velocities caused by the swirl flow close to the pipe wall. Hence the turbulence energy of the mean flow is transferred to the secondary flows, which in turn, preserve the turbulence level over a longer distance.

As the swirl decays, Bali (1998) observed a transition region between the forced vortex and free vortex zone, marked by a rapid decrease of tangential velocity to zero close to the wall. The profiles of the axial velocity exhibited a low velocity in the core region surrounded by a high velocity annular region. However, axial velocity decreased in the core region as the swirl decayed. The wall boundary region saw the maximum axial velocity, which decreased as the swirl decayed. As a result of the swirl decay, the peak tangential velocity was found to decrease with the axial distance from the swirl generator. Also, it was noted that the location where the tangential velocity is maximum moved towards the centre of pipe with axial distances, i.e., the core region shrinks as swirl decays. This finding is supported by Algifri et al. (1988) who showed that during swirl decay, the magnitude of turbulence intensities decreased radically at the core while the change was only slight closer to the wall.

Kitoh (1991), among many other researchers showed that swirl intensity decayed exponentially along the pipe axis. The decay of swirl with distance along the pipe is attributed to shear at the pipe wall. Swirl decay is therefore expected to follow an exponential function, similar to the wall shear (Baker and Sayre, 1974). Yu and Kitoh (1994) demonstrated that the exponential decay of swirl only held if friction coefficient does not vary with downstream distance. The authors also showed that the swirl decay was dependent on the inlet conditions and therefore on the initial swirl intensity.

Kreith and Sonju (1965) indicate that the swirl decay rate β in Eq. 4.6 varied with Reynolds number but is independent of the pitch, or initial swirl intensity. Baker and Sayre (1974) furthered that argument and suggested that decay rate was always inversely related to Reynolds number. Kitoh (1991) contradicted the findings of Kreith and Sonju (1965) and claimed that the decay rate depended on the initial swirl intensity but was not a constant as conventionally assumed for example by Parchen and Steenbergen (1998) who reported that the swirl decay rate ranges between 0.02 and 0.03. Steenbergen and Voskamp (1998) established that the rate of swirl decay varies with the Reynolds number in the same way as the friction factor does and expressed the decay rate of swirl intensity in terms of λ , friction coefficient for fully developed flow as:

$$\beta = (1.49 \pm 0.07)\lambda$$

The consensus is that the swirl decay rate is dependent on Reynolds number. However, the authors of the literature reviewed disagree on the effect of the initial swirl intensity on the swirl decay rate. This will be addressed in this study.

4.4.2 Experiments in swirl flow pneumatic conveying

A new swirling flow technique, called Swirling Flow Pneumatic Conveying (SFPC) was applied to horizontal pneumatic conveying by Li and Tomita (1996). It was found that the critical and minimum air velocities, the pressure drop, fluctuation of wall static pressure, the power consumption and additional pressure drop for swirling flow pneumatic conveying are all lower than that of conventional axial flow pneumatic conveying. A reduction of 13% and 7.5-17% were reported for critical and minimum air velocities respectively, while the reduction in the rate of power consumption was 14-20 %. The swirl was observed to be fully formed at a non-dimensional distance of $x/D=50$ and to have completely decayed by $x/D=112$. Furthermore, the particle concentration profiles in the SFPC were found to be symmetrically distributed with respect to the pipe axis. Despite the advantages of SFPC, the authors' main complaint was the lack of understanding of the behaviour of the particles in this unsteady and complicated non-linear dynamic nature of the flow.

The SFPC techniques were extended to a vertical pipeline by Li and Tomita (1998) and again the authors reported a 13 and 5-20% reduction in the critical and minimum air velocities respectively. When SFPC was applied in a curved bend by Li et al. (1999), the authors found that lower overall pressure drop and reduced particle impacts on the wall could be achieved.

Miyazaki et al. (1999) have shown that the use of a spiral-flow generating nozzle to transport soil in a sewage pipe installation system can decrease the power consumption and increase the distance of transportation. PIV together with image processing techniques were applied to measure the particle velocities and to obtain the probability distribution of the particle locations. A 30% decrease in pressure drop is reported compared to the conventional system. The reason of the higher efficiency improvement was attributed to the spiral flow moving the particles away from the region close to the pipe wall, causing a decrease in particle-pipe contact, and hence a reduction of particle-pipe friction.

4.6 SWIRL MODELLING

Swirl flow has also been investigated numerically and analytically. Many researchers investigated the applicability of the standard k - ϵ turbulence model and its variations to simulate swirl flows. A concise summary of their findings is presented below.

The standard k - ϵ failed to calculate the Reynolds stresses in the momentum conservation equations for swirling flows (Kobayashi and Yoda 1987; Khodadadi and Vlachos, 1990; Bali, 1998; Speziale et al., 2000; Najafi et al. 2005) as such flows are turbulent and cause considerable degree of anisotropy in stress and dissipation tensors leading to a highly anisotropic eddy viscosity (Kitoh, 1991).

Kobayashi and Yoda (1987) argued that neither k - ϵ model nor its modifications with higher order terms in the Reynolds stress equation are capable of predicting the axial and tangential velocity profiles in swirl flow because the eddy viscosity components are anisotropic. They proposed a modified k - ϵ model which considered an anisotropic factor for eddy viscosity, which was much more successful in their simulations in predicting the velocity profiles. Nejad et al. (1989) also found that k - ϵ model is not successful in solving the velocity field in swirling flows.

However, Bali (1998) experimentally and numerically proved that the k - ϵ turbulent model was used successfully to predict the weak swirl flows. In the study, the turbulent viscosity was considered to be isotropic since a propeller type swirl generator only imparted a small tangential velocity to the air flow in the pipe. Good agreement was found between the experimental and numerical axial and tangential velocity distributions along the pipe. Axial velocity profile showed a decrement in the central portion of the pipe and an increased axial velocity was observed near to the wall. Tangential velocity profiles had a maximum value and its location moved radially with distance.

Speziale et al. (2000) also argued that traditional two-equation models such as the standard k - ϵ model with conventional near-wall treatments could not predict two critical effects associated with turbulent flow in an axially rotating pipe. These effects were identified as being the rotationally dependent axial mean velocity and the presence of mean swirl velocity relative to the rotating pipe. The study revealed that

the presence of a mean swirl velocity is generated by a non-zero Reynolds shear stress $\tau_{r\theta}$, which at high Reynolds numbers, is confined to the near-wall region. Thus, even though its effects are felt throughout the pipe, the generation of a non-zero mean swirl velocity is largely a near-wall effect at high Reynolds numbers. The author further argued that at high Reynolds numbers, the traditional two-equation models could be used to predict this only with the implementation of a more sophisticated near-wall treatment that predicts a non-zero $\tau_{r\theta}$. The author emphasised that this was not applicable to cases with low Reynolds number.

As perfectly summed up by Speziale et al. (2000), the traditional two-equation models lack the necessary three-dimensionality and anisotropy that are elemental to the successful closures of turbulence models. These can be either three-dimensional algebraic models with a cubic non-linearity or full second-order closures. It is therefore not surprising that a 2D algebraic stress model, applied with conventional near-wall treatments, failed to predict the presence of a nonzero mean swirl velocity of a turbulent flow in an axially rotating pipe despite correctly predicting the rotationally dependent axial mean velocity. Conversely, the three-dimensional explicit algebraic stress model was able to correctly predict both the rotationally dependent axial mean velocity and the nonzero mean swirl velocity. The authors however found that the model would yield incorrect predictions at high Reynolds numbers for unbounded flows. Speziale et al (2000) affirmed that most of the existing second-order closure models have pressure-strain that have been developed for two dimensional mean turbulent flows that are close to equilibrium. It is reported that this is decidedly the case in the quadratic pressure-strain model, which is also known as the SSG model (Speziale, Sarkar and Gatski, 1991), and is implicit in the linear pressure-strain model of Launder and Spalding (1974). However, since the second-order closures contain production and Coriolis terms – the very effect which produces the rotationally dependent axial mean velocity and the nonzero mean swirl velocity, they were found to provide a good description of the rotationally dependent axial mean velocity and the nonzero mean swirl velocity.

4.5.1 Swirl decay modelling

All the authors agree that although the standard $k-\varepsilon$ is inadequate for or incapable of resolving the complex non-isotropic effects that are characteristic of strong swirling flows, it is adequate for simulating the more isotropic flow regimes of weak swirl flows and can also predict well the trends and the extent of the decaying tangential velocity in the turbulent pipe flow. This is because the decay is based on an isotropic eddy viscosity.

Hirai et al. (1988) analysed an axially rotating pipe flow using the standard $k-\varepsilon$, modified $k-\varepsilon$ and RSM models. They observed that the results of the modified $k-\varepsilon$ model gave better performance than the standard $k-\varepsilon$ model, and the results were comparable with that of the RSM. In their modified model, the source term in the dissipation equation was corrected by using the Richardson number, to take into account the effects of the curvature streamline. The Richardson number corrections are defined to increase the turbulence level in the regions with the negative tangential momentum gradient and to decrease it where this gradient is positive.

Khodadadi and Vlachos (1990) assessed the applicability of the standard $k-\varepsilon$ turbulence model and one of its variations in the prediction of swirl decay in developing turbulent pipe flow. The variation consisted of adjusting the constants in the $k-\varepsilon$ model from those recommended by Rodi (1975) when applied to confined swirling flows as follows:

Constants	Rodi (1975)	Khodadadi and Vlachos (1990)
C_μ	0.0900	0.1250
C_1	1.4400	1.4400
C_2	1.9200	1.5942
σ_k	1.0000	1.0000
σ_ε	1.3000	1.1949

Table 4.2: $k-\varepsilon$ model constants

It was found that the modified $k-\varepsilon$ model gave a slower decay than the standard $k-\varepsilon$ model, but that no substantial improvement was observed.

Parchen and Steenbergen (1998) also compared the standard k- ϵ model and the Reynolds Stress model for turbulence modelling in predicting the swirling flow. Based on the predictions on the decay of swirl and comparisons to experimental data, they concluded that the standard k- ϵ model, although insensitive to initial velocity distribution, predicted the decay more accurately.

Najafi et al. (2005) numerically compared the applicability of the standard k- ϵ model, the RNG k- ϵ model and the RSM model. The authors used both the standard wall function and the two-layer zone model for wall treatment to predict the turbulent swirl decay from a rotating honeycomb pipe in a vertical straight fixed pipe. The comparison between the numerical and the existing experimental results showed that the RSM with a two-layer zone model was generally more accurate than the standard k- ϵ and the RNG k- ϵ models in predicting the swirl decay. The findings also indicated that the two-equation models with either near wall treatments predicted correctly the swirling flow in solid body rotation regions, even if they failed to predict the pressure distribution along the pipe wall. It was also found that for all the models tested, the final solution was highly sensitive to the inlet axial velocities.

Good predictions of the flow were obtained from computations based on the Reynolds stress model for a swirling jet (Gibson and Younis, 1986); a swirling flow within two concentric cylinders (Hirai et al., 1987); and for a swirling flow inside both a diverging and a constant radius tube in predicting the vortex breakdown (Spall and Ashby, 2000).

Swirl decay seems to be just as well predicted by the standard k- ϵ model, as by the RNG k- ϵ model and the RSM model. The suitability depends on the application of the results, the level of results required and also the swirl inlet conditions.

4.5.2 Modelling of swirl flow pneumatic conveying

Li and Tomita (2000) carried out a numerical simulation for swirling flow pneumatic conveying in a horizontal pipe using a Eulerian approach for the gas phase and a stochastic Lagrangian approach for the particle phase. The irregular bouncing model of particle-to-wall collision by Tsuji et al. (1983) was used, where the point at which

the particle collides with the wall is assumed to be on an inclined plane. The particle-to-particle collision model by Tashiro and Tomita (1990) that employs a probability method is also used. The k - ε turbulence model was used to characterise the time and length scales of the gas-phase turbulence. Particle rotation, pressure gradient force, the virtual mass force, the Basset force, the Magnus effect and the Saffman force were however neglected. The results showed that the particle velocity and concentration has almost the same value along flow direction in swirling flow pneumatic conveying. The profile of particle concentration for swirling flow pneumatic conveying exhibits symmetric distribution towards the centreline and the higher particle concentration appears near the wall in the acceleration region. A uniform profile of particle concentration and particle velocity profile is observed downstream. The calculations were compared with the measured data and good agreement within an average error of less than 15 percent was obtained.

Sommerfeld and Ho (2003) also reported the inadequacy of full Reynolds-stress turbulence models and the k - ε turbulence for the numerical simulation of strongly swirling flows ($S > 0.5$). In the numerical modelling, the authors considered the following dominating micro-physical transport phenomena:

- turbulent transport of particles described by a Langevin model,
- particle-wall collisions with consideration of wall roughness,
- inter-particle collisions based on a stochastic modelling approach,
- agglomeration of dry solid particles.

The calculation indicated that by neglecting wall roughness effects on particle/wall collisions and inter-particle collisions, the results for the profiles of particle properties in the developed flow, namely concentration, mean velocity and mean fluctuating velocity components were completely wrong. Without wall roughness, the particles mean velocity was considerably over-predicted since the wall collision frequency and the associated momentum loss are too low. This effect also resulted in an under-prediction of the fluctuating components. The inclusion of wall roughness improves the agreement with measurements considerably, but still a rather strong gravitational settling of the particles was predicted. A further particle dispersion in the calculated

results was achieved by considering both wall roughness and inter-particle collisions. The latter was also found to cause an isotropisation of the particle fluctuating motion. It was therefore concluded that wall roughness plays an important role in the pneumatic transport of particles in pipes or channels and inter-particle collisions cannot be neglected even at a particle volume fraction of about 5×10^{-4} for a gas–solid system under atmospheric conditions.

4.7 SUMMARY

Swirl flows are widely used in industry in gas turbine engines, furnaces, burners and cyclones as they offer good fluid mixing and fluid turbulence for reactions to take place. However, the swirl flow patterns are extremely complex with limited data available to describe the flow regime. Popular swirl-generating mechanisms include tangential slots, propeller type swirl generators, swirl vane packs, swirlers, honeycomb structures, inserts of twisted tapes, wires or tubes mounted at the inlet of the pipe and rotating pipes.

Swirl generators impart a swirl or tangential velocity component to the laminar flow, resulting in a helical winding of the streamlines, characteristic to swirling flows. The swirling flow tends to fade away with distance until it eventually reverts to a turbulent non-swirling flow at a few pipe diameters downstream. A swirling flow was described as a combination of primary and secondary flows, whereby the primary flow is parallel to the flow direction and the secondary flow is a circulatory fluid motion about the axes parallel to the primary flow.

Swirling flows were classified as forced vortex (where vorticity is sustained), free vortex (vorticity is not sustained and it eventually disappears) or Rankine vortex flows (central vortex core in which the vorticity is non-zero, and an outer region where the vorticity decreases to zero, as in swirling pipe flows). Depending on Reynolds numbers of flows and initial flow conditions, three different types of swirl are reported based on the radial distribution of tangential velocity components: a “concentrated vortex” (CV) with a rotation concentrated near the pipe centre, a “solid body rotation” (SB) or “forced vortex” with an almost uniform rotation, and a “wall jet” (WJ) with the angular momentum concentrated near the wall.

Swirl intensity or number S is most commonly used for quantifying the degree or the strength of a swirl inside a pipe. It is a non-dimensional ratio of the swirl/angular momentum to the axial momentum of the swirling flow. The swirl intensity was reported to decay exponentially due to shear at the pipe wall. Although contradictions exist in the literature as to what affects the decay exponent, most of the reported work concluded that swirl decay was dependent on the inlet conditions and hence due consideration is given to the initial swirl intensity and Reynolds number of the flow.

Swirling flow has been applied to horizontal pneumatic conveying (Swirling Flow Pneumatic Conveying). It resulted in lower critical and minimum air velocities, pressure drop, fluctuation of wall static pressure, and power consumption than for the conventional axial flow pneumatic conveying. Furthermore, the particle concentration profiles were found to be symmetrically distributed with respect to the pipe axis. This is encouraging for the proposed application of the swirl inducing pipe to a horizontal lean phase pneumatic system. The dominating micro-physical transport phenomena in swirling flow pneumatic conveying were considered to be the turbulent transport of particles, particle-wall collisions with consideration of wall roughness and inter-particle collisions. Numerical results indicated it is important to consider wall roughness effects and inter particle collisions in the estimation of particle properties in terms of concentration, mean velocity and mean fluctuating velocity components.

Traditional two-equation models were reported to unsuccessfully solve the velocity field in strong swirling flows ($S > 0.5$) as it fails to calculate the Reynolds stresses in the momentum conservation equations for strong swirling flows. This is attributed to such flows being turbulent and causing considerable degree of anisotropy in stress and dissipation tensors which further lead to a highly anisotropic eddy viscosity. Against this, the two-equation models lack this necessary three-dimensionality and anisotropy that are elemental to the successful closures of turbulence models. On the other hand, it was reported that second-order closures, such as the Reynolds Stress Model, were found to provide a good description of the flow, in terms of the rotationally dependent axial mean velocity and the nonzero mean swirl velocity, since the model contains production and Coriolis terms.

The opposite was however true for modelling weak swirls ($S < 0.5$) or decaying swirl and vortex breakdown. The traditional two-equation models were found to be adequate for simulating the more isotropic flow regimes of weak swirl flows and can also predict well the trends and extent of the decaying tangential velocity in the turbulent pipe flow. It is believed that this because the decay is based on an isotropic eddy viscosity. This is however contested and some researchers still maintain that the Reynolds Stress Model is generally more accurate at predicting swirl decay than standard or modified $k-\epsilon$ models. Swirl decay seems to be just as well predicted by the standard $k-\epsilon$ model, as by the modified $k-\epsilon$ model and the Reynolds Stress model. The suitability depends on the application of the results, the level of results required and also the swirl inlet conditions.

This final chapter of literature review is central to the research work that was proposed. Firstly, it introduced a quantitative measure that captures the significant attributes of swirl flows and in turn allows a better definition of the parameters for the proposed experiments. Secondly, it provided a preliminary set of evidence of how swirl flows can mitigate the localised velocity drop experienced in pneumatic conveying lines, for example after pipe enlargements. Thirdly, it identified a void in research on the understanding of the extremely complex swirl flow patterns as a result of the limited data available to describe the flow regime. This research will address these empirical gaps by collecting an extensive set of experimental data with respect to the geometrically induced swirl. The dependency of the swirl decay rate on in the initial swirl intensity and Reynolds number was also identified in this chapter as being controversial and will be addressed in this study. Finally, from this chapter, it was possible to identify the adequacy of the Reynolds Stress model for the purpose of this study in which the inducement, development and decay of the swirl flow will be modelled.

CHAPTER 5

EXPERIMENTAL RIG DESIGN

5.1 INTRODUCTION

In order to address the research questions of the thesis, it was required to build a rig to empirically test the influence of geometrically induced swirl on a lean phase pneumatic flow. This chapter concerns the design and building of such a rig. Preliminary tests were first conducted by altering an existing experimental rig in the School of Mechanical Engineering at the University of Nottingham. This allowed identification of the boundaries of the flow conditions for the experiments. Because the initial rig lacked characterisation and commissioning data, and the required finesse of control on the solids and airflow rates, it was decided to build a better version of the rig to meet the requirements of this research within the School of Chemical, Environmental and Mining Engineering laboratory.

The considerations given to the design or selection and adaptation of each final rig components, including the conveyed material, the pipework, the pressure monitoring system, the air flowrate evaluation system, the particle feeding system, the gas-solid separation device and the air mover, are detailed in separate sections of this chapter, along with the assessment of alternatives.

5.2 EXPERIMENTAL FACILITY AT THE UNIVERSITY OF MANCHESTER

In order to achieve an optimum rig design, other experimental facilities were studied. An experimental rig at the University of Manchester, depicted in Figure 5.1 and detailed by Jaworski and Dyakowski (2001), was of special interest for the flexibility it provided in the variability of flow rates and the visualisation facility.

The rig was designed to investigate discrete flow instabilities related to slug and plug flows using a high-speed video camera and a twin-plane electrical capacitance tomography (ECT). The granular solids were fed from a lower tank by rotary feeders into 56mm ID stainless steel conveying pipelines. These comprised a 7m long

horizontal conveying section, 3m vertical section and another 7m return horizontal section into an upper tank. The flow rig was equipped with three removable sections. Each could be replaced by either a glass viewing section for the purpose of flow visualization purposes or a transparent Perspex section with a sliding twin-plane ECT sensor for tomographic measurements.

The mass flow rate of solids was calculated as an increase of the mass of the top tank, which was suspended on three load cells, divided by the time elapsed from the moment the gate valve between the top and bottom tank had been shut. The gas stream was introduced into the system by an 11 kW blower. The gas flow rate through the rig was monitored by using a sonic nozzle, and the gas velocity (for an empty pipe) could be varied between 1.0 and 5.0 m/s. The conveyed solids were solid polyamide cuboids of dimensions $3\text{ mm} \times 3\text{ mm} \times 1\text{ mm}$ approximately. The maximum solids feed rate was about 0.028kg/s.

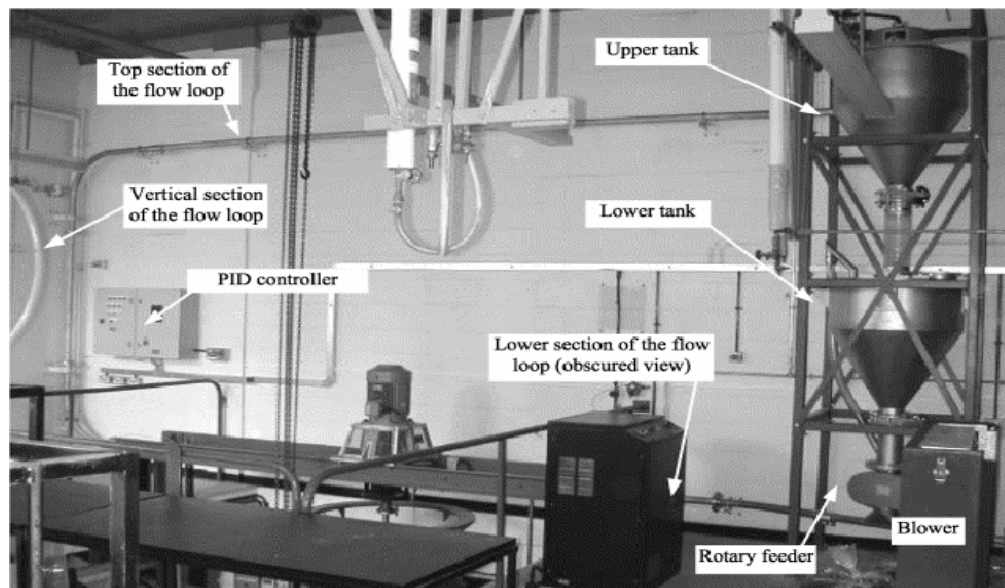


Figure 5.1: Experimental Facility at the University of Manchester

5.3 PRELIMINARY WORK

Initial tests of the swirl pipe were carried out on an existing experimental rig, as shown in Figure 5.2, in the School of Mechanical Engineering at the University of Nottingham.



Figure 5.2: Initial experimental rig

The facility was a simplified $1/9^{\text{th}}$ scale rig of the primary conveying lines in coal power stations such as Ratcliffe, Ferrybridge and Didcot and was being used to study roping phenomenon post bends. The flow was driven by two 1800W blowers in series and the solids were fed by a gravity hopper. The internal diameter of the original pipes was 74mm. In order to test the swirl inducing pipe, the bottom horizontal section was replaced with 50mm ID pipes to correspond to the average ID of the swirl inducing pipe. A 1.3m straight 50mm ID pipe was thus mounted before the swirl inducing pipe to allow the flow to develop before entering the swirl inducing pipe. According to White (1994), development length for single phase turbulent flows is given by $L_e = 4.4D \text{Re}^{1/6}$. Another 1.4m of straight 50mm ID pipe was then mounted after the swirl inducing pipe to observe the turbulence decay. This allowed the testing of a maximum length of 40cm of swirl inducing pipe. The initial tests showed that the helix pipe was in effect inducing swirl in the flow and it was then decided to replace the rest of the rig with 50mm ID pipes and bends. Pressure tappings were also included to improve flow monitoring. Despite these efforts, confidence in the experimental data was poor due to a lack of characterisation and commissioning data. For example the airflow rate and solids flow rate were not easily quantifiable and monitored. In order to have better access to the rig, it was also decided to rebuild the rig.

From these preliminary studies, it was possible to establish the range of conveying velocities and hence the volumetric air flow rate. The conveyance velocity range was estimated to go up to 25m/s, giving a volumetric air flow rate of $0.05\text{m}^3/\text{s}$. The corresponding air mass flow rate is 0.06kg/s . Since dilute phase conveying was under investigation, it was also possible to work out that the range of solids feed rate required would be a maximum of 0.34kg/s for a solids to air volume ratio of one percent.

5.3.1 Choice of pressure system

Conventional pneumatic systems are usually powered by either a positive or a negative pressure system. Low pressure positive systems are typically used for medium range distances in case of dilute phase conveying and shorter distances for medium phase conveying (Mills, 2004). For positive systems, the air mover, generally a fan or blower, is located at the start of the conveying line, before the feed hopper, as in the rig used by Jaworski and Dyakowski (2001). The air is delivered into the pipeline and blows the material feed along the pipeline. On the other hand, low pressure negative or vacuum systems operate on the suction side of fans or blowers with the air mover located at the opposite end of the conveying line to the feed hopper. Low pressure negative systems tend to have lower conveying capacities and conveying distances than the equivalent positive pressure systems (Mills, 2004). A clear advantage that the negative systems have over positive ones is that all gas leakage is inward, thereby tightening flange linkages.

The choice by Jaworski and Dyakowski (2001) of a low pressure positive system powered by a blower is justified for the denser slug flow that was being conveyed. In the current study however, a lean phase flow was to be conveyed over a distance of about 9m. Hence a low pressure negative system was considered appropriate.

Mills (2004) supports that negative pressure systems provide a major advantage with regards to the solid feeding mechanism. The advantage being that the pressure gradient is in the direction of the material feed, with the latter being at atmospheric pressure and the pipeline in which the material is to be fed being at a lower pressure relative to the material feed. This encourages the flow, under suction, of materials into the pipeline; and does not require special design of the feeder to sustain a pressure

difference or prevent air leakages, as this would be the case for a positive conveying system.

5.4 FINAL EXPERIMENTAL RIG LAYOUT & SPECIFICATION

In order to scientifically investigate the effect of the swirl pipe on a lean phase pneumatic flow, the following requirements for the pneumatic conveying rig are specified:

- Sufficiently long horizontal section to allow a turbulent flow to develop, to test the influence of the swirl inducing pipe, and to observe the decay of the induced swirl in horizontal pipelines
- Clear pipe sections to enable visualisation studies, LDA and PIV measurements
- To keep costs to a minimum

The following features also had to be included in the final design specification:

- Pressure and flow rate measurements
- Solids feeder and a material recovery device
- Exchangeable pipe sections to allow future testing of the swirl inducing pipe at different locations

The pipeline system was built on a 4m by 5m backing board made of medium density fibreboard (MDF), which was fastened to the steel super-structure of a pre-existing rig. The perspex rig used in the study is shown in Figure 5.3 and a photograph shown in Figure 5.4. It consisted of a conical inlet, gravity hopper feeder followed by a 1.6m horizontal section, 0.4m of the test swirl inducing pipe, a second 1.5m horizontal section for visualisation purposes, a 90° horizontal-to-vertical bend, a 2m vertical section, a 90° vertical-to-horizontal bend and a 3.5m upper-horizontal section leading into a 0.4m diameter cyclone and finally two 1800W fans in series. The internal pipe bore was 50mm and the total running length of the rig was 9m (180D), with a maximum horizontal straight of 3.5m (70D) and a maximum vertical of 2m (40D). The radius to diameter ratio of the bends was 1.9.

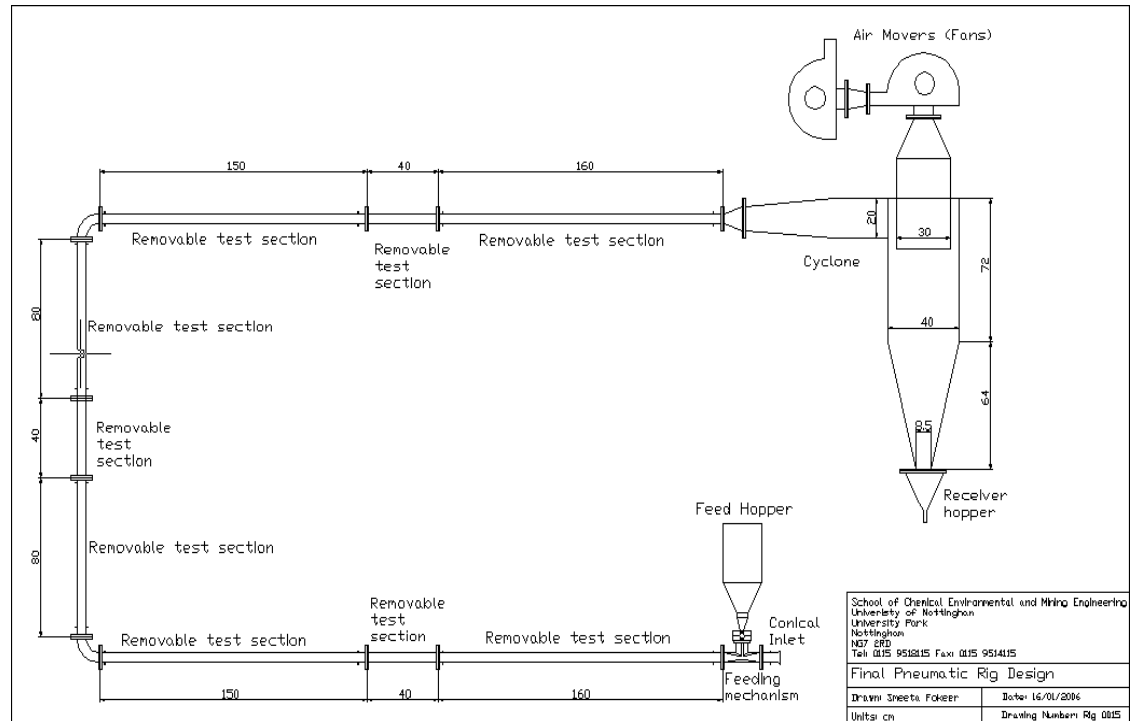


Figure 5.3: Schematic illustration of pneumatic conveying rig



Figure 5.4: The final pneumatic conveying rig for the present study

5.5 RIG COMPONENTS

5.5.1 Conveyed material

Based on the work of Crowe (1991), detailed in section 2.2, it was established that for any given conveying air velocity, the two crucial particle parameters which decide the flow regime are particle density and particle size. It was important to choose a material for conveying that would be light and small enough to be conveyed in suspension at the available velocity range of 10 to 40m/s. In addition, the following characteristics were desirable:

- spherical shape – to ease the subsequent CFD simulation of the experimental cases
- a narrow and consistent particle size distribution– to ensure that the particle trajectory observed is a direct effect of the conveying velocity imposed on the flow.
- non-abrasivity – to minimise erosion of the conveying pipes
- non-friability – to minimise particle breakage
- inertness

The suitability of polystyrene, plastic and glass beads were assessed. Polystyrene and plastic were discarded in favour of hollow glass spheres. The selected conveyed material was a commercially available loose powder called Fillite. It is a derivative of PFA (pulverised fly ash), where only the inert hollow silicate microspheres have been retained (see Figure 5.5).

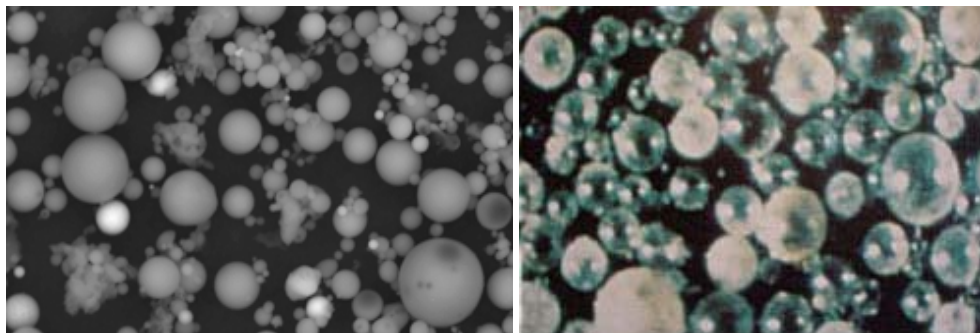


Figure 5.5: a) PFA particles; b) Fillite particles

The material selected had the advantage of being available as different grades for different particle sizes ranging from tens to thousands of microns. The particular grade of Fillite used for the experiments was FG (300), with particle size ranging from 5 to 300 microns. The supplied particle size distribution by mass was as shown in Figure 5.6. This particle size distribution by mass characterisation was supplemented with that of particle size distribution by volume from a Malvern Mastersizer 2000 analyser and this is shown in Figure 5.7. Even though it was not possible to obtain a uniform size distribution for the conveyed material, for the purpose of this study the size distribution of Fillite was considered adequate, with less than 20% of the material being less than 30 microns, 65% in the 30 to 200 microns range and the top 15% being in the 200 to 300 microns.

Despite the selected material not being friable and being non-abrasive, there was the concern that the particles would break up by getting bashed around the pipes during conveying, causing a change in the particle shape and making it more abrasive. An analysis of the particle size distribution was performed using the Malvern Mastersizer 2000 analyser on a sample that had been through the rig three times and the decrease in particle size was found to be less than ten microns and therefore considered non-significant. As a further measure of precaution, it was decided to discard any Fillite powder that had been through the rig three times.

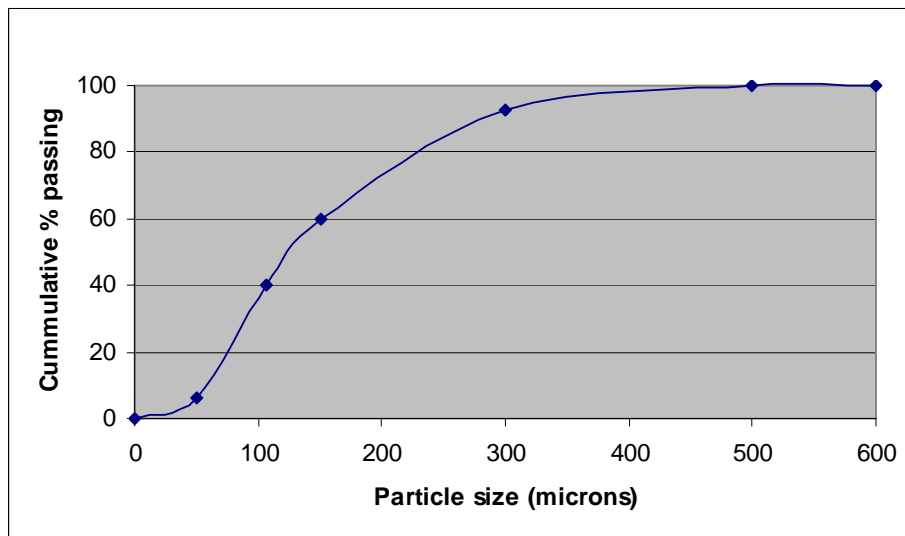


Figure 5.6: Fillite size distribution by weight

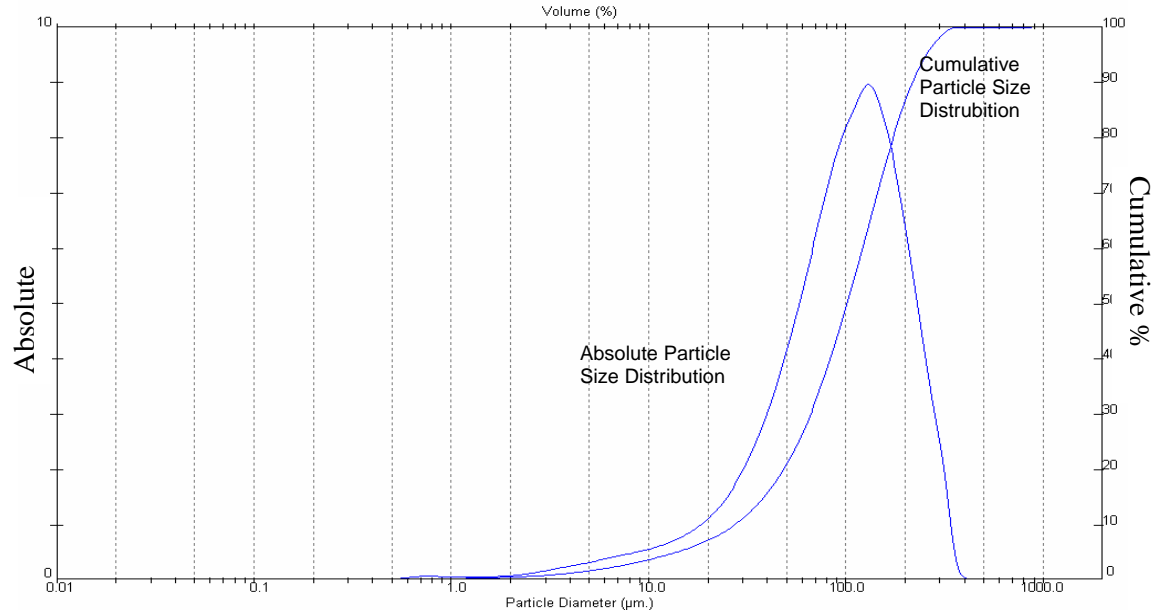


Figure 5.7: Fillite size distribution by volume

Fillite is a lightweight, free-flowing powder off-white or grey in colour. The particle itself is composed of carbon dioxide and nitrogen housed in a hard glass shell composed of oxides of aluminium, silicon and iron. The percentages of composition are as follows:

Shell	Al ₂ O ₃	27%-33%
	SiO ₂	55%-65%
	Fe ₂ O ₃	6% maximum
Gas	CO ₂	70%
	N ₂	30%

Table 5.1: Chemical properties of fillite

The other physical properties of fillite are summarised in Table 5.2

Average particle density	0.6-0.8 g/cc
Average bulk density	0.35-0.45 g/cc
Packing factor	60%-65%
Average wall thickness	5%-10% Sphere Diameter
Hardness	Mohs Scale 5
Crush strength	105-210 kg/cm ²
Thermal conductivity	0.11 Wm ⁻¹ K ⁻¹
Melting temperature	1200°-1350°C
Loss on ignition	2% maximum
Surface moisture	0.3% maximum
Oil Absorption	16-18g oil/100g

Table 5.2: Physical properties of fillite (from manufacturer's information)

5.5.2 Pipework

Regarding the pipework, it has an internal diameter of 50mm, in keeping with the average internal diameter of the test swirl inducing pipe. Since the material that was being conveyed is not abrasive, 3mm thick clear acrylic pipe was deemed adequate as it not only helped to keep the overall cost of the rig down, but also allowed the flow within the rig to be fully visualised. However, the main disadvantage of using acrylic pipe sections in a pneumatic conveying pipeline is the build up of static electricity from the friction between the moving particles and the pipe wall. Attaching conductive copper strip along the length of the pipe and connecting it to the ground proved to help to a small extent.

To achieve a flexible layout, the pipe loop consisted of sections of between 0.4m and 1.6m in length. The pipe sections were assembled by flanges containing O-ring seals (Appendix A) for leak proof joints. The 2m vertical section and horizontal 3.3m sections were further divided into shorter pipe lengths so that future testing of swirl inducing pipe could be investigated in the following locations:

- Pre horizontal-to-vertical 90° bend
- Post horizontal-to-vertical 90° bend
- In a vertical section
- Pre vertical to horizontal bend
- Post vertical to horizontal bend

Even if the whole rig was optically transparent and the flow could be visualised within the whole rig, reflection and refraction has to be kept at a minimum. A thinner pipe wall was also required for the LDA experiments, as thicker walls tend to cause more refraction and suppression of the laser beams. It was hence decided to replace the 3mm thick Perspex pipe for the visualisation section with a pipe section made of optical fused silica (SiO₂ glass) of wall thickness of 1.6mm. Transparent fused silica is distinguished by its exceptionally good optical transmission in all wavelengths. The refractive indices of optical fused silica, synthetic fused silica, glass and Perspex are shown in Table 5.3.

Wavelength (nm)	Refractive index			Transmittance (%)		
	Optical fused silica	Glass	Perspex	Optical fused silica	Glass	Perspex
589.3	1.45853	1.45843	1.49500	92.578	92.428	92.100
514.5 Ar	1.46181	1.46169	1.50000	92.392	92.307	92.000
632.8 Ho/Ne	1.45718	1.45709	1.49500	92.664	92.549	92.100

Table 5.3: Refractive indices (from Duran/Schott Lab glassware catalogue, 1994)

Despite the optical properties of optical fused silica and glass varying only by a very small degree, the optical difference observed during the experiments was significant.

5.5.3 Pressure monitoring

The rig was instrumented to monitor the pressure drop along each of the major sections of pipes. This was achieved by having four tappings, equally spaced around the circumference of the pipe, drilled at either ends of each removable test pipe section and connected to pressure monitors to measure the gauge pressure.

The construction of the tapplings was guided from the specification described in BS 848, clause 7. Hence each tapping took the form of a hole of diameter a through the wall of the airway. The specified limits on the bore diameter of the tapping, a , were between 1.5 mm and 5 mm but no greater than $0.1D$. A sketch of the location and dimensions of the pressure tapplings is shown in Figure 5.8. It was made sure that the hole was drilled so that the bore was normal to and flush with the inside surface of the pipe, and that all internal protrusions were removed. The tapping were situated in a section of the pipe that is free from joints or other irregularities for a distance of D (50mm) upstream and $D/2$ (25mm) downstream, D being the internal pipe diameter. A 10mm stem was glued to each hole and a metal pipe with a threaded end was screwed into the stem. The four tapplings were then linked together by means of rubber tubing and plastic T-shape and \times -shaped connectors. The resulting tapplings are shown in Figure 5.9. With hindsight, it was concluded that fabric filters from air felt should have been installed into each of the tapplings to prevent solids from moving up the tubing and affecting the transducers.

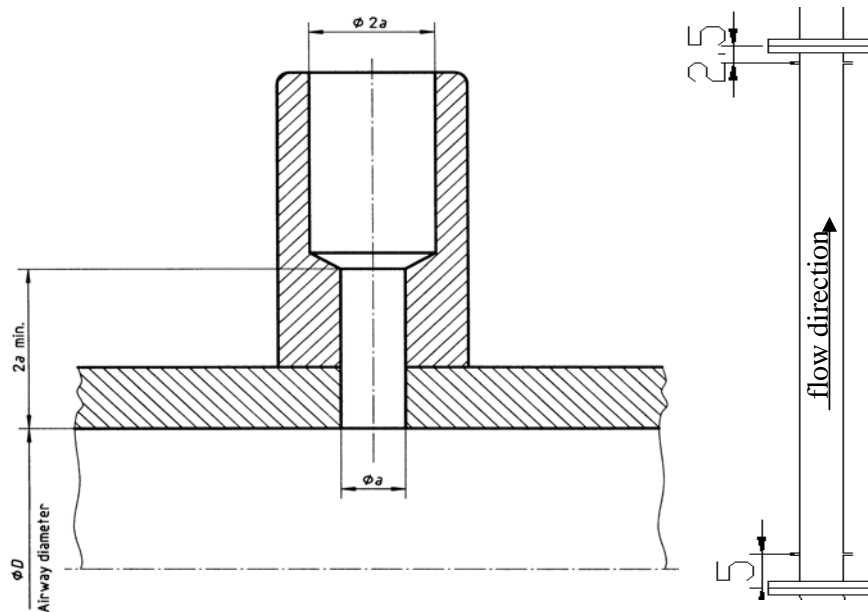


Figure 5.8: Construction of wall tapplings in cm (from BS 848)



Figure 5.9: Resulting pressure tapings

U-tube water manometers and inclined manometers filled with a liquid of specific gravity 0.8 were used to measure the gauge pressure. A photograph illustrating an example of the inclined and vertical manometers is shown in Figure 5.10.



Figure 5.10: Manometers

5.5.4 Air flow rate evaluation

In order to ensure a specific lean phase density seeding of the airflow, it was important to determine the air mass flow rate into the system and the seeding mass flow rate. To evaluate the inlet air mass flow rate of the system, a conical inlet was employed. Again, BS 848 was used as guidance for the construction of the conical inlet.

The conical inlet dimensions and tolerances are given in Figure 5.11, with the angle of the convergent section less than 30°. The pressure tapings were constructed according to the above guidelines.

As per BS 848 instructions, steps were taken to ensure that within the inlet zone there was no external obstruction to the free movement of the air entering the inlet, and that velocity of any cross-currents should not exceed 5 % of the nozzle throat velocity.

Such a conical inlet, manufactured in accordance with the above requirements, is adequate to be used uncalibrated for a pressure difference of up to 4kPa. However, the use of conical inlets is limited to flows of Reynolds Number greater than 20 000. This limitation did not apply in the present case as Reynolds Number of the flow was maintained over 20 000.

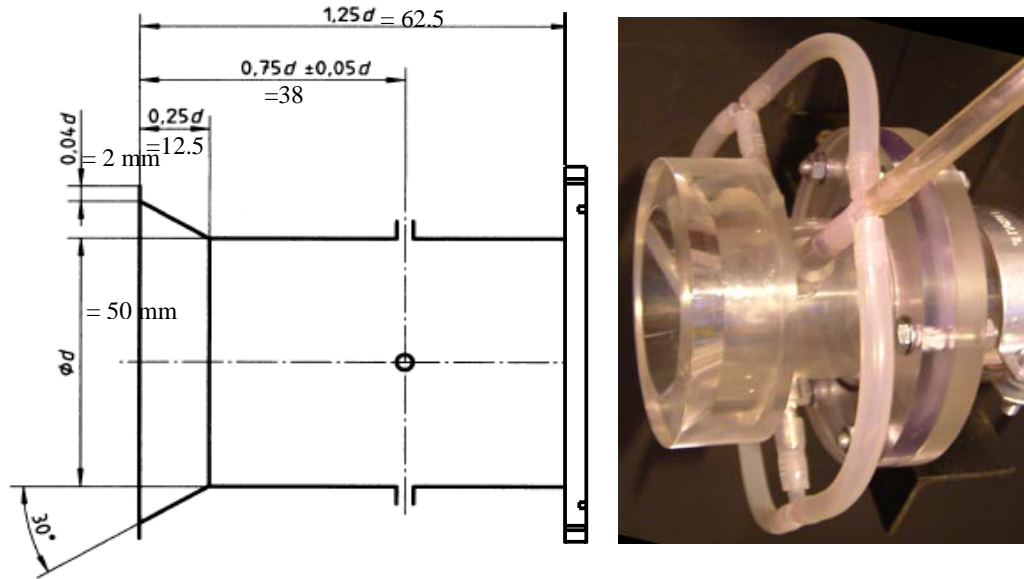


Figure 5.11: Geometry of conical inlet (BS 848)

The differential pressure between the static pressure of the conical inlet and atmospheric pressure was measured. The mass flow rate is given by the following expression:

$$Q_M = \alpha \varepsilon \pi \frac{D^2}{4} \sqrt{2 \rho_{air} \Delta p} \quad (5.1)$$

where Δp is the differential pressure between the static pressure of the conical inlet and atmospheric pressure and $\alpha\epsilon$ is the compound coefficient, which is dependent on the Reynolds number. $\alpha\epsilon$ is plotted in Figure 5.12.

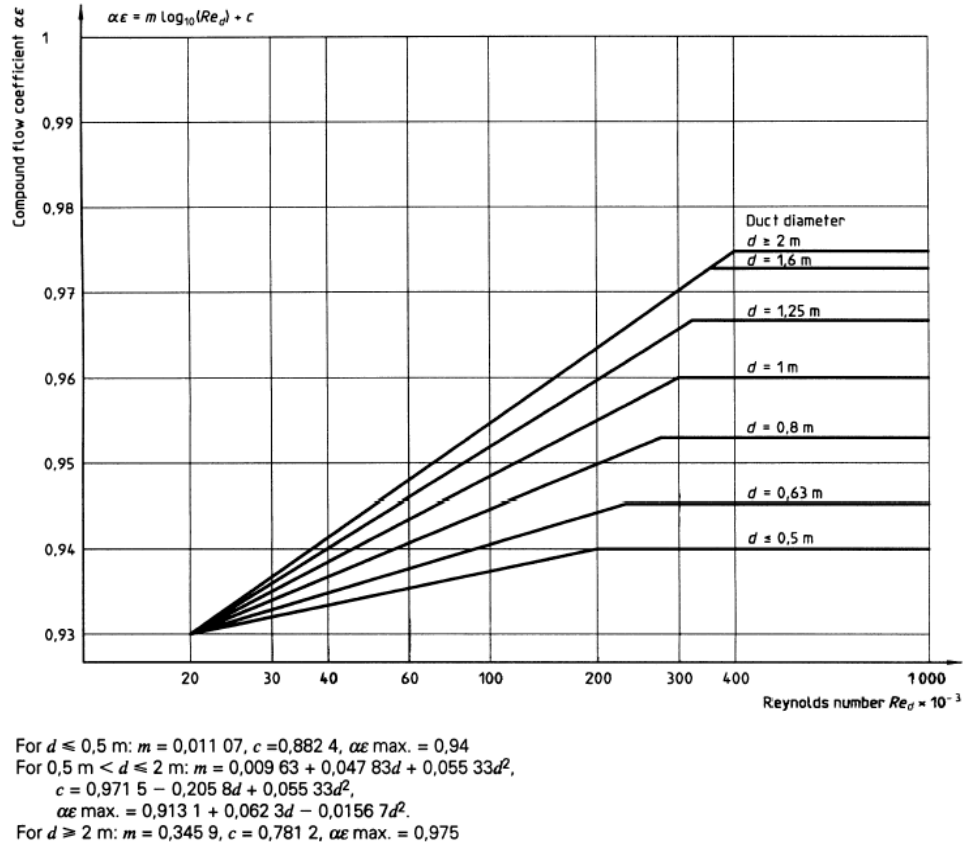


Figure 5.12: Compound flowrate coefficients of conical inlets (BS 848)

Approximation uncertainties in the air flow rate calculations from the conical inlet is mainly associated with the value used for the compound coefficient, $\alpha\epsilon$. BS 848 states that “The basic uncertainty, applicable when Reynolds Number $> 3 \times 10^5$ is $\pm 1.5\%$, while for low Reynolds Number (i.e. $2 \times 10^4 < \text{Reynolds Number} < 3 \times 10^5$) is :

$$\pm \left(\frac{2 \times 10^4}{\text{Re}} - \frac{1}{15} \right),$$

5.5.5 Swirl inducing helix pipe

At the University of Nottingham research has been carried out in the development of swirl inducing pipe for hydraulic conveying to promote suspension of particles at

relatively low velocities. The idea was first suggested by Jones in 1993, and work was carried out by Raylor (1998), and then continued by Ganeshalingam (2002), Tonkin (2004) and Ariyaratne (2005).

Raylor conducted an experimental and numerical investigation to study the use of swirl pipes to reduce wear and produce better particle distribution downstream of a pipe bend. The swirl inducing pipe used was patented by Spanner (1945) to improve heat exchanger efficiency in marine boilers as illustrated in Figure 5.13. From an analysis of his experimental and numerical studies, Raylor concluded that the swirl pipe produced a greater pressure drop across its length than a length of standard straight pipe section. This was mainly attributed to the presence of the swirl and the greater surface roughness of the electroplated steel used to manufacture the swirl pipe compared to the Transpalite used for standard pipes.

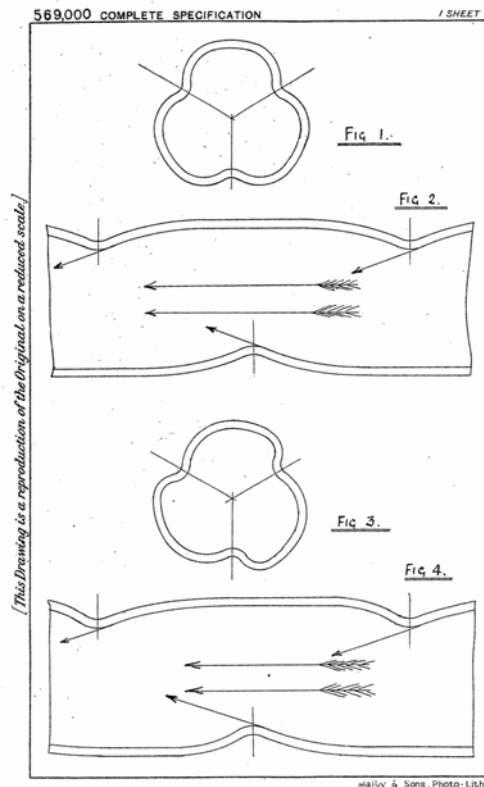


Figure 5.13: Patented design of a 3-lobed boiler tube by Spanner (1945)

It was also observed that high pressure losses were measured at the entry and exit of the pipe due to sudden change in cross-section and sudden constriction and

enlargement. Raylor recommended the re-design of the entry and exit ducts to minimise these losses. It was however concluded that the onset of swirl flow resulted in an even distribution of particles throughout the bend. It was concluded that the use of a swirl pipe before a bend had the potential of reducing wear zones at downstream bends. The computational (CFD) model constructed by Raylor to represent the effects of downstream swirl flow could not be directly validated as no experimental measurements of the cross-sectional velocity were taken.

Ganeshalingam (2002) later continued the work of Raylor and validated the CFD models with data obtained from a series of experimental studies employing the use of PIV, ERT and pressure measurements. The CFD model simulations were found to be in close agreement with pressure measurements and PIV results of axial velocity. Since the pipe cross sectional shape was affecting the flow, Ganeshalingam also expanded the study to investigate the effect of different pipe cross sections (triangular, square, pentagonal, hexagonal and 2, 3, 4, 5, and 6 lobe cross-sections) and applied CFD simulation models to optimise the design of a swirl-inducing pipe for hydraulic conveying. It was found that pipes with a 4-lobe cross-section had a small advantage in terms of pressure drop over the others. Ganeshalingam also found that the total angle by which the cross-section twisted was an important factor and determined an optimum pitch-to-diameter ratio of 6 for the 3-lobe pipe and 8 for the 4-lobe pipe. Furthermore, the optimum lengths for the 3 and 4-lobe pipes were recommended as being 0.6m and 0.4m respectively at the optimum pitch-to-diameter ratios.

Although the CFD model predictions by Ganeshalingam showed a significant difference between the 3 and 4 lobe swirl pipe configurations, the analysis of the experimental differential pressure measurements across the swirl pipes revealed little difference between the 3 and 4 lobe designs. Ganeshalingam attributed it to the fact that the experimental work was not carried out using the optimal lengths of pipe as per the conclusions reached from the CFD simulation models.

Using stereolithography, a rapid prototyping method, 0.2m lengths of 3 and 4-lobe pipe were therefore produced from an Epoxy Photopolymer. The lengths of the pipes were limited by the size of the tank in the stereolithography machine. The sections were then bolted together to form the specified 0.4m and 0.6m length. Ariyaratne

(2002) then performed experimental tests using these rapid prototyping pipes in an attempt to experimentally confirm the findings of Ganeshalingam. As recommended by Raylor, Ariyaratne also designed and optimised, using CFD modelling, a transition section to bridge the cross-sectional change in transferring from circular pipe to swirl pipe, and vice versa. The optimised transition pipes were experimentally and numerically proven to reduce pressure losses. Greater swirl at the exit of the swirl pipe and reduced swirl decay also resulted from the use of the transition section.

Against this accumulated knowledge of swirl inducing pipes for hydraulic transport, it was decided to adopt the 3-lobed pipe for pneumatic conveying instead of the 4 lobed pipe. This decision was made by considering the lower density and viscosity of air in relation to water (0.001 and 0.018 respectively), making air more easily subjected to swirl.

Another feature to consider is the pitch to diameter ratio (or dimensionless pitch) which is defined as the axial length of the pipe when it has been twisted through 360 degrees. The available 3-lobe pipe was of average diameter 0.05m and had a pitch of 0.3m, making its pitch-to-diameter ratio 6. Because only two 0.2m sections of the 3-lobed pipe were available, the recommended optimum length of 0.6m could not be achieved. In view of the susceptibility of air to swirl, it was decided to use the available length of 0.4m for the tests. The test pipe and its internal dimensions are shown in Figure 5.14

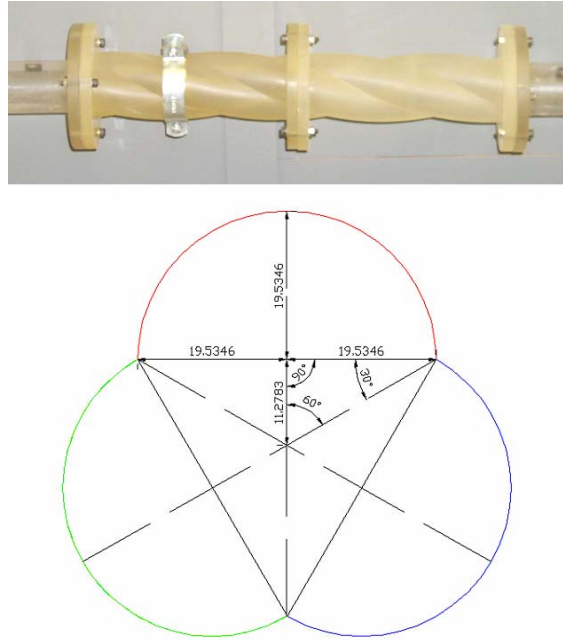


Figure 5.14: Helical turbulence inducing test pipe geometry (in mm)

5.5.6 Solids mass flow rate/Particles feeder

In choosing the particles feeding mechanism, there were two main criteria: the delivery of a stable feed with time and the delivery of a uniform feed across the cross section of the pipe. The powder delivery system should have the potential to deliver the particles in a controlled manner and allow for adjustment of the material feed rate. There are a number of mechanisms available to feed particles to a conveying air stream in a negative pressure system and these include simple gravity hoppers fitted with a gate valve, screw feeders, vibratory feeders and rotary feeders.

In order to improve the initial mixing, pick up and conveyance of the particles fed into the conveying of air stream, these feeding mechanisms are often supplemented with a venturi section. A venturi feeder works on the principle of reducing the pipeline cross sectional area in the throat region where the material is to be fed, as shown in Figure 5.15. This increases the air velocity at that location and causes the particles to be more easily entrained into the flow.

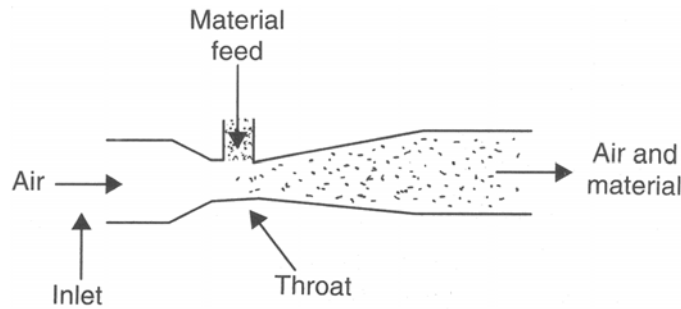


Figure 5.15: Venturi feeder (Mills, 2004)

As mentioned previously, since the conveying system is under negative pressure, the pressure gradient is in direction of the material feed. The particles are thereby encouraged to flow into the pipeline under suction (Mills, 2004). The application of a venturi feeder is particularly adapted to a negative pressure system as a further decrease in pressure occurs in the throat region of the venturi, thereby encouraging the material to flow more readily into the pipeline.

The simplest feeding device for a negative pressure system argued by the author consists of a supply hopper feeding directly into the conveying pipeline under gravity and a simple slide or gate valve to regulate the material feed rate (Figure 5.16). This can be supplemented with a venturi section to improve the initial conveyance of the particles. Since the conveying system is under negative pressure there is no risk of air leaking out of the gravity hopper. This feeding mechanism design provides a cost effective solution with minimum mechanical parts, yet this is limited to conveying free flowing materials at low rates and over short distances.

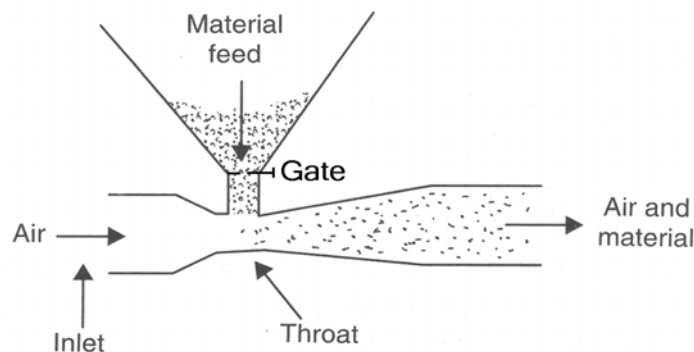


Figure 5.16: Simplest feeding device for negative pressure systems (Adapted from Mills, 2004)

Screw feeders provide precise material flow control with a practically linear relationship between screw speed and material feed rate. A simple screw feeder consists of a screw, enclosed in a barrel casing, sitting at the base of a feed hopper. As the screw rotates, a continuous plug of material is dispersed and entrained into the conveying air into the pipeline. The simple screw feeder can be improved by inclining it to an angle, as shown in Figure 5.17, so that the effect of gravity can be used to move the particles. The screw feeder can also be combined with the venturi to facilitate entrainment.

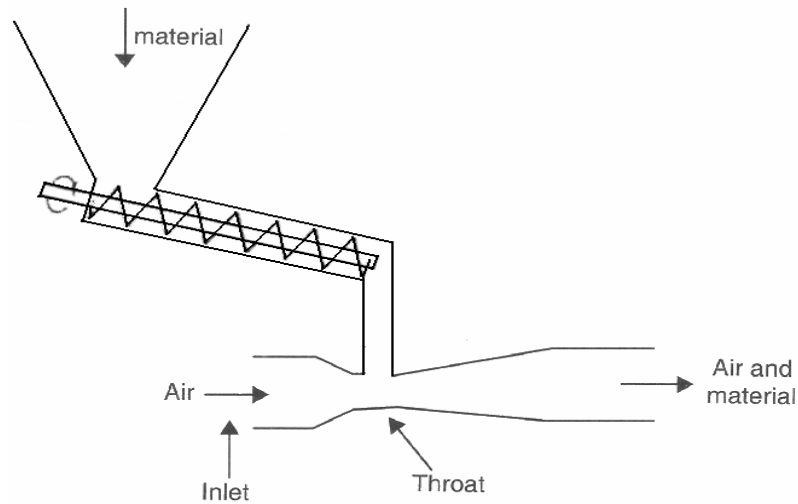


Figure 5.17: Inclined screw feeder with venturi

Despite providing a high control of the material flow rate, the screw feeder has several disadvantages. Because of its inherent design, the screw feeder is prone to clogging up and is also difficult to clean without taking the parts apart. Material degradation is another concern as the material is compressed between the screw and the barrel. If the material does degrade and become abrasive, deterioration of the screw integrity becomes an issue. Over time, wear and tear of the mechanical parts will also affect the accuracy of the screw feeder. There is also an additional cost associated with the screw feeder as a motor is required to drive the screw shaft.

A vibratory feeder consists of two primary components: a hopper containing the material to be fed and an electronically controlled vibratory tray. The material flows from the hopper into the vibratory tray, from where it moves in what appears to be a

uniform flowing stream, but which is in fact a series of continuous, rapid, short forward hops, caused by the vibration and which are imperceptible to the eye. The rate of vibration can be altered, resulting in varying feeding rate. However, the vibratory nature of the movement tends to sort the material according to its size.

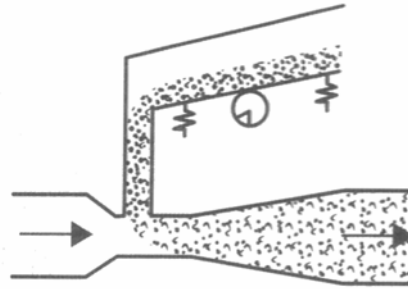


Figure 5.18: Vibratory feeder with venturi (Mills, 2004)

The preliminary tests carried out employed feeding device which constituted of a gravity hopper fitted with a gate valve. It was found that Fillite tends to “flood,” that is to flow uncontrollably and hence it was very difficult to regulate the flow with a simple slide/gate valve. The tests were useful in delimiting the range of feeding rate required. In order to ensure very lean flow, the volume concentration of solids was to not to exceed 10%, which corresponded to a maximum solids mass flow rate of 6g/s at the maximum available conveying air velocity of 25m/s. The use of a screw feeder and a vibratory feeder was investigated in order to feed the material into the conveying pipe in conjunction with the gravity feed hopper and the venturi.

Screw feeders were first considered because they provide an improved material flow control. As the Fillite particles are pushed down the barrel casing, their potential degradation due to friction between the casing and the screw was a major concern when assessing the feasibility of using a screw feeder. A preliminary test was therefore undertaken using an adapted hand screw drill with the speed set to the maximum of 300rpm. The size of Fillite particles were analysed before and after they have been passed through the screw feeder 3 times. The average particle size difference was found to be minimal, a decrease by about less than 10 microns. The result is shown in Figure 5.19.

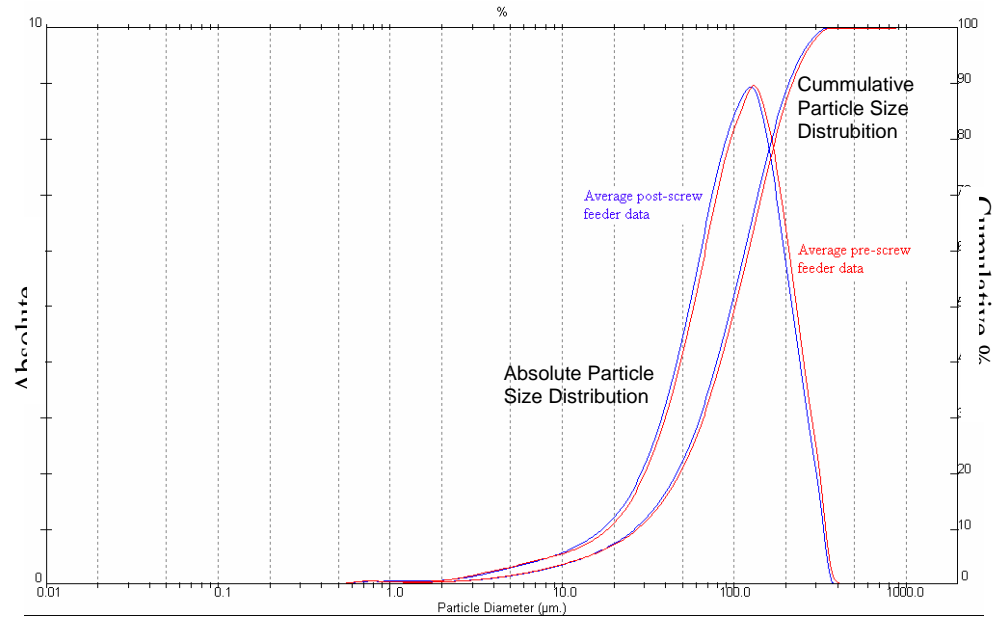


Figure 5.19: Pre- and post-screw feeder fillite particles size analysis

The main problem encountered with the screw feeder was finding an adequate motor that would drive the screw shaft, without escalating the cost of the rig. It was calculated that for the screw feeder to maintain a lean phase, the screw rotation speed should be between 10rpm (for an equivalent phase density of 0.01) and 400rpm (for an equivalent phase density of 0.5). This posed two separate problems: firstly the Perspex enclosure in which the screw feeder tipped would be vulnerable to the vibration caused by the rotation of the screw, and secondly the speed of the motor that was available for use was 1400rpm. A phase controller was added to it to bring the speed down to 400rpm. However in so doing, the motor lost the torque required to drive the loaded screw feeder. Also during the calibration of the inclined screw feeder using a hand power drill, it was found that the screw did not fit perfectly into its barrel, thereby moving from side to side and incorporating a pulsation in the material feed. For all these reasons, the inclined screw feeder with venturi was therefore abandoned.

Tests were also carried on a vibratory feeder. A uniform material mass flow rate was achieved using the vibratory feeder, with up to 4g of Fillite particles fed into the pipeline per second. However, the concern surrounding the use of the vibratory feeder was the additional air that it introduces to the system. Because this was unquantifiable, it would have made reproducing the experimental conditions in the CFD modelling impossible. Hence, the vibratory feeder with venturi was also abandoned.

It was finally decided to pursue with the simplest feeding mechanism, a supply hopper feeding under gravity, but to improve the gate so as to better control the materials' mass flow rate. After considering different designs, it was decided that the gate would be in the form of a metal plate at the end of a threaded metal rod. This metal rod was in turn attached to a dial so that as the dial is rotated through one revolution, the orifice plate moved by 1 mm. It required 10 revolutions of the dial for the orifice to be completely opened. Photographs of the feeding system along with the dial and gate are shown in Figure 5.20.

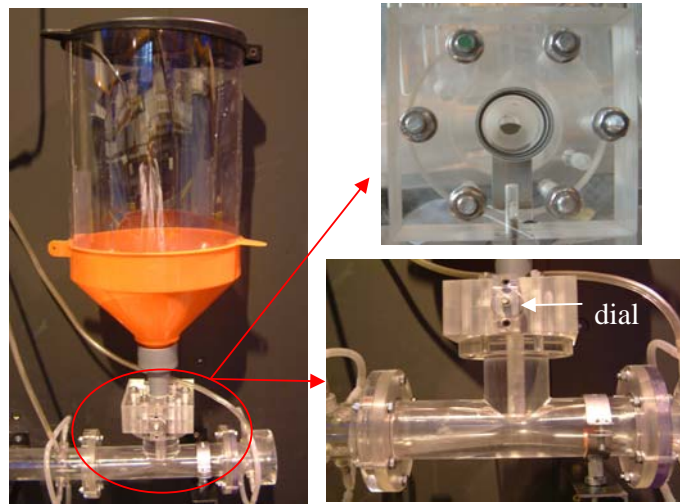


Figure 5.20: Solids feeding mechanism

A bench study was carried out to calibrate the feeding system. The weight of solid material fed for over 1, 3 and 5 minutes were recorded for each number of revolutions of the dial. The performance results are shown in table Table 5.4 and Figure 5.21. The feed rate was found to be smooth and reproducible. A maximum feed rate of about 4.13 g/s was achievable, ensuring that a very lean phase is maintained. When connected to the rig, the negative pressure, produced by the fan sucking air through the pipe, is expected to slightly increase this feed rate.

Number of revolutions	Area of orifice open (mm ²)	% of orifice open	Feed rate (g/s)
0	0	0	0
1	4.09	5.20	0.19
2	11.18	14.24	0.59
3	19.82	25.23	1.13
4	29.34	37.35	1.71
5	39.27	49.99	2.30
6	49.21	62.65	2.87
7	58.73	74.77	3.39
8	67.37	85.76	3.82
9	74.46	94.80	4.06
10	78.55	100.00	4.13

Table 5.4: Orifice plate calibration data

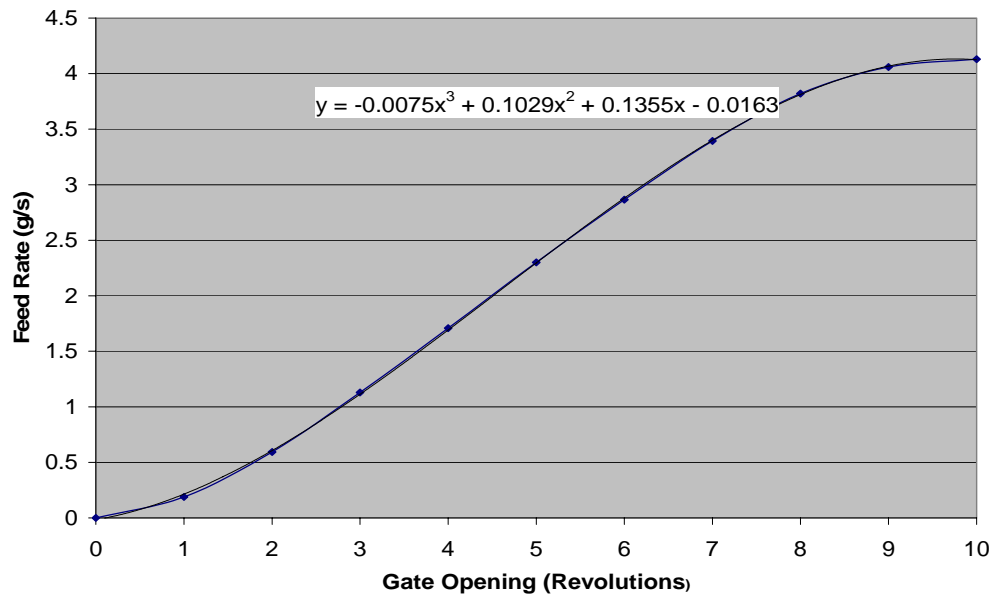


Figure 5.21: Orifice plate performance curve

5.5.7 Gas-solid separation device

A method of separating the Fillite particles from the conveyed air at the end of the conveying line was required. The recovered Fillite particles would then be re-fed into the conveying line. It was decided that since the whole of the conveying line was located inside the laboratories, collection efficiency of the separation device would have to be very high in order to minimise pollution of the working environment by the particles. A dry cyclone separator was consequently the choice for separating the

particles from the gas flow as they are simple to construct, have no moving parts, and have low capital and operational costs. In addition, the collected particles are in a dry form and can be re-used straight away.

5.5.7.1 Principle of operation of a cyclone

Particle-laden gas enters the cyclone tangentially through the gas inlet duct and forms a double vortex which centrifuges the dust particles to the walls within the cyclone body (see Figure 5.22a). The two distinct vortices are described by Cheremisinoff and Young (1975): firstly as a large diameter descending helical current in the body and cone; and secondly as an ascending helix of smaller diameter extending up from the dust outlet section, through the gas outlet. These vortices in turn give rise to three main flow patterns involved in the operation of a cyclone:

- Descending spiral flow, which carries the separated dust down the walls of the cyclone to the dust hopper
- Ascending spiral flow, which rotates in the same direction as the descending spiral, but carries the cleaned gas from the cyclone to the gas outlet
- Radially inward flow, which feeds the gas from the descending to the ascending spiral.

On entering a cyclone, the dust-laden gas whirls through several revolutions in the body and cone. The induced spiralling action of the gas/particle stream subjects particles to substantial centrifugal forces, acting more strongly on the larger, denser particles and flinging them preferentially toward the inside wall of the cyclone. The dust-laden gas thereby drops its dust load. Collected dust moves along the cyclone walls to the dust exit due to the descending spiral flow at the cyclone walls. The clean gas is emitted through the axial cylindrical air outlet due to the ascending spiral flow. The radially inward flow, which is created near the bottom of the cyclone and which spirals upward feeding the gas from the descending to the ascending spiral, also carries finer dust particles. The stream of clean air exiting from the gas exit duct is therefore contaminated by these finer dust particles.

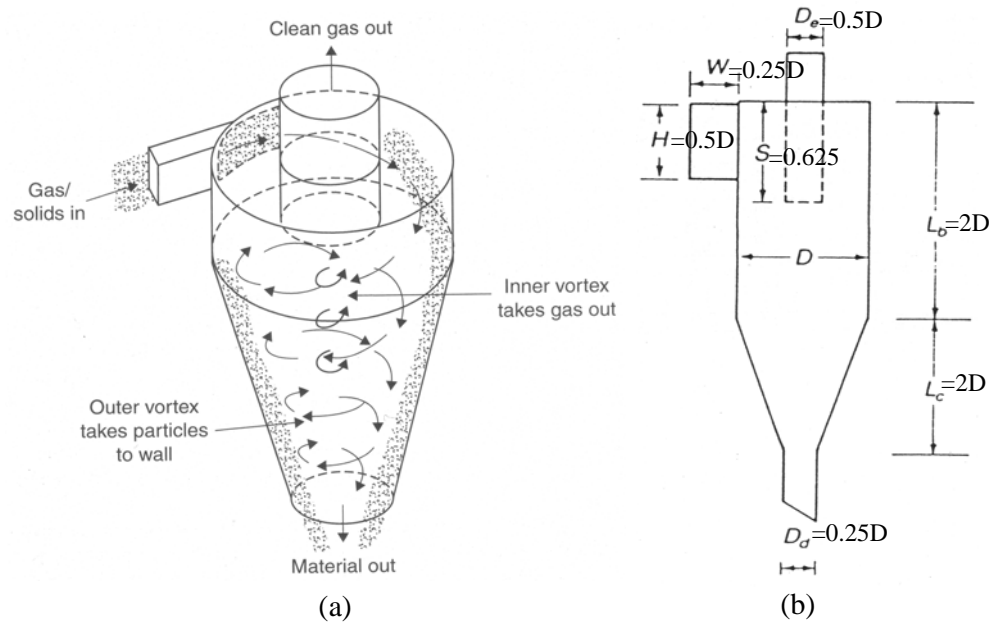


Figure 5.22: a) Operation principle of cyclones; b) standard Lapple cyclone measurements (Adapted from Mills, 2004)

The collection efficiency of cyclones varies according to the particle size being separated in relation to the dimensions of the cyclone itself. Furthermore, the cyclone contributes significantly to the pressure drop of the whole system. It was considered that the required cyclone would be a standard one fit for general purpose and which would provide a good balance between separation efficiency and pressure drop. A comparative desk study was therefore carried out to find the optimum dimensions of a standard Lapple cyclone (Figure 5.22b).

The design methodology adopted that of Lapple (1951) for the collection efficiency and estimation of cyclone pressure drop. Leith (1979) supports that the Lapple approach for determining the cyclone pressure drop was simple to use and produced results which were as good as those produced from more complex calculation methods such as that of Barth (1956) and Stairmand (1951). As regards the estimation of cyclone efficiency, again the Lapple approach was selected as it uses a timed flight approach, which is more popular among researchers (Leith, 1979) to calculate the critical particle diameter. The timed flight approach is based on calculating the residence time inside the cyclone for a particular size of particle and the assumption that the particle has to reside inside the cyclone for a sufficient duration for collection.

The design methodology involved varying the cyclone body diameter and calculating for each case the collection efficiency and corresponding pressure drop. The overall collection efficiency is given by:

$$\eta_0 = \sum \eta_j m_j \quad (5.1)$$

where m_j is the mass percent of particles in the j^{th} range and η_j is the collection efficiency of the j^{th} range, given by

$$\eta_j = \frac{1}{1 + \left(\frac{d_{pc}}{d_{pj}} \right)^2} \quad (5.2)$$

where d_{pj} is the characteristic diameter for the j^{th} particle size range and d_{pc} is defined by Lapple (1951) as the diameter of particles collected with 50% efficiency

$$d_{pc} = \sqrt{\frac{9\mu W}{2\pi N_e V_i (\rho_p - \rho_g)}} \quad (5.3)$$

where N_e is the number of revolutions the gas spins through the outer vortex

$$N_e = \frac{1}{H} \left(L_b + \frac{L_c}{2} \right) \quad (5.4)$$

and V_i is the inlet gas velocity

$$V_i = \frac{Q_v}{HW} \quad (5.5)$$

The pressure drop caused by the gas going through the cyclone is given by

$$\Delta P = \frac{1}{2} \rho_g V_i^2 K \frac{HW}{D_e^2} \quad (5.6)$$

where K is a constant which depends on the cyclone configuration and operating conditions. A value of 16 is recommended for K. Hence the pressure drop equation reduces to

$$\Delta P = \frac{8\rho_g Q_v^2}{HWD_e^2} \quad (5.7)$$

It was found that a cyclone diameter of at least 25cm would provide very good separation and minimal pressure drop. The results are shown in Figure 5.23.

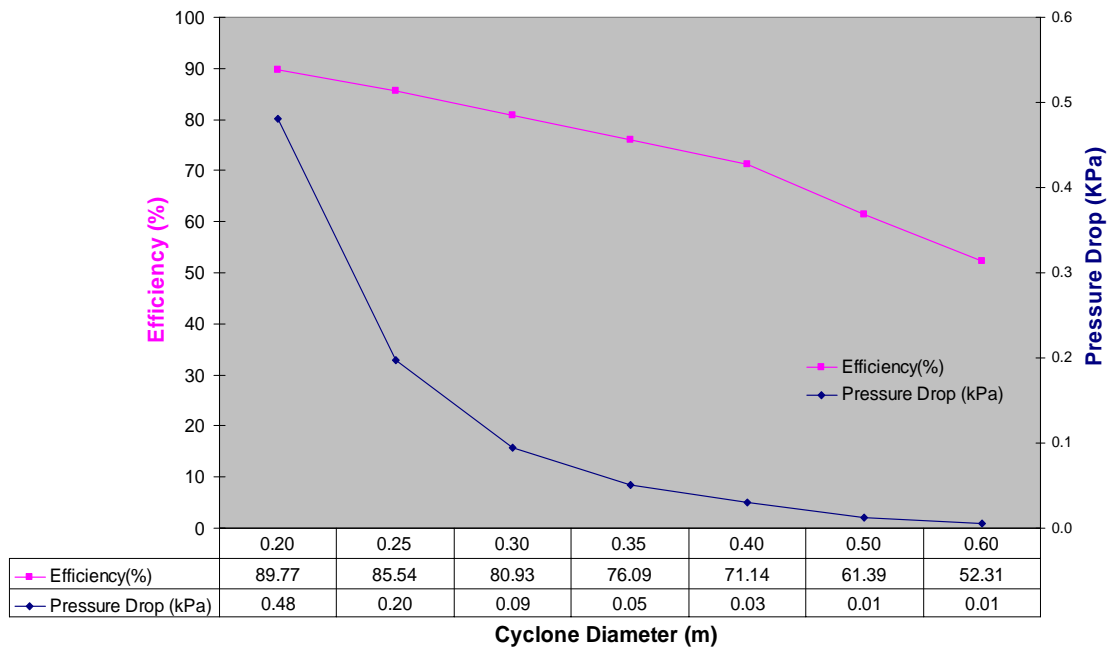


Figure 5.23: Finding the optimum cyclone diameter

A cyclone of diameter 40cm was available for use. The corresponding efficiency was calculated to be 71.14% with a corresponding pressure drop of 0.03 kPa at the maximum air volumetric flow rate of 0.05 m³/s.

5.5.8 Air Mover

Air movers are at the heart of the pneumatic conveying system and can often be the largest single item of expenditure. Selection of a suitable air mover is an important design step as poor selection can lead to high capital, operation and maintenance costs, downtime, vibration, noise and poor conveying capability (Tonkin, 2004).

Air movers range from fans to blowers and positive displacement compressors, as summarised in Figure 5.24.

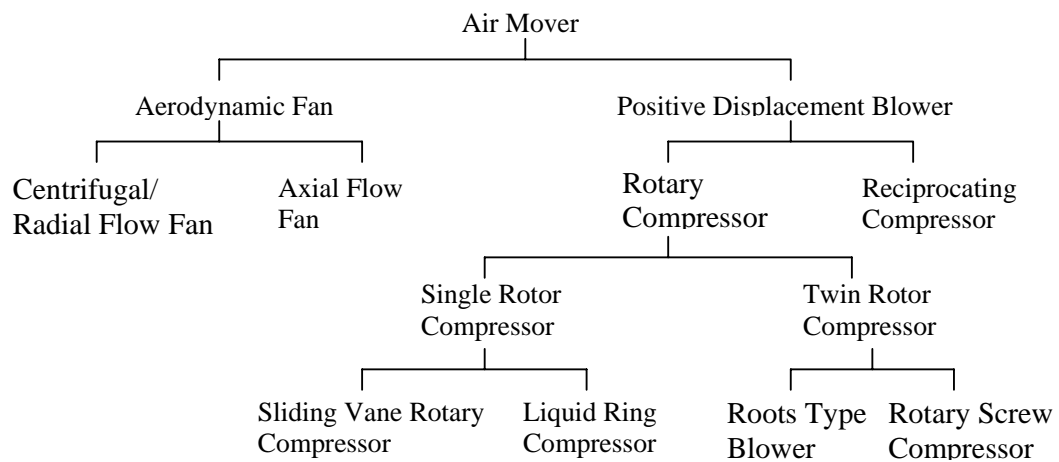


Figure 5.24: Classification of air movers (Mills, 2004)

Fans typically produce high volumetric flow-rates at relatively low pressures and are therefore typically suited to short distance dilute phase pneumatic conveying where the risk of pipe blockage is very small. They may be used both as blowers for a positive pressure system and as vacuum pumps for a negative pressure system. The main drawback of fans, however is that the airflow rate is very dependent upon the line pressure drop. Should there be a surge in the solids feed rate, the line pressure would increase significantly, reducing the airflow rate, with the risk of blocking the pipe. A constant solids feed rate is therefore important should fans be used as the air movers. There are two main types of fans: centrifugal or radial flow fans and axial flow fans. Centrifugal or radial flow fans are characterised by the air entering the impeller in an axial direction and is discharged at the periphery, with the impeller rotation being towards the outlet (Figure 5.25a). On the other hand, for axial fans the flow is substantially parallel to the axis of the impeller (Figure 5.25b).

Roots type, or positive displacement, blowers are used on pneumatic conveying applications where the operating gauge pressure does not exceed about 1bar (Mills, 2004). They are generally bi-directional, so that they can be used as exhausters as well as compressors and are available in sizes handling up to $500\text{m}^3/\text{min}$. The operating principle of the roots blower is based on two rotors, rotating in opposite direction, as depicted in Figure 5.25c. The air trapped between them and the casing wall is thus transported from the inlet to the outlet, where air from the delivery pressure pipe flows back and meets the trapped air, causing shock compression. Because of this, pulsations, noise and poor thermodynamic efficiencies are the main drawbacks of the roots type blower.

Single stage sliding vane compressors are generally capable of delivering in excess of $50\text{ m}^3/\text{min}$ at a maximum pressure of 4bar. In this case, compression occurs within the compressor itself, between the rotor and the casing. The air delivered is therefore free of the marked pulsations observed in roots type blowers, as shown in Figure 5.25d. However, water or oil cooling is required due to the high temperature resulting from the air compression and the mechanical friction of the rotor. The sliding vane compressor is designed to perform equally well as a compressor and exhauster.

Liquid ring compressors' capabilities range from about $1\text{ m}^3/\text{min}$ up to $70\text{ m}^3/\text{min}$ at pressures of up to about 4bar. Liquid ring compressors tend to be generally used in vacuum conveying systems due to their high tolerance to dust. These are trapped in the liquid ring that is formed during operation when the service liquid between the casing and the rotor is thrown outwards towards the casing. The liquid ring also cools the air that is compressed in the spaces between the rotor and the liquid ring. The process is illustrated in Figure 5.25e.

Dry single stage rotary screw compressors have capacities ranging from 4 to $700\text{m}^3/\text{min}$ and pressures of up to 4bar and they are free from pressure pulsations. The operating principle of the rotary screw feeder is based on male and female intermeshing rotors mounted on parallel shafts, as shown in Figure 5.25f. The air enters one of the cavities of the female rotor and is trapped by a male lobe and as the rotor turns, the trapped air is compressed and moved from the inlet to the discharge end of the compressor.

For the sliding vane and rotary screw compressors, oil or water are commonly used for lubrication and/or cooling purposes and enable the production of higher pressures. In these instances, adequate injection, separation and filtration processes and equipment have to be looked into and can incur substantial cost.

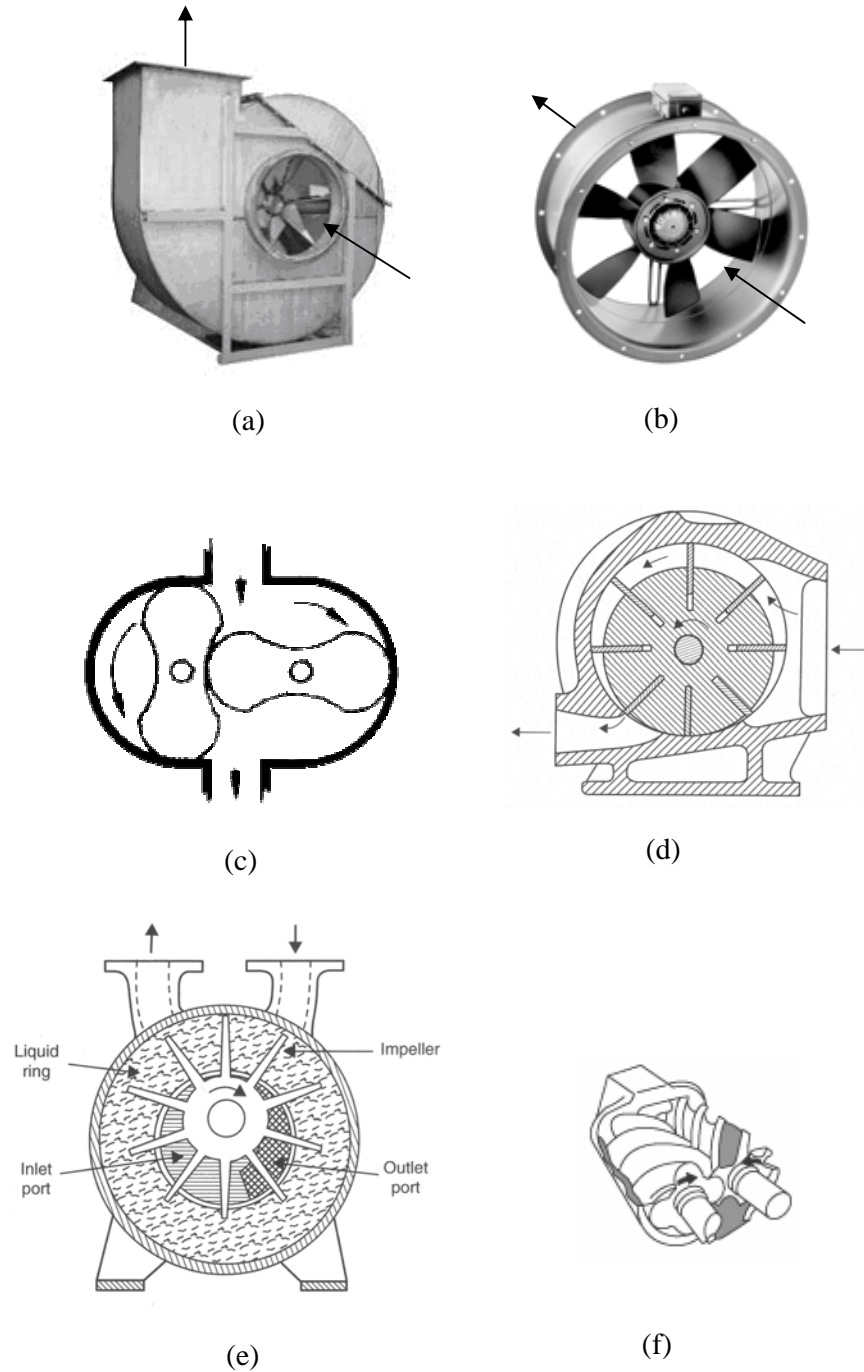


Figure 5.25: Air Movers: (a) Centrifugal fan; (b) axial fan; (c) roots type blower; (d) sliding vane compressor; (e) liquid ring compressor; (f) rotary screw compressor

Mills (2004) states that the main parameters affecting the choice of an air mover are the required volumetric flow rate of air and the pressure at which it is to be delivered. Both of these parameters are primarily dependent upon the material to be conveyed, the phase density, the required material flow rate and the conveying distance. Other considerations would be stability, combined use of air movers, limitations imposed by installation and running cost.

The most important of these considerations for this application was the volumetric flow rate and the delivered pressure. At this stage, since it was already decided that a low negative pressure system would be used to convey the dilute phase flow over the required distance of about 10m, an adequate air mover was chosen. Since positive displacement compressors produce relatively low volumetric flow rates at high pressures, making them more suitable for long distance or dense phase pneumatic conveying, they were thus discarded from further consideration.

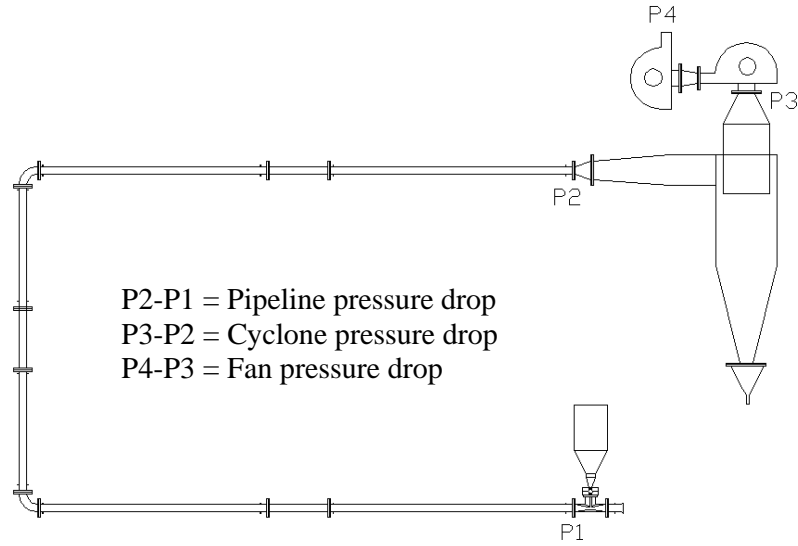
For the reasons justified in section 5.1.1, it was decided that a low negative pressure system would be used to convey the dilute phase flow over the required distance of about 10m. Since positive displacement compressors produce relatively low volumetric flow rates at high pressures, making them more suitable for long distance or dense phase pneumatic conveying, they were also discarded from further consideration.

Mills (2004) states that the main parameters affecting the choice of an air mover are the required volumetric flow rate of air and the pressure at which it is to be delivered. Both of these parameters are primarily dependent upon the material to be conveyed, the phase density, the required material flow rate and the conveying distance. Other considerations would include stability, combined use of air movers, limitations imposed by installation and running cost.

The fans used for the preliminary work were two 1800W centrifugal fans in series. The fans were effectively garden “blower vacs” which could be operated both on the positive blowing side and on the negative vacuum side. Rigorous fan characteristic tests (Osborne, 1977) were performed to establish the suitability of these fans in

delivering the range of pressure 6kPa and airflow ranges required for conveying the Fillite particles in a dilute flow mode over a distance of 9m.

From the preliminary work, it was established that the fans were capable of delivering a maximum volumetric airflow rate of $0.05\text{m}^3/\text{s}$. For a 50mm bore pipe, this equates to about maximum air velocity of 25m/s. Using this maximum air velocity value, the total pressure drop across the rig was calculated.



The straight-line pipeline static pressure drop was calculated on an air-only basis following Darcy's Equation:

$$\Delta p_{static straight} = \frac{4fLU^2}{2D} \quad (5.8)$$

where

$$\begin{aligned} f &= \text{friction coefficient} = 0.02, \text{ obtained from Moody Chart for drawn tubing of surface roughness } 1.5 \mu\text{m} \text{ and Reynolds} \\ \text{Number} &= \frac{\rho DU}{\mu} = \frac{1.2011 \times 0.05 \times 25}{0.000018} = 8.5 \times 10^4 \end{aligned}$$

Hence,

$$\Delta p_{static straight} = \frac{4fLU^2}{2D} = \frac{4 \times 0.02 \times 9 \times 1.2011 \times 25^2}{2 \times 0.05} = 6518.13 \text{ Pa}$$

On an air-only basis, the dynamic pressure is given by

$$\Delta p_{dynamic_{straight}} = \frac{1}{2} \rho U^2 \quad (5.9)$$

while that of bends are given by

$$\Delta p_{dynamic_{bend}} = \frac{k \rho U^2}{2} \quad (5.10)$$

where k is the number of velocity heads lost for the particular bend configuration and in the case of 900 bends, k depends on the bend diameter to pipe radius ratio. For the bends used on the rig, the latter was 1.9 and hence a value of 0.6 was used for k. Two 900 bends with bend diameter to pipe radius ratio of 1.9 had to be accounted for.

Hence,

$$\Delta p_{dynamic} = \frac{1}{2} \times 1.2011 \times 25^2 + 2 \times \frac{0.6 \times 1.2011 \times 25^2}{2} = 851.75 Pa$$

The elevation pressure drop due is given by:

$$\Delta p_{elevation} = h \rho g \quad (5.11)$$

and hence calculated to be

$$\Delta p_{elevation} = 2 \times 1.2011 \times 9.81 = 23.57 Pa$$

The total pipeline pressure drop was therefore 5607.79Pa + 8507.75Pa + 23.57Pa = 6.49 kPa

As calculated in section 5.5.7, the pressure drop associated with the 40cm diameter cyclone is 0.03kPa. The total system pressure drop across the rig is therefore 6.52 kPa. All the above calculations were performed on an air-only basis. The addition of particles into the flow is expected to create further pressure drop. Hence, in order to drive the flow, the fan needs to supply a pressure drop in excess of 6.52 kPa. A fan

test was carried out to determine the useful fan pressure and hence the adequacy of the fans.

The fan test is based on the principle that useful fan pressure or the fan static pressure (defined as the total fan pressure, which is the difference between the total pressures at the fan outlet and inlet, minus the fan velocity pressure corresponding to the average velocity at the fan outlet) is dependent upon the volumetric air flow rate through the fan. The static fan pressure is equal to zero when the fan is operating with open inlet and outlet. As the fan inlet orifice is reduced, and the volumetric air flow rate through the fan decreases, and causes the static fan pressure to increase to a maximum, which is effectively the useful fan pressure.

A fan test was carried out individually with the single fans and both fans attached in series. The conical inlet was used to measure the volumetric flowrate going into the fan and this value was double-checked with a portable anemometer. The static pressure at the inlet and outlet of the fans were also measured using water manometers. The fan inlet orifice was gradually blocked by sliding a piece of card with a circle cut into it between the flanges of the conical inlet and the pipe section attached to the fan as shown in Figure 5.26.



Figure 5.26: Experimental setup for fan tests

It was found that the maximum volumetric air flowrate through each individual fan was $0.1\text{m}^3/\text{s}$ and an average useful pressure of 6kPa was obtained. When the two fans were connected in series, the combined fans static pressure is theoretically expected to be the sum of the individual static fan pressures since the volumetric airflow rate

through each fan is still the same as what would go through a single fan. However, it was found that the combined volumetric flowrate was $0.14\text{m}^3/\text{s}$ and the useful pressure was only 9.1kPa . This was thought to be due to losses at the connections. The resulting characteristic fan curves are shown in Figure 5.27. The garden “blower vacs” were considered to be suitable for the required purpose.

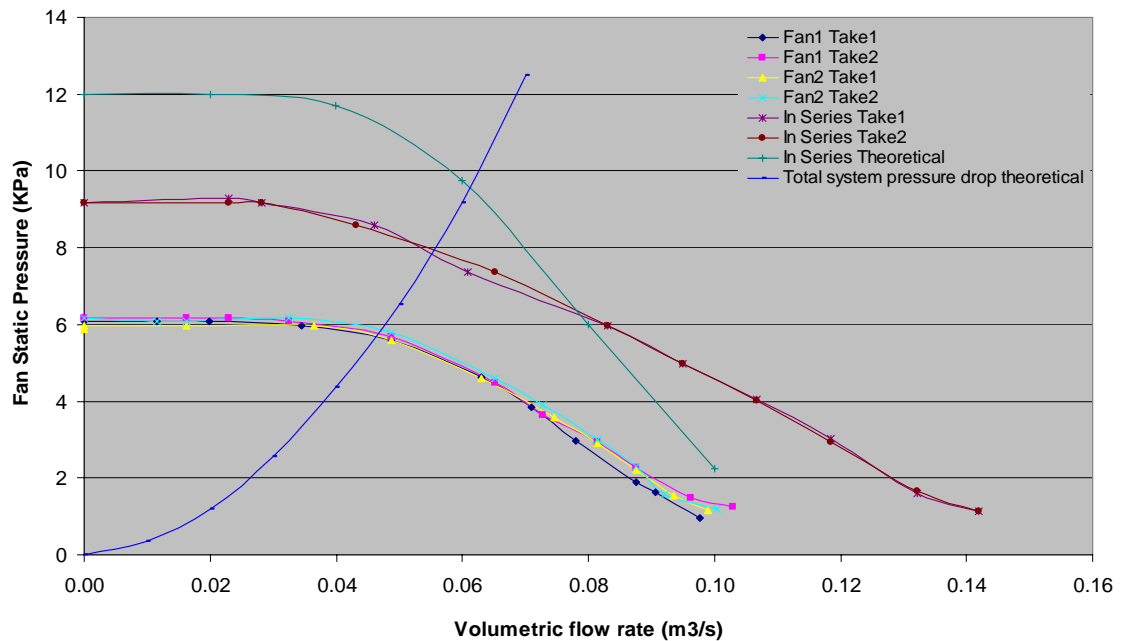


Figure 5.27: Experimental fan characteristic curves

5.6 CONCLUSIONS

An experimental rig was constructed in order to investigate the influence of swirl on the distribution of particles in a lean phase conveying mode. This chapter details the design process. The entire rig was designed in modular sections to enable the testing of the existing swirl inducing pipe at different locations. Two 1800W centrifugal fans were employed as the air mover after assessing different options to power the pneumatic rig. Different mechanisms for feeding the solid particles into the airflow and later recovering the same particles from the airflow were also assessed during the design process. The choice of feeding device was gravity hopper fitted with a gate and used in conjunction with a venturi while a cyclone was chosen to separate the solids from the airflow. Hollow spherical silicate microspheres, commercially available under the trade name of Fillite, were selected as the conveyed material for its physical

characteristics. Perspex tubes were used for the main part of the rig. Conductive copper strip was attached to the rig to prevent the build up of static electricity developed from the friction between the particles and the pipe wall. Pressure tappings were fitted to the rig to enable pressure monitoring. The airflow rate was monitored with a conical inlet, which was designed according to British Standard 848.

The conceptual design of this experimental facility was conceived so that the rig would allow the testing of the three lobed helix swirl pipe with a pitch-to-diameter ratio of 6 in a series of experiments described in the next chapter. These experiments include visualisation of the flow, LDA and PIV velocity measurements. Because these experiments require high optical transparency, fused silica glass was used instead of Perspex for the visualisation and measurement pipe section. The rig was designed firstly to allow the testing of a circular cross sectional control pipe against the three lobed helix swirl pipe; and secondly to allow easy implementation of the different experimental conditions through varying the air or solids flowrates. The experimental conditions and the experiments carried out are described in the next chapter.

CHAPTER 6

EXPERIMENTAL INVESTIGATION

6.1 INTRODUCTION

In the previous chapter, the experimental rig was designed and built to meet the unique requirement of each empirical investigation detailed in this chapter. This chapter examines various experimental techniques employed to investigate the influence of geometrically induced swirl on an airflow and also on a lean suspended flow of particles.

Prior to the experiments, the operating boundaries and conditions of the experimental rig were identified for the experimental programme. These are described in section 6.2. Also, in order to adequately address the overall aim of this study, four experimental investigations were conducted. Hence, they were sequentially dependent such that the results of the first set determined the aims and objectives of the second set, and so forth. The four sets of experimental investigations included: a pressure study, high speed camera recordings, Particle Image Velocimetry (PIV) and Laser Doppler Anemometry (LDA). The first set of the experimental investigations is the pressure study which aimed to establish the effect of the presence of the swirl pipe on the pressure drop of the system. The second set of experimental investigations employing high speed camera recordings aimed to obtain visual proof that the swirl pipe is effectively inducing swirl to the flow of particles. The third and fourth sets of experiments were carried out to obtain a better characterisation of the induced swirl flow and its behaviour downstream of the swirl pipe. The presentation, analysis and discussion of the findings of the first, second, third and fourth set of experimental investigations are reported in sections 6.3, 6.4.5, 6.5.5 and 6.6.5 respectively. Finally, the experimental errors and uncertainties are assessed in section 6.7.

6.2 EXPERIMENTAL CONDITIONS

Prior to conducting the detailed experimental programme, it was necessary to identify the baseline conditions against which they would be performed. To ensure that a lean particulate phases suspension was achieved, the two major experimental variables were

identified to be the solids and the air mass flowrates. The analysis of the results of the performance tests carried out on the particle feeder and the fans, reported in Chapter 5, enabled the determination of the required experimental conditions. The maximum solids and air mass flowrates attainable with the current solids feeder and fans, were 4g/s and 75 g/s respectively. It was therefore decided to carry out the experiments at five different solids and air mass flowrates, or 0.2, 1.1, 2.3, 3.4, 4.0 g/s and 24, 35, 47, 59 and 71g/s, respectively. The resulting conveying phase densities are very low compared to those commonly used in industries. The construction of an experimental test matrix employing this combination of solid and air mass flowrates enabled the following phase densities to be tested:

Phase density ϕ	Average conveying air velocity (m/s)				
	10.150	14.850	19.920	25.140	29.950
	Air mass flow rate (g/s)				
	23.926	35.024	46.989	59.300	70.629
0.190	0.008	0.005	0.004	0.003	0.003
Particle mass flow rate (g/s)	0.047	0.032	0.024	0.019	0.016
1.129	0.096	0.066	0.049	0.039	0.033
2.301	0.142	0.097	0.072	0.057	0.048
3.394	0.170	0.116	0.086	0.068	0.057
4.060					

Table 6.1: Phase density conditions for experiments

In order to reduce the number of experiments down from the possible 25, it was decided that only the highlighted conditions in Table 6.1 would be used to still convey an array of conditions.

The high speed camera experiments were first carried out on the original test rig to investigate whether the swirl pipe had any effect on a lean pneumatic flow suspension. However, following the analysis of the preliminary experimental data, it was concluded that the original experimental rig did not offer the required finesse of control required to test the operational conditions detailed in Table 6.1. Hence the high speed camera experiments were only carried out at the maximum solids and air flowrates. From the analysis of the results obtained from the high speed camera experiments, it was concluded that the particles were in full suspension in the flow. It was therefore postulated that the particles would follow the same path as that of the

airflow. The motion of the particles was therefore inferred from the streamlines of airflow identified from an analysis of the PIV and LDA experiments. It was also decided that the operating conditions of the original experimental schedule as detailed in Table 6.1 would be time consuming and produced redundant data sets for the PIV and LDA experiments. The experimental schedule had to be revised and only three air flow rate settings were used: low (24g/s), medium (47g/s) and high (71g/s). As shown in Table 6.2, these were equivalent to a Reynolds number of $4.5 \times 10^4 \pm 791$, $9 \times 10^4 \pm 404$, $1.4 \times 10^5 \pm 269$ at the inlet and hereby referred to as the low, medium and high Reynolds number flow settings. The associated experimental errors are discussed in Section 6.7.

Conditions at inlet			
	Mean air mass flowrate (kg/s)	Mean velocity (m/s)	Reynolds number
Low	0.024 ± 0.00169	10 ± 0.015	$4.5 \times 10^4 \pm 791$
Medium	0.047 ± 0.00086	20 ± 0.016	$9.0 \times 10^4 \pm 404$
High	0.071 ± 0.00057	30 ± 0.019	$1.4 \times 10^5 \pm 269$

Table 6.2: Inlet conditions used in experiments

6.3 PRESSURE MEASUREMENT

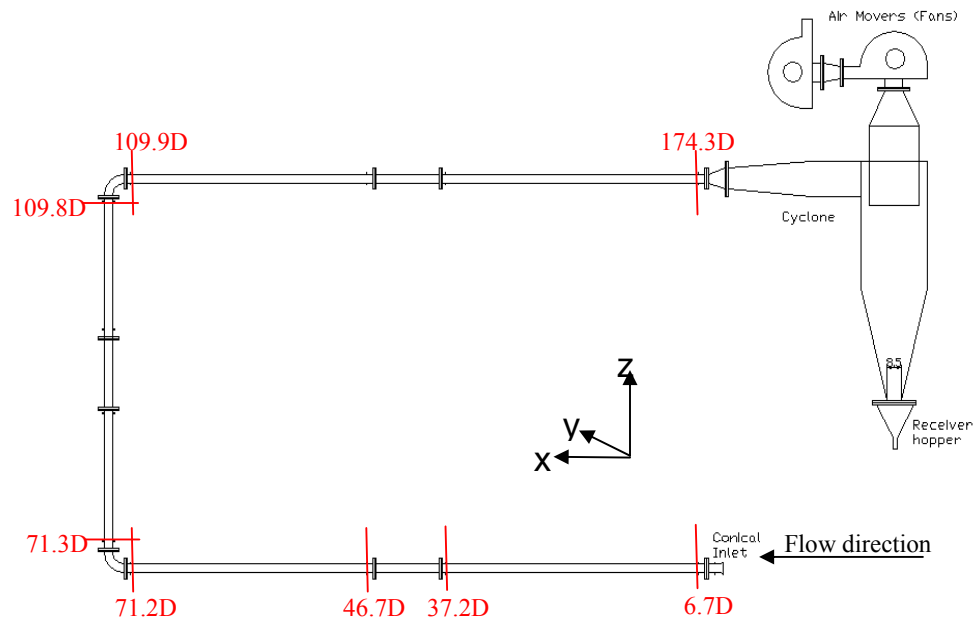


Figure 6.1: Pressure measurement locations on the experimental rig

Gauge pressure was measured at the pressure tapping locations as shown in Figure 6.1. At each pressure measurement, a series of four pressure tapings (0° , 90° , 180° and 270°) were equally spaced around the circumference of the pipe. These tapings were connected by a pipe manifold to a manometer. This arrangement is shown in Figure 5.9. A series of pressure measurements were first carried out at the five air mass flowrates identified in Section 6.1, which correspond to Reynolds numbers of $4.5 \times 10^4 \pm 791$, $7 \times 10^4 \pm 540$, $9 \times 10^4 \pm 404$, $1.1 \times 10^5 \pm 320$, $1.4 \times 10^5 \pm 269$ respectively at the inlet. A series of two experimental regimes were explored, the first using the straight control pipe section and then using the swirl pipe section. The results are displayed Figure 6.2. The measurement error was calculated to be 9.81 Pa, as discussed in Section 6.7.

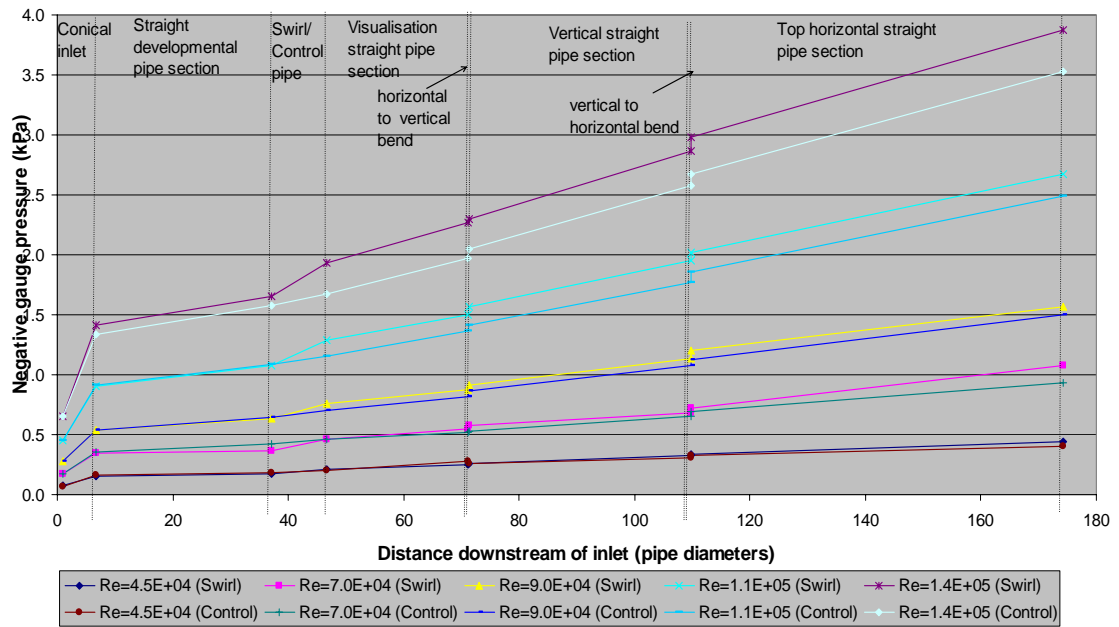


Figure 6.2: Pressure drop distribution (Standard error ± 0.00981 kPa)

The pipeline pressure drop was observed to increase with an increase in pipeline air velocity. A steeper pressure gradient was observed, first at the swirl pipe and again at the horizontal-to-vertical and vertical-to-horizontal bends along the run of the pipe rig. The degree of pressure drop experienced due to the presence of the swirl pipe was observed to be directly proportional to the pipeline air velocity, with a higher pipeline air velocity resulting in a higher pressure drop. This is confirmed in a linear plot of the

pressure drop per unit length of swirl pipe, as shown in Figure 6.3 for the five different air flowrates investigated.

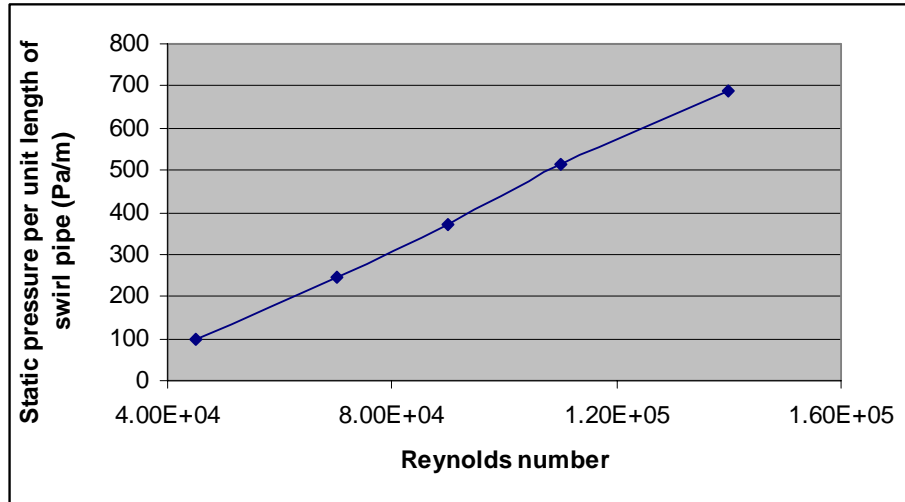


Figure 6.3: Pressure drop per unit length of pipe

The increase in the gauge static pressure drop within the swirl pipe section can be attributed to the generation of secondary flows which are responsible for inducing the swirling flow by converting axial momentum into angular momentum, as shown in Section 6.6.4.2. It is however very likely that the drop in static gauge pressure was enhanced by the sudden change in cross sectional geometry between the helical swirl pipe and the circular pipe, as shown in Figure 6.4. A pipe section which provides a smooth transition between the two cross sectional geometries can be designed (Ariyathne, 2005) to test this hypothesis.

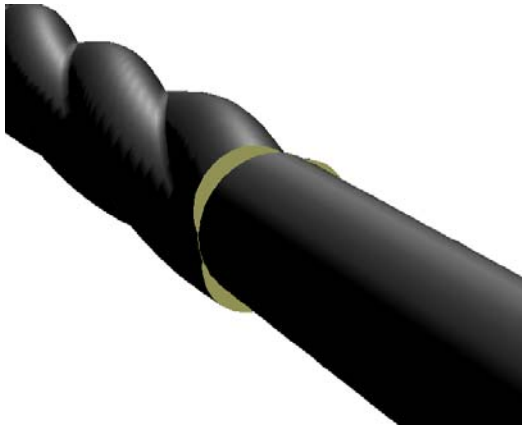


Figure 6.4: Sudden change in geometry at swirl/circular pipe intersection (close up)

6.4 HIGH SPEED VIDEO IMAGING & LASER SHEET

The complexity of high speed flows has motivated researchers over the last few decades to devise a wide range of experimental methods to visualise the complex flow regimes. Various imaging concepts have recently been developed to produce single plane cross-sectional images. These studies have been mostly concentrated on yielding new insight into the boundary layer structures, shock wave/boundary layer interactions, and the transition from laminar-to-turbulent flows.

These techniques are generally based on light scattering methods using short-pulsed lasers, coupled with digital cameras with large format charged couple device (CCD) chips and high receptivity to light. The short-pulsed lasers enhance camera performance by illuminating the flow with ultra-short pulses of light. Image blur is thus eliminated, even for flow particles moving at high velocity. Using light optics, the laser light can be formed into a thin sheet of light (known as a lightsheet), which enables a 2D slice visualisation of a 3D flow.

6.4.1 Objectives and scope of the high speed video experimental programme

The objective of the application of the high speed camera technique was to obtain a visual evidence to indicate the influence that a swirl pipe may have on the trajectory path of particles suspended within a lean phase pneumatic flow. These initial high speed camera experiments were carried out on the original experimental rig configuration (as detailed in section 5.3), which did not offer the finesse of control of operation required to test at the conditions identified in Table 6.1. The scope of this initial experimental programme was restricted to determining the effects of a swirl pipe on the maximum solids and air flowrates of the rig, or a phase density of 0.17. It was decided that this would be enough to achieve the aim of these initial tests. For this one flow condition, it was however expected to obtain visualisation data of the flow both along and across the flow axis, using white light and laser sheeting respectively.

6.4.2 Experimental apparatus and instrumentation

6.4.2.1. High speed camera

The high speed camera used was a Kodak Motion Corder SR Ultra, as depicted in Figure 6.5. It is a monochrome 512 x 480 pixels digital CCD system, with recording rates from 30 to 10,000 frames per second (fps) (Eastman Kodak Company, 1998). Higher recording rates are made at the expense of spatial resolution and/or recording time as shown in Table 6.3.



Figure 6.5: Kodak motion corder SR ultra

Recording rate (fps)	Resolution (pixels)	Recording time (seconds)	Images captured
30	512 x 480	72.8	2,184
60	512 x 480	36.4	2,184
125	512 x 480	17.5	2,184
250	512 x 480	8.7	2184
500	512 x 240	8.7	4368
1,000	256 x 240	8.7	8,738
2,000	256 x 120	8.7	17,476
3,000	128 x 120	11.6	34,952
5,000	128 x 80	10.4	52,428
10,000	128 x 34	12.3	123,360

Table 6.3: High speed recording specification (from Kodak Motion Corder Analyser User's Manual, Kodak Company, 1998)

The recorded images were then downloaded to a personal computer via a small computer system interface (SCSI). The digital data output was in the form of 8 bit monochrome tag image file format (TIFF) files, corresponding to 256 levels of grey scale. There was no need to calibrate the camera as velocity information was not going to be determined from the images.

6.4.2.2. Laser

A pulsed Twin Quantel Nd:YAG (neodymium-doped yttrium aluminium garnet) laser equipped with a sonohysterogram (SHG) module to double the frequency of the light was used. The resulting laser pulses were 532 nm (visible green light) of frequency 15Hz. A pulse energy of 150mJ was used. The laser was mounted on a movable bench. The light optics, a cylindrical lens, was located at the end of a 2m long flexible optical arm. The cylindrical lens spread the laser beam into an approximately 1mm thick light plane of intense green light of wavelength 532nm. Thus to locate the light sheet across the flow plane of interest, it was achieved by simply moving the position of the optics arm.

6.4.3 Set-up and procedures

The first objective of this experimental programme was to obtain a general view of the flow in order to gauge whether a swirl flow was indeed present. This was achieved by recording the flow with the high speed camera in white light. The line of sight and focus of the camera was positioned at a 10 degree angle to the flow axis upstream of the point of interest (see Figure 6.6(1)). The best available compromise between recording rate and image resolution for that camera location was determined to be 500 frames per second. The width of the image size allowed by the recording of the flow was within a length of pipe of about 10D from the outlet of the swirl pipe.

The second objective of the experimental programme was to determine the effect that the swirl had on the transported particles. Consequently a laser sheet study was carried out according to the experimental guidelines specified by Huber and Sommerfeld (1994). The light sheet was made to intersect the pipe at an angle of about 45° with respect to the pipe flow axis. Video images of the scattered light were then taken by placing the camera perpendicular to the light sheet but on the opposite side of the incident light (see Figure 6.6(2)). This experimental configuration had the advantage

of minimising the light reflections experienced from the outer and inner sides of the pipe wall. Moreover, this camera position ensured that the lengths of the paths of the incident and reflected light were the same for locations at the top and bottom of the pipe cross-section, thereby reducing the problem of path attenuation. The optics arm of the pulsed laser projected a sheet of intense green light across the ‘region of interest’ pipe. The light sheet intersected the pipe at a distance of about 1m from the cylindrical lens in the optics arm. This guaranteed that only the centre of the laser sheet, where the light intensity is almost uniform, intersected the pipe. The recordings were made at 250 frames per second at one pipe diameter intervals from the inlet of the visualisation pipe section, as shown in Figure 6.7.

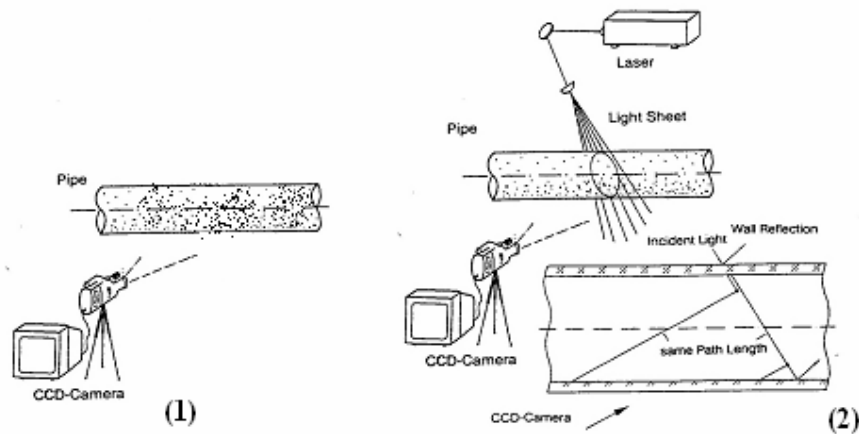


Figure 6.6: High speed camera recording arrangement (modified from Sommerfeld, 1994)

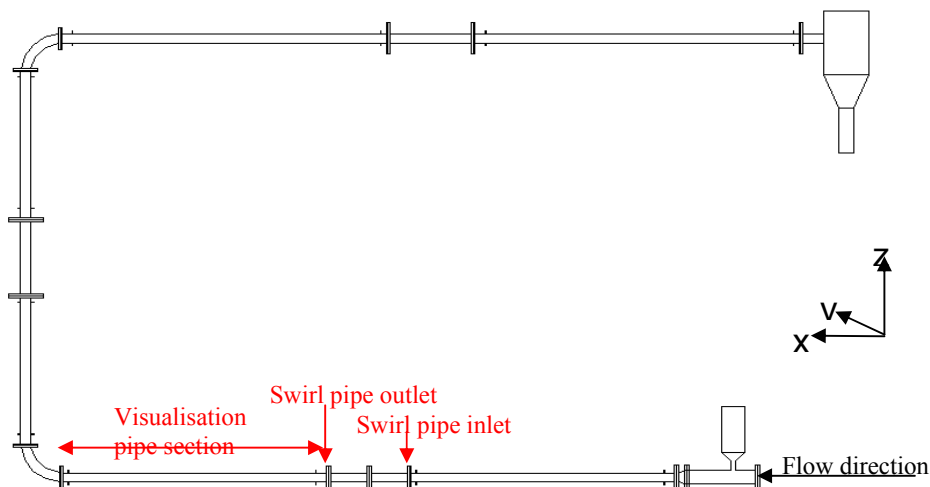


Figure 6.7: Measurement location

Figure 6.8 shows a photograph of the layout of the experimental apparatus for the laser sheet experiments. Both the white light and laser sheet high speed recording were carried out first with a straight 40cm control pipe section, followed by the insertion of the 40cm swirl pipe section. The experimental procedure was:

- The rig was first drained of particles.
- The fans were switched on and allowed to run at maximum setting for 2 minutes before opening the gate to introduce particles.
- The flow was allowed to develop for 30 seconds before any recordings were made.

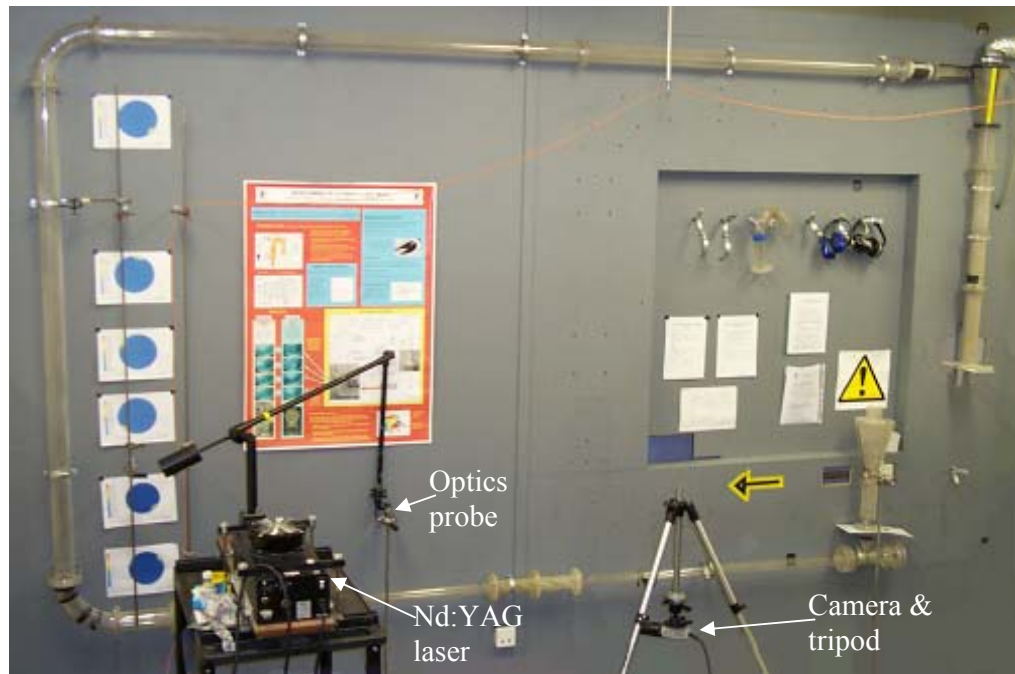


Figure 6.8: Experimental setup

6.4.4 High speed video imaging results

The images obtained from the high speed camera recordings were translated into a grey scale TIFF format. The image contrast and brightness were digitally enhanced using Paintshop Pro version 9. The images captured using the laser sheeting were subsequently translated to negative images. A more comprehensive description of the image processing conducted is provided in section 6.4.4.2. An audio video interleaved (AVI) file was then created using the images in sequential order. This was achieved

with Animation Pro version 3.05. The animations are included in Appendix B contained in the CD attached.

6.4.4.1. Flow visualisation using white light

Figure 6.9 and Figure 6.10 show the flow patterns recorded from 0 to 10 pipe diameters downstream of the 40cm control pipe section and the 40cm swirl pipe section respectively. These recordings employed a white light source and the frames were captured at 500 frames per second. For reasons of clarity, Figure 6.9 and Figure 6.10 show only the images of the flow captured over a time span of 0.6 seconds. However, the AVI movie, contained in the attached CD (Appendix B-File 1) , of the flow images recorded employs 500 images of the flow regime captured over 1 second of recording time.

As was expected, when the control pipe (40cm straight circular pipe section) was used, no distinct differences in flow pattern could be observed downstream of the control pipe section as shown in Figure 6.9. Over the 0.6 seconds shown, i.e. from t_0 to t_4 , the flow was constant. The flow regime was observed to be homogeneous and the particles were fully suspended.

On the other hand, when the swirl pipe section was inserted, a rotational swirl pattern was observed in the same direction as the twists present in the swirl pipe geometry. The observed swirl patterns can be clearly observed on the captured images shown in Figure 6.10. The swirl pattern took the form of a ribbon effect, with the suspended particles following three distinct ribbon-like paths rotating around each other. This effect is more clearly observed on the AVI movie file contained on the CD attached to this thesis (Appendix B-File 2). The “ribbon effect” resulted in high and low regions of particle concentrations, with particles being concentrated in the “ribbon” regions. It was proposed that the particulate ribbons were formed as the result of particles travelling along the cusps and ridges of the geometry of the swirl pipe and being released off the ridges existing at the transition of the cusps of the swirl pipe and the circular visualisation pipe section. It was also observed that the wavelength of the “ribbons” tended to increase with distance downstream of the swirl pipe, indicating that the swirl effect decayed over the downstream length of pipe. The effect of swirl

was approximated to a complete decay at a distance of approximately eight pipe diameters downstream of the swirl pipe.

It was also noted that when the particles were in full suspension. Their motion was fully influenced by that of the air surrounding them. Hence, it was postulated that for lean phase flow, the particles followed the streamlines of the conveying air flow.

The “ribbon effect” provided the evidence required that the swirl pipe was inducing swirl to the lean phase pneumatic flow and hence accomplished the first objectives of the high speed video experimental programme.

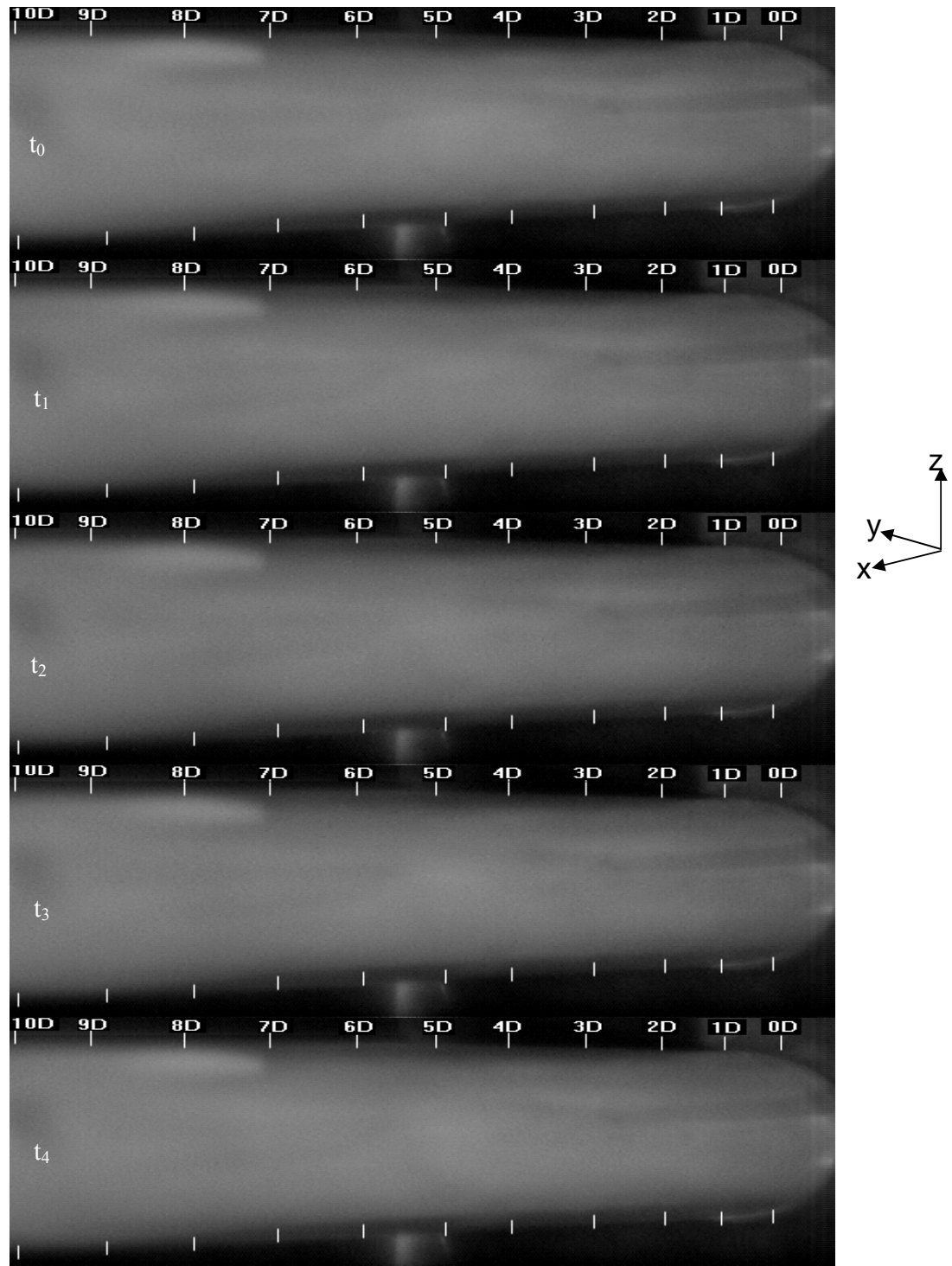


Figure 6.9: Flow pattern 0-10D downstream of control pipe section (with white light)

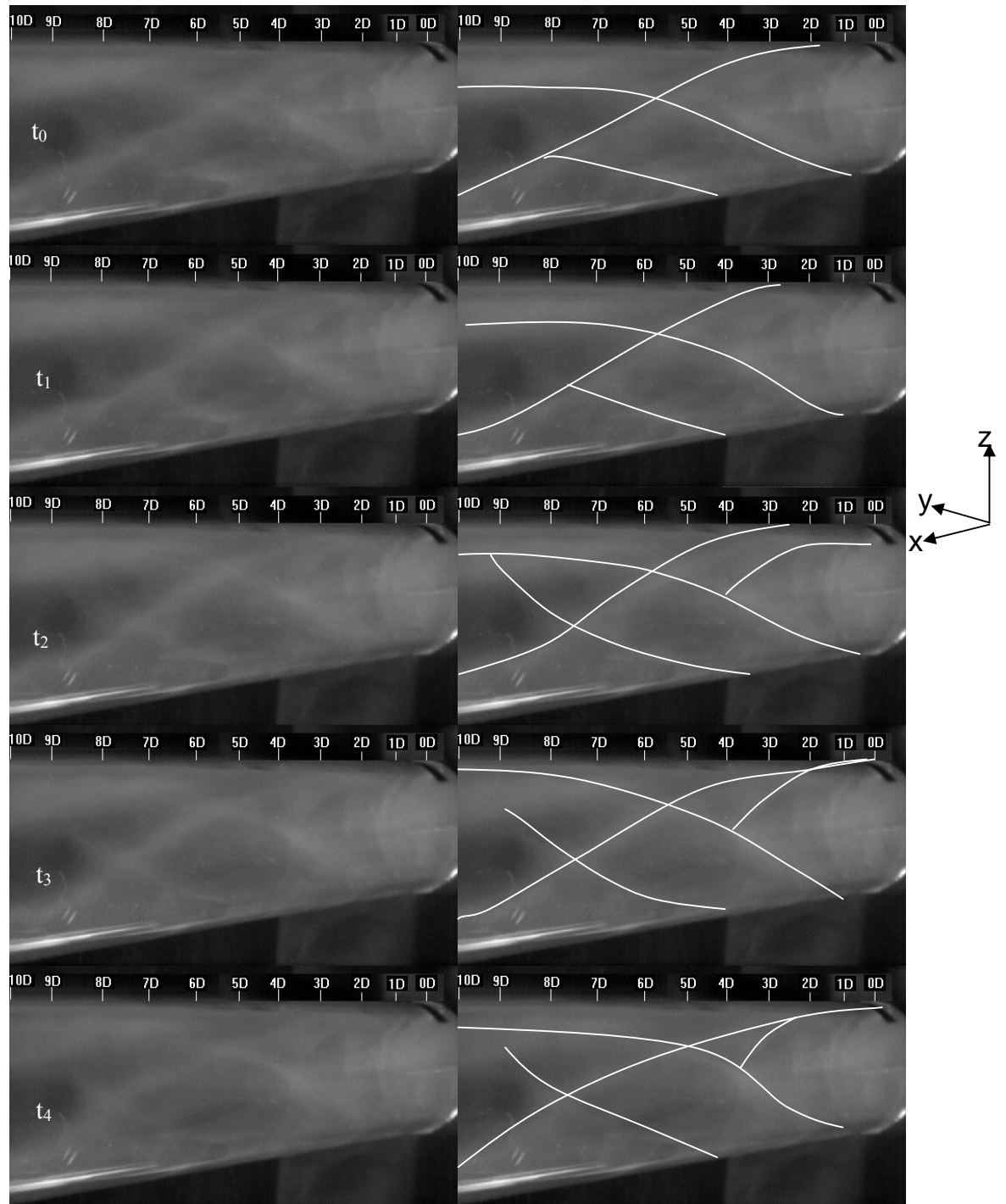


Figure 6.10: Flow pattern 0-10D downstream of swirl pipe section (with white light)

6.4.4.2. Flow visualisation using laser sheeting

Figure 6.11 to 6.14 show the flow pattern at various pipe diameters downstream of the 40cm control pipe section and the 40cm swirl pipe section. These visual recordings were taken using a laser sheet to illuminate the cross sectional area of the pipe at the required distance downstream of the test section over a time span of 8.7 seconds. The visual images were captured at 500 frames per second at intervals of one pipe diameter downstream of the outlet to the circular control pipe or the helical swirl pipe test sections. Before the regions of high particle concentrations could be identified, the images required to be digitally “cleaned” to reduce the inherent noise in the quality of the captured image. One type of noise is random noise, which is characterised by a statistical variation in the grey level from pixel to pixel (Busch, 2003). It may be an inherent part of the image formation process such as the granularity associated with the image. If the noise is correlated from pixel to pixel, its variation can be reduced by a low pass filter. Another type of noise is called isolated noise (Busch, 2003). Isolated noise can occur in certain pixels or even in lines due to poor data transmission. Non-linear filtration techniques have been used to remove such specs or streaks. The detail of the image enhancement techniques used are discussed below.

Background noise subtraction is a procedure by which most of the background noise can be subtracted from the original image (Copestake, 2001). In order to suppress the background noise that remains constant in all these images, an image of the flow field was captured prior to introducing the particles. The intensity values of this image are then subtracted from the subsequent images with particles.

Contrast enhancement was applied to the images as the unprocessed captured images exhibited a low contrast, i.e. the grey level histogram had a narrow intensity range (Copestake, 2001). The contrast enhancement was achieved by linearly stretching a smaller range of grey levels across the original range of grey levels in the intensity histogram. The intensity range was defined by the limiting values I_{hi} and I_{low} . For each pixel with intensity at or below I_{low} , the intensity value was reassigned to zero (black). Similarly, for intensities at or above I_{hi} , the intensity value was reassigned to 255 (white). The remaining pixels underwent a linear transformation mathematically represented as:

$$I_{out} = \left(\frac{I_{in} - I_{low}}{I_{hi} - I_{low}} \right) \times 255 \quad (\text{Eq. 6.1})$$

Suitable values for I_{low} and I_{hi} were determined to be 25 and 245 respectively based on subjective evaluation.

Further image processing such as median and smoothing filters could have been carried out to improve the visual quality of the images. However, these would have altered the grey intensity value of each pixel relative to its neighbours. The median filter replaces the grey level of each pixel with the median value of its 8-pixel neighbourhood (Copestake, 2001). Similarly, the smoothing filter replaces the grey level of each pixel in the image with the arithmetic mean of the eight pixel neighbourhood (Copestake, 2001). Median and smoothing filters were therefore not used to process the images.

Despite image enhancement, the resulting visual quality of the images was still poor, as can be seen from Figure 6.11 to 6.14. This was mainly due to the degree of reflection of the laser light off the pipe wall experienced in relation to the amount of laser light reflected by the particles. The reflections experienced from the pipe wall could have been further minimized by using a thinner tube, such as optical fused silica glass, but this was only identified to be a problem when analysing the high speed recording images and was taken into consideration for future PIV and LDA experiments. As a lean particulate phase was required, that implied that only few particles would reflect the laser light at any one cross section at any one time. The small diameter of the particles also meant that they could only reflect a small amount of light.

An analysis of the images captured when the control pipe was in place, Figure 6.11 and Figure 6.12 (and Appendix B-File 3a-f) concluded that the observed particle concentration distributions were homogeneous and that the particles were fully suspended.

When the swirl pipe was used, a slightly darker region was observed in the centre of the pipe, representing the region of slightly higher particle concentration, as shown in Figure 6.13 and Figure 6.14. This core flow of particle suspension and transport was

sustained up to eight pipe diameters downstream of the swirl pipe. AVI movie files showing this effect are available on the attached CD (Appendix B-File 4a-f).

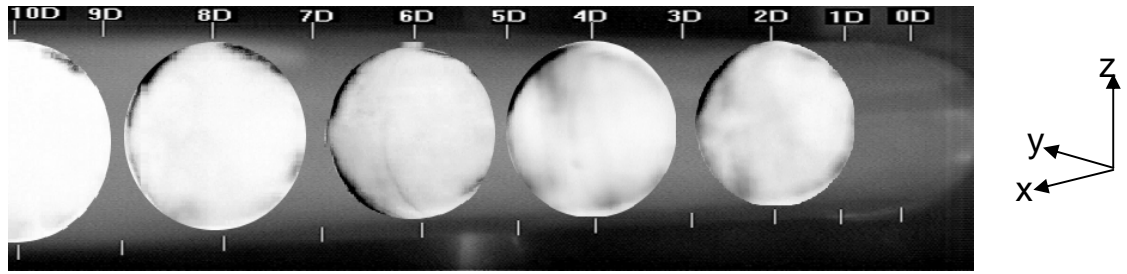


Figure 6.11: Flow pattern 0-10D downstream of control pipe section (with laser sheet)

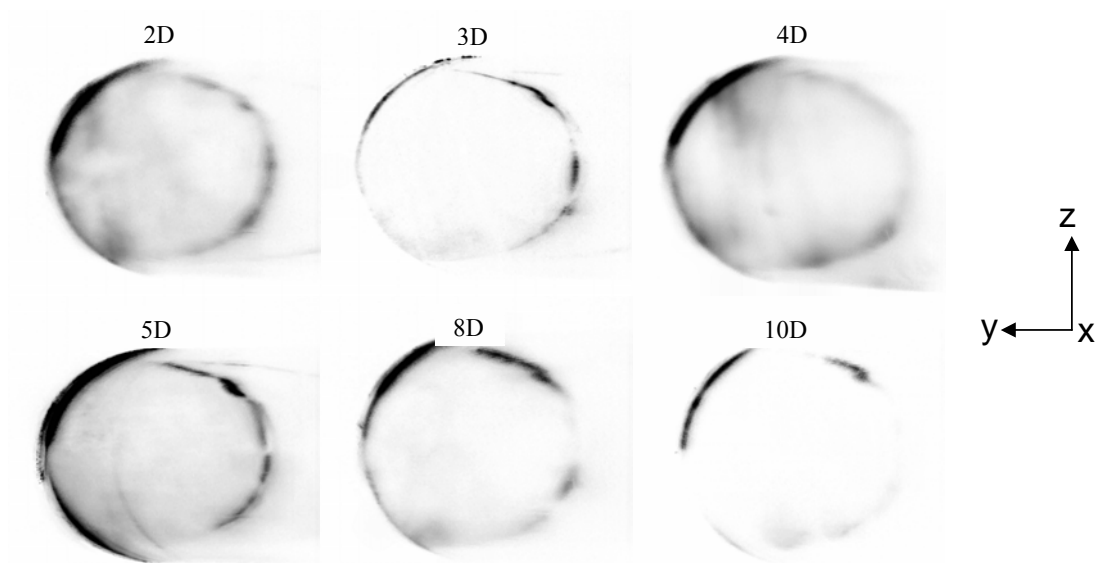


Figure 6.12: Flow pattern at 2, 3, 4, 5, 8 and 10 pipe diameters downstream of control pipe section (with laser sheet)

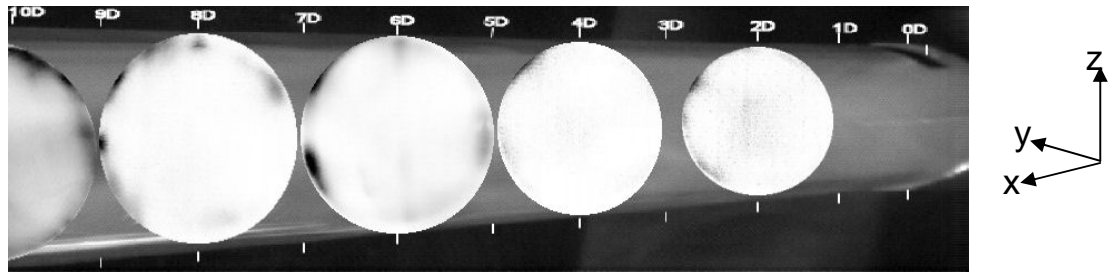


Figure 6.13: Flow pattern 0-10D downstream of swirl pipe section (with laser sheet)

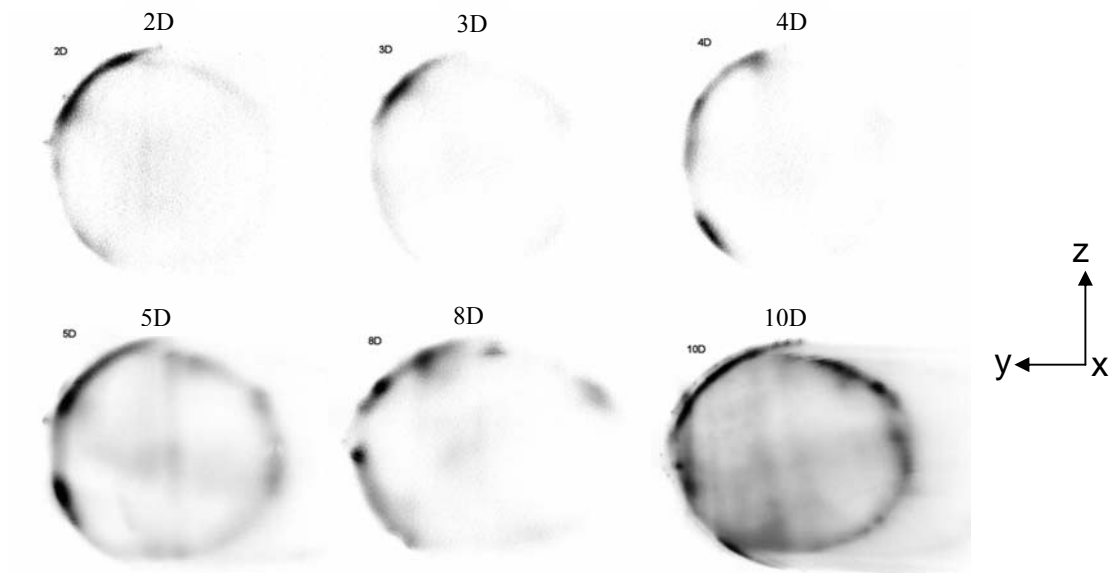


Figure 6.14: Flow pattern at 2, 3, 4, 5, 8 and 10 pipe diameters downstream of swirl pipe section (with laser sheet)

6.4.5 Conclusions from high speed video experiments

The high speed camera technique was applied to obtain visual evidence to indicate the influence that a swirl pipe may have on the trajectory path of particles suspended within a lean phase pneumatic flow. The flow was visualised both along and across the flow axis, using white light and laser sheeting respectively. Due to a lack of finesse of operational control of the original experimental rig configuration, the experiments could only be carried out at a single phase density.

White light recordings were made at 500 frames per second recording a distance of 10 pipe diameters downstream of the 40cm control pipe section in the first set of experiments and in the second set of experiments, 10 pipe diameters downstream of the 40cm swirl pipe section. When the control pipe was in place, the captured images showed a homogeneous distribution of particles, with the particles fully suspended. Under the same flow conditions, when the swirl pipe was inserted, a general swirl in the same direction as the twists in the swirl pipe geometry could be clearly observed. The swirl patterns of the particles took ribbon-like paths, rotating around each other and resulting in high and low regions of particle concentrations. The “ribbon effect” was also shown to decay over a length of pipe equivalent to eight pipe diameters.

Images of the cross-sectional flow recordings with laser sheeting captured at 500 frames per second at one pipe diameter intervals downstream of the 40cm control pipe section and the 40cm swirl pipe section were of poor quality despite using several image enhancement techniques. When the control pipe was in place, no regions of higher particle concentrations were observed. When the swirl pipe was used, a region of very slightly higher particle concentration was observed in the centre of the pipe. This core flow of particles was sustained up to eight pipe diameters downstream of the swirl pipe.

The analysis of the results from the high speed recording using laser sheeting were not conclusive due to the poor quality of the image. This is due to the amount of reflection of the laser light off the pipe wall in relation to the amount of laser light reflected by the particles. On the other hand, the “ribbon effect” observed along the flow axis with the white light recordings, provided the evidence required that the swirl pipe was inducing swirl to the lean phase pneumatic flow. Since it was observed that the

particles were in full suspension, it was concluded that the motion of the particles was completely influenced by that of the flowfield and that it could therefore be inferred from the flowfield. The analysis of the data justified the building of a better experimental rig to carry out further experiments, such as PIV and LDA and to enable a better understanding of the flow structure.

6.5 PARTICLE IMAGE VELOCIMETRY (PIV)

Particle image velocimetry (PIV) has become one of the more popular methods for establishing the instantaneous planar velocity field within a flow. It is an optical technique which has been applied to a diverse range of flows including water dynamics, aerodynamics, air-conditioning systems, acoustics, blood circulation and boundary layer turbulence. A major advantage of PIV is that it is a whole-flow-field technique and it can carry out two-dimensional and three-dimensional instantaneous velocity measurement, as opposed to the single-point capability of the pitot tube, the hot wire anemometer and the laser Doppler anemometer. PIV can also produce real-time 2D velocity vector maps, or 3D ones if a stereoscopic approach is used.

The main disadvantages of PIV visualisation techniques is that they are expensive (typically £100,000 for a simple system), they require an optically transparent flow conduit and a transparent flowfield through which the light beams can pass, the characteristics of the flow is inferred from the seeding of the observed flow regime by particles and finally depending on the application, it can be an intrusive technique. The basic principles of PIV are provided in Appendix C.

6.5.1 Objectives and scope of the PIV experimental programme

The application of PIV technique was employed to obtain a better characterisation and understanding of the resulting flowfield downstream of the swirl pipe section. The use of PIV techniques would allow the determination of vector flowfield maps of the flow downstream of the swirl pipe section. The PIV equipment was specified and subsequently rented from DANTEC technologies, Bristol. The scope of the PIV experimental programme was to firstly test the experimental setup to determine if it was adequate for PIV measurements for this specific flowfield; and secondly to obtain 2D vector maps of the flowfield at cross-sectional planes located at intervals of two

pipe diameters downstream of the control and swirl pipe sections for the three different Reynolds number flow settings (low = $4.5 \times 10^4 \pm 791$, medium = $9 \times 10^4 \pm 791$ and high = $1.4 \times 10^5 \pm 269$).

6.5.2 Experimental apparatus and instrumentation

The DANTEC FlowMap 2100 Particle Image Velocimetry (PIV) system was used in the experiment (depicted in Figure 6.15). Various seeding generators were available to attain the optimum seeding level. These included a High Volume Liquid Seeding Generator (10F03), Smoke Generator (10D90) and a Powder Seeding Generator (10F01). The liquid and smoke generators produce spherical seed particles with diameters between 0.1 and $5 \mu\text{m}$. A straight probe was available for delivery of the seeding.



Figure 6.15: DANTEC PIV system

The laser used was a pulsed Nd:YAG (Neodymium-doped yttrium aluminium garnet) laser with a maximum energy of 120 mJ per pulse with each pulse lasting about 10 nano seconds. The laser beam diameter is approximately 3 mm and the wavelength of the light is 532 nm (green light). These lasers have small, compact optical heads and can therefore be transported and positioned very easily. Nd:YAG light-sheet optics were used to illuminate the flow. The dimensions of the light-sheet could be defined by changing the focal length of the optics. The second laser burst was set for 125

micro-seconds, optimised for maximum particle displacement 25% of a 32x32 pixels interrogation area.

The PIV images were recorded with a HiSense MkI PIV camera. The camera uses a high-performance progressive scan interlines CCD chip. This chip includes 1280 by 1024 light-sensitive cells and an equal number of storage cells. The camera has no shutter, therefore the PIV delay time between two subsequent images was achieved by adjustment to the timing of the laser pulses.

DANTEC's FlowMap Analysis Software, FlowManager version 4.5, was available with the PIV system. The software provides the capability of processing camera images into velocity vector map results in real-time. Fast Fourier Transform algorithms are used by the software to process the signals. The software provides an integrated measurement-user interface which enables the user to control the set-up of PIV system instrumentation and the data-acquisition and data-analysis options. FlowManager version 4.5 also includes an improved PIV processing algorithm known as the adaptive correlation technique which improves the recovery of a good signal-to-noise ratio from the PIV signal when the flow includes large velocity gradients, such as boundary layer flows.

DANTEC literature on the fundamental principle of Adaptive correlation algorithm describes it as an iterative procedure as follows: "From an initial guessed offset value, an offset is introduced from the first window (the interrogation area in the image frame from laser pulse one) to the second window (the equivalent interrogation area in the image frame from laser pulse two). The obtained vector is validated and is used as a new estimate for the window offset. A new run is made, but this time with a smaller window (interrogation area)". Two of the main benefits from using the shifted window are that particles which have left the interrogation area during the time between the two light pulses (in-plane dropout) can be identified and ignored, as they would otherwise result in erroneous vectors.

To maintain the accuracy of the processed data using the cross correlation technique requires the difference between the largest and smallest velocity within an interrogation area to be less than 5% of the mean velocity, as velocity gradients

produce low signal peak in the correlation and in turn results in poor vectors. Because the adaptive correlation algorithm applies an adaptive window offset, a refinement of the interrogation area is possible, thereby reducing the velocity gradient and improving the signal.

6.5.3 Set-up and procedures

The DANTEC FlowMap 2100 Particle Image Velocimetry (PIV) system was used to acquire multi-point velocity measurements in a plane orthogonal to the flow direction. Pulsed 120mJ Nd:YAG laser were then used to illuminate the y-z measurement plane normal to flow direction. For this experiment, it was decided that the best way of achieving this was to use an endoscope, mounted onto the camera. The endoscope has a 90 degree mirror at the tip and was placed at the downstream end of the swirl pipe so that its view was upstream and along the axis of the pipe. The endoscope focuses at a point 100mm upstream of its location and the field of view diameter reaches 50mm, which was the same as the pipe diameter. Hence the camera could view the same plane inside the tube that the light sheet was cutting. However this entails the use of an intrusive measurement probe. Access ports for the 8mm diameter endoscope were drilled into the pipe at 100mm downstream of the measurement planes locations. The optics configuration used in the experiment is shown in Figure 6.16.

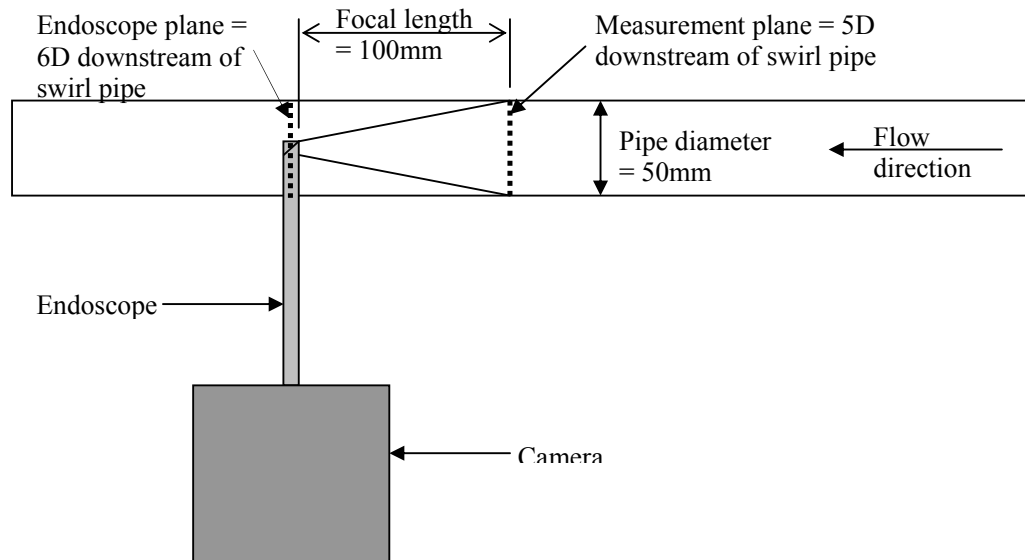


Figure 6.16: The configuration of the measurement optics

The general procedure for PIV image acquisition is:

- the laser is synchronized with the digital imagers, which was achieved using the FlowManager software,
- the laser light is positioned to illuminate the test volume,
- the scattered light from the tracer particles is recorded using the digital camera,
- an image analysis is performed on the captured image.

However, before any image can be processed so that pixels can be converted into distance, the camera needs to be calibrated. Calibration requires the user to focus the camera on an object of known size, acquire an image, and then select points on the image which are separated by a known distance.

The camera was calibrated by focussing the camera on a piece of calibrated adhesive tape attached to a piece of cardboard, as shown in Figure 6.17. The calibration on the adhesive tape was checked against a steel ruler for accuracy. Given that the camera has a fixed number of pixels in each direction (1280 x 1024) the magnification ratio can be determined. For the experimental set-up shown in Figure 6.16 this calculation yields a ratio of $42\mu\text{m}/\text{pixel}$.

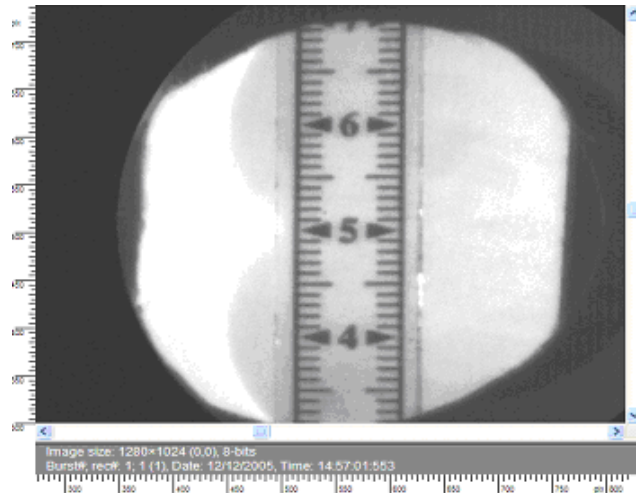


Figure 6.17: Calibration of PIV system

The seeding particles were introduced directly upstream of the conical inlet and allowed to travel to the measurement plane. The lasers were then pulsed at time separation intervals of 70, 50 and 30 μ s for the three different mean transport velocities and hence Reynolds numbers. The interframe delay was selected to provide ample time for the fastest moving particles to traverse roughly 25% the width of the interrogation area between frames. As each laser was pulsed the HiSense MkII digital camera was triggered and captured a 54mm x 54mm image of the seeded flow at a distance of five pipe diameters downstream of the outlet of the swirl pipe section as the flow passed through the test section.

The DANTEC processing algorithm partitions each captured image into a series of 40 \times 32 interrogation areas, each 32 \times 32 pixel in size. DANTEC's FlowManager 4.5 software was used to apply a Gaussian window and a digital bandpass filter. These were followed by the cross-correlation as well as the sub-pixel interpolation necessary to accurately determine the statistical shift in the seed particles between frames.

Figure 6.18 presents an example of a 32 \times 32 pixel interrogation area at two times separated by an appropriate time interval of Δt . Whilst this example is merely intended to illustrate the process of extracting a velocity of two sequential images, each particle typically covers 2 to 4 pixels. Figure 6.18 show the seeding dropout. For the cross correlation technique to produce an accurate representation, a minimum of 5 seeding particles are recommended for each interrogation area. Computing the two-dimensional cross-correlation between these two successive digitally captured frames yields a peak shifted from the origin by 4 pixels horizontally and vertically. Therefore, an interpolation is performed to locate the peak in the correlation. Following the location of the peak, this shift is converted to a distance and used to compute the corresponding velocity.

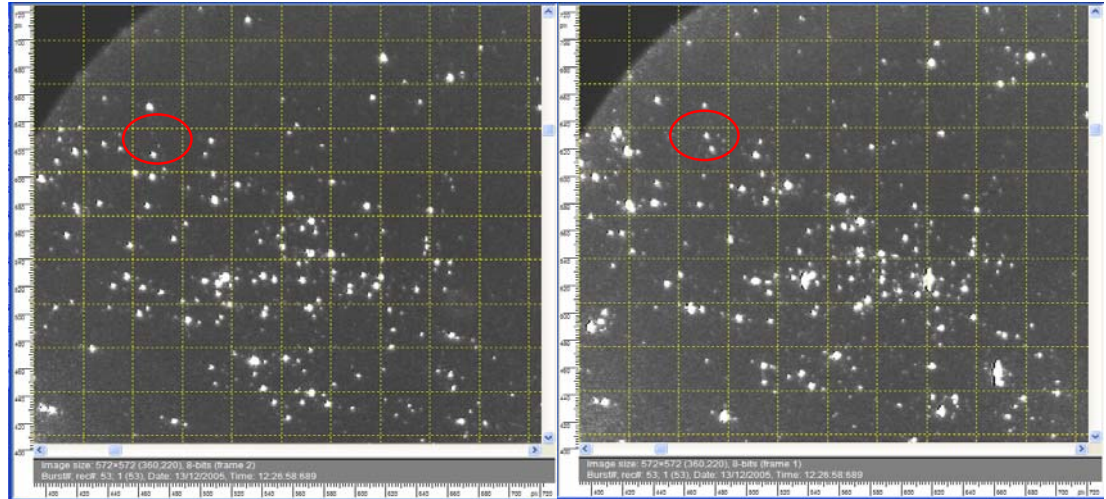


Figure 6.18: Typical image pairs as captured by PIV system, showing seeding dropouts (circled in red)

6.5.4 Presentation of the PIV measurements results

Once the PIV system had been calibrated, some preliminary tests were carried out to ensure that the results were representative of the true flow conditions. These tests were carried out at a single location, i.e. five pipe diameters downstream of the swirl pipe, and at the high mean transport velocity and hence high Reynolds number flow settings.

6.5.4.1. PIV results downstream of a swirl-inducing pipe

The first set of test was carried out using an aerosol seeder from a fog generator using Ondina Oil. The aerosol seeder produced an aerosol of oil droplets of an average size of 3 microns, which would be expected to follow the airflow field streamlines faithfully based on a maximum Stokes number of 0.0048 for the range of conveying velocities considered. Velocity vector maps as shown in Figure 6.19 were derived from individual image pairs. These velocity vector maps depicted small localised vortices within the flow region. These swirl regions also seem to correspond to where the “roping effect” was observed. They were therefore believed to be due to the influence of the swirl pipe, the same effect that was causing the “ribbon effect” observed from the high speed camera recordings.

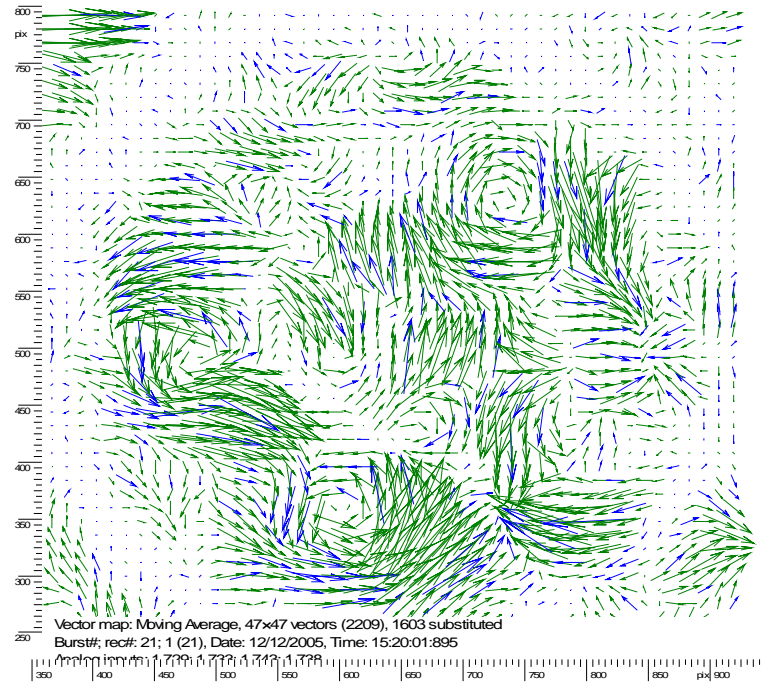


Figure 6.19: Vortices observed on velocity vector map from single image pair

In order to achieve good repeatability of the results, vector maps should be derived from at least fifty image pairs. When this was performed, vortices could no longer be observed. In fact there was no other general trend than a swirl of the flowfield in the same direction as the geometry twist of the swirl pipe.

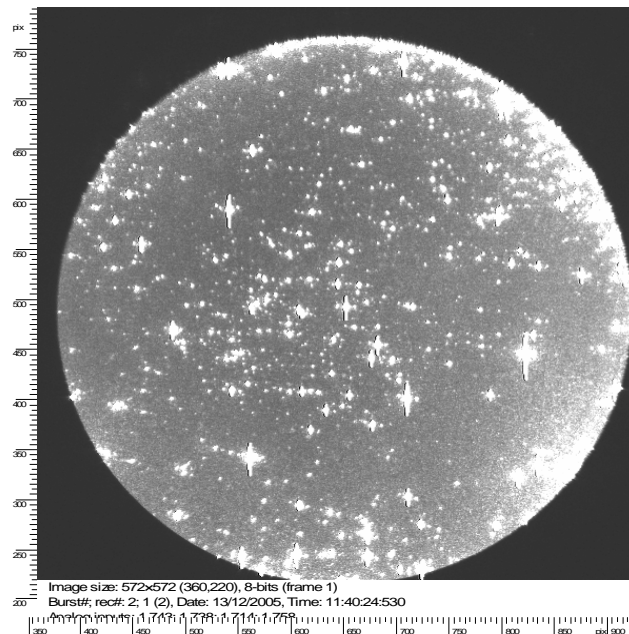


Figure 6.20: Clouded image

Moreover, the seeded oil was causing the endoscope to produce clouded images as shown in Figure 6.20. As a result, the endoscope had to be removed and cleaned several times in order to capture fifty image pairs. Frequent cleaning of the endoscope added considerable time to what is required for the measurement and also increased the risk of damaging the sensitive tip of the endoscope. It was decided to change the seeder from an oil based one to a water based system using a high volume liquid seeder (10F03). Unfortunately, a clouding of the endoscope still occurred, restricting the maximum number of image pairs that could be taken to twenty. Since the high speed camera experiments showed that the motion of the Fillite particles was the same as that of the flowfield, it was thus decided to test the use of Fillite particles as a seeder using the solid seeding generator (model 10F01).

With the Fillite particles used as seeder, no clouding of the endoscope was noted. However, the Fillite particles were too large and resulted in poor seeding distribution. Consequently the same sample was air sieved down to ($-100\mu\text{m}$) and the end image result is shown in Figure 6.21.

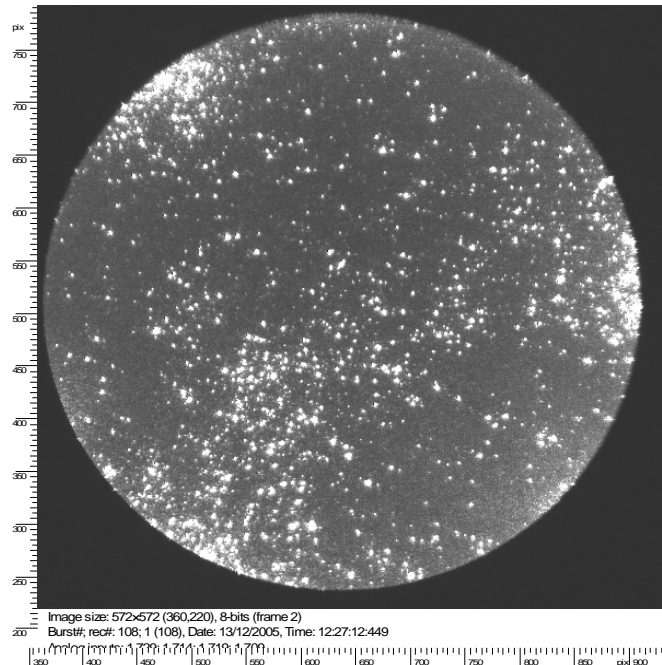


Figure 6.21: Image from sieved Fillite particles as seeder

Using the $-100\mu\text{m}$ Fillite particles as seeder, it was possible to capture a hundred instantaneous image pairs. The velocity vector map of the flowfield resulting from

averaging these image pairs is shown in Figure 6.22. A general swirl in the same direction as the twists in the swirl pipe geometry was observed, with definite changes in the direction of the velocity vectors along two “S” shapes across the pipe diameters. In these regions, the flow appears to be radially outwards instead of the general swirling movement.

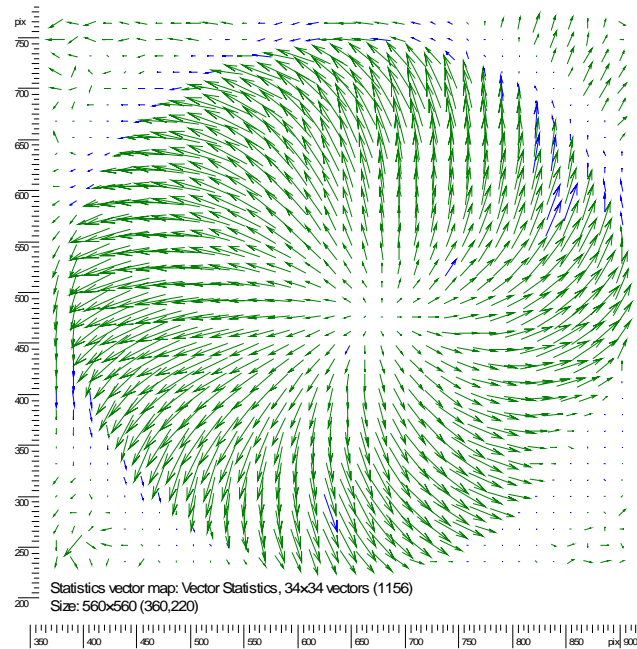


Figure 6.22: Velocity vector map resulting from averaging 100 image pairs when -100 μ m Fillite seeding particles was used

A limitation of the PIV technique is that a minimum of five seeder particles are required in every interrogation area in order to obtain consistently accurate results using the cross correlation technique. For the -100 μ m Fillite particles as seeder, this condition was satisfied when a 32x32 pixels interrogation area was used. However, the small localised vortices downstream of the swirl pipe depicted earlier were not being captured by the 32x32 pixels interrogation area. It was concluded that a finer grid was required. The interrogation area was therefore refined to 16x16 pixels. Cross correlation was poor for this grid size as the minimum of five seeding particles per interrogation area rule was no longer satisfied, as shown in Figure 6.23.

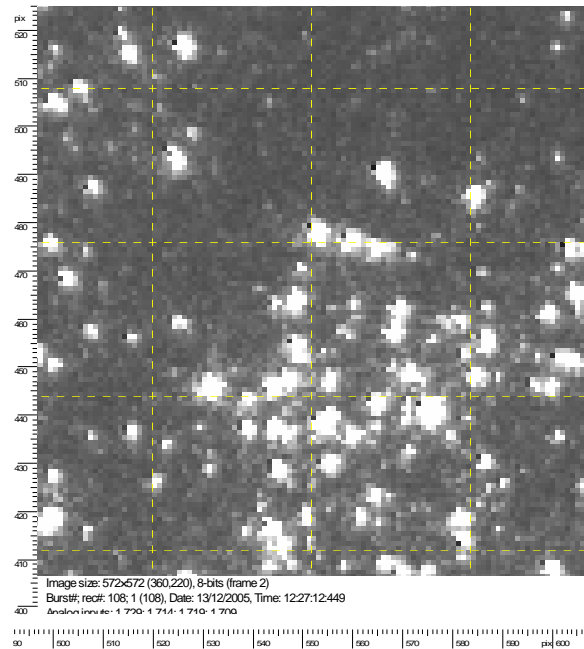


Figure 6.23: Number of ~100mm Fillite seeding particles per interrogation area

It was concluded therefore that smaller seeding particles were required. Titanium dioxide is a commonly used seeder for PIV purposes because of its high reflective index of 2.4 and average particle size of $5\mu\text{m}$. Titanium dioxide powder was sourced locally in the School of Chemical and Environmental Engineering from two different ongoing projects. As titanium dioxide is exposed to UV light, it becomes increasingly hydrophilic and the individual particles tend to stick together as a result. None of the samples acquired could be used as in both cases, the particles had agglomerated. Fresh titanium dioxide was required. It was decided to perform a series of laser Doppler anemometry experiments (LDA) in the meantime and to resume the PIV experiments if the LDA ones proved to be unsuccessful.

6.5.5 Conclusions from PIV experiments

The application of PIV technique was applied in order to attain a better understanding of the resulting flowfield downstream of the swirl pipe through the analysis of the 2D vector maps based on the PIV experiments. Testing of the setup was performed at five pipe diameters downstream of the control and swirl pipe at the high Reynolds number flow setting in order to determine the adequacy of the PIV technique and the completeness of the PIV results for such an application. These findings revealed that

the measurement was intrusive since an endoscope had to be introduced downstream of the plane at which measurement was being carried out. It also revealed problems in adequately seeding the flow. Oil and water based aerosol feeders caused the endoscope to cloud up, requiring frequent cleaning of the endoscope, increasing the measurement time and restricting the maximum number of image pairs that could be taken to less than half the number required to achieve good repeatability of the results. Sieved Fillite and titanium dioxide were tested as possible solid seeding particles. These powder samples size ranges were however too large and resulted in poor seeding.

When the aerosol seeder was used, velocity vector maps derived from individual image pairs showed the presence of small localised vortices within the flow region. However, these findings were not confirmed when more image pairs were averaged. Using sieved Fillite particles as seeder, it was possible to obtain a velocity vector map of the flowfield from averaging of hundred instantaneous image pairs. A general swirl in the same direction as the twists in the swirl pipe geometry was observed, corresponding to the “ribbon effect” observed in the high speed camera recordings. However, because of the large size of the seeding particles, the vector map was that of the particle flow rather than one of the air flow.

A lack of good seeding implied poor quality of the results and it was not possible to obtain a seeding material which would produce seeding particles in the three microns range, without dirtying the endoscope. It was therefore decided to perform a series of laser Doppler anemometry experiments (LDA) which are non-intrusive, and provide a similar interpretation and understanding of the flow field under investigation.

6.6 LASER DOPPLER ANEMOMETRY (LDA)

The laser Doppler anemometry (LDA) technique was first proposed by Yeh and Cummins (1964) for the measurement of the velocity of small tracer particles suspended in a flowing fluid. Over the last forty years, the technique has been intensively refined and now presents an ideal technique for obtaining temporally and spatially resolved velocity and turbulence distribution in both free flows and internal flows of liquid and gases.

A laser doppler anemometer measures the velocity at a point in a flow using light beams. This optical method of measurement of local instantaneous velocity is hence non-intrusive. Its optical nature also implies that LDA can be employed where physical sensors are difficult or impossible to use as measurement distance can range from centimetres to meters (Durrani and Clive, 1977). Moreover, it offers very high accuracy without calibration since a laser Doppler anemometer measures the absolute velocity components in a sequence of near instantaneous samples. An LDA system can measure one, two or three instantaneous and time-averaged velocity components simultaneously with velocities ranging from zero to supersonic. Because it is directionally sensitive and provides high spatial and temporal resolution of the velocity data, an LDA is very suitable for applications with reversing flow, or flows of unknown direction and it can give accurate measurements in unsteady and turbulent flows where the velocity is fluctuating with time (Durst, 1981).

The major disadvantages of LDA techniques are that they are expensive (typically £60,000 for a simple system), that they need an optically transparent flow conduit and flowfield through which the light beams can pass, that they do not give continuous velocity signals and that they require the use of light-scattering tracer particles suspended in the flow. Since, it is the velocity of the particles that is measured, the relationship between the particle velocity and that of the fluid must be known. To make this problem tractable, it is important to ensure that the particle sizes and concentrations are small enough to be insignificant ($St < 1$).

Swirl flows are known for their inherently three-dimensional nature and the curvature of their streamlines. Swirl flows are also highly sensitive to the presence of small obstacles in the flow, suggesting that the validity of any experimental investigation based on intrusive measurement systems such as hot wire anemometry is questionable. On the other hand, LDA has been used successfully in a number of swirl flow studies, including those by Parchen and Steenbergen (1998), Nejad et al. (1989), Itoh and Harada (1996) and Rocklage-Marliani et al. (2003).

The basic principles of an LDA is provided in Appendix D.

6.6.1 Objectives and scope of the LDA experimental programme

This study used the measurements derived from a two-component laser-Doppler anemometer to prove that the swirl pipe induces a swirl to the airflow; to characterise the type of swirl; to study the downstream behaviour of the swirl flow; and to examine the effect of Reynolds number on the induced swirl. Large enough measurement data were collected to form the basis of future validation work of numerical simulation of the same flow conditions.

Instantaneous local fluid velocities components in the x, y and z directions would have to be measured at several planes, perpendicular to the pipe axis, and downstream of the control and swirl pipe sections. These measurements are to be carried out for three flows of low, medium and high Reynolds number: $4.5 \times 10^4 \pm 791$, $9 \times 10^4 \pm 791$ and $1.4 \times 10^5 \pm 269$ respectively.

6.6.2 Experimental apparatus and instrumentation

Velocities were measured within the pneumatic swirl flow rig using a DANTEC Flowlite 1D laser-Doppler anemometry system. This a dual beam single component system. It consists of a Fibre Flow Probe, fibre-optic cable, an optics unit and Burst Spectrum Analyser (BSA) enhanced signal processor. The main components of the LDA system are shown in Figure 6.24. This system uses a 10mW Helium Neon laser which produces red light of wavelength 632.8nm. The laser and beam splitter are housed in the optics unit. A Bragg cell, used to shift the frequency of one of the beams by 40MHz is also installed. Theoretical maximum throughput of samples is 620kHz.

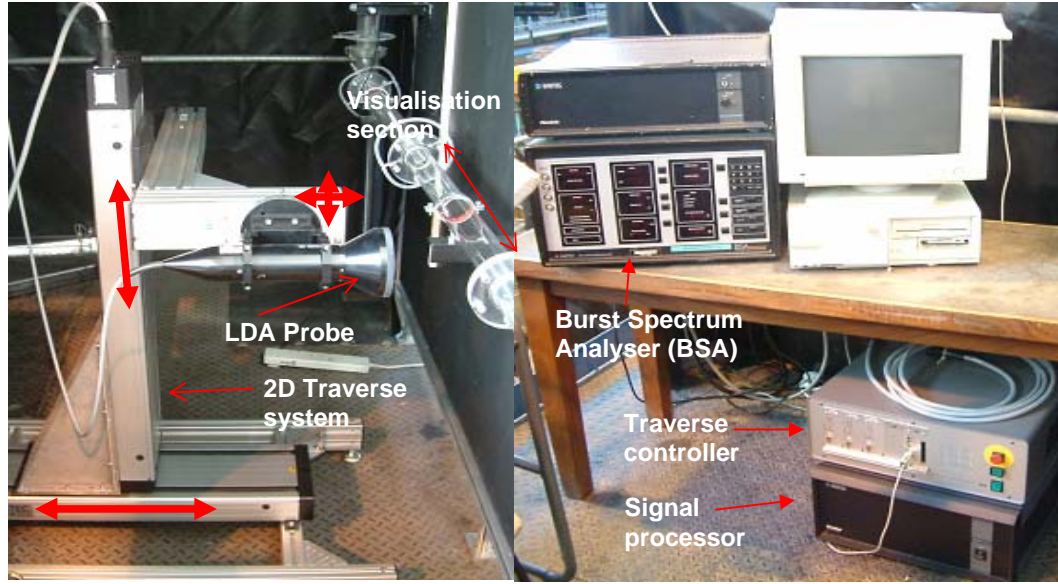


Figure 6.24: Main components of the LDA system

The laser beams are passed through the optical fibres to the Fibre Flow probe of diameter 60mm, where the beams are positioned and focussed at 160mm by the sending lens, producing a measurement volume.

The beam spacing, D_b , at the sending converging lens of the laser probe is 38mm. With a focal length, f , of the sending converging lens of 160mm, the measurement volume is formed 160mm away from the sending lens. The half angle of the beam in air, $\alpha/2$, is therefore given by (Sislian and Cusworth, 1984; Robinson et al. 1986),

$$\frac{\alpha}{2} = \tan^{-1} \frac{D_l}{2f} \quad (\text{Eq. 6.2})$$

In this case, the beam half angle is 6.77° and the fringe spacing (from Equation 6.2) is $2.68 \mu\text{m}$ since the wavelength is 632.8nm.

The laser beam diameter, D_l , at the converging lens is 1.3mm. The beam diameter at the focal waist, d_e , in this case is 0.099mm, approximated according to Goldstein (1983) as:

$$d_e = \frac{4f\gamma}{\pi D_l} \quad (\text{Eq. 6.3})$$

The measurement volume created by the intersection of the laser beams is an ellipsoid whose dimensions can be calculated using Equations 6.4 to 6.6 (Goldstein, 1983). The measurements of the ellipsoid in the x, y and z directions are l_m , d_m and h_m respectively.

$$l_m = \frac{d_e}{\sin \frac{\alpha}{2}} \quad (\text{Eq. 6.4})$$

$$d_m = \frac{d_e}{\cos \frac{\alpha}{2}} \quad (\text{Eq. 6.5})$$

$$h_m = d_e \quad (\text{Eq. 6.6})$$

The dimensions of the LDA probe volume can therefore be approximated to 0.840 mm, 0.100 mm and 0.099 mm in the x, y and z directions respectively. Thus the length of the measuring volume along the optical axis was approximately 1.7 % of the pipe diameter and considerably less in the other two directions giving adequate spatial resolution for the measurement of velocity profile. The volume of the ellipsoid can then be calculated as 0.0043 mm^3 using (Goldstein, 1983):

$$V_d = \frac{\pi d_e^3}{6 \cos \frac{\alpha}{2} \sin \frac{\alpha}{2}} \quad (\text{Eq. 6.7})$$

The spacing of the fringe, d_f , or fringe distance is defined by the wavelength of the laser light, i.e. the distance between the centrelines of two consecutive dark fringes. It is a function of the half-angle between the laser beams, α , and the wavelength of the laser illumination, γ :

$$d_f = \frac{\gamma}{2 \sin \left(\frac{\alpha}{2} \right)} \quad (\text{Eq. 6.8})$$

Thus the particle will generate a signal (Doppler shift) of frequency

$$f_D = \frac{U}{d_f} = \frac{2U \sin\left(\frac{\alpha}{2}\right)}{\gamma} \quad (\text{Eq. 6.9})$$

This expression is known as the LDA equation and relates the frequency of signals from an LDA, f_D , to the velocity of the flow, U .

The major operating parameters of the LDA system are summarized in Table 6.4.

LDA system parameter		Value
Focal length	f (mm)	160
Beam separation at converging lens	D_b (mm)	38
Fringe spacing	d_f (μm)	2.68
Beam diameter at converging lens	D_l (mm)	0.099
Length of measurement volume in x-direction	l_m (mm)	0.840
Length of measurement volume in y-direction	d_m (mm)	0.130
Length of measurement volume in z-direction	h_m (mm)	0.099
Volume of measurement volume	V_d (mm^3)	0.0043

Table 6.4: Main operating parameters of LDA system

The Flowlite probe is mounted on a 2D traverse gear. The weight of the traverse gear provides a stable means of positioning the measurement volume at any point in the test section. The velocity measured by the LDA system is the one that is parallel to the laser beams. Therefore in order to measure the streamwise, spanwise and planwise velocity components, the laser probe requires re-orientation. Rotation of the laser probe about its axis by 90 degrees is allowed by the probe mount. The probe can thus be used to measure either horizontal streamwise or vertical velocity component. In order to measure the planwise (z) velocity component, the laser probe needs to be revolved through 90 degrees so that the laser beams are parallel to the z velocity component. These orientations are shown in Figure 6.25.

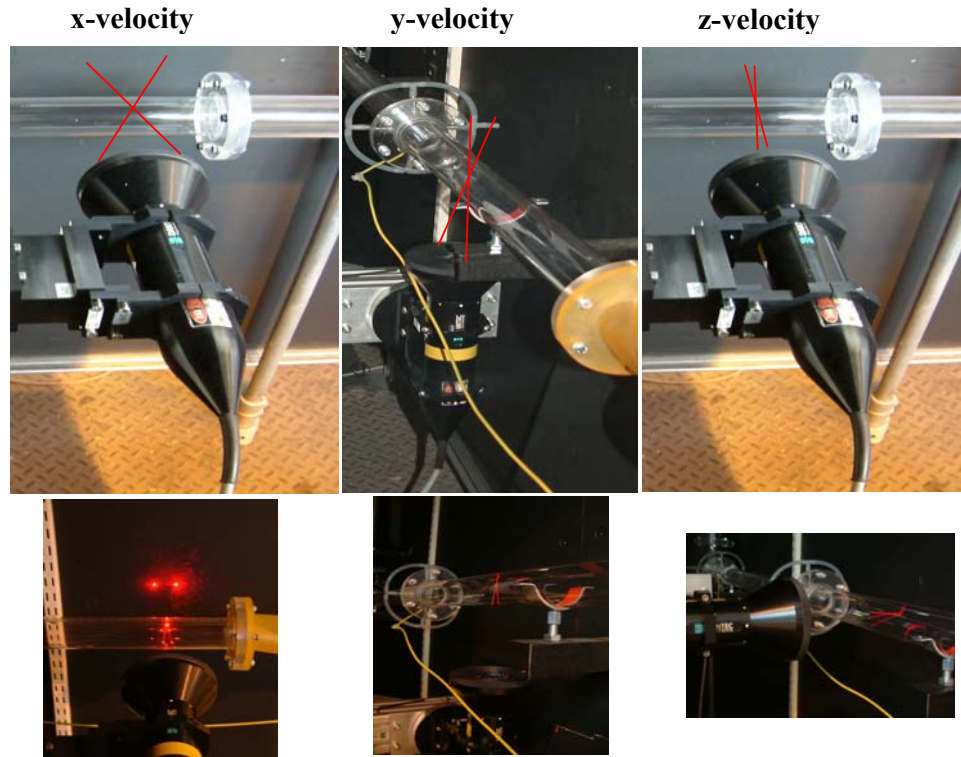


Figure 6.25: Laser optics probe orientation for x, y and z velocity component measurement

The Fibre Flow Probe operates in backscatter mode, so that the scattered light is collected by the same lens used to focus the beams. The scattered light is then focussed into a third optical fibre which carries it back to the optics unit where it is fed into a photomultiplier (PM) tube. Signals from the PM tube are sent to the BSA processor. This is an autocorrelation processor that is interfaced to a computer. The burst detection criteria and processing parameters of the processor are set from the computer, which is also used to read the results. DANTEC Burstware flow software, version 3.21, is used to control the LDA system from the computer, and to collect the measurements made.

The flow is artificially seeded using white Shell Ondina oil smoke produced by an SPT smoke generator (model 90, as shown in Figure 6.26) and delivered through a straight probe. The smoke fluid has a specific gravity of 0.835 and a nominal diameter of 1.5 μm .



Figure 6.26: SPT smoke generator (model 90)

6.6.3 Set-up and procedures

Proper alignment of the probe head with respect to the test section is required for accurate LDA data. The LDA probe head, which consists of both the transmitting and receiving optics, was first mounted on a three-dimensional computer-controlled traverse. The probe head was then aligned to the horizontal x-y plane using a spirit level so that the LDA probe head remained at a constant y-distance from the test section for all axial locations of interest.

When measuring the x-velocity component, the two laser beams enter the glass pipe horizontally along its horizontal midplane. These will be referred to as the “horizontal beams”. Since the beam diameter is much smaller than the pipe radius, the horizontal beams do not experience the curvature of the pipe wall. On the other hand, when measuring the z-velocity component, the laser beams enter the pipe vertically on a line perpendicular to the pipe axis and their path is affected by the curvature of the pipe wall. These beams will be referred to as the “vertical beams”.

The laser beam alignment is carried out as follows: first, the probe head is traversed upwards along the z-axis, until the horizontal beams are both above the pipe. The laser beams directly hit the backing board of the rig, corresponding to location P1 on Figure 6.27. The probe head is then traversed downwards along the z-axis, towards the pipe, in 0.25 mm increments until the horizontal beams cross the glass pipe. The z-location of the laser beams when they first hit the wall of the glass pipe at P2 can be easily

determined by observing the backing board of the rig; when the beams first hit the glass wall, they are no longer visible on the board because they are then reflected off the outer surface of the pipe wall. The data rate also falls to zero at this location, which corresponds to the outer surface of the glass pipe: $z = \frac{D}{2} + t = 26.6\text{mm}$ where t is the thickness of the glass pipe. The probe head is then traversed 26.6mm downwards along the z -axis. At this location (P3), the horizontal beams should cross the pipe at $z = 0$, i.e. the beams enter the pipe through its horizontal midplane. The probe head is then traversed along the x -axis until the perpendicular beams are at the first axial (x) location for the measurement of the radial velocity profiles, or 2 pipe diameters downstream of the swirl pipe.

The uncertainty associated with this alignment on the y and z -axis, was noted to be $\pm 0.25\text{ mm}$, i.e. the accuracy with which the tube wall surface could be located with respect to the cross section of the beam. Refractions on the tube surfaces were taken into account while computing the true location of the beam intersection point with the tube.

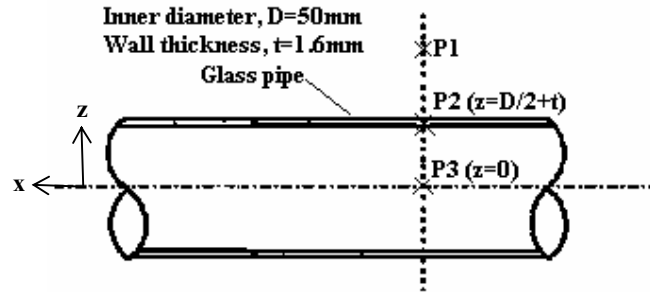


Figure 6.27: Illustration of procedure used to align the horizontal laser beams with the midplane of the pipe

A measurement matrix, constituting of coordinates of measurement points, was then derived to cover the maximum possible cross sectional area of the pipe. This is shown in Figure 6.28. From a setup test, it was found that for both the horizontal and vertical beams, readings could be taken as close as 2mm from the pipe wall in the y -direction and 3mm from the pipe wall in the z -direction, due to pipe curvature effects. That provided coverage of 92% and 88% of the pipe diameter in the y -direction and z -direction respectively. The measurement matrix comprised 130 measurement points

over a pipe cross sectional area of 1963.5mm^2 . The matrix was used as the coordinates to direct the traverse to these exact measurement locations.

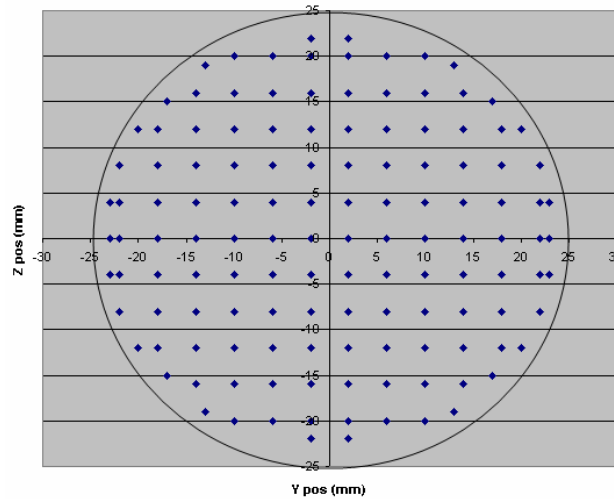


Figure 6.28: Matrix of measurement points in any y-z plane

The laser beams and detection system were optimised in order to obtain the best possible amplitude, volume and regularity of the fringe pattern. This was achieved by first of all maintaining the difference between the intensity of the two beams to less than 5% to ensure a good signal-to-noise-ratio, and secondly by ensuring that the beam separation angle is small enough to produce a regular fringe pattern.

In the measurement of all three velocity components, the LDA signal was filtered with a band pass filter (1–12 kHz) to reduce the noise level in the signal and to eliminate the signal pedestal. The three average Reynolds number flow settings, low, medium and high, created Doppler signals with frequencies of about 3.73, 7.45 and 11.18 kHz respectively. To resolve negative velocities from positive velocities, the system uses a Bragg cell to obtain a frequency shift of 40 MHz for all velocity measurements.

The experimental programme was set to measure the three velocity components (x, y and z) at four different planes (2, 6, 10 and 14 pipe diameters downstream of the control and swirl pipe sections, as shown in Figure 6.29) for the three different Reynolds number flow settings (high, medium and low).

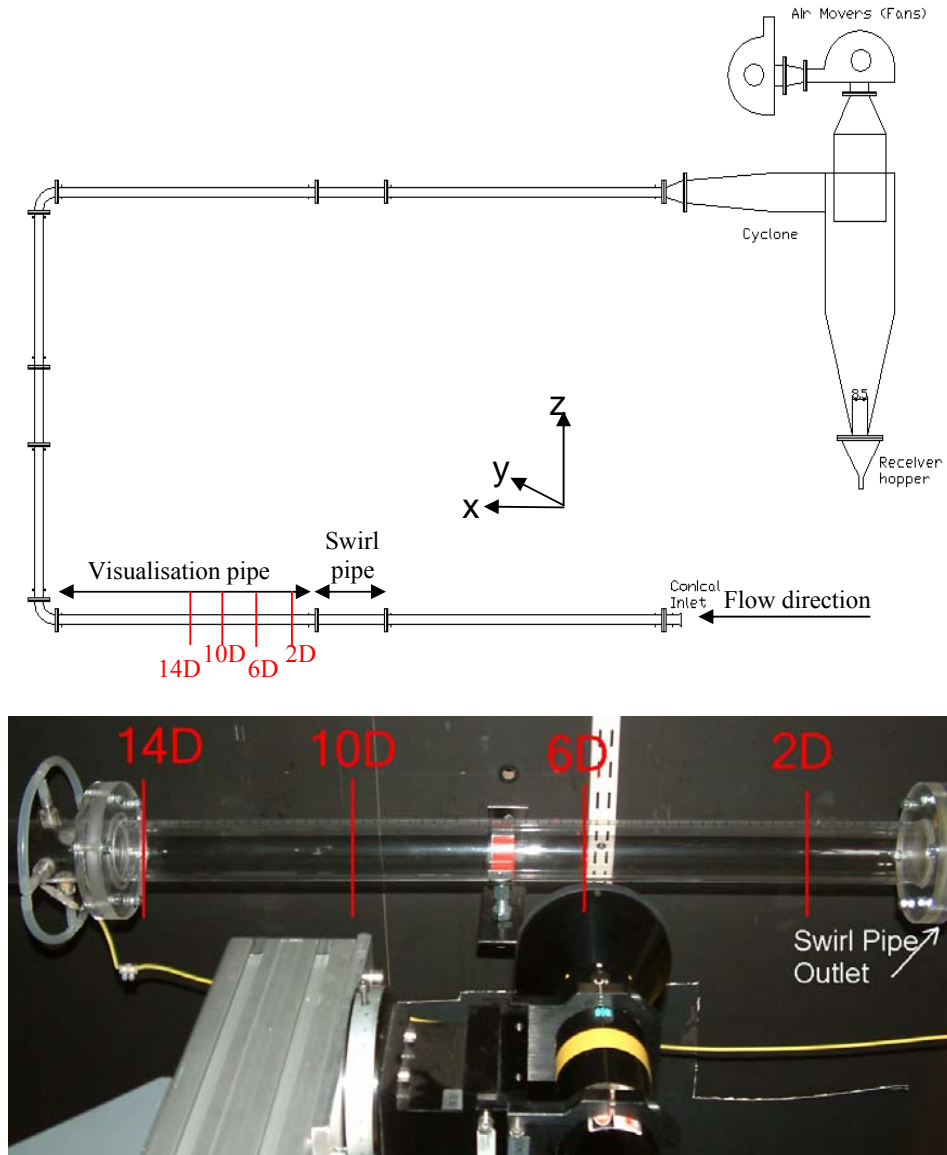


Figure 6.29: Location of measurement planes

The LDA experiments were carried out on the carrier phase, i.e. air-only, with fog seeding. The experimental procedures followed during the measurement of the velocity profiles are described in the following paragraphs.

- The fans, the fog generator and the LDA system were turned on and the software initialized.
- Two red beams emerging from the probe and passing through the test section were visible. The probe was aligned so that the beams are parallel to the velocity

component being measured (x-velocity component was measured first, followed by the z-component and finally the y-component)

- The laser probe was positioned to the start of the measurement series of the measurement locations using the three-dimensional computer controlled traversing mechanism.
- The operational performance of the fans was adjusted by the use of a variac controller until the desired flowrate was achieved. The static gauge pressure at the conical inlet was recorded. This was converted to give the mean air mass flowrate at the inlet using equation 5.1. A vane anemometer was also used to measure the mean air speed at the inlet, which was recorded. The air speed was converted to air volume flowrate at the inlet to double check the mean air flowrate obtained from the static gauge pressure at the conical inlet and equation 5.1.
- The LDA velocity measurements were commenced. The maximum number of samples to be taken per measurement location was prespecified to be 2500 and the measurement time set as 20s per location. Measurement was considered complete if either of these two conditions was satisfied.
- During the measurement, the LDA signal burst was manually monitored to reduce noise and ensure that the spectrum was always centred and bell-shaped. High voltage of the photomultiplier and signal gain were altered to get a high data rate with an acceptance rate of about 80%. However this was not always possible due to reflections, local glass pipe quality and dust on the glass.
- When measurement at one location was completed, the LDA probe head was traversed automatically along the y and z direction, stopping at particular locations as specified by the y and z coordinates in the measurement matrix. Measurement at these locations would also start automatically until measurement point 130 was reached.
- The static gauge pressure at the conical inlet and the vane anemometer reading were again recorded.
- The optic probe was then rotated to measure the z-velocity component at the same measurement locations and again to measure the y-velocity component.

- The operational setting of the fans was then altered using the variac control to the next desirable air flowrate and the LDA velocity measurements were repeated.
- Once all three velocity components had been measured for the three desired Reynolds numbers at a specific plane, the probe was moved so that the measurement could be repeated at another plane.
- When all measurements were completed, the fans, the fog generator and the LDA system were turned off.

Due to limited time available during which to conduct the LDA experiments, the experimental schedule had to be altered. Instead of collecting velocity measurements at the pre-defined measurement points for every planes, w velocity data was collected at 25 points along a single horizontal diameter of the pipe, extending between $d/D = \pm 0.92$ to save time. Table 6.5 summarises which of the measurements were planar or linear.

		Low Reynolds number flow			Medium Reynolds number flow			High Reynolds number flow		
		u vel	v vel	w vel	u vel	v vel	w vel	u vel	v vel	w vel
Swirl pipe	2D	plane	plane	plane	plane	plane	plane	plane	plane	plane
	6D	plane	plane	plane	plane	plane	plane	plane	plane	plane
	10D	plane	plane	plane	plane	plane	plane	plane	plane	plane
	14D	plane		line	plane		line	plane		line
Control pipe	2D	plane		line	plane		line	plane		line
	6D	plane		line	plane		line	plane		line
	10D	plane		line	plane		line	plane		line
	14D	plane		line	plane		line	plane		line

Table 6.5: Summary of measurement method

6.6.4 LDA measurements results

The LDA data files for each measurement plane reported 130 measurement points (or 25 measurement points in cases where data was being obtained from points along a line), their individual x, y and z coordinates, the mean velocity being measured, the root mean square (rms) value of the velocity and turbulence in the data. The data had to be cleaned so as to remove erroneous data. These were identified by rms values of 10 or greater. The erroneous data tended to occur close to the pipe wall in the high and

low z regions due to the high curvature of the pipe wall experienced by the laser beams as they pass through the glass pipe wall. The erroneous velocity value was substituted with an interpolated value of its neighbouring points. Ten substitutions were made in total.

The data was analysed using Tecplot, version 10. The software was chosen for its 2D contour plotting feature with a high level of customisation. This was important for the future validation work that will be carried out by comparing the experimental results to that of the Computational Fluid Dynamics software, Fluent release 6.2.16. It was therefore crucial that both softwares used the same colour map and number of levels in the contouring process. The colour map used by Fluent was therefore imported into Tecplot for the data analysis.

The data file for each planar measurement set was first loaded into Tecplot as a space delimited file. In order to have a 2D Cartesian plot, the y -values had to be plotted against z values. Once these are defined, a mesh of the data is plotted. The data then needs to be triangulated. The data resulted in 130 nodes and 228 triangles. Since the outer measurement points did not lie on a smooth circular edge, a circular zone was created. This also allowed a higher mesh density to be created onto which to interpolate the data. The 23mm diameter circular zone was created with 20 cells in the radial direction and 50 in the circumferential direction. The original data was then interpolated onto this more refined mesh using the “kriging” technique. This is a method of optimal prediction through interpolation which predicts unknown values from data observed at known locations. This method uses variogram to express the spatial variation, and it minimizes the error of predicted values which are estimated by spatial distribution of the predicted values. For a detailed discussion of the kriging algorithm, see Davis (1986). Contours could then be plotted using 20 levels and the imported colourmap from Fluent. The resulting plots are shown in the following sections.

The velocity measurements were carried out in the Cartesian frame of reference. It was required to change the measured Cartesian velocity components, i.e. u , v and w velocities (x , y and z velocities), into cylindrical polar velocity components, i.e. u , u_r and u_θ (axial, radial and tangential velocities).

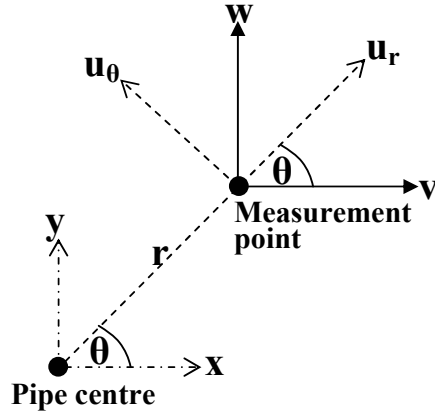


Figure 6.30: Illustration of a measurement point in Cartesian coordinates system

Hence Point P has coordinates (x, y) in Cartesian coordinates system and (r, θ) in Cylindrical Polar coordinates system. x, y, r and θ are related as follows:

$$x = r \cos\theta \quad (\text{Eq 6.10})$$

$$y = r \sin\theta \quad (\text{Eq 6.11})$$

v velocity is defined as the rate of change of distance travelled in the x -direction with respect to time

$$\text{i.e.} \quad v = \frac{dx}{dt} \quad (\text{Eq 6.12})$$

Similarly, w velocity is defined as the rate of change of distance travelled in the y -direction with respect to time

$$\text{i.e.} \quad w = \frac{dy}{dt} \quad (\text{Eq 6.13})$$

Radial velocity, u_r , is defined as the rate of change of the radial distance with time.

$$\text{i.e.} \quad u_r = \frac{dr}{dt} \quad (\text{Eq 6.14})$$

Similarly, tangential velocity, u_θ , is the angular velocity which is defined as the product of radial distance and the rate of change of the angle with time.

$$\text{i.e.} \quad u_{\theta} = r \frac{d\theta}{dt} \quad (\text{Eq 6.15})$$

Differentiating Equation 6.10 with respect to t and substituting Eqs. 6.12 to 6.15 results in:

$$v = u_r \cos \theta - u_{\theta} \sin \theta \quad (\text{Eq 6.16})$$

Differentiating Equation 6.10 with respect to t and substituting Eqs. 6.12 to 6.15 results in:

$$w = u_r \sin \theta + u_{\theta} \cos \theta \quad (\text{Eq 6.17})$$

Solving Eq. 6.16 and 6.17 simultaneously yields:

$$u_r = v \cos \theta + w \sin \theta \quad (\text{Eq 6.18})$$

$$u_{\theta} = w \cos \theta - v \sin \theta \quad (\text{Eq. 6.19})$$

Equations 6.18 and 6.19 were therefore used to transform Cartesian velocity components into cylindrical velocity components.

6.6.4.1 LDA results on a horizontal circular control pipe section (no swirl)

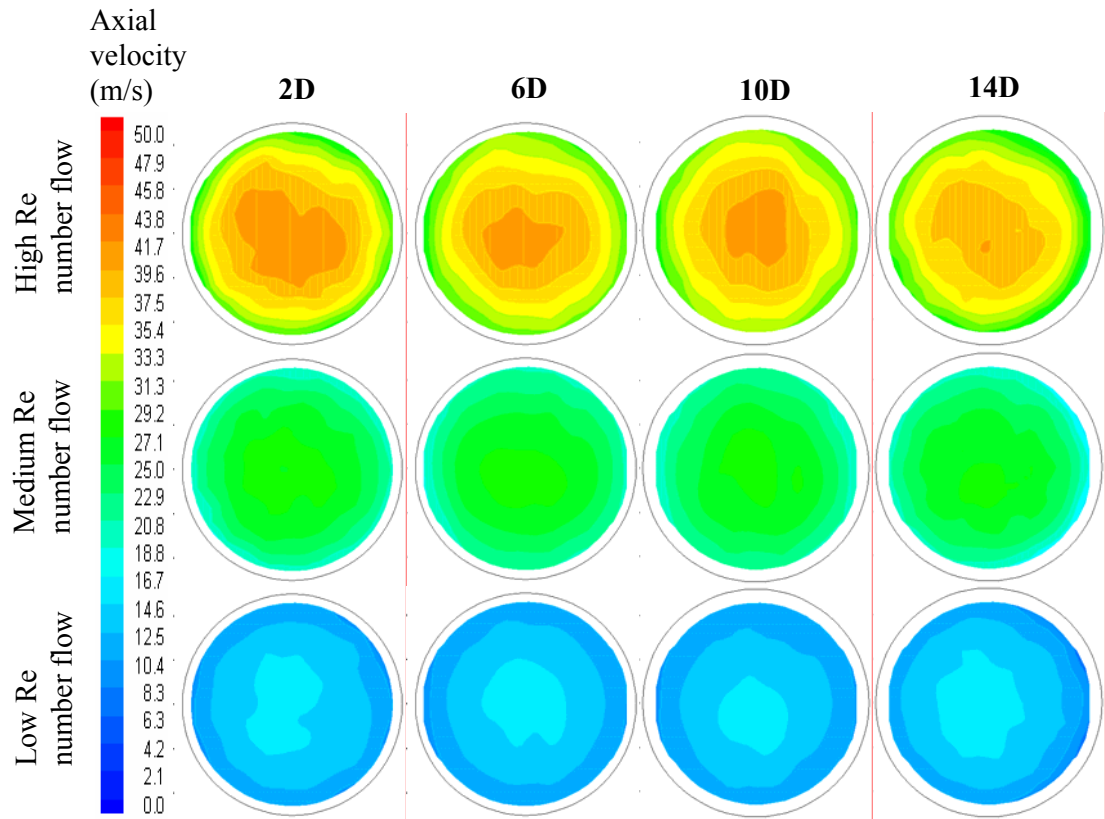


Figure 6.31: Axial air velocity contours at 2D, 6D, 10D and 14D planes downstream of the outlet of the control pipe section under air-only conditions

Since planar measurements were only carried out for the u velocity component, only the axial velocity contours could be produced. Figure 6.31 shows the resulting axial velocity contours at 2, 6, 10 and 14 pipe diameters downstream of the control pipe section. The contours have been plotted to a uniform scale to show a velocity range of 0 to 50 m/s and to facilitate comparison. An analysis of this data concluded that the cross sectional axial velocity distribution were reflective of the air flowrates, with the higher velocities at the higher Reynolds number flow resulting from higher air flowrates used and lower velocities at the lower Reynolds number flow resulting from lower air flowrates used. Similarly the centreline velocity decreased with increasing distance downstream. Although the velocity contours were not as circular as in an ideal case, they were close enough to being circular. For all three air flowrates, the results show the same profiles, with low velocity closer to the wall and increasing to a maximum at the centre of the pipe.

The velocity gradient at the centre of the pipe for all the flows was the almost flat, indicating that all the flows were turbulent, even at the furthest location measured. These findings were confirmed in Figure 6.32 (a) and (b), which show a plot of 14 axial velocity measurements along the horizontal centreline of the pipe at plane 2D downstream of the control pipe at low, medium and high Reynolds number flows and at planes 2, 6, 10 and 14D downstream of the control pipe at high Reynolds number flow.

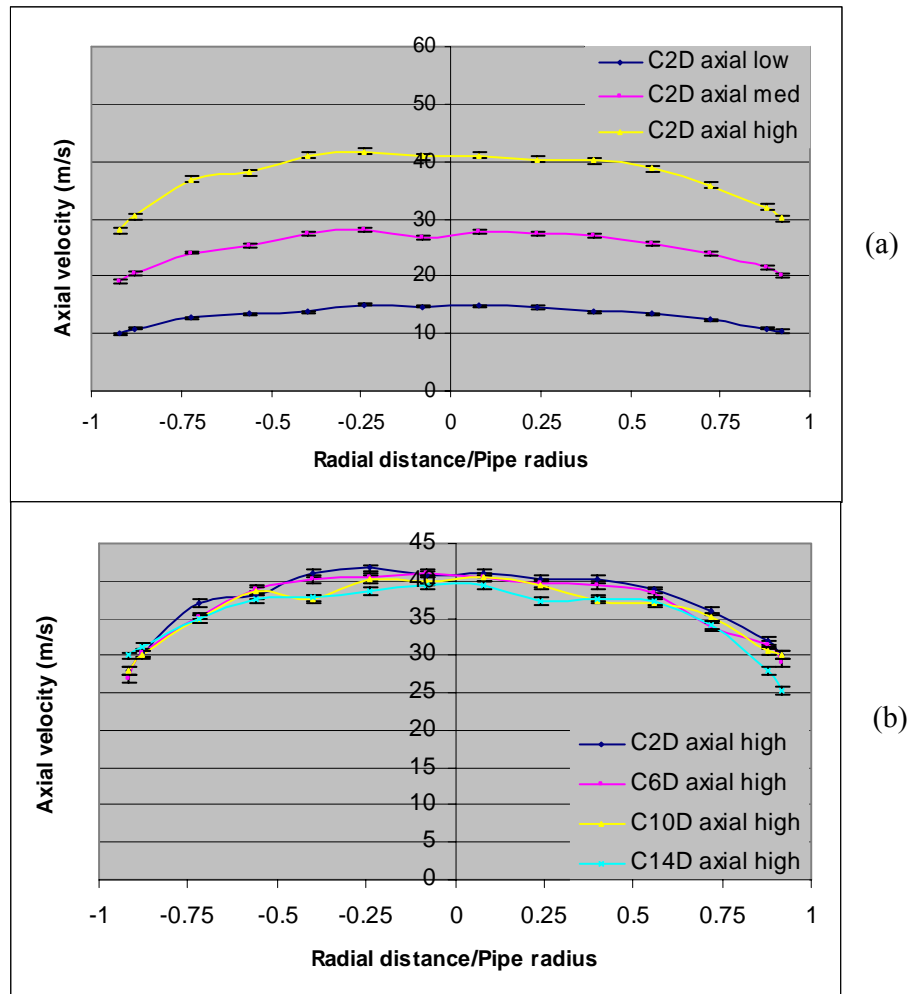


Figure 6.32: (a) Axial air velocity along the horizontal centreline of the pipe at plane 2D downstream of the control pipe at low, medium and high Reynolds number flows and (b) Axial velocity along the horizontal centreline of the pipe at planes 2, 6, 10 and 14D downstream of the control pipe for the high Reynolds number flow (all readings were taken across the horizontal diameter)

6.6.4.2 LDA results downstream of a swirl-inducing pipe

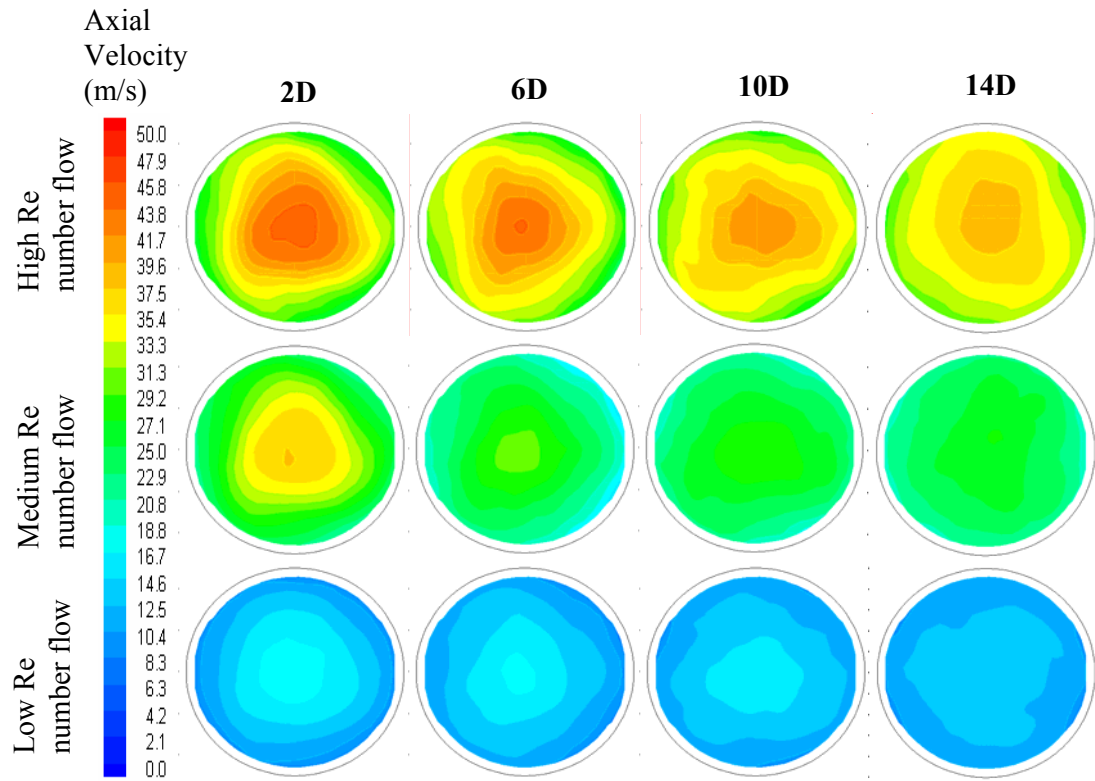


Figure 6.33: Axial air velocity contours at planes 2, 6, 10 and 14 diameters downstream of swirl pipe

Figure 6.33 shows the resulting axial velocity contours at 2, 6, 10 and 14 pipe diameters downstream of the swirl pipe section. Once again the contours have been uniformed to show a velocity range of 0 to 50 m/s to facilitate comparison.

The main striking feature in these plots is the triangular shape of the contours. It is believed to be the direct consequence of the 3-lobed helical swirl pipe, whereby each vertices of the triangular shape is caused by one of the lobe of the helical tube. The triangular shape is most distinct closer to the exit of the swirl pipe and fades with increasing distance downstream. Remnants of the triangular shape still persisted at 14 pipe diameters downstream of the swirl pipe. It is observed that the triangular shaped contours subsist better at a high Reynolds number flows despite increasing distance downstream of the swirl pipe. The orientation of the triangular contours shifted with increasing distance downstream of the swirl pipe as it reflects a rotating flow.

The pitch to diameter ratio of the swirl pipe is 0.6, i.e. the cross sectional geometry of the 50mm equivalent diameter pipe revolves about 360 degrees over a distance of 30cm. If the flow follows the geometry of the swirl pipe closely and continues to do so downstream of the swirl pipe, the triangular contours would have been offset by 120° , 0° , 240° and 120° (with reference with the positive x-axis) at 2, 6, 10 and 14 pipe diameters respectively downstream of the swirl pipe. With the exception of the contour orientation at 2D, this is however not the case. It can therefore be deduced that the induced swirl decays with increasing distance downstream of the swirl pipe.

As expected, the velocity closer to the wall was low and increased to a maximum at the centre of the pipe. Again, as expected, the cross sectional axial velocity distribution reflected the air flowrates, with higher velocity for higher Reynolds number flow resulting from high air flowrate used and lower velocity for lower Reynolds number flows resulting from low air flowrate used. Similarly the centreline velocity decreased with increasing distance downstream.

The velocity gradient at the centre of the pipe for all the medium and low Reynolds number flows was almost flat, indicating that all the flows were turbulent, even at the furthest location measured. These findings were confirmed in Figure 6.34 (a) and (b), which show a plot of 14 axial velocity measurements along the horizontal centreline of the pipe at plane 2D downstream of the control pipe at low, medium and high Reynolds number flows and at planes 2, 6, 10 and 14D downstream of the control pipe at high Reynolds number flow. However, for the high Reynolds number flow, a sudden increase in the axial velocity was observed at $r/R \approx \pm 0.5$. This trend was observed at two and six pipe diameters downstream of the swirl pipe, but faded away further downstream. This higher core velocity is believed to be caused by the swirl induced by the swirl pipe.

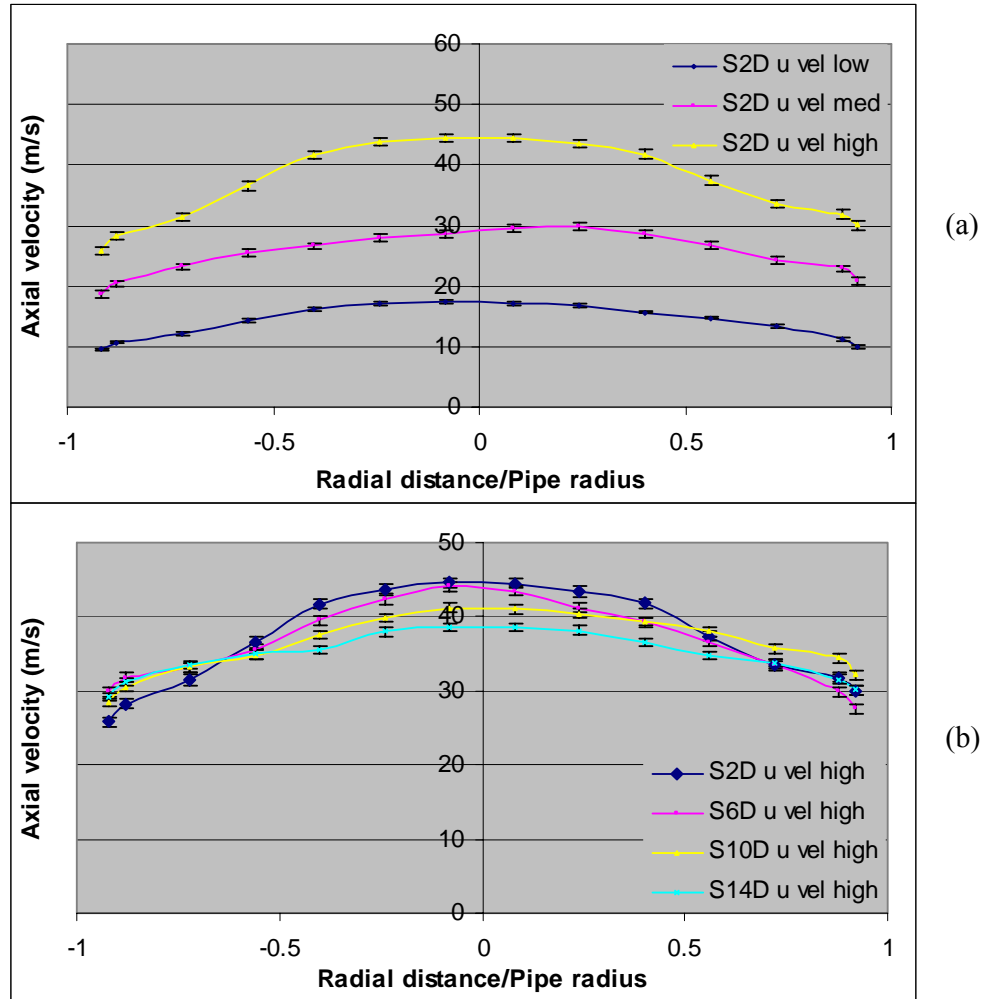


Figure 6.34: (a) Axial air velocity along the horizontal centreline of the pipe at plane 2D downstream of the swirl pipe at low, medium and high Reynolds number flows and (b) Axial velocity along the horizontal centreline of the pipe at planes 2, 6, 10 and 14D downstream of the swirl pipe for the high Reynolds number flow (all readings were taken across the horizontal diameter)

These trends are confirmed when comparing the contour plots of axial velocity downstream of the swirl and control pipe for low, medium and high Reynolds number flows as shown in Figure 6.35. Here different ranges of velocities are used to plot the contours for the low, medium and high air flowrates so as to enable better rendering.

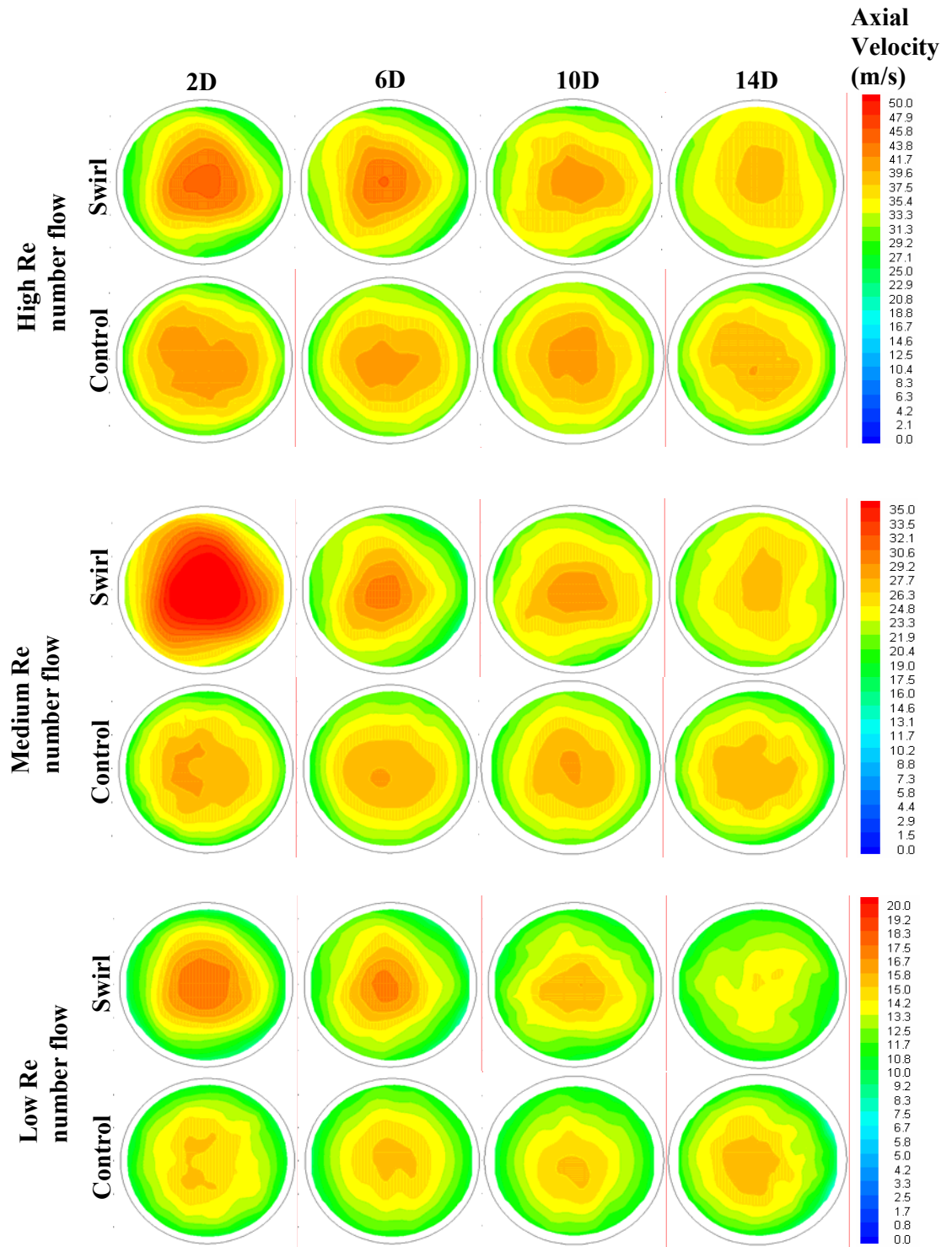


Figure 6.35: Comparison of axial air velocity contours downstream of the swirl and control pipe for low, medium and high Reynolds number flows

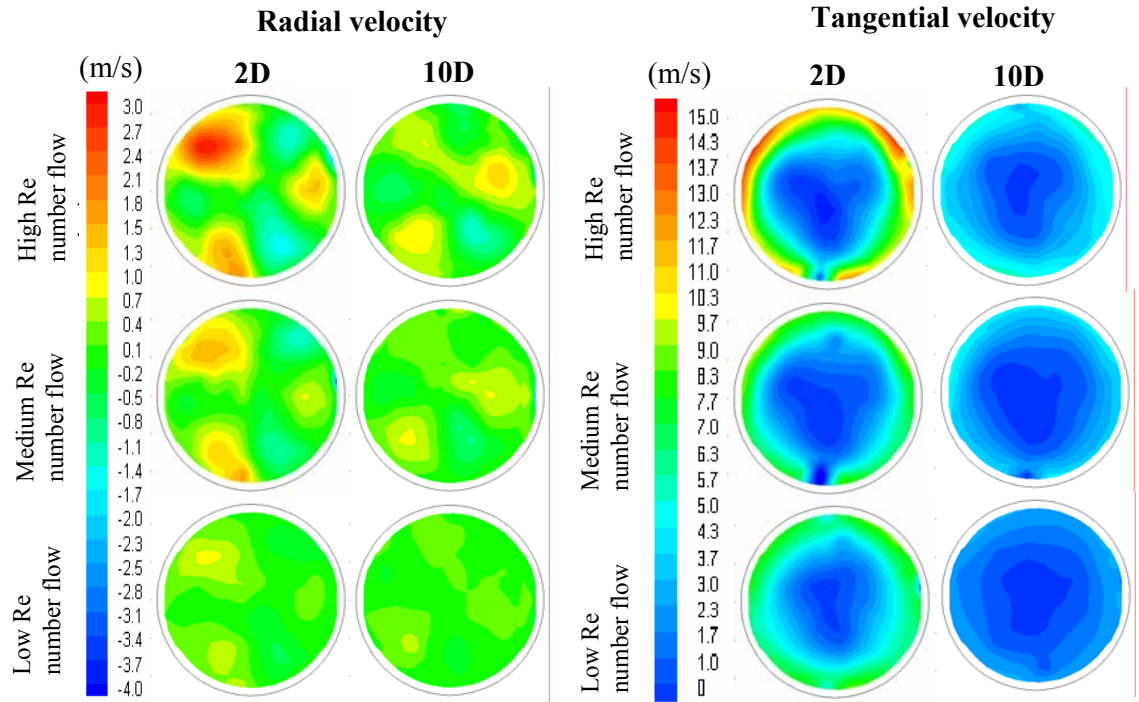


Figure 6.36: Radial and tangential air velocity contours at planes 6 and 10 diameters downstream of swirl pipe

The radial velocity contours in Figure 6.36 showed alternate radial velocity hot-spots and low-spots in the pipe cross section. These hot-spots are more evident at the high Reynolds number flow and closer to the exit of the swirl pipe. They correspond to the vertices of the triangular axial velocity contours. They also correspond to the expected regions of high particle concentrations from the high speed camera recording with laser sheeting and align with the S-shapes observed in the PIV results. The alternative radial velocity hot-spots and low-spots, as depicted in the pipe cross section at two diameters downstream of the swirl pipe for high Reynolds number flow, would cause localised vortices in that plane. However, in the three dimensional flow, the vortices may not be present due to the effect of the axial velocity.

The tangential velocity contours also have a core triangular profile with a higher tangential velocity magnitude closer the walls, decreasing to zero at the centre of the pipe. This is typical of swirl flows. From Eq. 6.19, it can be seen that for the horizontal centreline of the pipe cross section, where θ is 0° or 180° , tangential velocity is equivalent to the modulus of w -velocity. Hence, Figure 6.37(b) shows the tangential velocity profile along the horizontal centreline of planes located at 2, 6, 10 and 14

diameters downstream of the control and swirl pipe sections. The tangential velocity profiles downstream of the swirl pipe, are distinctively higher at the walls, positive on one half of the pipe cross section and negative on the other, indicating swirl. At the pipe centre, tangential velocity falls to zero. These S-shaped profiles are typical of wall jet swirls.

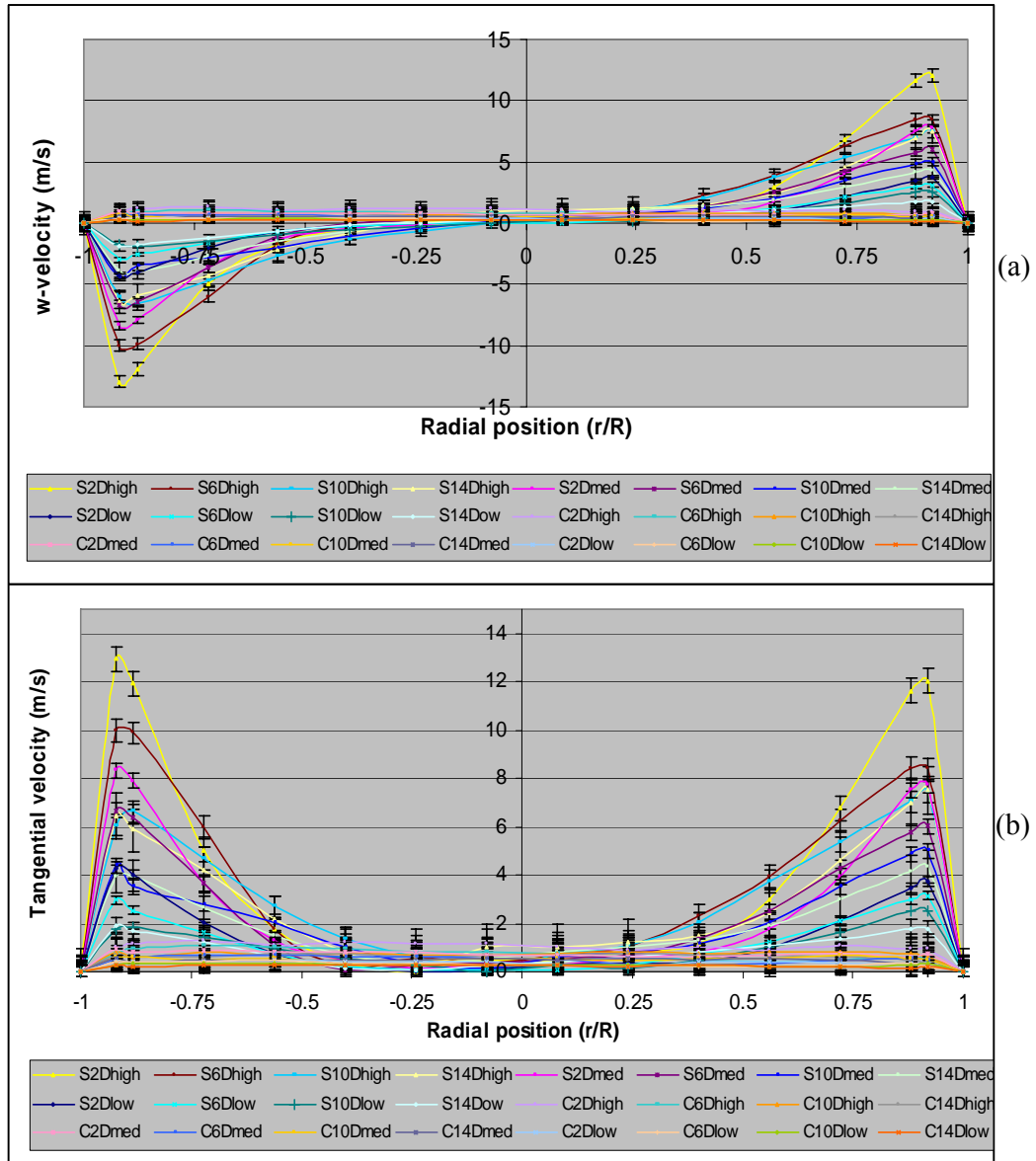


Figure 6.37: (a) w-air velocity (b) Tangential air velocity profiles downstream of the swirl and control pipe sections for all three Reynolds number flows (all readings were taken across the horizontal diameter)

It can be seen that the maximum tangential velocity attained decreases with decreasing Reynolds number flows and increasing distance downstream of the swirl pipe. It can therefore be concluded that the induced swirl decays with increasing distance downstream of the swirl pipe.

On the other hand, the tangential velocity generated downstream of the control pipe section is almost non-existent with a flat profile. Even with a low Reynolds number flow at a location of six diameters downstream of the swirl pipe, higher tangential velocity is generated as a result of the swirl pipe than with a high Reynolds number flow at a location of only two diameters downstream of the swirl pipe. It can therefore be concluded that the induced swirl has not completely decayed at a distance of fourteen diameters downstream of the swirl pipe.

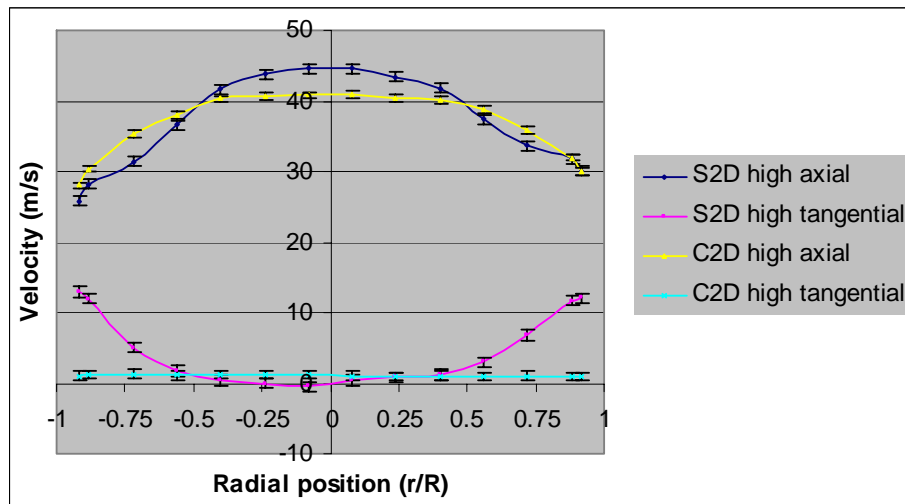


Figure 6.38: Comparison of axial and tangential air velocity at the cross sectional horizontal line at a distance of two diameters downstream of the swirl and control pipe sections (all readings were taken across the horizontal diameter)

Figure 6.38 shows that the centreline axial velocity resulting from the swirl pipe is higher than that resulting from the control pipe. This is accompanied by the reverse effect closer to the pipe wall. On the other hand, the magnitude of tangential velocity as a result of the swirl pipe increases with radial distance from the pipe centre. It appears that the swirl pipe causes a redistribution of the velocities from axial to tangential, whereby energy shifts from axial momentum to angular momentum. This gives rise to a swirl component.

The degree of the swirl component at each location can be quantified with the swirl number, as defined in Equation 4.5. In order to obtain the swirl number for a specific plane, two functions, $u_\theta u_x r^2$ and $u_x^2 r$, need to be integrated over the specified interval, i.e. the area of that plane. Since the exact values of the two functions are known, numerical approximation scheme, by using a straight summation, is used to compute the integration. That is, summing up the quotient of the function values and the approximate area of influence. Equation 4.5 was interpreted as

$$S = \frac{\int (u_\theta u_x r^2) dA}{R \int (u_x^2 r) dA} = \frac{\sum_{i=1}^n (u_\theta u_x r^2) \partial A_i}{R \sum_{i=1}^n (u_x^2 r) \partial A_i} \quad (\text{Eq. 6.20})$$

In order to apply the equation to the measurement data, the measurement plane had to be discretised, i.e. the area around each measurement location points in the measurement plane, shown in Figure 6.39(a), had to be divided into smaller regular regions of influence. Eighteen measurement points close to the pipe wall had to be discarded in order to achieve a more regular grid.

From Equation 6.20, it can be seen that the integrand is proportional to r^2 , the velocities near the wall therefore have a relatively large contribution to the swirl number. Inaccuracies in the swirl number estimation may occur because of the absence of velocity data in the region $0.92 < r/R < 1$. 30 points were therefore later added to minimise error from any grid cell having too large an area of influence. The original, the original points post the deletion of 18 original points and final points including the 30 new points are shown in Figure 6.39 (a), (b) and (c) respectively.

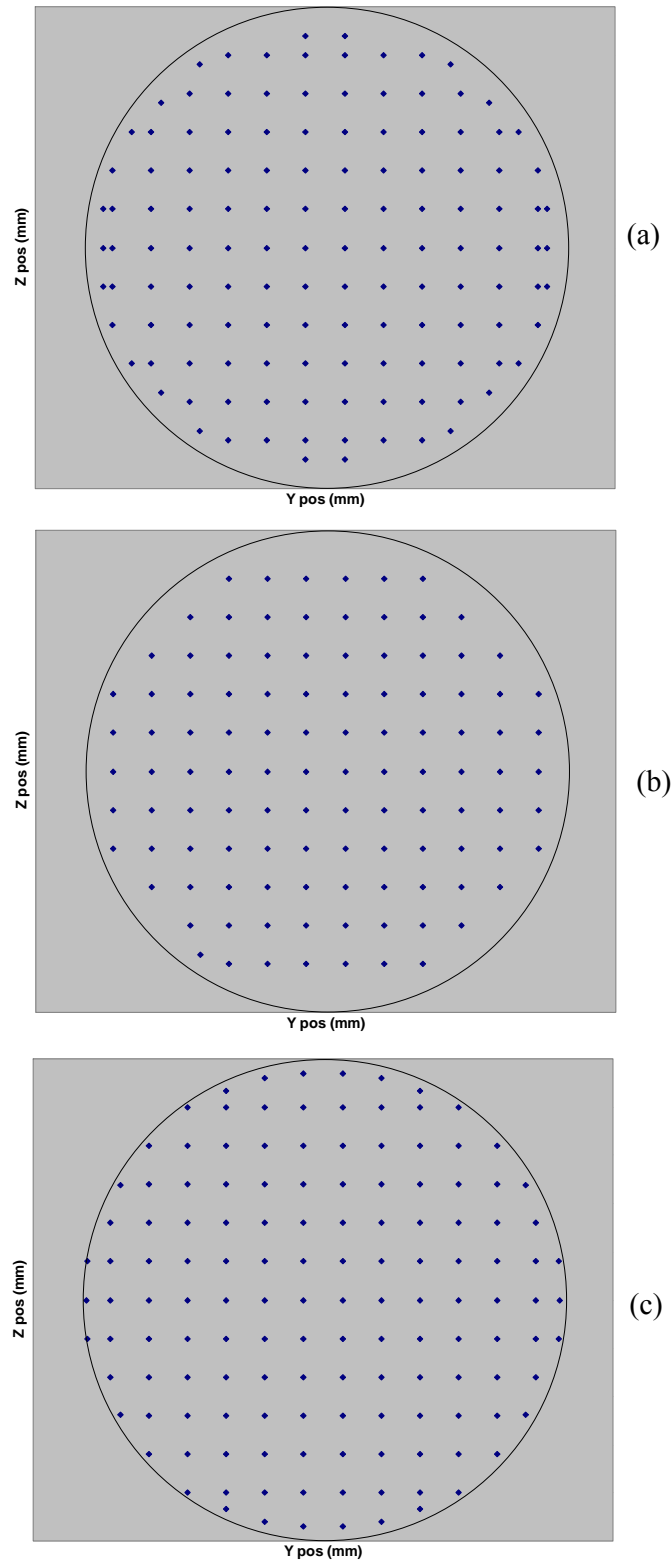


Figure 6.39: (a) The original points, (b) The original points post the deletion of 18 of the original points, (c) The final points including the 30 new points

The value of the axial and tangential velocities at these 30 new points were estimated using the average result of linear interpolation between the last measurement point and the wall, where all velocities are zero, and linear extrapolation towards the wall of the line connecting the last two measurement points.

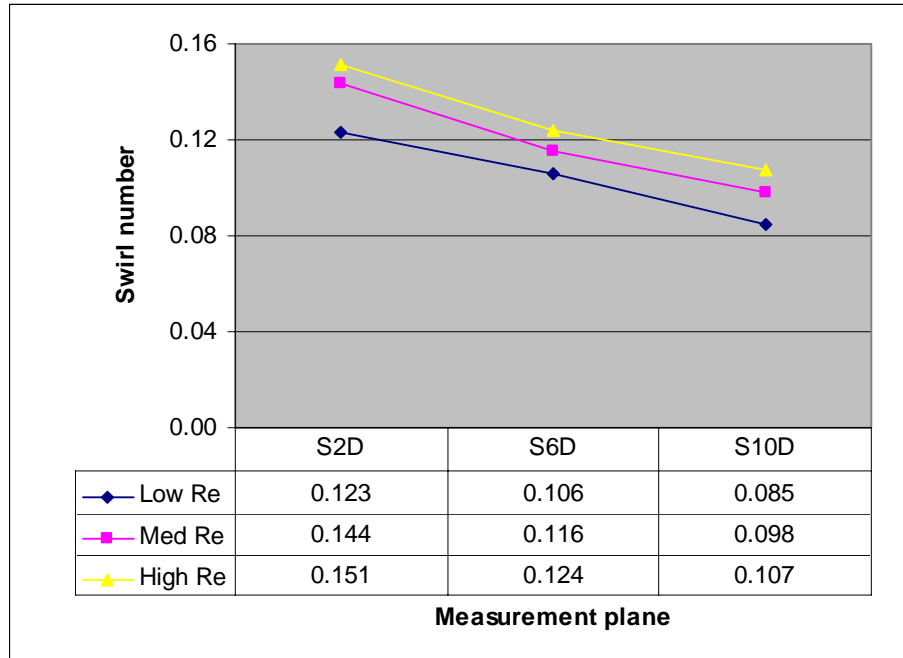


Figure 6.40: Swirl numbers at planes 2, 6 and 10D downstream of swirl pipe for the low, medium and high Reynolds number flows

The swirl number was then computed as explained above and are presented in Figure 6.40. The interpolated data introduces an error into the calculation of the integrals in Equation 6.20. Nonetheless, these swirl number values can still give an idea about the strength of the swirl that is induced by the swirl pipe at 2, 6 and 10 pipe diameters downstream of the swirl pipe for the three different Reynolds number flows. As shown in Figure 6.40, the swirl number decreases with increasing distance downstream and with decreasing Reynolds number. This supports the earlier conclusion that the swirl decays with respect to these two variables.

As mentioned in Chapter 4, Parchen and Steenbergen (1998) showed that the swirl intensity decayed exponentially as

$$S = S_0 e^{-\frac{\beta x}{D}}$$

where S_0 is the initial swirl intensity, β is the decay rate, x is the distance downstream of the swirler and D is the pipe diameter. A trendline following an exponential trend was hence fitted to the curves as shown in Figure 6.41 to find the decay rate for all three Re number flows. Table 6.6 summarises the swirl decay equations and the decay rate for the three Reynolds number flows.

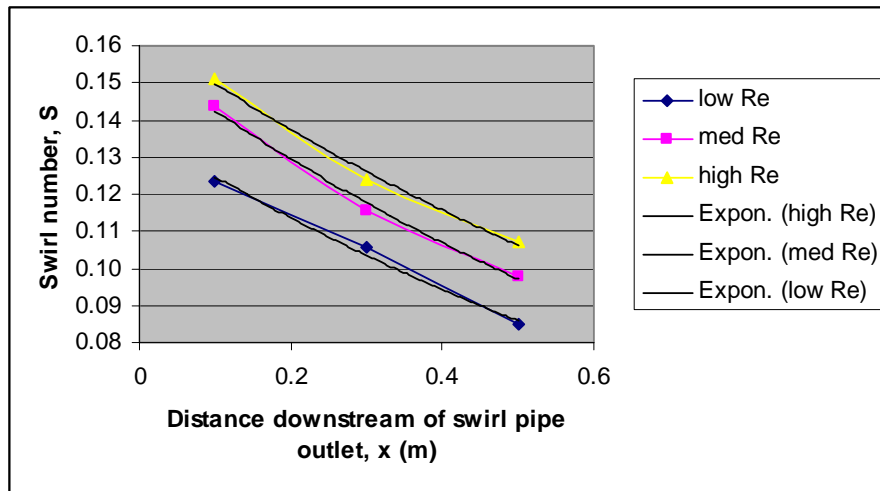


Figure 6.41: Trendline for estimating swirl decay rates

Reynolds number flow	Swirl decay equation	Decay rate
High	$S = 0.1632e^{-0.8596x}$	17.19
Medium	$S = 0.1567e^{-0.9312x}$	18.62
Low	$S = 0.1368e^{-0.9569x}$	19.13

Table 6.6: Swirl decay rates for the three Reynolds number flows

The swirl decay rate was calculated by dividing the exponential factor in the equation by the pipe diameter (0.05m). It can therefore be concluded that the swirl decays rapidly downstream of the swirl pipe and decay rates vary inversely with the Reynolds number of the flow. These findings therefore agree with those of Keith and Sonju (1995), Baker and Sayre (1974) and Steenbergen and Voskamp (1998) who concluded that the decay rate is dependent on the initial conditions of the flow and hence on its Reynolds number.

6.6.5 Conclusions from LDA experiments on an air-only flow

Laser-Doppler anemometer was employed to study the flowfield downstream of the swirl pipe for three different Reynolds number flows. Instantaneous local fluid velocities components in the three directions were measured at four planes perpendicular to the pipe axis (130 measurement points per plane), downstream of both the control and swirl pipe sections. Due to the limitation that the LDA technique poses on the size of the seeding particles, the LDA experiments were carried out on an-air only flow, seeded with oil droplets of an average diameter of 3 microns instead of the Fillite particles.

The measured u , v and w velocity components were converted into cylindrical polar velocity components, i.e. u_x , u_r and u_θ . Contour plots were created using Tecplot, version 10 by interpolating the measurement data at the measurement point, and then interpolated over a circular region of radius 23mm by using the “kriging” technique.

LDA measurements could be taken as close as $r/R = 0.92$ in the y -direction and $r/R = 0.88$ in the z -direction. Erroneous data tended to occur close to the pipe wall in the high and low z regions due to the high curvature of the pipe wall experienced by the laser beams as they passed through the glass pipe wall.

The cross sectional axial velocity distribution downstream of the control pipe showed low velocity closer to the wall and increasing to a maximum at the centre of the pipe for all three Reynolds number flow. The mean velocity was also shown to be higher, the higher the Reynolds number, but decreased with increasing distance downstream.

The contours plots of cross sectional axial velocity distribution downstream of the swirl pipe showed a core triangular shape, believed to be a direct consequence of the 3-lobed helical swirl pipe. A rotating flow was deduced from the shifting of the orientation of the triangular contours with increasing distance downstream of the swirl pipe. It was also deduced that the flow was decaying as the orientation of the triangular contours was not offset by 360° over a distance of 30cm, as the geometry twist of the swirl pipe, but occurred over a longer distance. Again minimum velocities were observed at the wall and increased to a maximum at the centre of the pipe for all

three Reynolds number flow. The mean velocity was again shown to be higher, the higher the Reynolds number, but decreased with increasing distance downstream.

A contour plot of tangential velocity and a plot of tangential velocity measurements along the horizontal centreline of the pipe revealed that the tangential velocity was close to zero at the centre of the pipe with a sudden increase in the region $0.25 < r/R < 0.88$, before decreasing to zero again at the walls. The presence of wall jet swirls could be concluded from these S shaped profiles. It was also deduced that the induced swirl slowly decayed with increasing distance downstream of the swirl pipe since maximum tangential velocity attained decreases with decreasing Reynolds number flows and increasing distance downstream of the swirl pipe. It was concluded that these effects were due to the presence of the swirl pipe as no such effects could be observed with the control pipe. It also appeared that the swirl pipe caused a redistribution of the velocities from axial to tangential, whereby creating a transfer of momentum from axial to angular momentum.

The degree of the swirl component at each location was calculated using the swirl number. It was necessary to discretise the measurement plane into a regular grid. This entailed the deletion and addition of some points by linear interpolation and extrapolation close to the wall. Swirl numbers of the order of 0.085 to 0.15 were obtained at a distance of 10D downstream of the swirl pipe for the low Reynolds number flow and at a distance of 2D downstream of the swirl pipe for the high Reynolds number flow, respectively. The earlier conclusion that the swirl decays with respect to the flow Reynolds number and distance downstream of the swirl pipe was supported. The swirl decay rates for the flows were calculated and it was found that they are inversely proportional to the Reynolds number of the flow.

6.7 EXPERIMENTAL ERRORS AND UNCERTAINTIES

Primary sources of uncertainty affecting the experimental data can be attributed to a wide variety of factors, which were identified as being:

- errors due to issues inherent to LDA measurement systems
- errors due to air leak into the experimental rig

- errors due to alignment of the test section with the LDA probe head
- uncertainty associated with conical inlet and water manometer
- errors due to fluctuations in the fan
- errors due to variations in LDA sampling

The errors which may arise due to issues which are inherent to the LDA system include:

- the accuracy with which the seeding particles actually follow the flow of the air – flow tracers on the order of 1 micron were used, so error associated with flow tracers not following the flow were considered as negligible
- the beam alignment of the LDA apparatus - as the optics themselves are calibrated by the manufacturer, errors associated with these are also considered negligible
- the lack of ability for LDA systems to provide accurate velocity measurements near the walls of pipes. The three main reasons for the difficulty in measuring very close to the wall are:

- gradient broadening due to the boundary layer for non-dimensional radial distance within 0.15 of the wall resulting in an increase in the rms of the measured frequency fluctuations
- refraction of the laser beams by the pipe wall. This difficulty arises because of the differences in refractive index of the material of the pipe (i.e., optical silica glass with $n=1.46$), and the test fluid (i.e air with $n=1.0$).
- reflections of the laser light from the pipe wall due to curvature of the pipe wall. The horizontal laser beam and the vertical laser beam, are most sensitive to such disturbances when measuring the top/bottom and the far left/right regions of the pipe respectively.

However, the closest measurement to the wall was carried out at $r/R=0.92$, so the near wall effects were limited. Ten measurement data with turbulence intensities higher than 10 were substituted by an interpolated value from neighbouring measurement points.

Maximum precaution was taken to ensure that air did not leak into the rig by using O-rings, tightening the flanges and making sure of air-tight connections at the pressure tapings. The uncertainty associated with air leakage into the system will therefore be considered as negligible in this error analysis.

Errors due to alignment of the test section with the LDA probe head was identified in section 6.6.3 as being the accuracy with which the tube wall surface could be located with respect to the cross section of the beam, ± 0.25 mm.

Since the degree of measurement accuracy for the U-tube water manometer was 1mm, the absolute pressure measurement is therefore $(P_0 \pm 9.81)\text{Pa}$, where P_0 is the measured value.

As discussed in section 5.5.4, the basic approximation uncertainty associated with the conical inlet for flows of Reynolds number between 2×10^4 and 3×10^5 is

$\pm \left(\frac{2 \times 10^4}{\text{Re}} - \frac{1}{15} \right)$. However, the error associated with the water manometer propagates

to the volumetric air flowrate expression of the conical inlet: $Q_m = \alpha \varepsilon \pi \frac{D^2}{4} \sqrt{2 \rho_{air} \Delta P}$

and that of Reynolds number: $\text{Re} = \frac{\rho_{air} U D}{\mu} = \frac{\alpha \varepsilon D \rho_{air}^{\frac{3}{2}}}{\mu} \sqrt{2 \Delta P}$. The absolute value of

the flowrate is therefore $Q_m = Q_{m_0} \pm \frac{0.014}{\sqrt{P_0}}$ and that of Reynolds number is

$$\text{Re} = \text{Re}_0 \pm \frac{6569}{\sqrt{P_0}}.$$

Experimental error due to the fan is mainly due to its fluctuations and can be quantified by the intensity of the free stream turbulence and the uniformity of the mean flow.

LDA measurements were therefore carried at ten pipe diameters downstream of the control pipe section (i.e. without the swirl pipe) for all three Reynolds number flows.

It was found that the higher the speed of the fan, the higher its fluctuations.

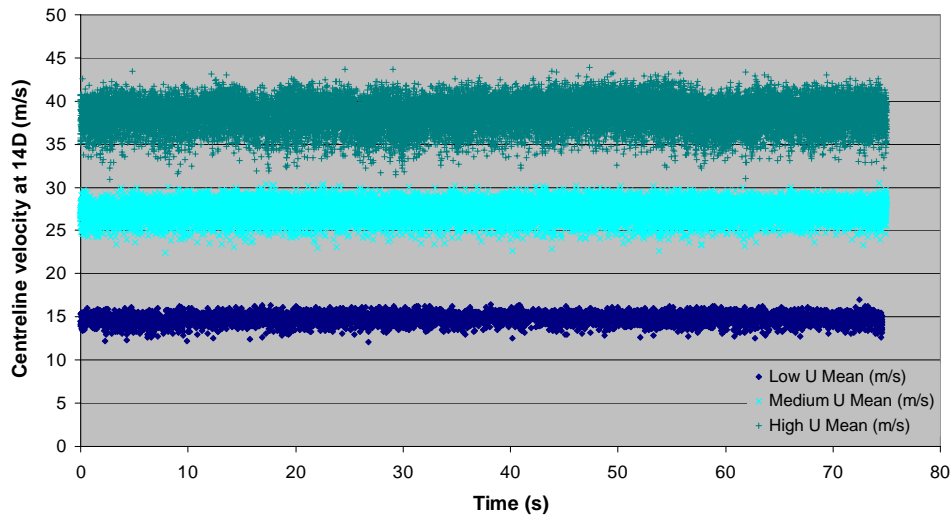


Figure 6.42: Time series measurement of axial velocities for low, medium and high Reynolds number flows

Figure 6.42 shows the axial mean velocities obtained for 6464, 16567 and 29244 measurements taken for each flow respectively. A statistical analysis was performed on the data to calculate the mean, standard deviation and standard error. Table 6.7 summarises the results.

Reynolds Number	Mean velocity (m/s)	Standard deviation σ (m/s)	Standard error (m/s)
Low	14.83	0.61	0.015
Medium	27.29	1.04	0.016
High	38.45	1.58	0.019

Table 6.7: Error in Reynolds number calculation

The uncertainty of the mean velocity is given by: $\delta(U) = \frac{2\sigma}{\sqrt{N}}$ where U is the mean velocity estimated from N samples. Hence the errors associated with the fan are ± 0.015 , ± 0.016 and ± 0.019 m/s for the low, medium and high Reynolds number flows, evaluated at 95% confidence level. The resulting Reynolds numbers for the flows are therefore $4.5 \times 10^4 \pm 791$, $9 \times 10^4 \pm 404$, $1.4 \times 10^5 \pm 269$.

The last set of errors is due to the LDV system and its operation. The most important of these errors, is a result of the finite number of instantaneous velocity measurements (or the number of samples) at each location used to calculate the mean velocity and the turbulence intensity. While each velocity sample may be a perfectly accurate measurement of the velocity at the time the sample was obtained, it is not a very good estimate of the mean velocity. From the point of view of estimating the mean velocity, the uncertainty in each velocity sample can be taken as twice the standard deviation in its fluctuation, i.e. in effect this assumes the fluctuating velocity has a normal

distribution. The uncertainty of the mean velocity is given by: $\delta(U) = \frac{2u_{rms}}{\sqrt{N}}$ where U is the mean velocity estimated from N samples.

The uncertainty in the statistically averaged velocities by the LDA system for the low, medium and high Reynolds number flows, evaluated at 95% confidence level are shown in Table 6.7.

Uncertainty estimates from this source may be combined with uncertainty estimates from other independent sources by adding their squares and then square rooting the result to give the overall uncertainty estimates in the velocity data. The combined error for the fan and LDA sampling process is summarised in Table 6.8.

Investigated pipe	Velocity being measured	Reynolds number flow	Location plane	Standard error due to LDA (m/s)	Standard error due to Fan (m/s)	Combined standard error (m/s)	Combined % error
Swirl	u	low	2D	0.235	0.015	0.235	1.83
			6D	0.239	0.015	0.239	1.87
			10D	0.232	0.015	0.233	1.83
			14D	0.215	0.015	0.216	1.79
		medium	2D	0.564	0.016	0.564	1.96
			6D	0.425	0.016	0.425	1.84
			10D	0.425	0.016	0.426	1.78
			14D	0.405	0.016	0.405	1.73
		high	2D	0.684	0.019	0.684	2.01
			6D	0.627	0.019	0.628	1.84
			10D	0.601	0.019	0.602	1.75
			14D	0.574	0.019	0.575	1.69
	w	low	2D	0.176	0.015	0.177	4.41
			6D	0.170	0.015	0.171	3.42
			10D	0.160	0.015	0.161	4.02
			14D	0.351	0.015	0.351	3.51
		medium	2D	0.330	0.016	0.330	5.51
			6D	0.323	0.016	0.324	3.24
			10D	0.306	0.016	0.307	3.07
			14D	0.653	0.016	0.653	8.16
		high	2D	0.495	0.019	0.495	5.50
			6D	0.463	0.019	0.463	7.72
			10D	0.448	0.019	0.449	7.48
			14D	0.957	0.019	0.957	4.79
	v	low	2D	0.174	0.015	0.174	4.35
			6D	0.176	0.015	0.176	5.88
			10D	0.156	0.015	0.157	3.92
			2D	0.370	0.016	0.370	6.17
		medium	6D	0.349	0.016	0.350	6.99
			10D	0.315	0.016	0.316	7.89
		high	2D	0.492	0.019	0.492	9.84
			6D	0.583	0.019	0.583	9.71
			10D	0.446	0.019	0.446	5.58

Control	u	low	2D	0.188	0.015	0.189	1.51
			6D	0.192	0.015	0.193	1.53
			10D	0.189	0.015	0.189	1.53
			14D	0.195	0.015	0.196	1.56
		medium	2D	0.339	0.016	0.339	1.45
			6D	0.345	0.016	0.345	1.47
			10D	0.339	0.016	0.340	1.45
			14D	0.347	0.016	0.347	1.51
		high	2D	0.493	0.019	0.493	1.42
			6D	0.493	0.019	0.493	1.44
			10D	0.491	0.019	0.491	1.43
			14D	0.495	0.019	0.496	1.49
	w	low	2D	0.253	0.015	0.253	8.44
			6D	0.274	0.015	0.274	9.13
			10D	0.262	0.015	0.263	6.56
			14D	0.265	0.015	0.266	5.32
		medium	2D	0.431	0.016	0.432	7.19
			6D	0.435	0.016	0.435	8.70
			10D	0.443	0.016	0.443	7.38
			14D	0.465	0.016	0.466	6.65
		high	2D	0.616	0.019	0.616	7.70
			6D	0.623	0.019	0.623	6.92
			10D	0.623	0.019	0.623	8.90
			14D	0.649	0.019	0.649	7.21

Table 6.8: Error in LDA velocity measurements

Similarly, the propagated uncertainties in the axial, radial and tangential velocities are calculated and presented in Table 6.9.

Reynolds number flow	Location plane	Error in axial velocity		Error in radial velocity		Error in tangential velocity	
		Std error (m/s)	% error	Std error (m/s)	% error	Std error (m/s)	% error
low	2D	0.235	1.827	0.248	6.200	0.248	15.420
	6D	0.239	1.870	0.246	4.912	0.246	18.436
	10D	0.233	1.832	0.224	5.611	0.224	20.637
	14D	0.216	1.787	N/A	N/A	N/A	N/A
medium	2D	0.564	1.956	0.496	8.271	0.496	15.731
	6D	0.425	1.836	0.476	4.765	0.476	17.478
	10D	0.426	1.781	0.440	4.401	0.440	19.271
	14D	0.405	1.729	N/A	N/A	N/A	N/A
high	2D	0.684	2.006	0.698	7.758	0.698	14.523
	6D	0.628	1.840	0.744	12.406	0.744	17.974
	10D	0.602	1.752	0.633	10.544	0.633	17.888
	14D	0.575	1.693	N/A	N/A	N/A	N/A

Table 6.9: Error in calculation of cylindrical velocity components

6.8 CONCLUSIONS

Experiments were conducted at three Reynolds number (low = $4.5 \times 10^4 \pm 791$, medium = $9 \times 10^4 \pm 791$ and high = $1.4 \times 10^5 \pm 269$). Visualisation experiments with the high speed camera and subsequent PIV and LDA measurements proved that the swirl pipe was effectively inducing swirl to the lean phase pneumatic flow. A decaying swirl pattern was formed in the same direction as the twists in the swirl pipe geometry, which is non-existent when the control pipe was used. The swirl patterns for a lean phase pneumatic flow were of the form of a ribbon effect, resulting in high and low regions of particle concentrations.

Since the particles were fully suspended in the flow, it was also concluded that the particles were followed the same path as the airflow. The motion of the particles was therefore inferred from that of the airflow for the subsequent PIV and LDA experiments due to the nature of these techniques.

Axial velocities were found to be minimum at the pipe wall and maximum at the centre of the pipe. In contrast, tangential velocity is minimum at the centre of the pipe with a

sudden increase in the region $0.25 < r/R < 0.88$, before decreasing to zero again at the pipe wall. It was concluded from this that the twist in the lobed geometry of the swirl pipe caused a redistribution of the velocities from axial to tangential, whereby creating a momentum shift from axial to angular. This momentum shift generates the swirl motion observed. The tangential velocity profiles allowed the swirl type to be characterised as wall jet swirls. The pressure experiments showed that the transfer of axial to angular energy was accompanied by a pressure drop proportional to the Reynolds number of the flow.

The degree of the swirl component at each location was quantified using the swirl number. The geometrically induced swirl was found to decay with increasing distance downstream of the swirl pipe and inversely with the Reynolds number of the flow.

Primary sources of errors and uncertainty were identified and it was concluded that they were insignificant when compared to the actual values.

The current study has improved our understanding of the generation and decay of the geometrically induced swirl. This understanding will be consolidated in Chapters 7 and 8 by the application of CFD modelling to simulate the same flow conditions as in this empirical chapter.

CHAPTER 7

CFD MODELLING AND SOLUTION METHODOLOGY

7.1 INTRODUCTION

Computational Fluid Dynamics (CFD) provides a third approach with which to solve fluid dynamics problems by complementing firstly the experimental fluid dynamics approach and secondly the theoretical fluid dynamics approach. The development of high speed digital computers combined with the development of accurate numerical algorithms contributed to the application of CFD to a very broad range of applications in the last decade. CFD is now used as a research and a design tool across the engineering field because it is an accessible, cost effective and safe way of investigation. This method was employed in the present research to supplement and complement the experimental investigations because of its cost effectiveness and the limitations of the available experimental techniques.

The main commercially available CFD packages on the market are: FLUENT, CFX, STAR CD, FLOW 3D and PHOENIX. CFX version 5.6 and FLUENT version 6.2.16 were used in this study.

This chapter concerns the application of numerical and computational models to turbulent flows. It builds on chapter 3 and presents a basic introduction to the governing equations that CFD packages use to solve any basic fluid dynamics problems in section 7.4, the more complex turbulence ones in section 7.5, general CFD solution methodology in section 7.3 and 7.6 and how this was applied in this particular research in section 7.7.

7.2 BASIC PRINCIPLES OF CFD

Any CFD studies can be divided into three main stages (Anderson, 1995):

- Pre-processing: problem formulation whereby the region of fluid to be analysed (the computational domain) is designed and divided up into a number of discrete elements (the mesh); the properties of fluid acting on the domain,

including external constraints or boundary conditions to implement realistic situations are defined

- Solving: the solution of the CFD problem is calculated whereby the governing equations are solved iteratively to compute the flow parameters of the fluid as time elapses. Convergence is important to produce an accurate solution of the partial differential equations.
- Post-processing: visualisation, analysis and processing of the results from the solver. Commercial packages often provide post-processing facilities that enable the creation of vector plots or contour plots to display the trends of velocity, pressure, kinetic energy and other properties of the flow. A key component of post-processing is being able to visualise complex flows.

7.3 NUMERICAL CONCEPTUALISATION FOR CFD MODELLING

7.3.1 Numerical schemes

The governing integral equations describing the fluid flow are solved in CFD by using a control-volume-based technique, which consists of:

- Using a computational grid to divide the fluid domain into discrete control volumes
- The governing equations are then integrated on the individual control volumes to construct algebraic equations for the discrete dependent variables ("unknowns") such as velocities, pressure, etc.
- The discretised equations are then linearised and the resultant linear equation system is solved to yield updated values of the dependent variables.

FLUENT provides a choice of two numerical methods (Fluent Inc, 2004): the segregated solver and the coupled solver. Both numerical methods employ a finite-volume discretisation process, but the approach used to linearise and solve the discretised equations is either implicit or explicit. On the other hand, the coupled solver solves the governing flow equations simultaneously and governing equations for

additional scalars sequentially. Figure 7.1 shows the iteration process adopted by the two different numerical methods.

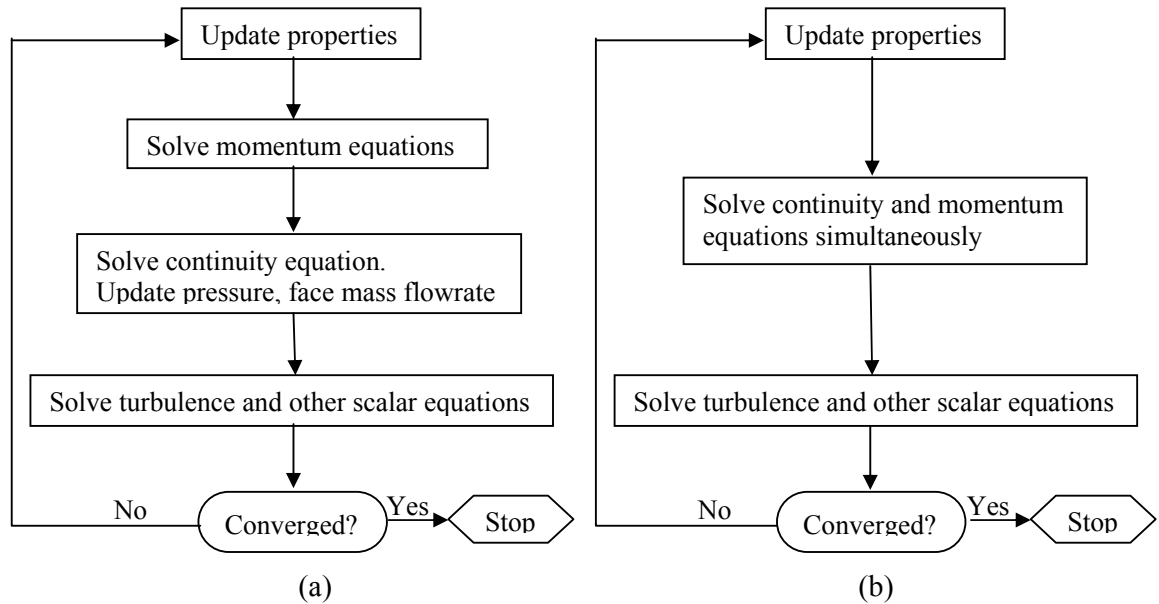


Figure 7.1: Overview of the (a) Segregated Solution Method (b) Coupled Solution Method (Fluent Inc, 2004)

In the segregated solution method each discrete governing equation is linearised implicitly with respect to that equation's dependent variable. This will result in a system of linear equations with one equation for each cell in the domain, hence the name “scalar” system of equations, which is solved using a point implicit (Gauss-Seidel) linear equation solver in conjunction with an algebraic multigrid (AMG) method.

In the coupled solution method, the coupled set of governing equations can be solved either implicitly or explicitly while equations for additional scalars are only solved segregated from the coupled set of governing equations. Implicit formulation of the coupled set of governing equation implied that the unknown value for a given variable in each cell is computed using a relation that includes both existing and unknown values from neighbouring cells, resulting in more than one equation which must be solved using a point implicit (Gauss-Seidel) linear equation solver in conjunction with

an algebraic multigrid (AMG) method to give the unknown quantities. Explicit formulation of the coupled set of governing equation implied that the unknown value for a given variable in each cell is computed using a relation that includes only existing values, resulting in only one equation which can be solved one at a time to give the unknown quantities. In this case, a linear equation solver is not needed. The solution is updated using a multi-stage (Runge-Kutta) solver instead.

In summary, for the segregated solver, every single variable in the governing flow equations are solved implicitly by considering all cells at the same time separately and sequentially. In the coupled solver, if an implicit approach is used, all variables in all cells are solved at the same time and if an explicit approach is used, all variables are solved one cell at a time. The use of the coupled implicit solver requires about 1.5 to 2 times more memory than the segregated solver. The coupled explicit solver requires less computing capacity than the coupled implicit solver, but FLUENT documentation notes that convergence is less readily reached with coupled explicit solver than with the coupled implicit solver.

7.3.2 Discretisation process

In order to solve a fluid flow numerically, the computational domain, including the surfaces and boundaries have to be discretised, i.e. the continuously varying quantities are approximated in terms of values at a finite number of points. This can be carried out using either one of three different methods (Versteeg and Malalasekera, 1995): Finite-Difference Method (FDM), Finite-Volume Method (FVM) or Finite-Element Method (FEM). However, recent CFD packages, including FLUENT, tend to apply FVM more because it can be used on either a structured or unstructured mesh, rigorously enforces conservation, is directly relatable to physical quantities (mass flux, etc.), and is easier to program in terms of CFD code development.

Three types of discretisation processes exist within CFD: spatial, equation and temporal. The first two are discussed in more detail, while temporal discretisation will be overlooked as it is only applicable to time-dependent formulations, or unsteady state systems by splitting the time in the continuous flow into discrete time steps.

7.3.2.1 Spatial discretisation

In FVM, the computational domain is divided into a finite number of elements known as control volumes by the regular and irregular arrangement of nodes, known as the mesh. Flow parameters are resolved around these nodes, so that the fluid flow can be described mathematically by specifying its velocity at all points in space and time. Structured, unstructured and multi-block structured meshes are the three main types of mesh that are generally used in CFD. The structured mesh is typically hexahedral in shape, and is ideal for simple cuboids geometries. The unstructured mesh was designed for more complex geometries as nodes can be placed within the computational domain depending on the shape of the body, resulting into a tetrahedral mesh. The multi-block subdivides the computational domain into different blocks which can be structurally meshed. It was introduced as a compromise between lower computing cost associated with structured mesh and the flexibility associated with unstructured mesh. The different meshing types are further discussed in section 7.7.3.

7.3.2.2 Equation discretisation

The governing equations in CFD consist of partial differential equations, which need to be discretised so they can be solved by the solver. In the FVM method, the governing equations of fluid flow are integrated and solved for each control volume iteratively based on the conservation laws. The discretisation process results in a set of algebraic equations that resolve the variables using an integration method at a specified finite number of points within the control volumes. The flow around the whole domain is then obtained through integration on the control volumes.

The equations solved by FLUENT apply to the array of control volumes, i.e. the computational grid or mesh, generated by the spatial discretisation. By default, the discrete variable values (e.g. pressure, velocities and turbulence) are calculated and stored at the cell centres by FLUENT. However, face values are required for the convection terms of the turbulence models and must be interpolated from the cell centre values. This is accomplished using an upwind scheme whereby the face value is derived from quantities in the cell upstream, or upwind relative to the direction of the mean velocity. Four upwind advection schemes are available in FLUENT: first-order upwind, second-order upwind, power law, and QUICK. These are described briefly.

Upwind advection schemes

In the first order upwind advection scheme quantities at cell faces are determined by assuming that for any variable, the cell-centre values represent the cell-average value. Hence when first-order upwind scheme is selected, the face value of a variable is set equal to the cell-centre value of in the upstream cell.

In the second order upwind advection scheme quantities at cell faces are computed using a multidimensional linear reconstruction approach, whereby higher-order accuracy is achieved at cell faces through a Taylor series expansion of the cell-centred solution about the cell centroid. Hence the face value of a variable is computed by averaging that from the two cells adjacent to the face using a gradient method.

The power-law discretisation scheme interpolates the face value of a variable, using the exact solution to a one-dimensional convection-diffusion equation. QUICK (Quadratic Upstream Interpolation for Convection Kinetics) discretisation scheme are based on a weighted average of second-order-upwind and central interpolations of the variable.

FLUENT documentation recommends that the first-order discretisation generally yields better convergence but less accurate results than the second-order scheme. First order upwind discretisation is applicable without any significant loss of accuracy when the flow is aligned with a quadrilateral or hexahedral grid, so that numerical diffusion will be naturally low. Also that for most complex flows, the first-order scheme may need to be used to perform the first few iterations and then switch to the second-order scheme to continue the calculation to convergence. The QUICK discretisation scheme is reported to compute higher-order value of the convected variable at a face more accurately on structured grids aligned with the flow direction, but to only provide marginal improvement on the second-order scheme for rotating or swirling flows solved on quadrilateral or hexahedral meshes. The power law is reported to generally yield the same accuracy as the first-order scheme.

Pressure interpolation schemes

Similarly, the face values of pressure from the cell values is computed using a pressure interpolation scheme. The ones available in FLUENT include: standard, linear, second

order, body-force-weighted scheme and PRESTO! A brief description of all five schemes is given below.

The standard scheme interpolates the pressure values at the faces using momentum equation coefficients and is only applicable when the pressure variation between cell centres is smooth. The linear scheme computes the face pressure as the average of the pressure values in the adjacent cells. The second-order scheme reconstructs the face pressure in the manner used for second-order accurate convection terms. The body-force-weighted scheme computes the face pressure by assuming that the normal gradient of the difference between pressure and body forces is constant. The PRESTO! (PREssure STaggering Option) scheme uses the discrete continuity balance for a “staggered” control volume about the face. Fluent documentation recommends the use of the PRESTO! scheme for flows with high swirl numbers, high-Rayleigh-number natural convection, high-speed rotating flows, and flows in strongly curved domains and the second-order scheme for compressible flows.

Pressure-velocity coupling

The momentum equation is normally solved with a guessed pressure field, and therefore the resulting face flux, does not satisfy the continuity equation. This is rectified by applying a pressure-velocity coupling algorithm, which adds a correction to the face flux so that the corrected face flux satisfies the continuity equation. Three pressure-velocity coupling algorithms are provided in FLUENT: SIMPLE (Semi-Implicit Method for Pressure Linked Equations), SIMPLER, and PISO. The SIMPLE or SIMPLER algorithm is recommended for steady-state calculations while PISO is recommended for transient calculations, or for cases with highly skewed meshes.

The SIMPLE algorithm substitutes the flux correction equations into the discrete continuity equation to obtain a discrete equation for the pressure correction in the cell. The SIMPLER algorithm is a variant of the SIMPLE algorithm, offering a different correction expression for the face flux correction. The use of this modified correction equation has been shown to accelerate convergence in problems where pressure-velocity coupling is the main deterrent to obtaining a solution. The Pressure-Implicit with Splitting of Operators (PISO) pressure-velocity coupling scheme, is based on the

higher degree of the approximate relation between the corrections for pressure and velocity.

7.3.3 Performance and monitoring criteria

In CFD study, another aspect of consideration of a simulation is the residual of the solutions (Anderson, 1995). The equations describing fluid flow are solved iteratively so residuals appear. The residual is the imbalance of the conservation equation for a general variable summed over all the computational cells. They are a measure of error in the discretised equations, summed over all control volumes and are a guide to convergence. Low residuals suggest a solution that converged and the simulation can be considered as stable if the residuals kept lowering. In engineering application, the momentum and continuity residuals are usually targeted between three to four orders of magnitude of the actual values to achieve convergence of the solution to an acceptable level. Low residuals do not however guarantee that the converged solution is correct. Additional reports of integrated quantities at surfaces and boundaries are often used to judge convergence. A physical variable of the solution flowfield therefore needs to be monitored to ensure true convergence of a physically correct solution, which is arrived at when the physical variable remain constant for a sufficient number of iterations and the residuals have reached the pre-determined criteria. Mass imbalance is also often used to monitor convergence. This is a report of the mass flowrates at inlet and outlet flow boundaries, which should logically add to zero for a converged solution.

7.4 GOVERNING EQUATIONS FOR TURBULENT FLOW

Any fluid flow, including turbulent ones, is governed by the following three fundamental principles and the three equations that have been derived to represent them (Versteeg and Malalasekera, 1995):

- conservation of mass (the continuity equation)
- Newton's second law for the conservation of momentum (the momentum equations or Navier Stokes equations)

- The first law of thermodynamics for the conservation of energy (the energy equation)

These governing equations are then solved subject to boundary conditions describing the physical aspects of the flow. Since this study assumes an isothermal condition, the focus will only be on the continuity and Navier Stokes equations.

7.4.1 Continuity equation for mass conservation

The law of conservation of mass is applied to a fluid flow by ensuring that the change of mass in a control volume is equal to the mass that enters through its faces minus the total mass leaving its faces. Hence for an incompressible flow, the continuity equation in Cartesian form is given by:

$$\frac{\partial(\rho u_i)}{\partial t} + \frac{\partial(\rho u_i)}{\partial x_i} = 0 \quad (\text{Eq. 7.1})$$

7.4.2 Navier-Stokes equations for momentum conservation

Newton's Second Law of Motion is applied to the fluid flow to ensure that the rate of change of momentum of the fluid particles is equal to the total force due to surface stresses and body forces acting in an aligned direction of a chosen coordinate axis. The momentum equation is expressed in terms of the pressure and viscous stresses acting on a particle in the fluid as:

$$\frac{\partial(u_i)}{\partial t} + \frac{\partial}{\partial x_j}(u_i u_j) = -\frac{1}{\rho} \frac{\partial p}{\partial x_i} + \frac{\partial}{\partial x_j} \left[\nu \left(\frac{\partial u_i}{\partial x_j} + \frac{\partial u_j}{\partial x_i} \right) \right] \quad (\text{Eq. 7.2})$$

To solve the Navier Stokes equations for high-Reynolds-number turbulent flows in complex geometries is currently impossible due to limitations on computational capacity. Hence approximate modelling methods have been developed to calculate statistical characteristics of the turbulent motion by averaging the flow equations.

7.5 TURBULENCE MODELLING – REYNOLDS AVERAGED NAVIER-STOKES EQUATIONS

RANS models have been developed based on the concept that a velocity scale and a length scale are sufficient to describe the effect of turbulence in a flow. Hence, the Navier-Stokes equations are time averaged over a large enough time compared to the typical timescale of turbulent fluctuation in order to average out the unsteadiness of a turbulent flow. This is usually referred to as the Reynolds Averaged Navier Stokes Equations. The flow is separated into mean and fluctuating components, also known as Reynolds decomposition:

$$u = U + u'_i \quad (\text{Eq. 7.3})$$

$$p = P + p'_i \quad (\text{Eq. 7.4})$$

$$\frac{\partial(u_i)}{\partial x_i} = 0 \quad (\text{Eq. 7.5})$$

Substituting the Reynolds decomposition into the equations for conservation of mass and momentum and taking the time average yields the Reynolds Averaged Navier Stokes Equations for incompressible flow:

$$\frac{\partial(u_i)}{\partial t} + \frac{\partial}{\partial x_j}(u_i u_j) = -\frac{1}{\rho} \frac{\partial p}{\partial x_i} + \frac{\partial}{\partial x_j} \left[\nu \left(\frac{\partial u_i}{\partial x_j} + \frac{\partial u_j}{\partial x_i} \right) \right] - \overline{u'_i u'_j} \quad (\text{Eq. 7.6})$$

The averaging results in new unknown terms in the equations of motion, $-\overline{u'_i u'_j}$, known as Reynolds stresses, which require extra assumptions or equations in order to achieve “closure”, i.e. sufficient number of equations for all the unknowns terms.

This will be illustrated in three widely used turbulence models, namely the k-ε model, the RNG k-ε model and the Reynolds Stress Model (RSM). In k-ε models, the Reynolds stress tensor can be calculated using the isotropic eddy viscosity assumption. The RNG k-ε model belongs to the k-ε family of turbulence models; however, unlike the standard k-ε model, the RNG k-ε model is derived using a statistical method based on Renormalization Group (RNG) methods by Yakhot and Orszag (1986). This model

has an additional term in the dissipation equation that improves the accuracy in case of rapidly strained flows. The k- ϵ model family is also known as two equations models since they involve the effect of the transport of turbulence quantities by considering the energy transfer in the flow in one equation and also the calculation of an empirical length scale from a second transport equation.

The RSM solves six transport equations for the Reynolds stresses. A brief description of the models follow, as it is beyond the scope of this research to describe them in further mathematical detail.

7.5.1 Standard k- ϵ model

Launder and Spalding (1972) proposed the k- ϵ model in 1972 and since then it has become the most widely used turbulence model in the engineering industry.

The k- ϵ turbulence model assumes that the rate of production and dissipation of turbulent flows are in near-balance in energy transfer, so that the dissipation rate, ϵ , of the energy is given as,

$$\epsilon = \frac{k^{\frac{3}{2}}}{L} \quad (\text{Eq. 7.7})$$

where k is the kinetic energy of the flow and L is the length scale involved. The dissipation rate, ϵ , is in turn related to the turbulent viscosity μ_t based on the Prandtl mixing length model

$$\mu_t = \rho C_\mu \frac{k^2}{\epsilon} \quad (\text{Eq. 7.8})$$

where C_μ is an empirical constant and ρ is the density of the flow.

When applied to the RANS equations, the k- ϵ model is obtained in terms of the k-equation and the ϵ -equation:

The k-equation: (Eq. 7.9)

$$\underbrace{\frac{\partial(\rho k)}{\partial t} + u_i \frac{\partial(\rho u_j k)}{\partial x_j}}_{\text{Convection term}} = \underbrace{\frac{\partial}{\partial x_j} \left(\frac{\mu_t}{\sigma_\varepsilon} \frac{\partial k}{\partial x_j} \right)}_{\text{Diffusion term}} + \underbrace{\mu_t \frac{\partial u_i}{\partial x_j} \left(\frac{\partial u_i}{\partial x_i} + \frac{\partial u_j}{\partial x_j} \right) \frac{\partial u_i}{\partial x_j}}_{\text{Production term}} - \underbrace{\rho \varepsilon}_{\text{Destruction term}}$$

The ε -equation: (Eq. 7.10)

$$\underbrace{\frac{\partial(\rho \varepsilon)}{\partial t} + u_i \frac{\partial(\rho u_j \varepsilon)}{\partial x_j}}_{\text{Convection term}} = \underbrace{\frac{\partial}{\partial x_j} \left(\frac{\mu_t}{\sigma_\varepsilon} \frac{\partial \varepsilon}{\partial x_j} \right)}_{\text{Diffusion term}} + \underbrace{C_{\varepsilon 1} \frac{\varepsilon}{k} \mu_t \frac{\partial u_i}{\partial x_j} \left(\frac{\partial u_i}{\partial x_j} + \frac{\partial u_j}{\partial x_i} \right)}_{\text{Production term}} - \underbrace{\rho C_{\varepsilon 2} \frac{\varepsilon^2}{k}}_{\text{Destruction term}}$$

The inherent production of turbulence is what is responsible for the transfer of energy from the mean flow to the turbulence, and is counterbalanced by the interaction of the Reynolds stresses and mean velocity gradient. On the other hand, the destruction term represents the dissipation of energy into heat due to viscous nature of the flow.

The constant parameters used in the equations are commonly taken as (Shimada and Ishihara, 2002):

$$C_\mu = 0.09; \quad C_{\varepsilon 1} = 1.44; \quad C_{\varepsilon 2} = 1.92; \quad \sigma_k = 1.0; \quad \sigma_\varepsilon = 1.3$$

The advantages of the k- ε model include a robust formulation which does not require excessive computer power but which provides reasonable accuracy for a wide range of turbulent flows. The model does not perform very well for flows with boundary layer separation, sudden changes in the mean strain rate such as swirling and rotating flows and flows over curved surfaces. Moreover, the k- ε model is based on the Boussinesq hypothesis, which inherently assumes that the turbulent viscosity is isotropic. This is a major source of error when using the k- ε model for simulating strong swirling flows as turbulent eddy viscosity is an anisotropic quantity which is affected by geometry.

7.5.2 RNG k - ε model

The RNG k - ε model is arrived at after the renormalisation group analysis of the Navier Stokes equations. The equations for turbulence production and dissipation are the same as those for the standard k - ε model, but the constants differ. The RNG k - ε equations are therefore given by:

$$\underbrace{\rho u_i \frac{\partial k}{\partial x_{ij}}}_{\text{Convection term}} = \underbrace{\mu_t S^2}_{\text{Production term}} + \underbrace{\frac{\partial}{\partial x_i} \left(\alpha_k \mu_{eff} \frac{\partial k}{\partial x_i} \right)}_{\text{Diffusion term}} - \underbrace{\rho \varepsilon}_{\text{Destruction term}} \quad (\text{Eq. 7.11})$$

where

$$S = \sqrt{2 S_{ij} S_{ij}}; \quad S_{ij} = \frac{1}{2} \left(\frac{\partial U_j}{\partial x_i} + \frac{\partial U_i}{\partial x_j} \right) \quad (\text{Eq. 7.12})$$

$$\underbrace{\rho u_i \frac{\partial \varepsilon}{\partial x_i}}_{\text{Convection term}} = \underbrace{C_{1\varepsilon} \left(\frac{\varepsilon}{k} \right) \mu_t S^2}_{\text{Production term}} + \underbrace{\frac{\partial}{\partial x_i} \left(\alpha_\varepsilon \mu_{eff} \frac{\partial \varepsilon}{\partial x_i} \right)}_{\text{Diffusion term}} - \underbrace{C_{2\varepsilon} \rho \left(\frac{\varepsilon^2}{k} \right)}_{\text{Destruction term}} - R \quad (\text{Eq. 7.13})$$

where R is an additional term related to mean strain and turbulence quantities, μ_{eff} is a combination of molecular and turbulent viscosities ($\mu_{eff} = \mu_0 + \mu_t$) and $C_{1\varepsilon}$, $C_{2\varepsilon}$, α_k , α_ε are derived using the renormalisation group mathematical technique.

The additional terms improve a little on the standard k - ε model for flows with rapid changes in the mean strain rate and the effect of swirl on turbulence.

7.5.3 Reynolds stress model (Second order closure model)

The Reynolds stress model (RSM) is the most elaborate turbulence model that FLUENT provides. The Reynolds stress model (RSM) copes with more complex flows by taking into account the anisotropic features of turbulence. In this model, the Reynolds stresses are expressed in terms of known mean flow quantities, such as the convective and diffusive nature of turbulence, to solve the fluid governing equations in

the turbulence models. The Reynolds stresses are solved using partial differential equations which take into account the effects of the dynamics of turbulence. These equations are then combined with the Navier-Stokes equations in order to solve the flow in a closed set of seven partial differential equations. One way of expressing the Reynolds Stress model is:

$$\rho U_k \frac{\partial \overline{u_i u_j}}{\partial x_k} = P_{ij} + D_{ij} - \varepsilon_{ij} + \Phi_{ij} + \Omega_{ij} \quad (\text{Eq. 7.14})$$

where

$$\text{Stress production term} = P_{ij} = -\rho \left(\overline{u_i' u_k'} \frac{\partial u_j'}{\partial x_k} + \overline{u_j' u_k'} \frac{\partial u_i'}{\partial x_k} \right) \quad (\text{Eq. 7.15})$$

$$\text{Diffusion term} = D_{ij} = \frac{\partial}{\partial x_k} \left(\frac{\mu_t}{\sigma_k} \frac{\partial \overline{u_i' u_j'}}{\partial x_k} \right) \quad (\text{Eq. 7.16})$$

$$\text{Dissipation term} = \varepsilon_{ij} = -2\mu \frac{\partial \overline{u_i' \partial u_j'}}{\partial x_k \partial x_k} \quad (\text{Eq. 7.17})$$

$$\text{Pressure strain} = \Phi_{ij} = \rho \left(\frac{\partial \overline{u_i'}}{\partial x_k} + \frac{\partial \overline{u_j'}}{\partial x_k} \right) \quad (\text{Eq. 7.18})$$

$$\text{Rotational term} = \Omega_{ij} = -2\rho \Omega_k \left(\overline{u_j' u_m'} \varepsilon_{ikm} + \overline{u_i' u_m'} \varepsilon_{jkm} \right) \quad (\text{Eq. 7.19})$$

$$\text{Turbulent kinetic energy} = k = \frac{1}{2} \left(\overline{u_i' u_i'} + \overline{u_j' u_j'} + \overline{u_k' u_k'} \right) \quad (\text{Eq. 7.20})$$

The above six Reynolds Stress equations are then solved with the following equation for the dissipation rate, ε :

$$U_i \frac{\partial \varepsilon}{\partial x_i} = \frac{\partial}{\partial x_i} \left(\frac{\nu_t}{\sigma_\varepsilon} \frac{\partial \varepsilon}{\partial x_i} \right) + C_{1\varepsilon} \frac{\varepsilon}{k} \nu_t \left(\frac{\partial u_i}{\partial x_j} + \frac{\partial u_j}{\partial x_i} \right) \frac{\partial u_i}{\partial x_j} - C_{2\varepsilon} \frac{\varepsilon^2}{k} \quad (\text{Eq. 7.21})$$

where ν_t is the kinematic viscosity and $C_{1\varepsilon}$, $C_{2\varepsilon}$ and σ_ε are constants.

RSM gives more accurate solutions since it simulates the anisotropic nature of turbulence more realistically. However, this model is computationally more demanding than the two equations models. FLUENT documentation recommends the use of the RSM model when the flow features of interest are the result of anisotropy in the Reynolds stresses. Among the examples quoted are cyclone flows, highly swirling flows in combustors, rotating flow passages, and the stress-induced secondary flows in ducts.

7.6 NEAR-WALL TREATMENT FOR WALL-BOUNDED TURBULENT FLOWS

The k- ε models and the RSM were designed for turbulent core flows and can therefore be predicted to be inaccurate in the near wall region, which is a crucial region for the successful predictions of wall-bounded turbulent flows. Special wall modelling procedures therefore need to be implemented to make these models suitable for wall-bounded flows.

The boundary condition at a stationary wall is one of no-slip. In order to satisfy this, the mean velocity at the wall has to be zero, thereby creating a steep velocity gradient (from zero at the walls to the mean flow velocity at the core) very close to the wall. This gives rise to the so-called “near-wall region” which can be largely subdivided into three layers Figure 7.2:

- The viscous sublayer (the innermost layer) where the flow is almost laminar, and mass transfer is dictated by molecular viscosity.
- The buffer region (the region inbetween the viscous sublayer and the fully turbulent layer) where both the effects of molecular viscosity and that of turbulence are equally important.
- The fully-turbulent layer (the outer layer) where turbulence plays a major role.

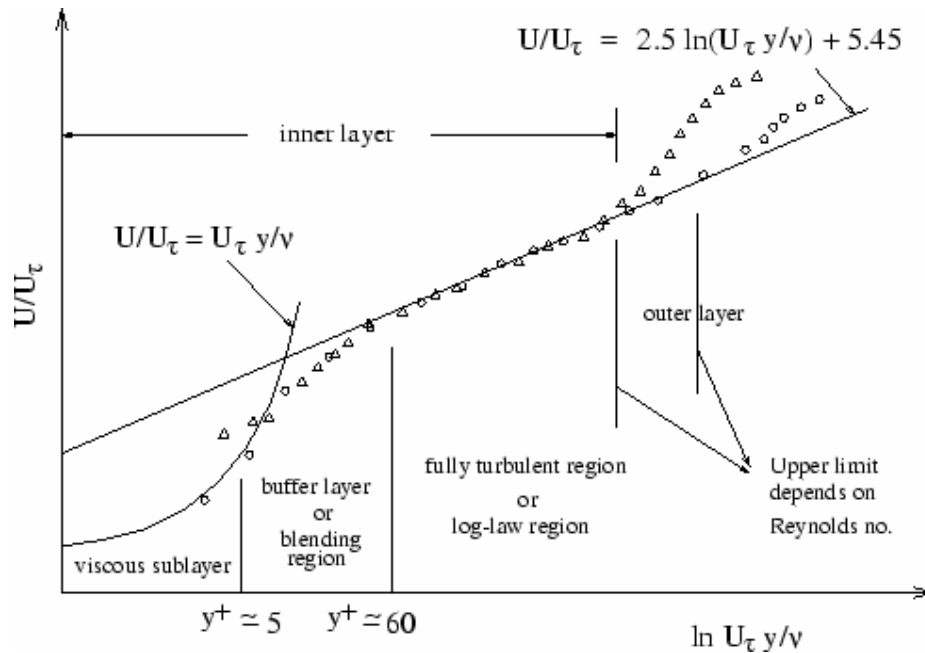


Figure 7.2: The near-wall regions of turbulent flows (Fluent Inc, 2003)

In order to resolve the velocity gradient and better predict the flow behaviour in the near-wall region, a higher mesh density and special wall modelling procedures are therefore required. Two approaches are available when modelling the near wall region: the wall function method and the near-wall modelling method.

7.6.1 Wall functions

Wall functions are a collection of semi-empirical formulas and functions that are used to “bridge” the solution variables at the near-wall cells and the corresponding quantities on the wall. The wall functions comprise of laws-of-the-wall for mean velocity (or other scalars) and formulas for near-wall turbulent quantities. Hence the viscosity-affected inner region, i.e. the viscous sublayer and buffer layer, is not resolved.

In high-Reynolds-number flows where there is no need to resolve the viscosity-affected near-wall region, in which the solution variables change most rapidly, the wall function approach saves on computational resources. The wall function approach has become popular as a practical option for the near-wall treatments for industrial flow simulations because it is economical, robust, and reasonably accurate.

FLUENT offers two choices of wall function approaches: standard wall functions and non-equilibrium wall functions

7.6.1.1 Standard wall functions

The assumption of the standard wall function is that the production and dissipation rate of turbulent kinetic energy is assumed to be equal in the cells adjacent to the wall. The standard wall functions are based on the log-law of the wall of Launder and Spalding (1974) whereby in the turbulent region, the velocity of the flow is expressed as a logarithmic function of the distance from the wall as:

$$U^+ = \frac{1}{\kappa} \ln(Ey^+) \quad 30 < y^+ < 60 \quad (\text{Eq. 7.22})$$

where U^+ = non-dimensionalised mean velocity = u/u_τ

where u = velocity tangent to wall at a distance y from wall

u_τ = friction velocity = τ_w/ρ

where τ_w = wall shear stress

ρ = fluid density

y^+ = non-dimensionalised distance from wall = $\frac{\rho y u_\tau}{\mu}$

where y = normal distance from wall

μ = dynamic viscosity of fluid

κ = von Kármán constant = 0.42

E = empirical constant = 9.793

The logarithmic law for mean velocity is known to be valid for $30 < y^+ < 60$. This is extended in FLUENT so the log-law can be employed for $y^+ > 11.225$.

For $y^+ < 11.225$, the laminar stress-strain relationship is applied so that

$$U^+ = y^+ \quad y^+ < 11.225 \quad (\text{Eq. 7.23})$$

Fluent documentation reports reasonably accurate predictions for the majority of high-Reynolds-number, wall-bounded flows with the standard wall functions and FLUENT therefore provides the standard wall functions as a default option. The standard wall functions however become less reliable in boundary layer separation flows when the near-wall flows are subjected to severe pressure gradients, or when the flows are in strong non-equilibrium and require the implementation of the Non-Equilibrium Wall Functions.

7.6.1.2 Non-equilibrium wall functions

The Non-Equilibrium Wall Functions is a two-layer-based wall function, whereby Launder and Spalding's log-law for mean velocity is sensitized to pressure-gradient effects and the production and dissipation of turbulent kinetic energy in the cells adjacent to the wall are computed. These are assumed to consist of a viscous sublayer and a fully turbulent layer so that the turbulence kinetic energy production and dissipation in those cells sensitised to the proportions of the viscous sublayer and the fully turbulent layer, which varies widely from cell to cell in highly non-equilibrium flows. The non-equilibrium wall function therefore improves on the local kinetic energy equilibrium assumption of the standard wall function. The non-equilibrium wall functions are therefore recommended in FLUENT documentation for use in complex flows involving separation, reattachment, and impingement where the mean flow and turbulence are subjected to severe pressure gradients and change rapidly.

7.6.2 Near-wall modelling

In the near wall modelling approach, the turbulence models are modified to enable the viscosity-affected region to be resolved with a refined mesh all the way to the wall, including the viscous sublayer.

However, the wall function approach becomes less reliable for:

- Pervasive low-Reynolds-number or near-wall effects (e.g., flow through a small gap or highly viscous, low-velocity fluid flow)
- Massive transpiration through the wall (blowing/suction)
- Severe pressure gradients leading to boundary layer separations
- Strong body forces (e.g., flow near rotating disks, buoyancy-driven flows)
- High three-dimensionality in the near-wall region (e.g., Ekman spiral flow, strongly skewed 3D boundary layers)

The near-wall modelling method provided by FLUENT is the enhanced wall treatment.

7.6.2.1 Enhanced wall treatment

In order to resolve the laminar sublayer, the near-wall mesh must be very fine, typically $y^+ \approx 1$. This imposes too large a computational requirement. The enhanced wall treatment is a near-wall modelling method that combines a two-layer model with enhanced wall function to overcome this problem. Hence turbulence dissipation energy and the turbulent viscosity in the near-wall cells are completely resolved from the viscosity-affected near-wall region all the way to the viscous sublayer.

The two-layer approach divides the whole domain into a viscosity-affected region and a fully-turbulent region according to a wall-distance-based, turbulent Reynolds number, Re_y . For the fully-turbulent region, where $Re_y > 200$, the k- ϵ models or the RSM are adopted, while for the viscosity affected region, where $Re_y < 200$, a one-equation model is employed (Wolfstein, 1969).

The enhanced wall functions formulate the law-of-the wall as a single wall law for the entire wall region (i.e., laminar sublayer, buffer region, and fully-turbulent outer region) by blending the linear (laminar) and the logarithmic (turbulent) laws-of-the-wall. This approach allows the fully turbulent law to be easily modified and extended to take into account other effects such as pressure gradients or variable properties. This approach also guarantees the correct asymptotic behaviour for large and small values of y^+ and reasonable representation of velocity profiles in the cases where y^+ falls inside the wall buffer region ($3 < y^+ < 10$).

7.7 MODEL FORMULATION FOR CFD

7.7.1 CFD software package

At the beginning of the research project the commercial computational fluid dynamics software CFX version 5.6 was initially used. A change to FLUENT version 6.2.16 was however required since the non-conformal geometrical boundaries that exist between the swirl and circular pipe intersections could not be modelled using the CFX code. Internal walls were being created when a structured multi-block technique was being attempted for meshing purposes.

FLUENT version 6.2.16 was therefore used to simulate the flow. The FLUENT package includes a pre-processor for geometry modelling and mesh generation, GAMBIT, and the solver itself, FLUENT. The following were considered in deciding the type of CFD software to be used: availability of turbulence models, mesh type (structured or unstructured), speed of solution, user friendliness, user support and users with similar flow problems.

FLUENT is written in the C computer language and uses a client/server architecture, which allows it to run as separate simultaneous processes on client desktop workstations and powerful compute servers. It was run on a 2GHz dual processor with Windows 2000 operating system.

FLUENT v. 6.2.16 is a general purpose 3D finite volume CFD code which solves RANS equations on 2D triangular/quadrilateral, 3D tetrahedral/hexahedral/pyramid/wedge, and mixed (hybrid) meshes. Various discretisation schemes, solution algorithms and turbulence models are supported by FLUENT v. 6.2.16, some of which have been described in sections 7.3, 7.5 and 7.6.

7.7.2 Construction of pipe geometry

The geometry of the pipe system was created in GAMBIT version 2.1.6. The model aims to be as true to the experimental rig as possible. However, modelling the whole rig would be computationally intensive. Hence only the bottom half of the rig was modelled, i.e. the conical inlet, the feeder section, the developmental pipe section, the

swirl pipe or the control pipe, the visualisation pipe, the horizontal-to-vertical bend and the first vertical section, as shown in Figure 7.3. The horizontal to vertical and the vertical section were also modelled so as to recreate the influence that the bend may have upstream and to prevent the influence of exit losses within the visualisation pipe section.

Two model geometries were created, one with the swirl pipe section and the other with the control pipe section.

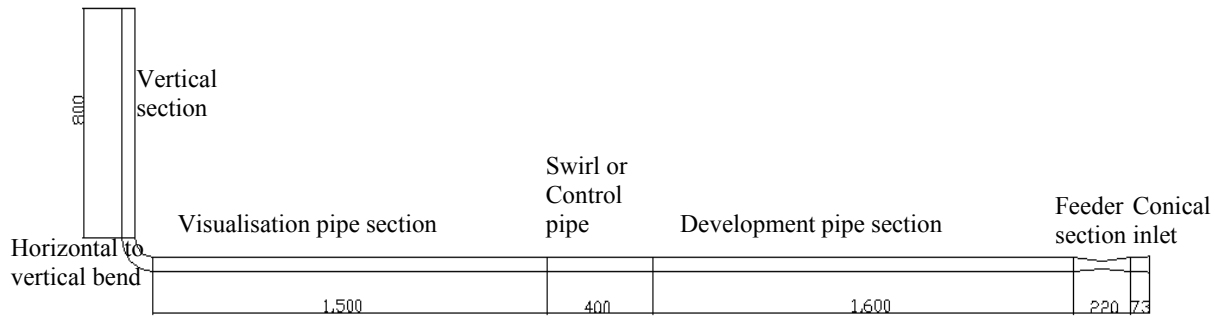


Figure 7.3: Dimensions of computational model geometry (units = mm)

The circular pipes were created in the positive x-axis using the “create real cylinder option” available in GAMBIT. The radius was specified as 25 mm and the height as 1600, 400, 1500 and 800 mm for the development, control, visualisation and vertical sections respectively. The individual cylinders were then moved and the adjacent volumes connected together. The conical inlet was constructed by joining a 60 mm long cylinder to a frustum of length 13 mm and a first and second radius of 32 and 25 mm respectively. The feeder section was geometrically simplified as two conical frustums, to represent the venturi, joined by a cylinder to represent the region where the particles are fed. The bend was constructed by rotating the face of the visualisation pipe outlet by 90° about a point located at 95 mm above the centre of the face of the visualisation pipe outlet. Unlike any other components of the rig geometry, the swirl pipe creation employed a bottom up approach involving the following steps:

- A circular face of radius 19.53 mm was created in the yz-plane
- The circular face was moved so that it was offset by (0, 0, 11.28)

- The circular face was then copied and rotated twice through 120° about the origin and the x-axis
- The three resulting overlapping circular faces were then united into a single face, giving the three-lobed shaped face.
- The three-lobed shaped face was then rotated about the x-axis with a twist of 480° over a distance of 400 mm.

The resulting final rig model in Figure 7.4 is shown and. the individual rig components in Figure 7.5



Figure 7.4: Complete model geometry

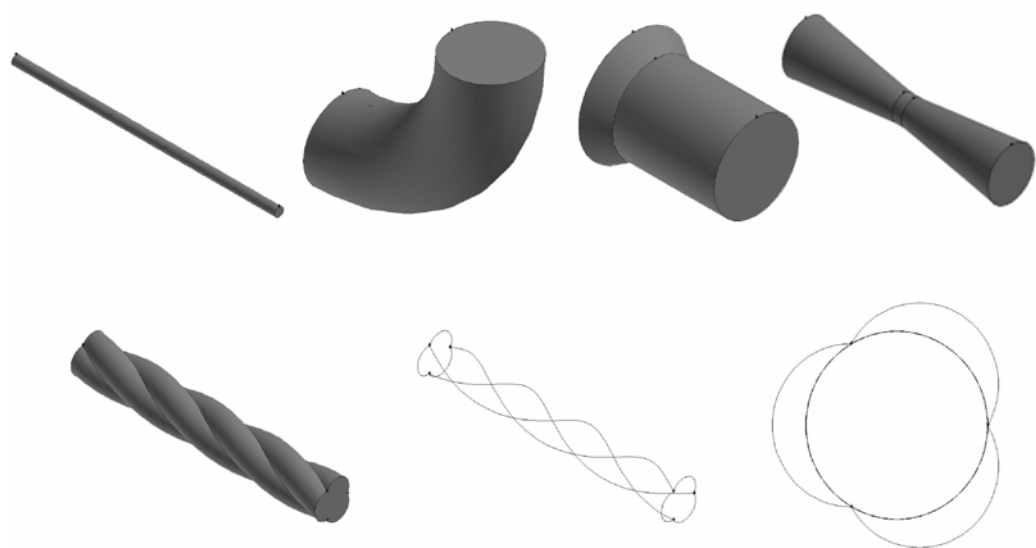


Figure 7.5: Geometries of rig components

7.7.3 Mesh generation

A volume grid inside the flow domain needs to be created and the surfaces of all the boundaries need discretised before the governing equations can be numerically solved. This as discussed in section 7.3.2.1 is known as spatial discretisation and is carried out by a process known as meshing. The way the mesh is built is generally influenced by the geometry of the domain and the positions of the critical regions of the flow are, i.e. where the gradients in space of the flow are high. A large number of points are required within the mesh at these locations to describe the variation accurately.

The mesh is made up of node points that form cell volumes or sometimes also called elements. 3D elements thus include: 4-noded tetrahedrons, 5-noded pyramids, 6-noded prisms (or wedges) and 8-noded hexahedrons. From these mesh elements, two types of mesh structures can be built:

- A regular structured grid where the node points are regularly arranged throughout a cuboid, which can be stretched to fit a particular geometry in a similar way to if the mesh was made of rubber. Hence the so-called topology, or form, of the mesh remains the same, with any point in the mesh still being connected to the same neighbouring points both before and after the stretching process. Due to this regular nature of the grid, knowledge of the location of a cell within the mesh enables the labels of the points at its corners to be found implicitly. These meshes are typically made up of hexahedrons and are called structured meshes as they have a well-defined structure.
- An irregular and unstructured grid where the node points are placed within the computational domain without having a regular topology. Hence the element to which any particular node is attached cannot be known. A numerical table must therefore exist for the irregular grid that describes the arrangement of the mesh by listing which nodes are attached to each element. A mesh with an irregular structure is often made up of tetrahedrons and is referred to as an unstructured mesh.
- Multi-block structured grid where the computational domain is subdivided into different blocks, which can be structurally meshed.

The implicit relationship that exists between the number of a node point or cell volume and the numbers of its neighbours in a structured mesh, forms the basis of one of the

main advantage of the structured grid as it enables data to be found easily, hence causing the solver program to run faster than if an unstructured mesh was used (Shaw, 1992). In addition the hexahedral elements associated with the structured mesh can be aligned with the flow, thereby minimising numerical diffusion. On the other hand, using an unstructured mesh significantly reduces the amount of time spent generating meshes as it is created by automatic mesh generation algorithms and can handle more complex geometries. However, the unstructured mesh requires more elements for refinement compared to a structured mesh on the same geometry, leading to higher computing cost. (Fluent Inc., 2003). The tetrahedral cells associated with unstructured mesh also tend to have a large aspect ratio, which affect the skewness of the cell, which can in turn impede the accuracy and convergence.

The multi-block structured mesh was introduced as a compromise between computing cost and flexibility. It is therefore more complicated to generate. It is more computer efficient than an unstructured mesh and yet provides ease of control in specifying refinement needed along certain surfaces or walls, especially for meshing around complex geometries.

7.7.3.1 Boundary layer mesh

A region of fine mesh, called the boundary layer mesh, was also included along the solid wall surfaces to numerically model the rapid velocity variation through the boundary layer. The boundary layer meshes for the swirl pipe and the circular pipes were created with similar specifications using the Uniform algorithm provided in GAMBIT version 2.1.6. This implied that all the first row boundary layer elements were equal to each other. The boundary layer was made up of five rows of equal number of cells, the first layer being 0.4 mm deep. With a growth factor of 1.2 (i.e. each row of the boundary layer mesh is 20% thicker than the previous one), the total depth of the boundary layer was 2.98 mm. The only difference between the boundary layer mesh of the circular and the swirl sections was that the boundary layer mesh for the swirl section required the use of a wedge-shaped boundary layer region around the connecting vertices of the three lobes. The resulting boundary layers for the circular and swirl sections are shown in Figure 7.6.

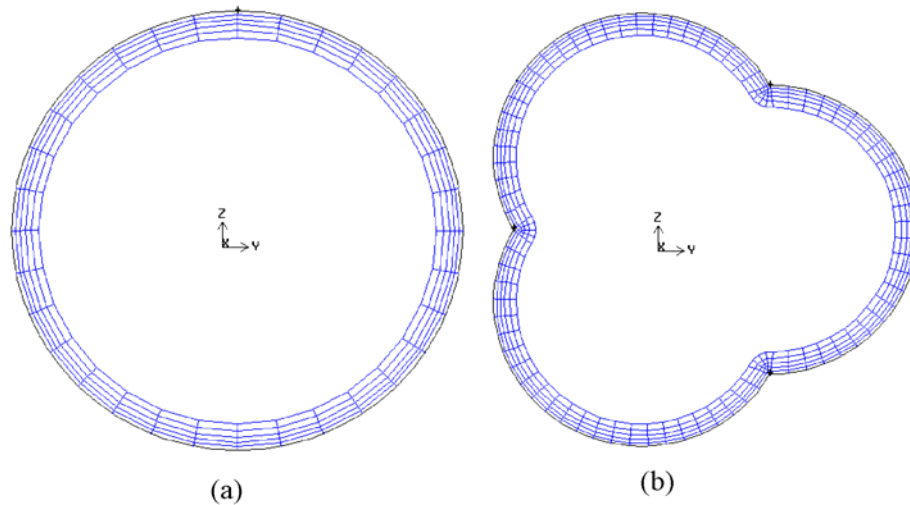


Figure 7.6: Boundary layer mesh for the (a) circular cross-section rig components and (b) swirl pipe

The mesh used in the current work was based on the unstructured hexahedral mesh system using the commercial mesh generation package GAMBIT version 2.1.6. The rig was subdivided into four volumes: the development pipe section (including the conical inlet), the swirl pipe, the visualisation section and the vertical section (including the horizontal to vertical bend). This was done so that the mesh density in each block could be controlled in a way that a denser mesh was required in the swirl and visualisation sections, while a leaner mesh was required in the vertical section. This allowed the computational resources to be concentrated on the regions of interest.

7.7.3.2 Face and volume meshing

The distribution of mesh points for all circular cross-sections were the same throughout the volumes with a circular cross sections (i.e. the conical inlet, the development, visualisation, bend and vertical pipe sections). It was achieved by creating an unstructured grid of quadrilateral mesh elements on the inlet face of the conical inlet using the “Pave” algorithm in GAMBIT v. 2.1.6. This 2D mesh was then smoothed using the “Centroid Area” algorithm to equalise the surface areas of adjacent elements. The resulting 2D mesh is shown in Figure 7.7.

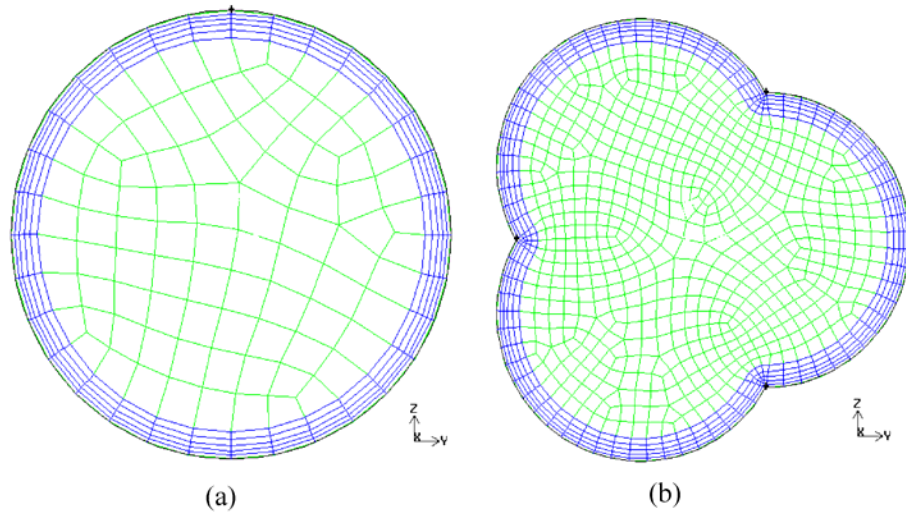


Figure 7.7: 2D unstructured mesh for (a) circular cross-section rig components (b) swirl pipe

The volume mesh for the conical inlet was then created by sweeping the mesh node patterns of this smoothed 2D mesh from the inlet face to the outlet face of the conical inlet. This was done using the “Cooper” algorithm so that hexahedral mesh elements would be created from the 2D quadrilateral mesh elements. The resulting 3D mesh is shown in Figure 7.8. The volume mesh for the development pipe section was then created by sweeping the face mesh at the outlet of the conical inlet to the outlet of the development pipe section. The process was carried out again for the other pipe sections.

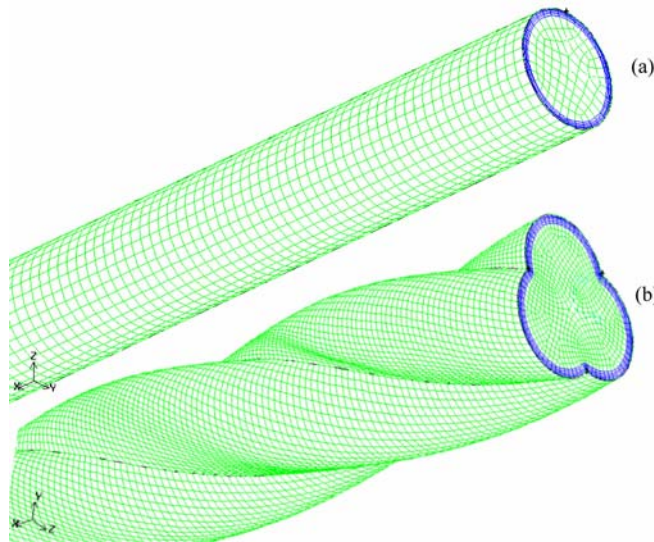


Figure 7.8: 3D hexahedral mesh for (a) circular cross-section rig components (b) swirl pipe

7.7.3.3 Mesh quality

The accuracy and robustness of the CFD solution is affected by mesh properties such as skewness (Fluent Inc., 2003). It is therefore required to check the quality of the mesh. Checks can be as simple as verifying that all of the elements in the mesh have positive area/volume or more complex and involving quality measures provided by GAMBIT. For hexahedral mesh elements, the EquiAngle Skew is included. This is a normalised measure of skewness defined as:

$$Q_{EAS} = \max \left\{ \frac{\varphi_{\max} - \varphi_{eq}}{180 - \varphi_{eq}}, \frac{\varphi_{eq} - \varphi_{\min}}{\varphi_{eq}} \right\} \quad (\text{Eq. 7.24})$$

Where

φ_{\max} and φ_{\min} are the maximum and minimum angles in degrees between the edges of the element

φ_{eq} is the characteristic angle corresponding to an equilateral cell of a similar form, so that for hexahedral elements, $\varphi_{eq} = 90^\circ$

Q_{EAS} therefore takes values ranging from 0 to 1, with 0 being a perfect (equilateral) elements and 1 being completely degenerate (poorly shaped) elements. Table 7.1 gives a breakdown of mesh quality with respect to Q_{EAS} .

QEAS range	Mesh Quality
$Q_{EAS} = 0$	Equilateral (perfect)
$0 < Q_{EAS} \leq 0.25$	Excellent
$0.25 \leq Q_{EAS} \leq 0.5$	Good
$0.5 \leq Q_{EAS} \leq 0.75$	Fair
$0.75 \leq Q_{EAS} \leq 0.9$	Poor
$0.9 \leq Q_{EAS} < 1$	Very poor (sliver)
$Q_{EAS} = 1$	Degenerate

Table 7.1: Breakdown of mesh quality with respect to Q_{EAS}

Table 7.1 reports the volume meshing algorithm, the elements type, the interval size of the elements, the resulting number of elements and the quality of the mesh. The

interval size determines how far away the mesh nodes are to be spaced out when the 2D face mesh is swept during volume mesh creation. Hence the smaller interval size of 2.5 generates a denser mesh for the swirl pipe and the visualisation pipe. All rig components successfully passed the mesh quality test.

Mesh Analysis	Conical Inlet	Feeder section	Dev. Pipe	Swirl Pipe	Vis. Pipe	Bend	Vertical pipe
Volume meshing algorithm	Cooper	Cooper	Cooper	Cooper	Cooper	Cooper	Cooper
Elements type	Hex	Hex	Hex	Hex	Hex	Hex	Hex
Interval size (mm)	5	5	5	2.5	2.5	5	5
No of elements	3486	11454	81174	179832	76194	5478	40089
% of cells within $0 < Q_{EAS} < 0.5$ range	99.96	100	100	98.88	100	100	100
Q_{EAS} maximum	0.52	0.49	0.48	0.71	0.48	0.48	0.48

Table 7.2: Mesh quality analysis

However, as can be seen in Figure 7.9, the volume mesh of swirl pipe is of a lower quality than that of the circular cross-section rig components. This was expected due to the higher curvature of the swirl pipe geometry.

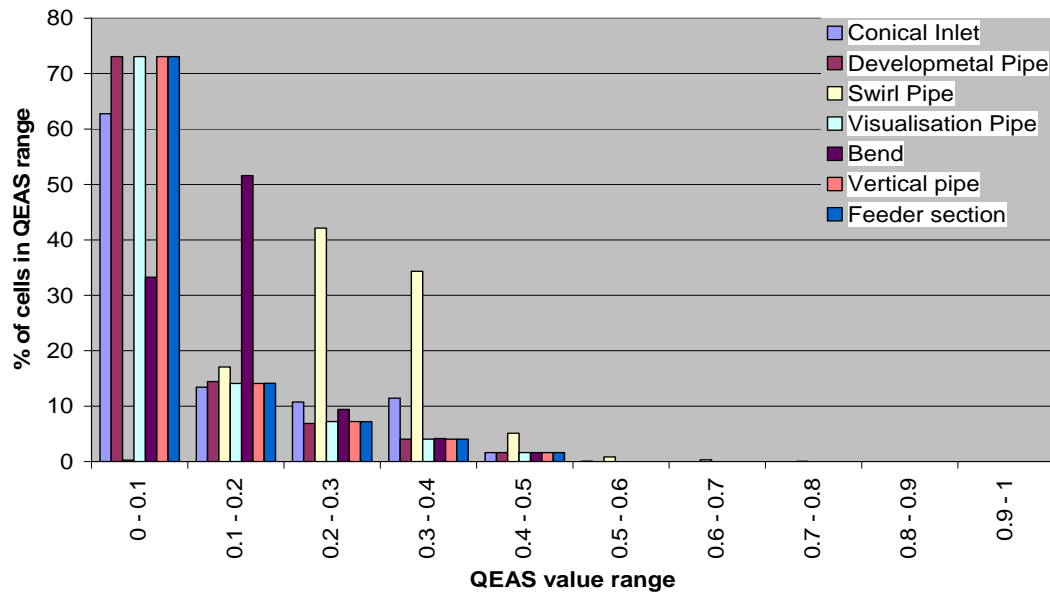


Figure 7.9: Q_{EAS} quality for the different rig components

7.7.3.4 Grid adaptation for y^+

Section 7.6 identified the importance of mesh size in the near wall region for successful modelling of the turbulent boundary layer. Hence it was necessary to make sure that the depth of the wall-adjacent cells fall within the distance over which the log-law is valid ($30 < y^+ < 60$). Table 7.3 reports the y^+ values for the different rig components when the $k-\epsilon$ turbulence model is used and Figure 7.10 shows how y^+ varies over the whole rig.

Rig component	y^+ value range
Conical inlet	$26.8 \leq y^+ \leq 44.6$
Feeder section	$15.2 \leq y^+ \leq 44.4$
Development pipe section	$21.5 \leq y^+ \leq 31.6$
Swirl pipe	$8.4 \leq y^+ \leq 36.5$
Visualisation pipe	$20.8 \leq y^+ \leq 33.2$
Bend	$17.7 \leq y^+ \leq 35.3$
Vertical pipe	$16.1 \leq y^+ \leq 35.2$

Table 7.3: y^+ values for different rig components

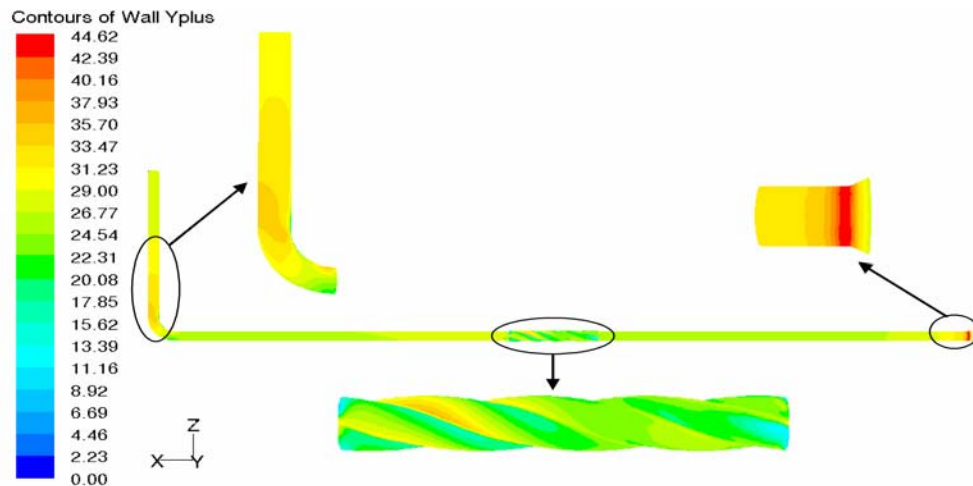


Figure 7.10: y^+ contours for rig model

Higher y^+ values are observed at the conical inlet and feeder section. This was seen as insignificant as the y^+ values were still within the acceptable range and the flow within the conical inlet was not subject of interest. As noted in section 7.6, FLUENT stretches the log-law so that it can to be employed for $11.225 < y^+ < 60$ and when $y^+ <$

11.225, the linear (laminar) law is employed. Hence the low y^+ values which occur in the swirl pipe are also insignificant.

7.7.3.5 Grid independence test

Grid independence means that the converged solution obtained from a CFD calculation is independent of the grid density. Increasing the number of cells in domain for a grid-independent model would not (ideally) change the flow-field solution and integrated quantities. In practice, grid independence is indicated when further mesh refinement yields only small, insignificant changes in the numerical solution.

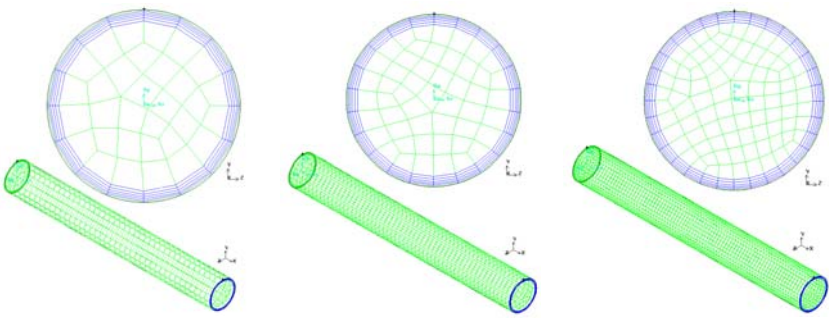
Earlier studies (Ganeshalingam 2002) have indicated that an interval size of 4mm between the cells may be sufficient for the swirl pipe. It would be very time-consuming to carry out grid independence tests for each case (or combinations of pipe) studied. Therefore grid-independence tests were carried out on 40 cm swirl and circular pipe section individually for $Re=1.5 \times 10^5$. All solver parameters, flow and boundary conditions were the same for each simulation case.

The grid independence tests consisted of refining the initial grid by approximately doubling the number of cells present in the initial grid. Hence a grid size of 4592 cells was refined to 8960 cells and again to 20418 cells for the circular pipe cross section. The swirl pipe required four mesh refining steps before a mesh independent solution was achieved with 179832 cells.

The values for static pressure and the average velocity in the x-direction (u-velocity) were used as monitoring parameters to judge grid independence. In addition, y^+ and Q_{EAS} values were also monitored to make sure they are within a reasonable range as discussed in sections 7.7.3.3 and 7.7.3.4. Table 7.4 and Table 7.5 present a summary of the results. The percentages shown are a comparison of the value to that obtained from the last refined grid.

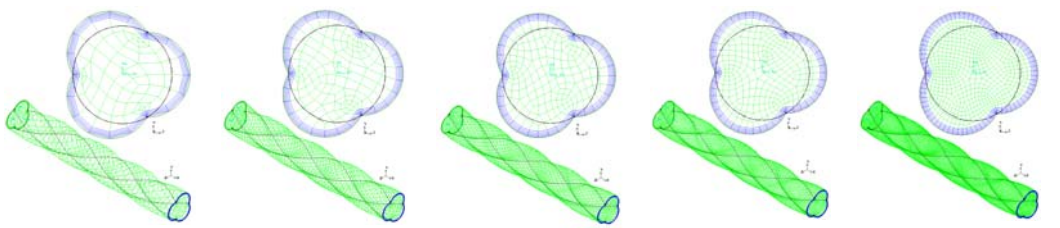
For the circular pipe, refined grid 2 was chosen as sufficiently grid independent since the difference in static pressure and u-velocity values between refined grid 1 and 2 were less than 1%. For the swirl pipe section, refined grid 4 was chosen as sufficiently grid independent despite the difference in static pressure values between refined grid 3

and 4 being just over 1%. That was because further mesh refinement took such a long time to mesh that it had to be abandoned.



	Initial grid	Refined grid 1	Refined grid 2
Total number of cells	4592	8960	20418
Static Pressure (Pa)	-114.37 (+5.62%)	-108.28 (+0.01%)	-108.27 (basis)
u-velocity (m/s)	42.66 (+1.23%)	42.15 (+0.72%)	41.84 (basis)
y^+	28.74	28.68	28.62
% of cells with $Q_{EAS} < 0.4$	99.11	98.75	98.40

Table 7.4: Mesh independence results for circular pipe



	Initial grid	Refined grid 1	Refined grid 2	Refined grid 3	Refined grid 4
Total number of cells	9196	19593	35112	64900	179832
Static Pressure (Pa)	-227.15 (+10.70%)	-202.84 (+4.28%)	-194.15 (+1.82%)	-190.61 (+1.39%)	-187.96 (basis)
u-velocity (m/s)	34.46 (+2.18%)	33.71 (+0.61%)	33.51 (+0.42%)	33.37 (+0.33%)	33.26 (basis)
y^+	67.77	24.47	25.27	25.52	27.15
% of cells with $Q_{EAS} < 0.4$	40.29	77.05	84.07	90.15	93.96

Table 7.5: Mesh independence results for swirl pipe

7.7.4 Solution methodology

7.7.4.1 Enabling assumptions

In order to solve any flow numerically, some assumptions must be made about the flow to simplify it. For a baseline model, the assumptions are as follows:

- The flow is isothermal
- The flow is incompressible
- The flow is steady
- The flow sticks to the wall which is stationary
- The pipe walls are hydraulically smooth
- Effects of molecular viscosity are negligible

Initial simulations were carried out with single-phase flow (air only) to provide a starting solution or baseline with which to compare different turbulence models and solver parameters. Moreover since the PIV and LDA experiments were carried out using air only, the CFD simulation cases also had to be single-phase flows (air only) for validation purposes.

A fully multiphase Eulerian approach is necessary to model the particles in lean phase pneumatic flow. As explained in Chapter 3 this poses many challenges and potential problems. For this reason, it is believed that the general applicability of the solutions might be lost if complex two-phase situations were attempted from the start instead of air-only flow.

7.7.4.2 Solver parameters

The k- ϵ turbulence models was used to obtain a baseline solution which was then improved by employing the Reynolds Stress model. For the near wall treatment, the standard wall function was used to implement the wall boundary condition. To solve the governing equations, the finite-volume scheme based on the FLUENT code was employed and the SIMPLE method was applied for the pressure–velocity coupling. The segregated solver was used as recommended for incompressible flows. Moreover, for convection terms, standard pressure discretisation scheme was employed and

second-order central difference is used for viscous terms. The inlet air mass flowrate was 0.048 kg/s, corresponding to an inlet air velocity of 25 m/s. The following sections elaborate on the parametric study that was carried out for the different solver parameters and explain why the final solver parameters were chosen.

7.7.4.3 Turbulence model

Three identical cases were run, each employing different turbulence models: the k- ϵ model, the RNG k- ϵ model and the Reynolds Stress model.

Figure 7.1 shows the distribution of static pressure and velocity magnitude throughout the model. As can be seen, the main difference between the three models occur at a distance of 41 pipe diameters downstream of the inlet. This is the location of the outlet of the swirl pipe. This was expected due to the difference in how the models handle the turbulence generated by the swirl pipe. The RNG k- ϵ model gave the most conservative predictions followed by RSM and the k- ϵ model. The highest percentage difference in static pressure predictions (10%) laid between the k- ϵ and the RNG k- ϵ models, while the lowest percentage difference (5%) laid between the k- ϵ model and RSM. The time taken for the RNG k- ϵ model and the RSM solutions to converge were 87% and 150% more than that required by the k- ϵ model.

Based on this information and on the recommendations from section 4.6, it was decided to first use the k- ϵ model to obtain a baseline solution, which can then be improved by employing the Reynolds Stress model.

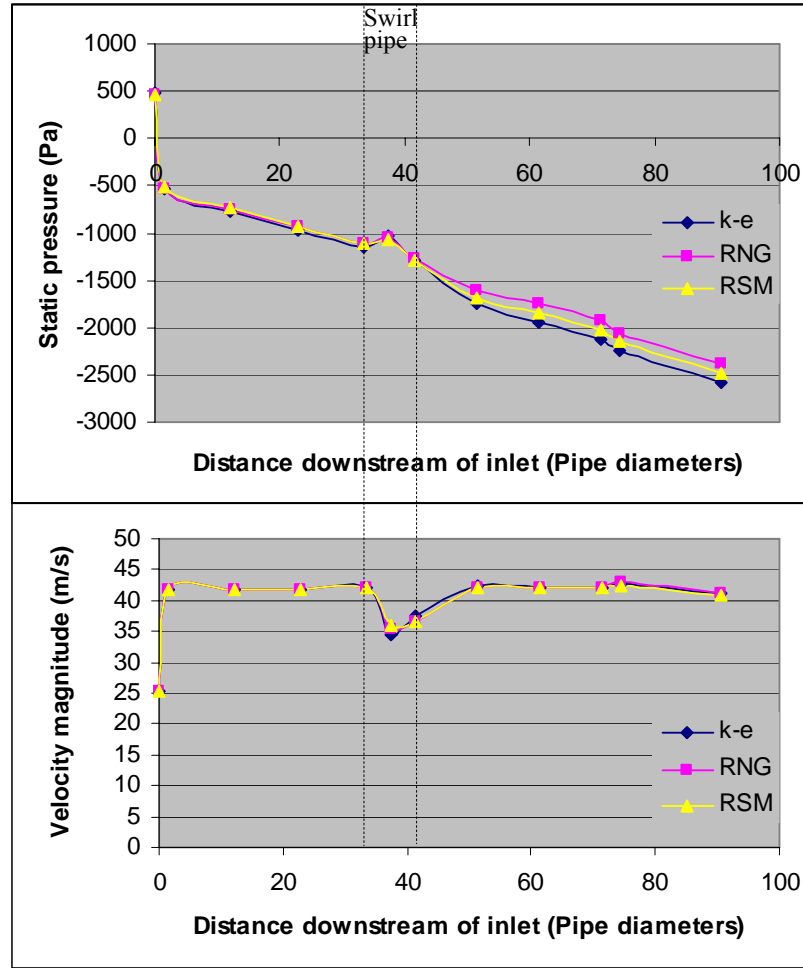


Figure 7.11: Performance monitors for turbulence models

7.7.4.4 Wall treatment

Two identical cases were run, one employing the standard wall function and the other the non-equilibrium wall function. As can be seen from Figure 7.12 showing the distribution of static pressure and velocity magnitude throughout the model, both wall functions produced very similar results. The maximum percentage difference between the two wall functions for static pressure and velocity magnitude parameters was only 0.9%. The standard wall function case also converged 1% faster than the non-equilibrium wall function case. Since no significant advantage resulted from using a non-equilibrium wall function, it was decided to employ the standard wall function.

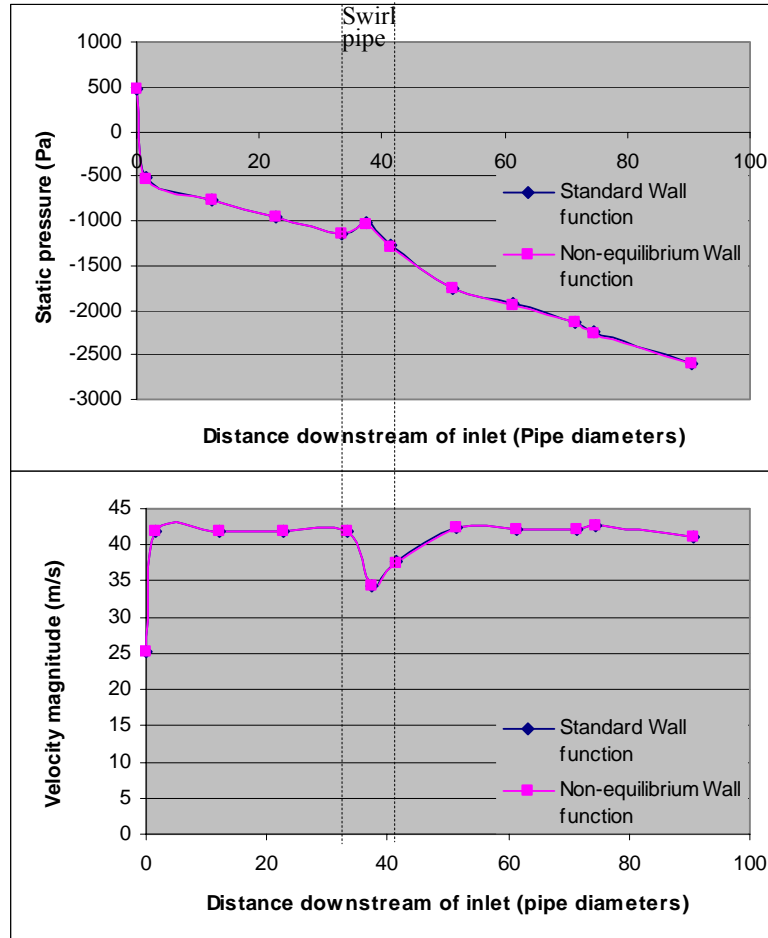


Figure 7.12: Performance monitors for wall functions

7.7.4.5 Advection scheme for viscous terms

Again three identical cases were run, each employing different advection schemes for viscous terms: First order upwind, Second order upwind and QUICK. The power law advection scheme was not tested since FLUENT documentation reported same accuracy as First order upwind advection scheme.

Figure 7.13 shows the distribution of static pressure and velocity magnitude throughout the model. No difference was observed in the prediction of the velocity magnitude. However, the second order upwind advection scheme yielded the most conservative prediction for static pressure throughout the domain, followed by QUICK and the first order upwind advection schemes. The highest percentage difference in static pressure predictions (22%) laid between the first and second order upwind advection schemes, while the lowest percentage difference (10%) laid between the

second order and QUICK upwind advection schemes. An extra 15% time was required for the solution to converge over that for the second order upwind advection scheme when QUICK upwind advection scheme was employed.

It was decided to use the second order upwind advection scheme as it provided a good compromise between conservative results and solution time. An initial first order solution was used still used as a starting solution for the second order simulations as recommended by FLUENT Documentation.

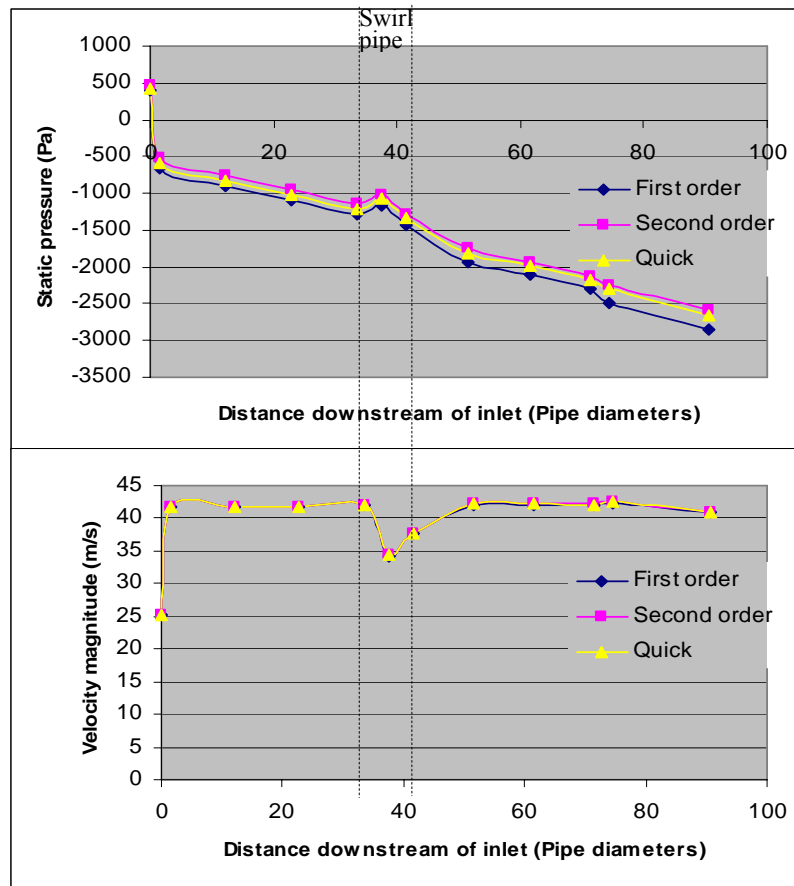


Figure 7.13: Performance monitors for viscous terms advection schemes

7.7.4.6 Pressure discretisation scheme

Two identical cases were run, one employing the standard pressure discretisation scheme and the other the PRESTO! discretisation scheme for pressure. It was found that for this particular case, the PRESTO! discretisation scheme for pressure was unstable and the solution did not converge.

It was therefore decided to employ the standard pressure discretisation scheme for future simulations.

7.7.4.7 Pressure-velocity coupling scheme

Both SIMPLE and SIMPLEC pressure-velocity coupling schemes were investigated by running two identical cases, but where one employs the SIMPLE pressure-velocity coupling scheme and the other the SIMPLEC pressure-velocity coupling scheme.

As can be seen from Figure 7.14 showing the distribution of static pressure and velocity magnitude throughout the model, both pressure-velocity coupling schemes produced almost identical results. The maximum percentage difference between the two pressure-velocity coupling schemes for static pressure and velocity magnitude parameters was only 0.04%. The SIMPLE pressure-velocity coupling schemes case also converged 15% faster than the SIMPLEC pressure-velocity coupling schemes case. Since no significant advantage resulted from using the SIMPLEC pressure-velocity coupling schemes, it was decided to employ the SIMPLE pressure-velocity coupling schemes.

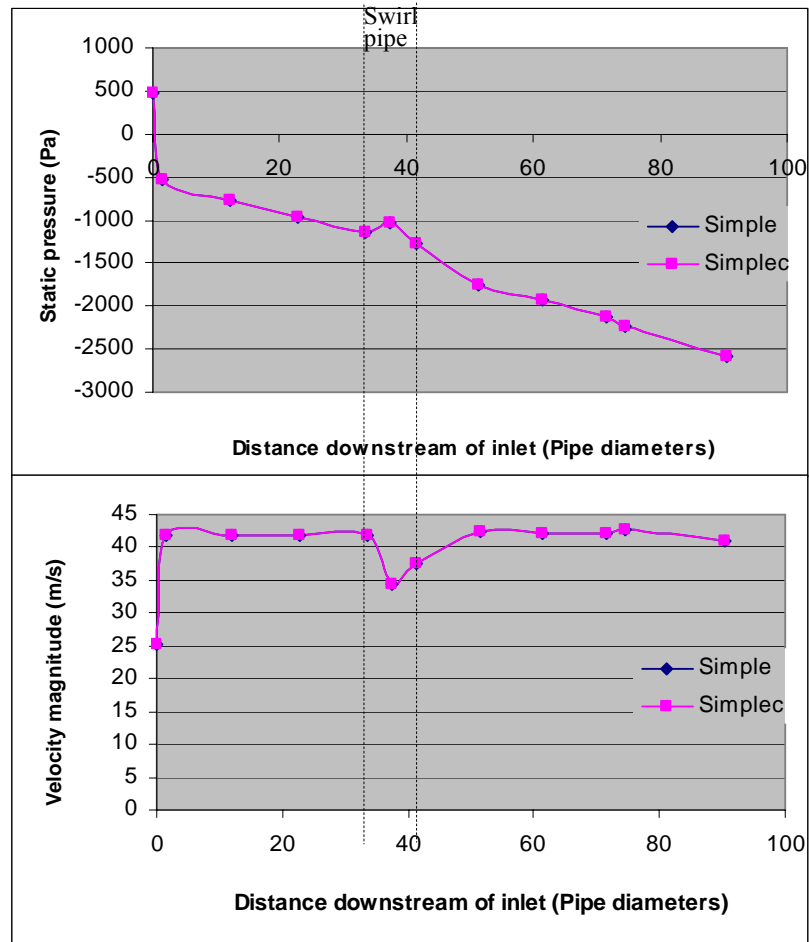


Figure 7.14: Performance monitors for pressure-velocity coupling schemes

7.7.5 Boundary conditions

7.7.5.1 Operating conditions

The operating conditions included specification of gravity acting along the negative y-axis at 9.81 ms^{-2} and the reference pressure location at the axis origin (also the centre point of the conical inlet). As recommended in FLUENT Documentation, the operating pressure was not specified as being atmospheric pressure, but instead as zero. This is to minimise errors due to the small pressure drop across the rig in relation to atmospheric pressure. Operating density was not specified, thereby allowing the solver to calculate it by averaging over all cells.

7.7.5.2 Inlet boundary conditions

The flow at the model inlet was specified using a mass flowrate approach into the conical inlet face. The direction of the flow was specified as being perpendicular to the inlet face and the initial gauge pressure was specified as zero. Three cases with the three flowrates identified in Chapter 6 were created as summarised in Table 7.6.

Case	Inlet mass flowrate (kg/s)	Reynolds number
Low	0.023	4.5×10^4
Medium	0.048	9×10^4
High	0.071	1.5×10^5

Table 7.6: Inlet boundary condition – mass flowrate

The turbulence was specified in terms of intensity and hydraulic diameter at the inlet. The turbulence intensity is defined as the ratio of the root-mean-square of the velocity fluctuations to the mean velocity. It was calculated from:

$$I = \frac{u'}{u_{average}} = 0.16(\text{Re})^{-\frac{1}{8}}$$

Therefore, for all three Reynolds numbers listed in Table 7.6, turbulence intensity is approximately 4%. The hydraulic diameter was taken to be the same as the pipe diameter, 0.05m.

7.7.5.3 Outlet boundary conditions

An outflow type boundary condition was imposed at the outlet of the rig model with a flow rate weighting of 1, indicating that all the flow through the domain has to come out of this outlet.

7.7.5.4 Wall boundary conditions

The pipe walls were specified as being stationary walls, with a no slip shear condition. Wall roughness, was modelled by specifying the roughness height, K_s , as 1.5×10^{-05} m. This value is so small that the walls may be considered to be hydraulically smooth.

7.7.5.5 Grid interface

It was necessary to define two grid interfaces due to the non-conformal boundaries at the intersection of the swirl and circular pipe geometries, as shown in Figure 7.15.

This ensured flow continuity between these geometries and that a wall was created to contain the flow where the interface zones do not overlap.

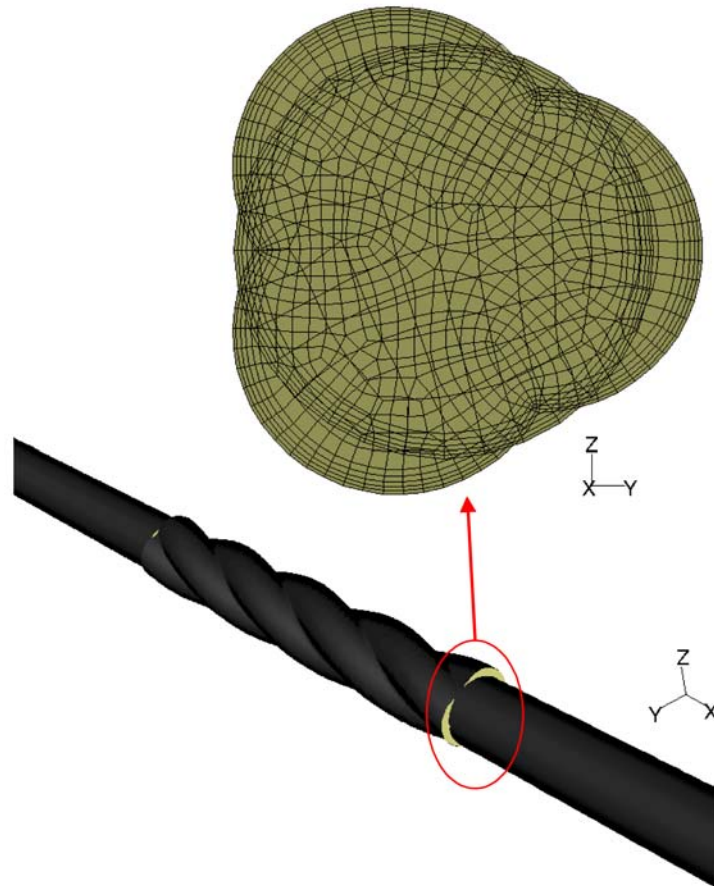


Figure 7.15: Non-conformal interface at swirl/circular intersection

7.7.6 Convergence

A solution is converged when all conservation equations are obeyed at all points to a specified tolerance (Fluent Inc., 2003). It is therefore important to monitor the convergence of the solution, as explained in Section 7.3.3.

The convergence criterion used for simulations was that the scaled residuals of x , y , z velocities and k and ϵ have decreased by four orders of magnitude and their residuals

are no longer changing with further iterations. It was also ensured that mass imbalance and outlet pressure no longer changed dramatically with more iterations. These criteria are illustrated and explained in the following sections.

7.7.6.1 Residual convergence

The residuals are the difference between the values of the solution field (velocity, pressure, continuity, turbulence, etc) for the preceding iteration and the current iteration.

At the end of each solver iteration, the residual sum for each of the conserved variables is computed and stored in Fluent, thus recording the convergence history. In an ideal case, a computer with infinite precision, would produce the residuals would converge to zero as a solution is reached. However, in a real case, with an actual computer, the residuals decay to some small value and then level out. Figure 7.15 shows the scaled residuals for a baseline case for the rig model.

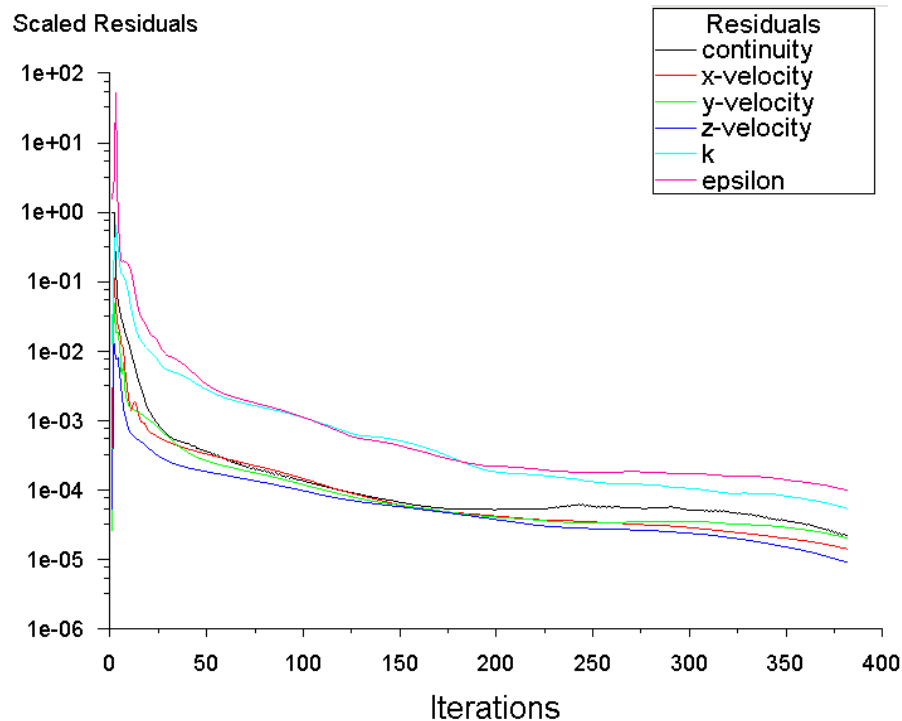


Figure 7.16: Scaled residuals for a baseline case for the rig model

7.7.6.2 Outlet pressure convergence

The outlet pressure convergence was checked as the solution proceeded as shown in Figure 7.17. The last 100 iterations were closely inspected as shown in Figure 7.18 to ensure that the pressure levelled out.

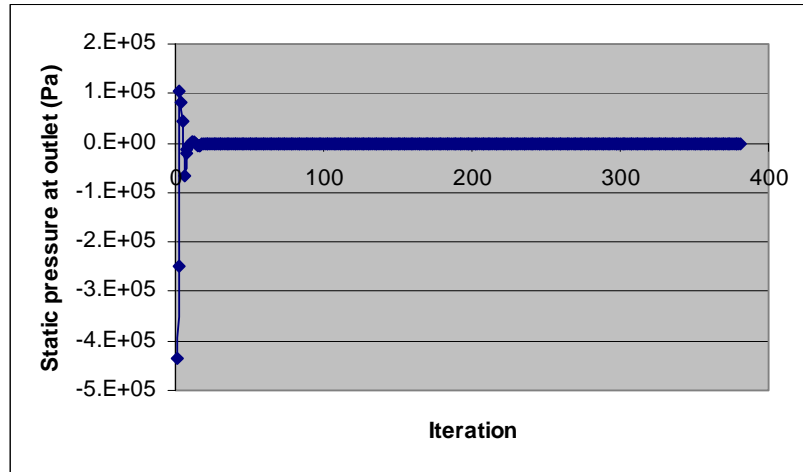


Figure 7.17: Variation of static pressure at inlet with iteration number for a baseline case

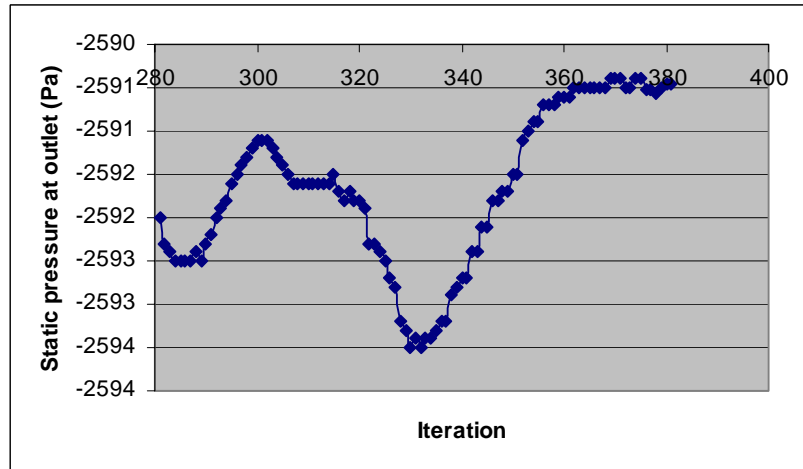


Figure 7.18: Variation of static pressure at inlet with iteration number for a baseline case (last 100 iterations)

7.7.6.3 Mass imbalance

The mass imbalance for all cells was of the order of 10^{-10} , as shown in Figure 7.19. In addition, the mass imbalance between the inlet and the outlet was monitored and it converges to zero, as expected. This is shown in Figure 7.20.

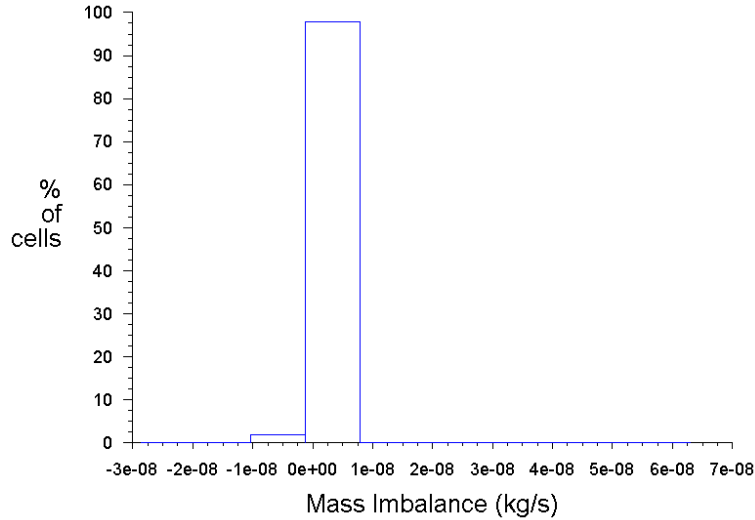


Figure 7.19: Histogram of mass imbalance for a baseline case

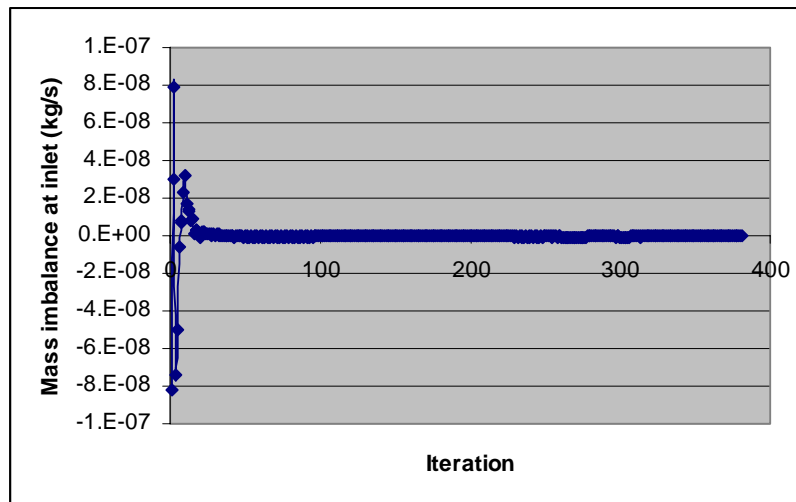


Figure 7.20: Variation of mass imbalance between the inlet and the outlet with iteration number for a baseline case

7.8 CONCLUSIONS

CFD was applied to simulate the flow conditions experienced in the experimental programme. This chapter introduced the principles underlying the technique. Discretisation of the flow, through special and equation discretisation were identified to be the enabling principles which make CFD possible. The various discretisation schemes were introduced and the need to monitor convergence of the solution was identified. The governing equations and three turbulence models, namely the $k-\varepsilon$, the

RNG k- ϵ and the Reynolds Stress models were described. The need for wall treatments in the near wall regions was highlighted and different wall functions were described.

In this study, the finite volume based scheme based on the FLUENT code version 6.2.16 was used to solve the governing equations. The geometry of the model was created in GAMBIT version 2.1.6. The model included a conical inlet, a feeder section, a developmental pipe section, a swirl or control pipe section, a visualisation pipe section, a horizontal to vertical bend, and a vertical section. Unstructured hexahedral mesh was used to grid the geometry and the region adjacent to the wall was refined using a denser mesh. The mesh was smoothed using smoothing algorithms available in FLUENT. The quality of the mesh was checked using a normalised measure of grid skewness. y^+ values were also checked to make sure that they lie within the log-law region. A grid independence test was also carried out to ensure that the final mesh was refined enough to show any rapid changes in the flow variables.

In order to simulate the flow, enabling assumptions had to be made. A baseline model was used for a parametric study of the solver parameters. From this parametric study, it was possible to determine that the k- ϵ turbulence models should be used to obtain a baseline solution. The Reynolds Stress model would then be used to improve the solution. The standard wall function would be implemented as the near wall treatment, the SIMPLE method would be applied for the pressure-velocity coupling. Moreover, for convection terms, standard pressure discretisation scheme would be employed and second-order central difference would be used for viscous terms. The operating conditions took into account the effects of gravity. Turbulence was specified in terms of intensity and hydraulic diameter. Three different mass flowrates were identified, based on the Reynolds number flows used for the experiments, as inlet conditions. An outflow type boundary condition was imposed at the outlet. The wall boundary condition was that of non-slip at the walls and a roughness height of 1.5×10^{-5} m. Grid interfaces also had to be applied due to the non-conformal boundaries at the intersection of the swirl and circular pipes.

This baseline CFD model can be employed to simulate the experimental flows as specified in Chapter 6. Once the accuracy of these models have been verified, their

use will be extended to obtain further information of the geometrically induced flow that was not possible to obtain from the experimental techniques employed in Chapter 6. This is addressed in the next chapter.

CHAPTER 8

CFD MODELLING VALIDATION AND FURTHER STUDIES PERFORMED USING THE VALIDATED CFD MODELS

8.1 INTRODUCTION

Experimental investigations can prove to be expensive, unsafe and limited by the existing available techniques. Computational Fluid Dynamics (CFD) simulations are being increasingly employed to overcome these limitations. It has to be acknowledged that assumptions need to be made to simplify the conditions that are to be modelled. These introduce approximation errors into the simulations. In an attempt to reduce the effect of such simplifications and approximations, the models first need to be verified and validated against experimental data to ensure their accuracy. They can then be used to investigate the effects of changing the experimental conditions.

CFD simulations were employed in this work to investigate the influence of the swirl pipe on the flow of air and on that of a lean phase pneumatic flow. The technique was valuable in this study since the presence of particles in the flow was limited by the main experimental method employed, Laser Doppler Anemometry (LDA). Instead, velocity data obtained from the LDA experimental work was used to validate the CFD models and confirm that the predicted behaviour of the flow was consistent with measurements made. The validated CFD models were then employed to study the influence of the swirl pipe on the lean phase pneumatic flow.

The first part of this chapter (sections 8.4 and 8.5) addresses the numerical validation of CFD models using static pressure and velocity data as validation parameters. The second part of the chapter (section 8.6) then presents the results obtained when the validated CFD model was used to further investigate the induced swirling flow.

Parameters used to this end include: static gauge and dynamic pressure variables, axial and tangential velocity variables, turbulence dissipation and turbulence kinetic energy

variables. The addition of particles into the flowfield is also addressed in the second part of this chapter.

8.2 VERIFICATION V/S VALIDATION

The fundamental strategy of verification and validation is the assessment of error and uncertainty in the computational simulation. The two main principles that are necessary for assessing credibility are validation and verification. Grace and Taghipour (2004) drew attention to the fact that improper use of the terms ‘verification’ and ‘validation’ are consistently being made in the literature, where they are being interchangeably used.

Verification is the process of determining if a computational simulation accurately represents the conceptual model; but no claim is made of the relationship of the simulation to the real world, i.e. verification does not address whether the model itself is a good representation of the physics of the problem at hand (Grace and Taghipour, 2004). Instead, verification starts with the concepts and the equations themselves and considers whether or not the numerical solutions are indeed accurate solutions of these. In essence verification provides evidence that the model is solved right as verification activities only evaluate whether the CFD model, the mathematical and computer code representation of the physical system are solved correctly and accurately (AIAA, 1998).

There are four predominant sources of error in CFD simulations:

- Insufficient spatial discretisation convergence
- Insufficient temporal discretisation convergence
- Lack of iterative convergence
- Computer programming

Verification hence addresses the issues of whether or not the numerical procedure that has been established is stable, consistent and robust, and where errors associated with

programming, spatial and temporal discretisation, convergence, iterative procedures and computer round-off are absent or fully resolved.

Grace and Taghipour (2004) acknowledge that it is only possible to prove that a numerical code contains errors, not that it is correct. From a practical point of view, the authors sums verification to involving the accumulation of a sufficient body of evidence, as in a legal case, to be able to accept, on the balance of probabilities, that the code does not contain errors. Such a body of evidence would include:

- a grid independence test
- the employment of second order accurate difference schemes
- an iterative convergence tolerance of four orders of magnitude of the actual values
- the employment of consistency checks – global checks on conservation of quantities such as mass imbalance.

On the other hand, validation is defined as “the process of determining the degree to which a model is an accurate representation of the real world from the perspective of the intended uses of the model”, hence whether the correct problem has been solved. The fundamental strategy of validation is the identification and quantification of error and uncertainty in the conceptual and computational models (AIAA, 1998). The method of measuring the accuracy of the representation of the real world is reported by AIAA (1998) to be achieved by systematically comparing CFD simulations with experimental data, while including the experimental uncertainty.

Grace and Taghipour (2004) reported the following as being the minimum testing process:

- The model has been applied to a broad spectrum of conditions and variables.
- Predictions have been compared with an extensive array of experimental data.
- The model and experimental results used in the comparison are independent of each other, i.e. that the experimental information has not been used for “calibration” of the model, e.g. to fit one or more constants or to fix boundary conditions, nor has the

set of experimental data been chosen as the one among some pool of data that provides the best fit.

- Differences between the model predictions and the experimental data have consistently satisfied pre-set tolerances or standards; for example, they consistently fall within the bounds of attributable experimental and numerical error at some predefined level of confidence.

8.3 THE CFD MODEL

As explained in Chapter 7, in order to keep computational cost and time reasonable, it was decided to only model the part of the rig which was crucial to the testing of the swirl pipe. Hence only the bottom half of the rig was modelled, i.e. the conical inlet, the developmental pipe section, the swirl pipe or the control pipe, the visualisation pipe, the horizontal-to-vertical bend and the first vertical section, as shown in Figure 8.1.

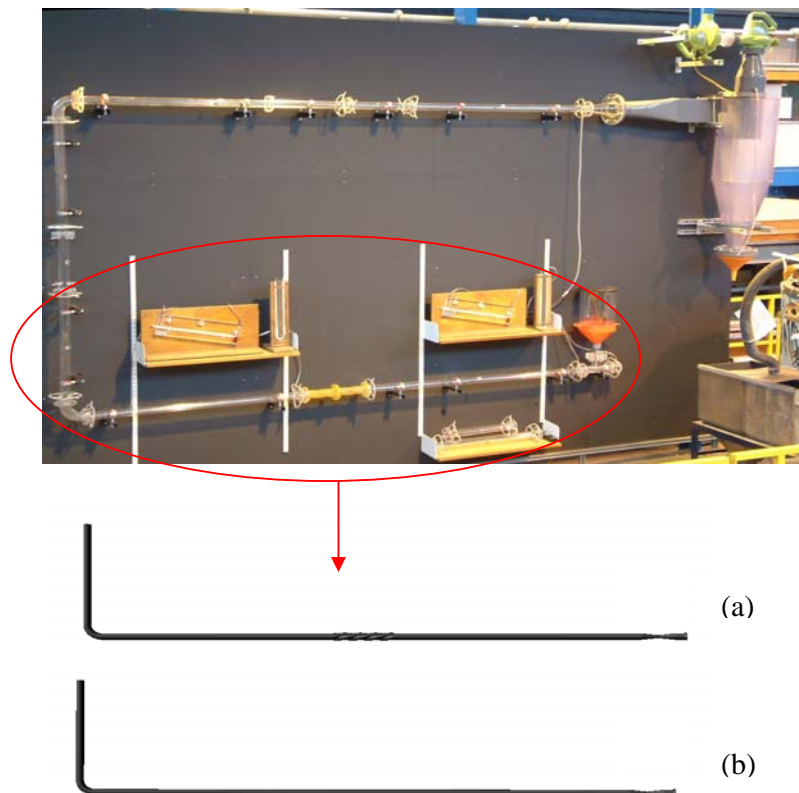


Figure 8.1: Rig model geometry

Six simulations were set up to account for the experimental conditions. The first set of three simulations were run with the circular control pipe section in place, as in Figure 8.1a, and the second set was run with the swirl pipe section in place, as in Figure 8.1b. Each set of simulations consisted of three simulations to account for the variation in the flow velocity at which the experiments were carried, as summarised in Table 8.1

Conditions at inlet			
	Mean air mass flowrate (kg/s)	Mean velocity (m/s)	Reynolds number
Low	0.024 ± 0.00169	10 ± 0.015	$4.5 \times 10^4 \pm 791$
Medium	0.047 ± 0.00086	20 ± 0.016	$9.0 \times 10^4 \pm 404$
High	0.071 ± 0.00057	30 ± 0.019	$1.4 \times 10^5 \pm 269$

Table 8.1: Inlet conditions for CFD models of low, medium and high Reynolds number flows

The experimental conditions were approximated using the following enabling assumptions and boundary conditions:

- The flow was assumed to be isothermal
- The flow was assumed to be incompressible
- The flow was assumed to be steady
- Effects of gravity was accounted for to act in the negative z-direction
- Single phase (air-only) simulations were carried out as flow seeding during the LDA experiments was considered not to affect the flow
- The pipe wall roughness was defined as 1.5×10^{-5} , which is effectively hydraulically smooth
- A non-slip boundary condition was imposed at the stationary walls, so that velocity at the wall is forced to be zero
- Air mass flowrates at inlet were specified as in Table 8.1 above.

The k- ϵ turbulence models was used to obtain an initial solution which was then improved by employing the Reynolds Stress model. The standard wall function was used to implement the wall boundary condition in the near-wall region. The

segregated solver was used. Standard pressure discretisation scheme was employed for convection terms and second-order central difference is used for viscous terms. Finally the SIMPLE scheme was employed for pressure–velocity coupling.

8.4 PRESSURE LOSS VALIDATION FOR AIR-ONLY FLOWS

The average value of the gauge static pressure for the planes located at 0.08, 6.7, 37.2, 46.7 and 71.2D downstream of the inlet (Figure 8.2) was obtained from the FLUENT simulation cases for the low, medium and high Reynolds number flows when both the swirl and control pipe sections were simulated. The 0.08D plane corresponds to the plane at which the physical pressure tapings are located on the conical inlet. Similarly, 6.7, 37.2, 46.7 and 71.2D correspond to the plane locations of the pressure tapings at the inlet and outlet of the physical developmental pipe section and the inlet and outlet of the physical visualisation pipe section respectively. The results are presented in the following sections.

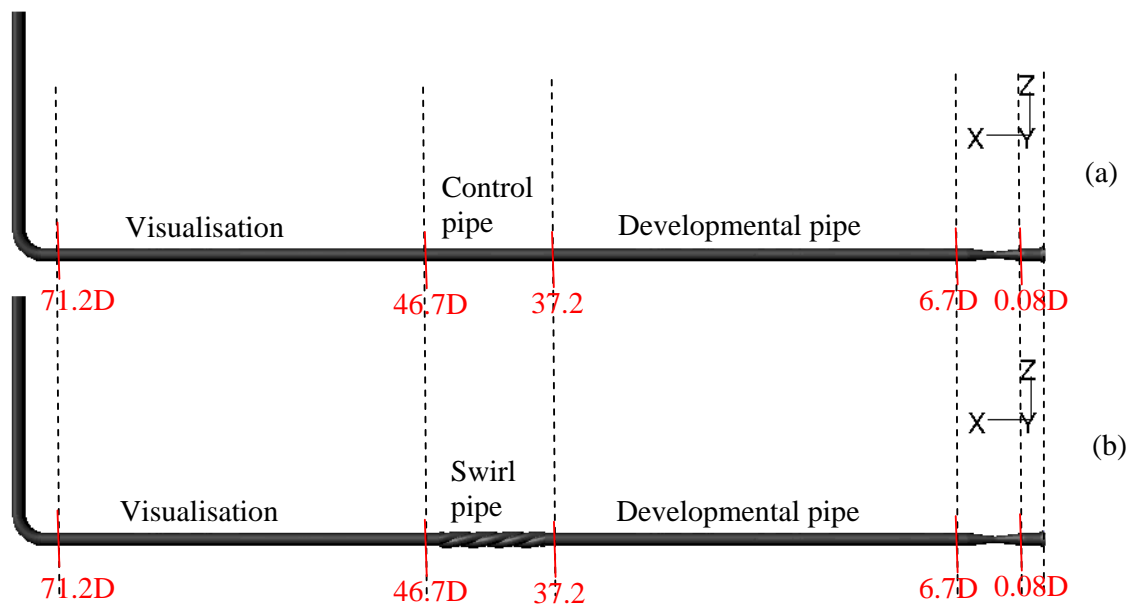


Figure 8.2: Pressure planes for rig model with (a) control pipe section; (b) swirl pipe section

8.4.1 Control pipe

With the control pipe section in place, the rig model was simplified to that of a straight horizontal circular pipe section between the feeder section and the horizontal to

vertical bend. The gauge static pressure was therefore expected to be steadily decreasing per unit length of pipe. This was precisely the results obtained from the computational models, as shown in Figure 8.3. The trend of the predicted results was similar to that obtained from experimental data. The average percentage difference between the predicted and experimental results was around 10%, as shown in Table 8.2. The reason for this difference is believed to be experimental shortcomings despite the precautions taken. These may include a dampening effect by the water in the U-tube manometer reducing the sensitivity of the instrument, air leakages at the tappings/rubber tubing, rubber tubing/plastic connector and rubber tubing/manometer linkages. During the experiments, fan fluctuations caused the manometer reading to fluctuate and the recorded reading was the average value over a short period of 30 seconds. The effect of these fluctuations could have been aggravated when experimental readings were taken consecutively from one pressure tapping to another. Unlike the experimental conditions, the CFD models assumed a steady flow and hence do not account for the observational fluctuations in static pressure. It is expected that this contributed to the difference observed in the measured and predicted gauge static pressure.

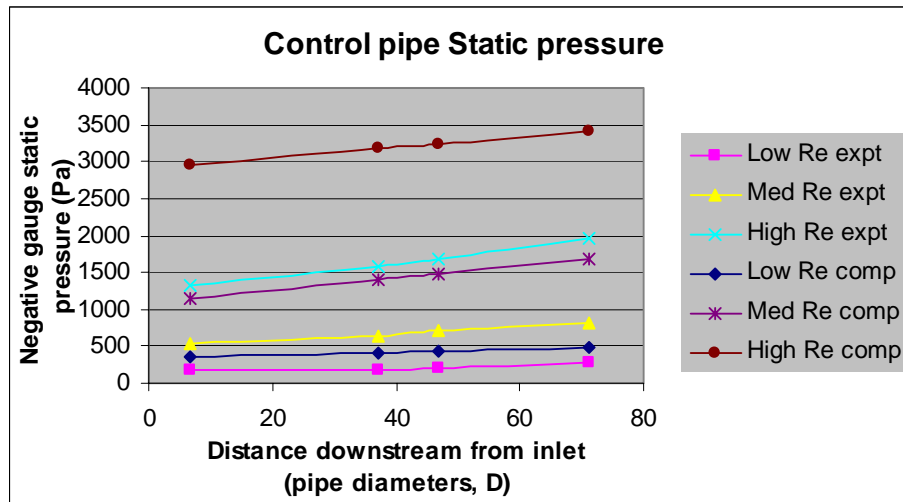


Figure 8.3: Gauge static pressure for the low, medium and high Reynolds number flow cases post control pipe section

Reynolds number flow	Average % difference between computational and experimental gauge static pressure
Low	9.40
Medium	14.79
High	7.97

Table 8.2: Percentage difference between computational and experimental gauge static pressure for low, medium and high Reynolds number flows post control pipe

8.4.2 Swirl pipe

Unlike the control pipe, a depression in the gauge static pressure was observed between planes 37.2D and 46.7D, i.e. within the swirl pipe. The surge in gauge static pressure was proportional to the Reynolds number of the flow, as shown in Figure 8.4.

In the case of the swirl pipe, the static gauge computational results were almost an exact match for the low Reynolds number flow, while that of the medium and high Reynolds number flow were over-predicted by an average of 19%, as shown in Table 8.3. The reasons for this disparity are believed to be the same as with the control pipe. These may include experimental shortcomings such as a dampening effect by the water in the U-tube manometer reducing the sensitivity of the instrument; air leakages at the tappings/rubber tubing, rubber tubing/plastic connector and rubber tubing/manometer linkages; the CFD model being steady-state while fluctuations in the flow was experienced, especially at high flowrates, due to the fan instability. Nonetheless, the predicted static pressure followed the same trend as that of the experimental static pressure.

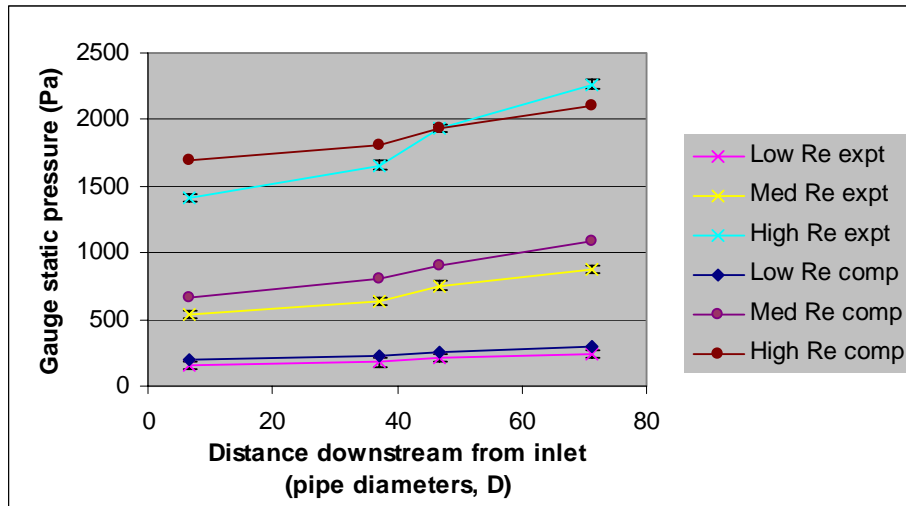


Figure 8.4: Gauge static pressure for the low, medium and high Reynolds number flow cases post swirl pipe section

Reynolds number flow	Average % difference between computational and experimental gauge static pressure
Low	19.02
Medium	18.83
High	4.34

Table 8.3: Percentage difference between computational and experimental gauge static pressure for low, medium and high Reynolds number flows post swirl pipe

8.5 LASER DOPPLER ANEMOMETRY (LDA) VELOCITY MEASUREMENT VALIDATION FOR AIR ONLY FLOWS

8.5.1 Control pipe validation results and discussion

Contours of axial velocity were plotted at locations of 2, 6, 10 and 16 pipe diameters downstream of the control pipe section to compare with those obtained from experimental investigations. The contours were uniformed, as the experimental ones, over a velocity range of 0 to 50 m/s to facilitate comparison. Figure 8.5 shows both the experimental and the computational results.

The computational results were exactly as expected: the Poiseuille flow velocity profile across the cross section of the pipe, with the central core lamina flowing at the

highest velocity and laminas of decreasing velocity further away from the centre until zero velocity is reached at the walls. The higher the Reynolds number of the flow, the higher was the central core velocity. The computational contours were almost circular in shape, showing a symmetrical flow within the pipe. Across the range of Reynolds number flows investigated, very little difference was observed between the contours at varying locations.

The two main differences between the contours obtained experimentally and those obtained computationally were that the computational contours were more circular in shape compared to the amorphous shapes of the experimental contours. This was due to a combination of:

- the computational contours being created from a very fine grid used in the computational models compared to the experimental contours being created from only 130 measurement points during the experimental study, and
- the steady state flow assumption in the computational models resulting in smooth averaged contours while pulsations to the flow were experienced while measuring instantaneous velocities and from one measurement coordinates to another.

The other difference was that the central core velocity was higher in all the computational contours compared to the experimental ones, especially for the high and medium Reynolds number flows.

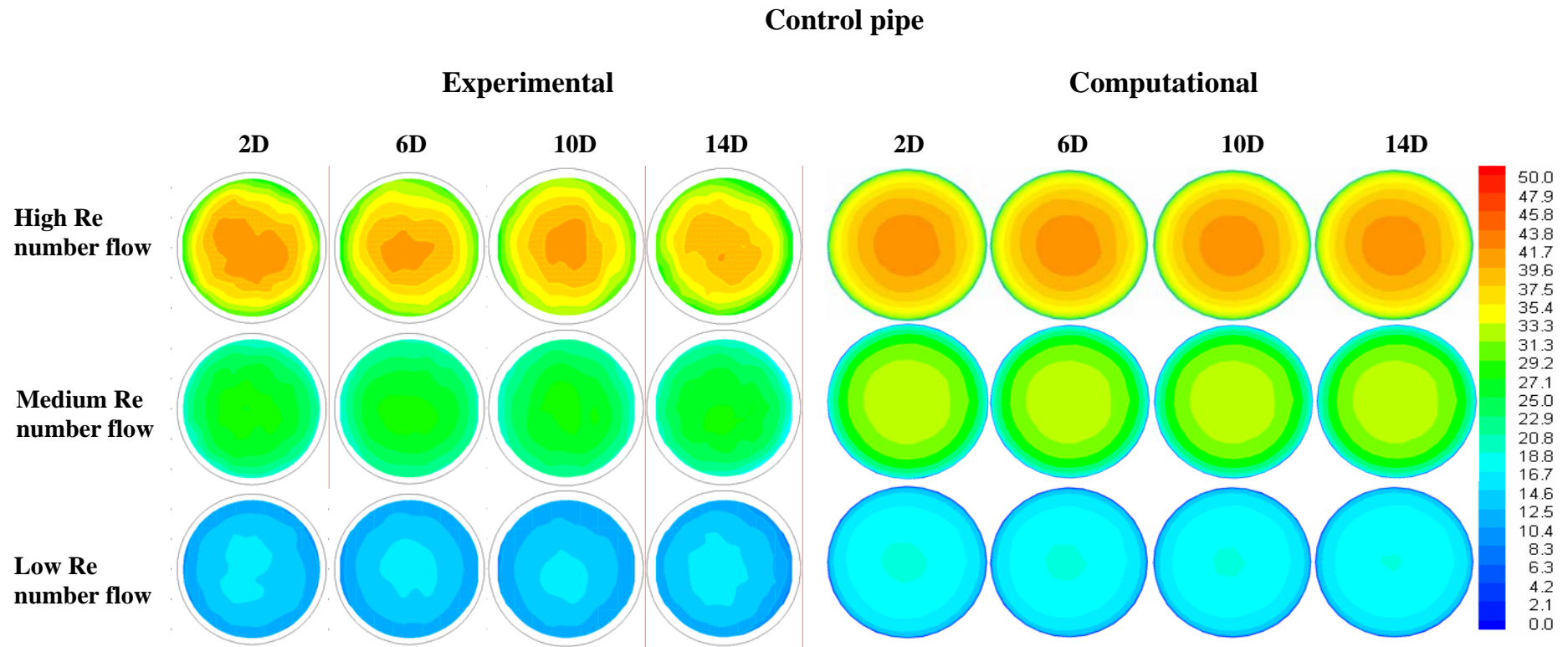


Figure 8.5: Comparison of axial air velocity contours from experimental and computational results (units = m/s)

The axial velocity at the coordinates of the measurement locations along the horizontal centreline were extracted at planes 2, 6, 10 and 14D downstream of the control pipe for all three Reynolds number flows to quantify this difference in core velocity between the computational models and the experimental observations. Figure 8.6(a) shows a plot of 14 computed axial velocities along the centreline of the pipe at a location of 2D downstream of the control pipe for flows of low, medium and high Reynolds number. Figure 8.6(b) shows a plot of the 14 computed axial velocities along the centreline of the pipe for the high Reynolds number flow at location of 2, 6, 10 and 14 pipe diameters downstream of the control pipe.

The axial velocity profile plots confirmed that the profiles did not vary with distance downstream of the control pipe. This can be attributed to the fact that the flow is fully developed at these distances from the inlet.

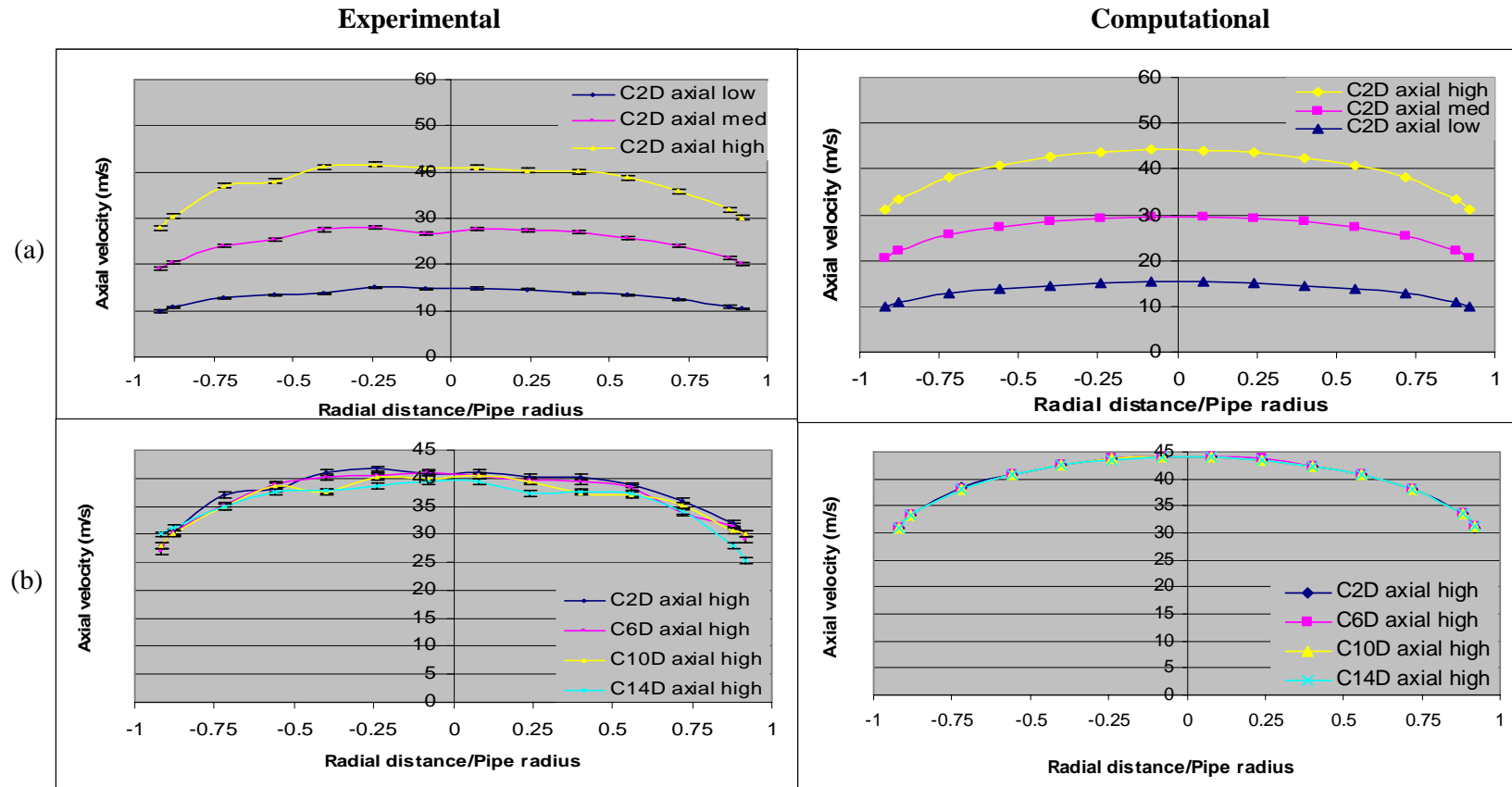


Figure 8.6: Computational horizontal centreline axial air velocity profiles post the control pipe

When comparing experimental results to simulation results (Figure 8.7), it was found that the axial velocity profiles for the low Reynolds number flows were an almost exact match, while the simulation over-predicted the axial velocities for the high and medium Reynolds number flows. Very good agreement was also obtained further downstream of the swirl pipe, as shown in Figure 8.8.

The average percentage difference between the experimental and computational axial velocity values for the three Reynolds number flows were calculated to be as follows:

Reynolds number flow	% difference between computational and experimental axial velocity values
High	5.95
Medium	5.62
Low	1.77

Table 8.4: Percentage difference between computational and experimental axial air velocity values for low, medium and high Reynolds number flows post control pipe

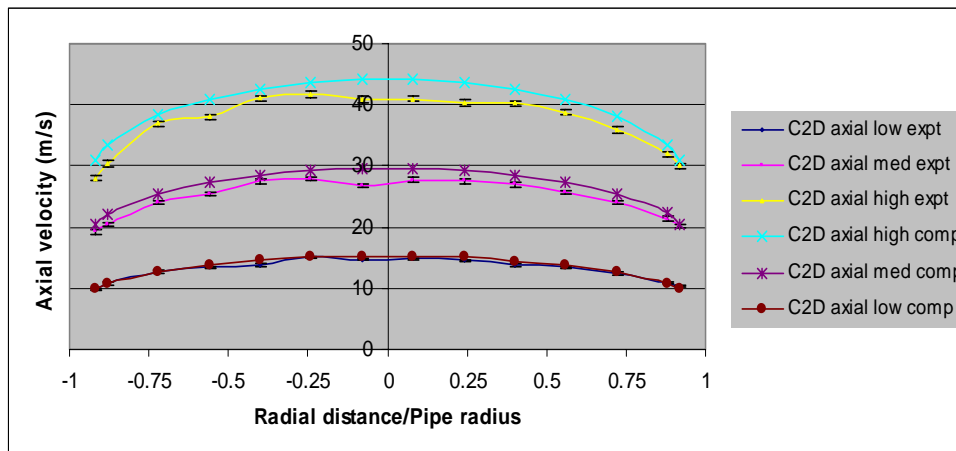


Figure 8.7: Comparison of horizontal centreline axial air velocity profiles post the control pipe section at plane 2D from experimental and computational results

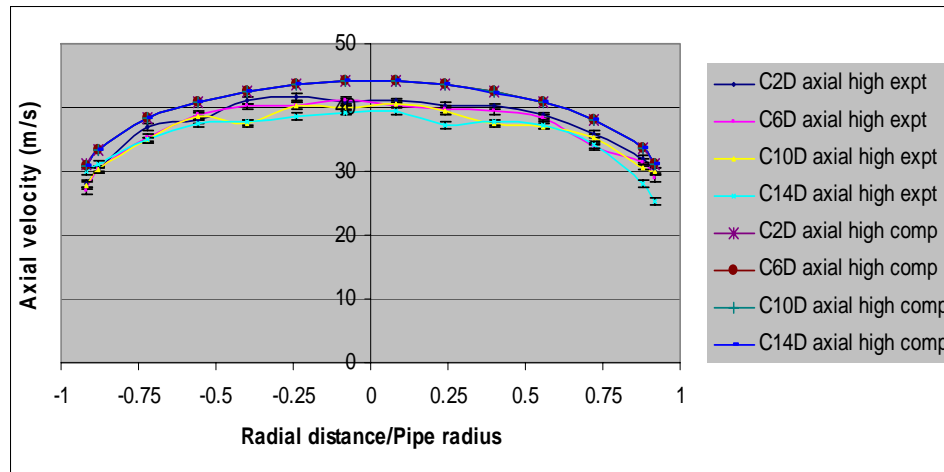


Figure 8.8: Comparison of horizontal centreline axial air velocity profiles post the control pipe section at planes 2,6,10 and 14D from experimental and computational results for the high Reynolds number flow

8.5.2 Swirl pipe validation results and discussion

Here again contours of axial velocity were plotted at locations of 2, 6, 10 and 16 pipe diameters downstream of the control pipe section and compared to those obtained from experimental investigations. The contours were represented on a common scale, over a velocity range of 0 to 50 m/s to facilitate comparison of the predicted computational and the measured experimental data. Figure 8.9 to Figure 8.12 shows a comparison of the experimental and the computational results.

The computational results showed higher central core velocities and laminas of decreasing velocity further away from the centre until zero velocity is reached at the walls. The higher the Reynolds number of the flow, the higher was the central core velocity.

Unlike the axial velocity contours of the control pipe, the computational results of the swirl pipe simulations revealed a triangular shape to the axial velocity contours. This same effect was observed in the axial velocity contours which resulted from the experimental investigations. This triangular shape was attributed to be a direct consequence of the 3-lobed helical swirl pipe, whereby each vertices of the triangular shape would have been caused by one of the lobe of the helical swirl pipe. Unlike in the experimental contours, where all three Reynolds number flows showed a triangular

profile, the computational contours were only triangular in shape for the high and medium Reynolds number flow. The low Reynolds number flow depicted a more circular profile. This is probably due to a lack of kinetic energy within the flow to effect swirl. As for the experimental results, the computational ones for the high and medium Reynolds number flows show that the triangular shape of the contours was more distinct closer to the exit of the swirl pipe. It also faded with increasing distance downstream, so that the triangular shape was barely noticeable at 14D length, downstream of the swirl pipe for the high Reynolds number flow, while at that same location, for the medium Reynolds number flow, the axial velocity contours had reverted back to a circular shape. It can be concluded from the computational results that the triangular shape of the axial velocity contours is dependent on the Reynolds number of the flow and the distance downstream from the swirl pipe outlet. This conclusion supports the experimental findings. Once again, as shown from the experimental results, the computational results also showed that the orientation of the triangular contours shifted with increasing distance downstream of the swirl pipe, reflecting a rotating flow. Similarly to the experimental results, the triangular shape of the axial velocity contours from the computational results were not offset by 120° at each plane, as would have been expected from a swirl pipe of pitch to diameter ratio of 0.6, confirming that the swirl decayed with increasing distance downstream of the swirl pipe.

The same two differences were observed between the contours obtained experimentally and those obtained computationally, as for the control pipe simulations. These were that the computational contours were more smoothly shaped compared to the amorphous shapes of the experimental contours and that the central core velocity was higher in all the computational contours compared to the experimental ones. The first difference is again explained by the computational contours being created from a very fine grid used in the computational models compared to the experimental contours being created from only 130 measurement points during the experimental study and the fan fluctuations observed during the experiments compared to the steady state of the simulations.

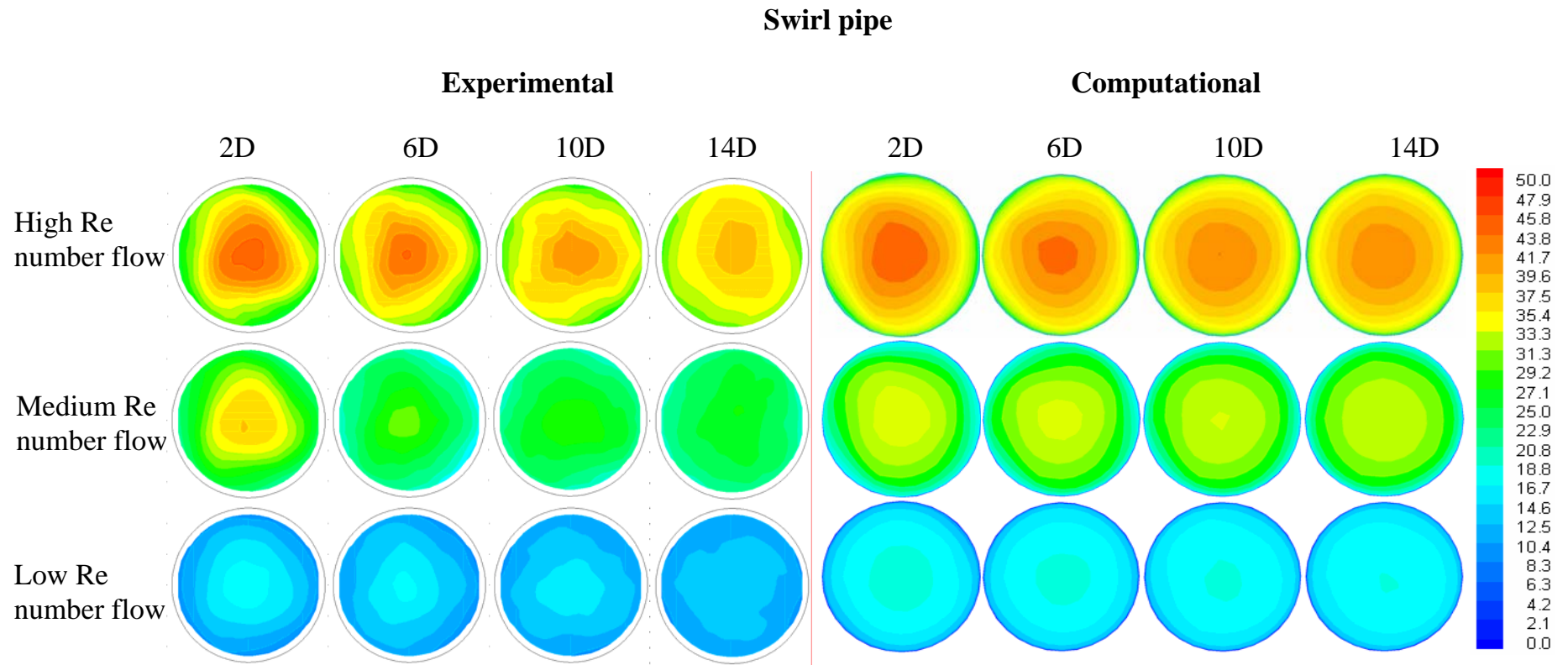


Figure 8.9: Comparison of axial air velocity contours post the swirl pipe from experimental and computational results (units = m/s)

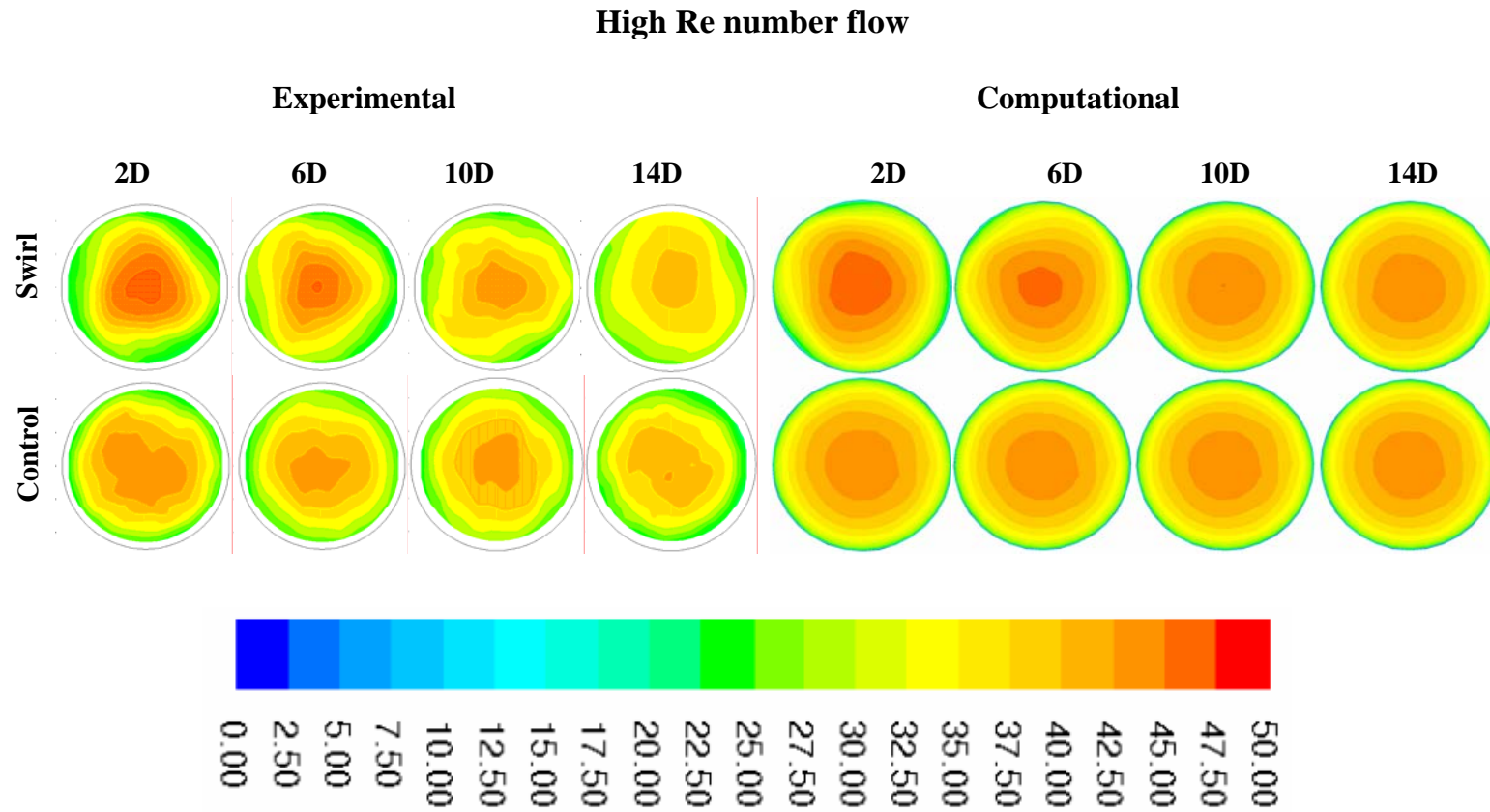


Figure 8.10: Comparison of axial air velocity contours post the swirl pipe from experimental and computational results for the high Reynolds number flow (units = m/s)

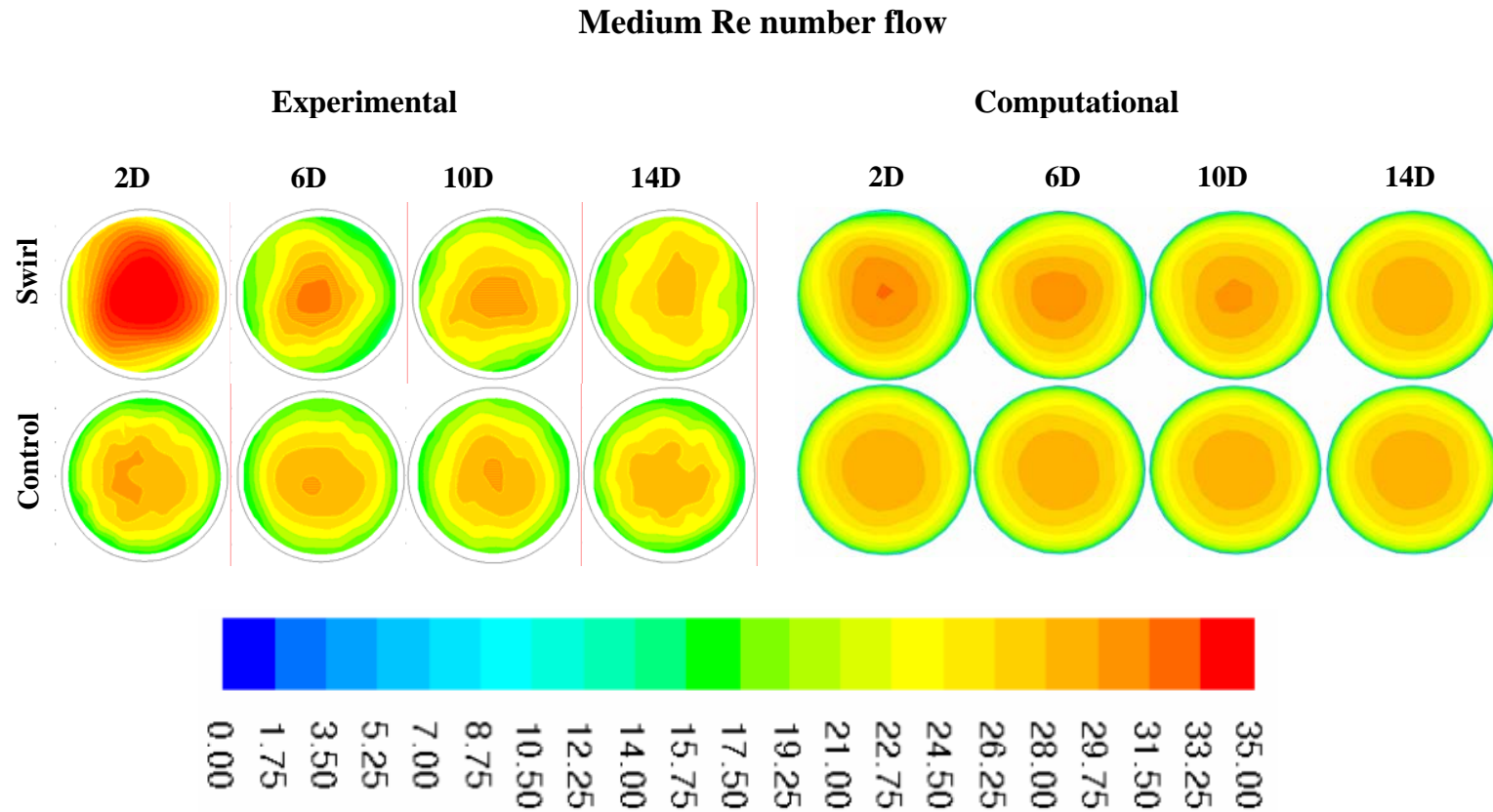


Figure 8.11: Comparison of axial air velocity contours post the swirl pipe from experimental and computational results for the medium Reynolds number flow (units = m/s)

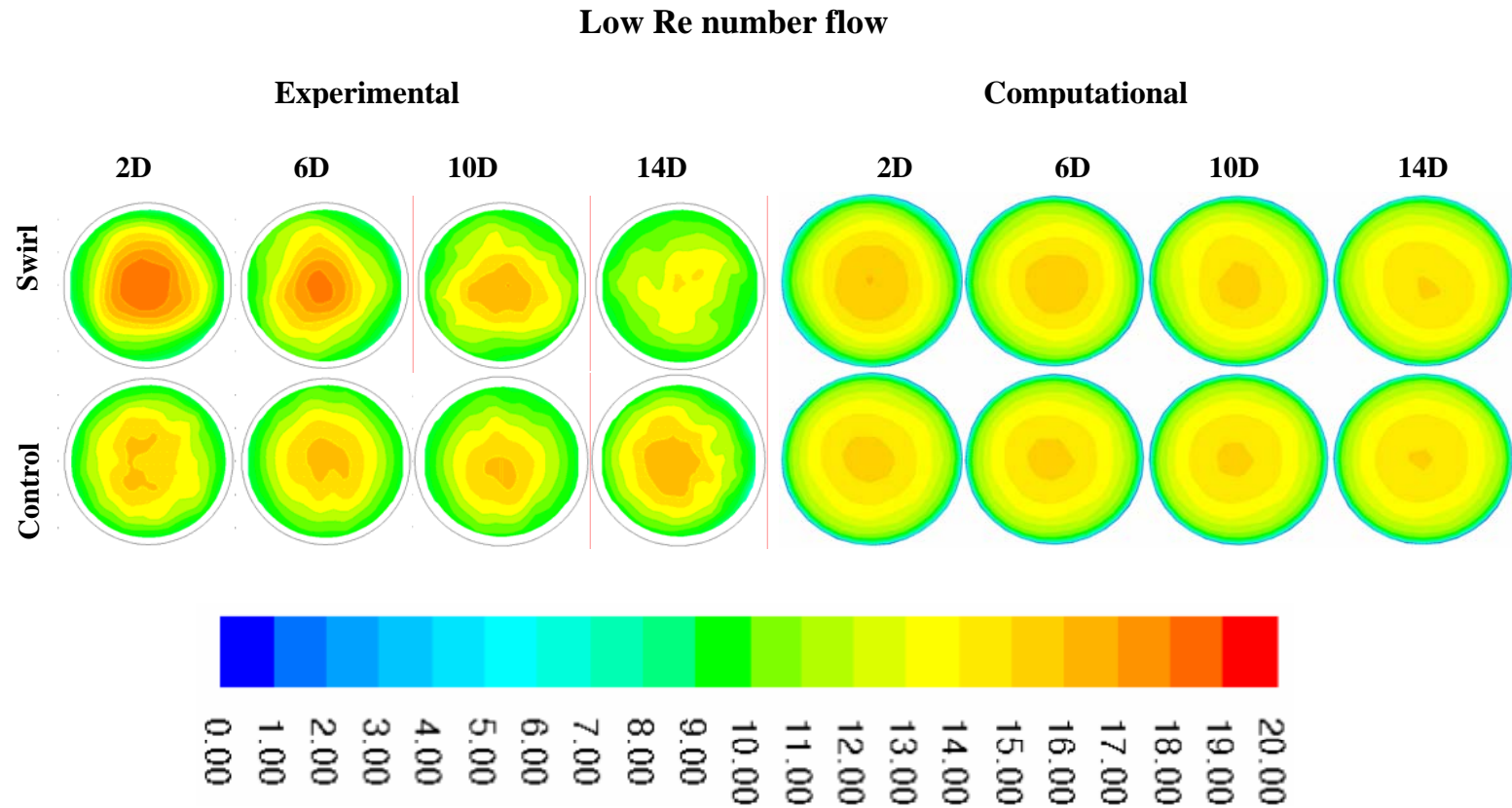


Figure 8.12: Comparison of axial air velocity contours post the swirl pipe from experimental and computational results for the low Reynolds number flow (units = m/s)

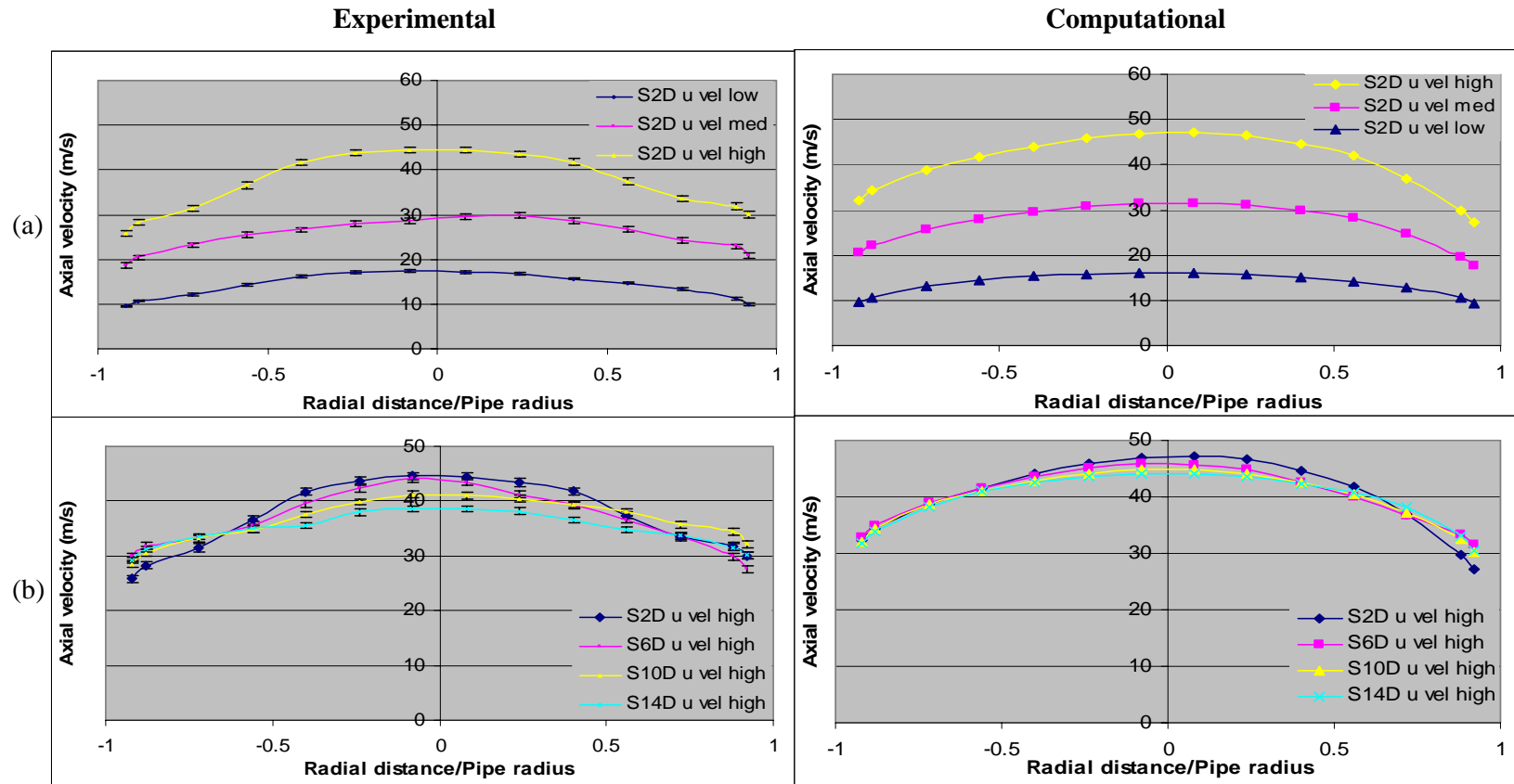


Figure 8.13: Computational horizontal centreline axial air velocity profiles post the swirl pipe

The axial velocity at the coordinates of the measurement locations along the horizontal centreline were extracted at planes 2, 6, 10 and 14D downstream of the swirl pipe for all three Reynolds number flows to quantify the difference in core velocity between the computational models and the experimental observations. Figure 8.13(a) shows a plot of 14 computed axial velocities along the centreline of the pipe at a location of 2D downstream of the swirl pipe for flows of low, medium and high Reynolds number. Figure 8.13(b) shows a plot of the 14 computed axial velocities along the centreline of the pipe for the high Reynolds number flow at location of 2, 6, 10 and 14 pipe diameters downstream of the swirl pipe.

The axial velocity profile plots confirmed that the core velocity decreased with distance downstream of the control pipe. This can be attributed to the higher velocity imparted to the flow by turbulence due to the swirl pipe, which decreased further downstream of the swirl pipe.

When comparing the computational results to the experimental ones, it was found that the simulation over-predicted the axial velocities of the medium and high Reynolds number flows, but under-predicted the low Reynolds number flow. Moreover the simulations did not show the steep axial velocity gradient at $r/R = \pm 0.6$ for the high Reynolds number flow, neither were the computed axial velocity profiles skewed for the medium and low Reynolds number flows as revealed by the experiments. These may be explained by the fact that the computational results are actually an averaged value over the timesteps, whereas the experimental measurements were instantaneous.

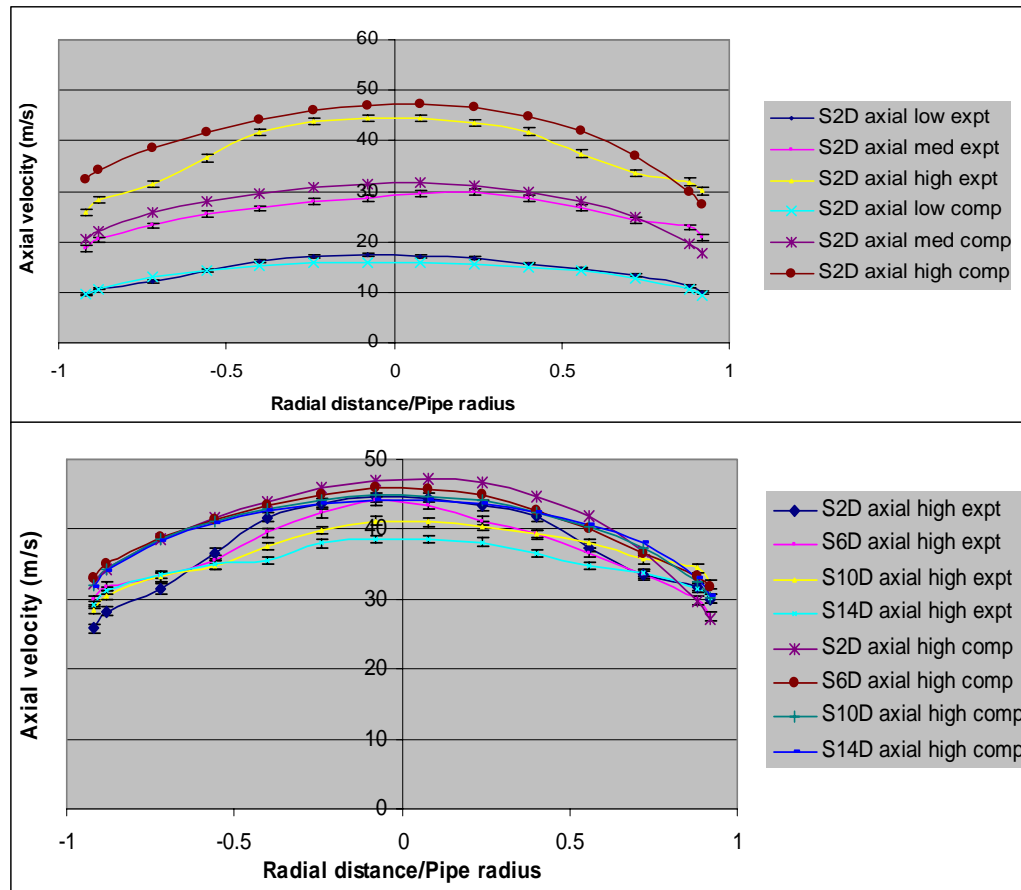


Figure 8.14: Comparison of horizontal centreline axial air velocity profiles post the swirl pipe section from experimental and computational results

The average percentage difference between the experimental and computational axial velocity values for the three Reynolds number flows were calculated to be as follows:

Reynolds number flow	% difference between computational and experimental axial velocity values
High	7.50
Medium	3.65
Low	-3.63

Table 8.5: Percentage difference between computational and experimental axial air velocity values for low, medium and high Reynolds number flows post swirl pipe

When compared to the computed axial velocity contours with the control pipe, the swirl pipe was found to generate higher core velocities than the control pipe for plane locations of 2, 6 and 10D downstream of the swirl pipe. For all three Reynolds number flows, the contours post the swirl at 14D seemed to be the same as that post the control pipe. This is confirmed in Figure 8.15(a) and (b), which shows a post swirl and post control pipe sections plot comparison of computed axial velocities along the centreline of the pipe at a location of 2D for flows of low, medium and high Reynolds number and a post swirl and post control pipe sections plot comparison of computed axial velocities along the centreline of the pipe for the high Reynolds number flow at location of 2, 6, 10 and 14D. The higher central core axial velocity for the high and medium Reynolds number flows at 2, 6 and 10D downstream of the swirl pipe is believed to be due to the kinetic energy imparted to the flow due to turbulence created by the swirl pipe.

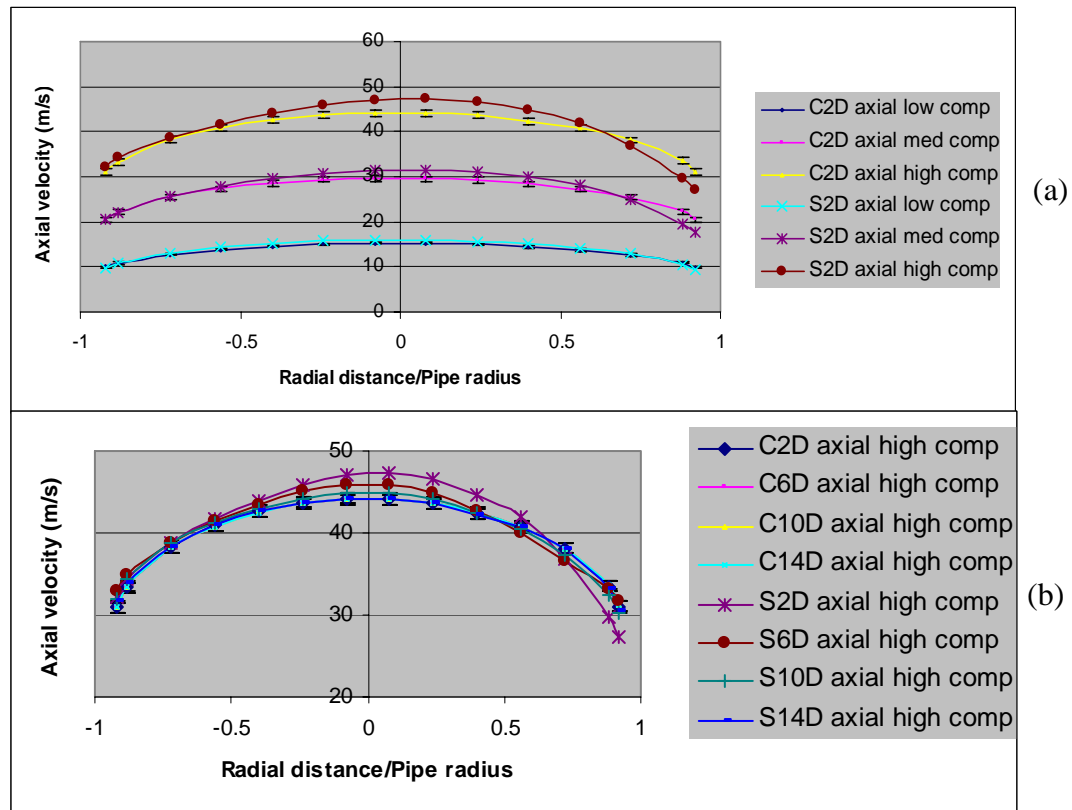


Figure 8.15: Comparison of horizontal centreline axial air velocity profiles from computational results post the swirl pipe and post the control pipe section

8.5.2.1 Validation of tangential velocity distribution of induced swirling flow

The range of tangential velocities from the computational results was similar to the experimental results. The core triangular profile of the tangential velocity contours as depicted during the experimental study was less obvious in the computational results (Figure 8.16). However, the computed tangential velocity followed the same trend as the experimental ones; with higher tangential velocity at the walls and decreasing to zero at the centre of the pipe, indicating the presence of a swirl flow. The computational results seemed to under-predict the tangential velocities, when compared to experimental results.

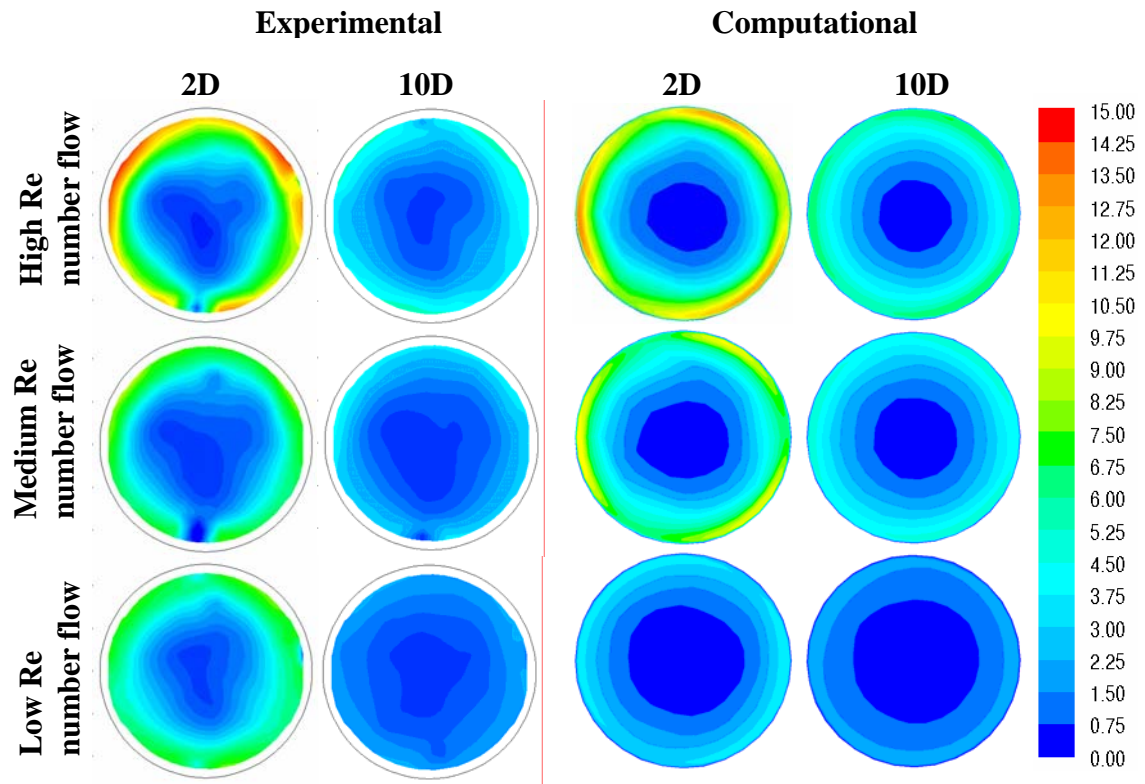


Figure 8.16: Comparison of experimental and computational tangential air velocity contours at planes 2 and 10D post the swirl pipe (units = m/s)

The tangential velocity at the coordinates of the measurement locations along the horizontal centreline were extracted at planes 2, 6, 10 and 14D downstream of the swirl pipe for all three Reynolds number flows to quantify this difference in core velocity between the computational models and the experimental observations. Figure 8.17(a) and

(b) shows a plot of 14 computed tangential velocities along the centreline of the pipe at a locations of 2 and 10D, respectively, downstream of the swirl pipe for flows of low, medium and high Reynolds number.

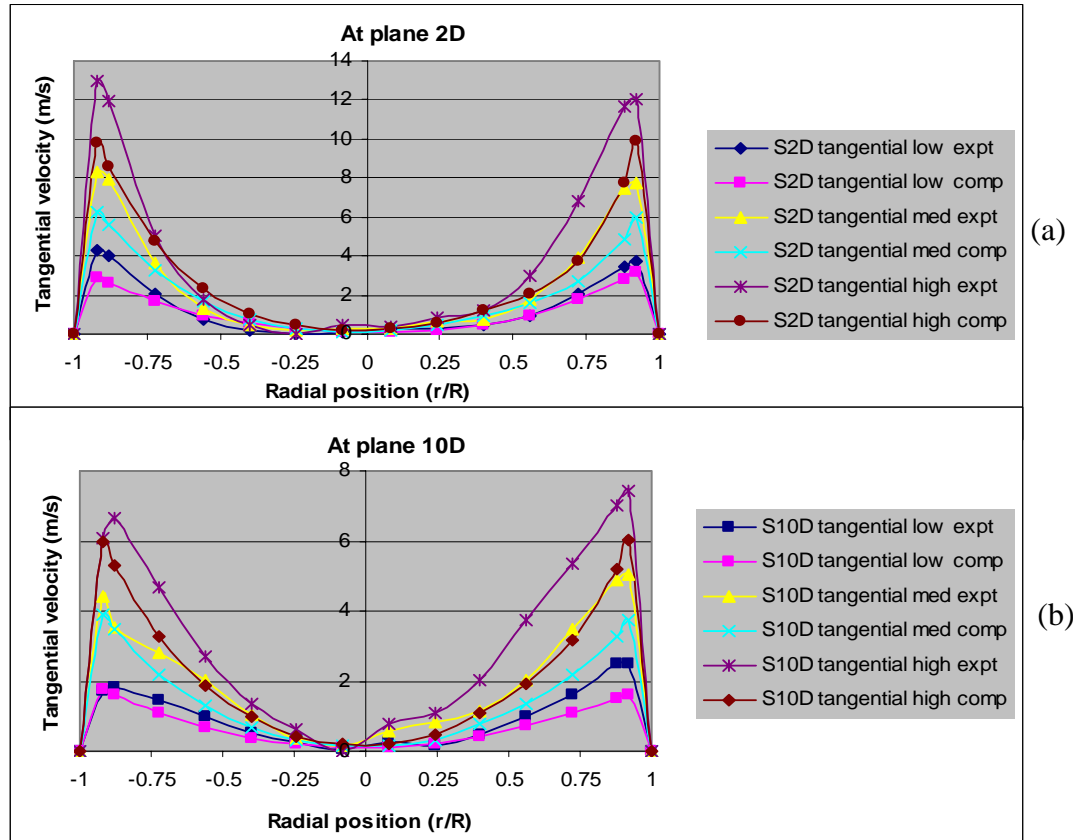


Figure 8.17: Comparison between computational and experimental horizontal centreline tangential air velocity profiles post the swirl pipe at plane 2 and 10D

The average percentage difference between the experimental and computational tangential velocity values for the three Reynolds number flows were calculated to be as follows:

Reynolds number flow	% difference between computational and experimental tangential velocity values at	
	2D	10D
High	-25.08	-56.03
Medium	-19.77	-59.89
Low	-18.20	-33.52

Table 8.6: Percentage difference between computational and experimental tangential air velocity values at 2 and 10D for the low, medium and high Reynolds number flows

Differences between the physical flow and the numerical solution could be due to one of the following (Shaw 1992):

- An inadequate mesh density being used in the regions of high rates of the flow variables, for example in a boundary layer;
- Inadequate physical modelling of the flow, especially due to the use of turbulence models which could not simulate the complex swirling flow;
- Inadequate specifications of the boundary conditions which have over- or under-constrained the flow.

A combination of grid independence, turbulence model sensitivity studies, examination of near wall modelling approaches and lengthening the pipes beyond the results determination points were carried out to ensure that the above stated errors were minimised (Chapter 7).

Despite the difference in the magnitude of the computed and experimental tangential velocity results, the computational w-velocity and tangential velocity profiles still followed the same trend as the experimental ones (Figure 8.18 and Figure 8.19). The w-velocities were close to zero at the centre of the pipe and higher at the walls, positive in one half of the pipe cross section and negative in the other, in an S-shape profile, which is typical of wall jet swirl flows.

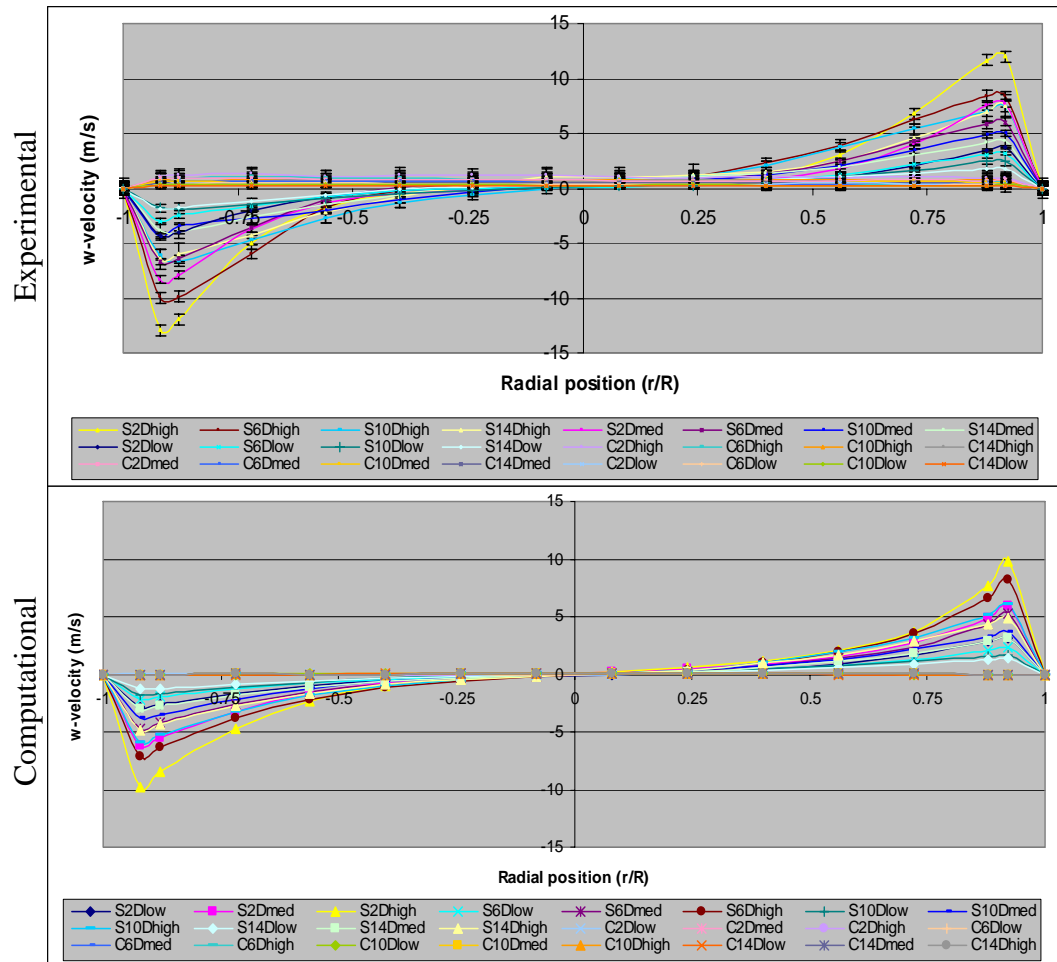


Figure 8.18: Comparison between computational horizontal centreline w-air velocity profiles post the swirl pipe and control

As the experimental results, the maximum computed tangential velocity attained decreased with decreasing Reynolds number of the flow and increasing distance downstream of the swirl pipe. The computed tangential velocity generated downstream of the control pipe section was zero. The computational results corroborated the experimental results by showing that even at plane 14D, the effects of the swirl was still present in the flow field, since the tangential velocity profile had not yet reduced to zero (Figure 8.19).

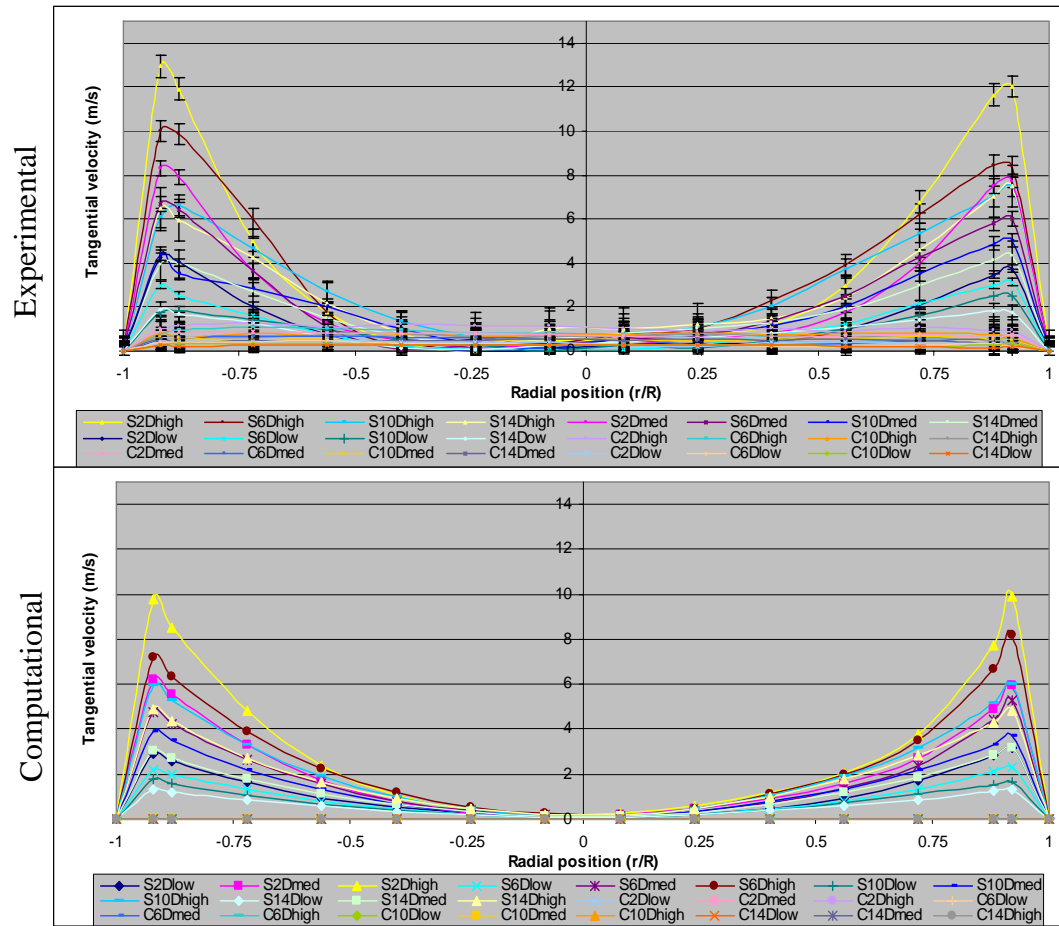


Figure 8.19: Comparison between computational horizontal centreline tangential air velocity profiles post the swirl pipe and control

8.5.2.2 Validation of rate of decay of induced swirling flow

Swirl number as defined in equation 4.4 was used to assess the amount of swirl induced to the flow field. The swirl numbers at planes 2, 6, 10, 14, 18, 22 and 26D were computed and presented in Figure 8.20. As can be observed, the swirl number decreases with increasing distance downstream and with decreasing Reynolds number. This supports the earlier conclusion that the swirl is decays with respect to these two variables.

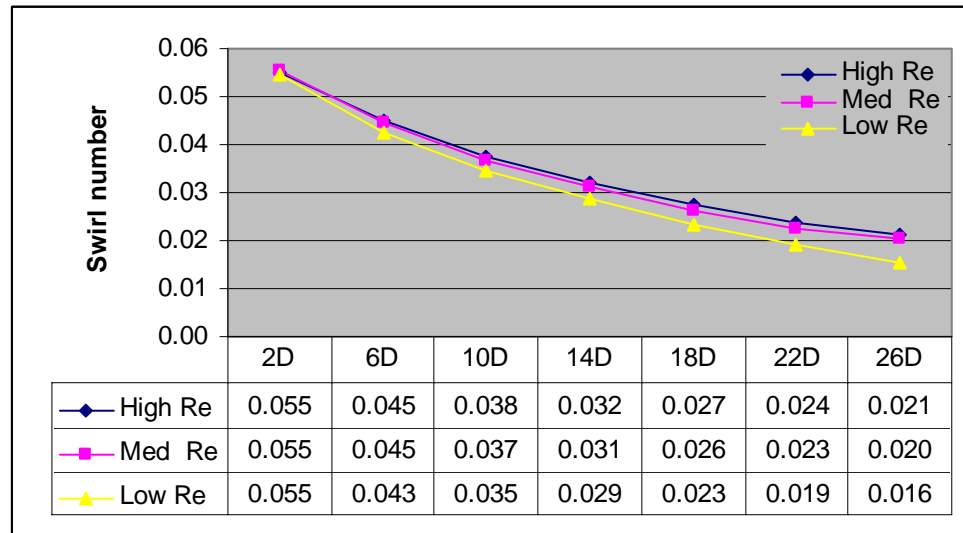


Figure 8.20: Swirl numbers at planes 2, 6, 10, 14, 18, 22 and 26D downstream of swirl pipe for the low, medium and high Reynolds number flows

Despite following the same trend as the experimental swirl numbers, the computed swirl numbers were lower, as shown in Figure 8.21 and summarised in Table 8.7. These were to be expected due to the high difference between the computed and experimental tangential velocities and the strong dependency of the swirl number on tangential velocity.

Reynolds number flow	% difference between computational and experimental Swirl numbers
High	64.00
Medium	61.80
Low	58.18

Table 8.7: Percentage difference between computational and experimental Swirl number values for the low, medium and high Reynolds number flows

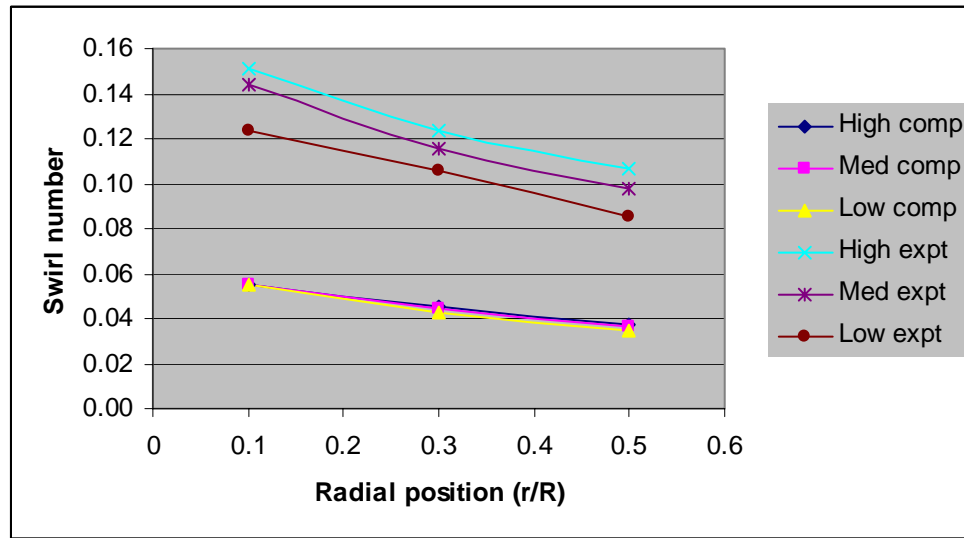


Figure 8.21: Comparison between computational and experimental Swirl number values for the low, medium and high Reynolds number flows

A trendline following an exponential trend was also fitted to the curves as shown in Figure 8.22 to find the decay rate for all three Re number flows. Table 8.8 summarises the swirl decay equations and the decay rate for the three Reynolds number flows.

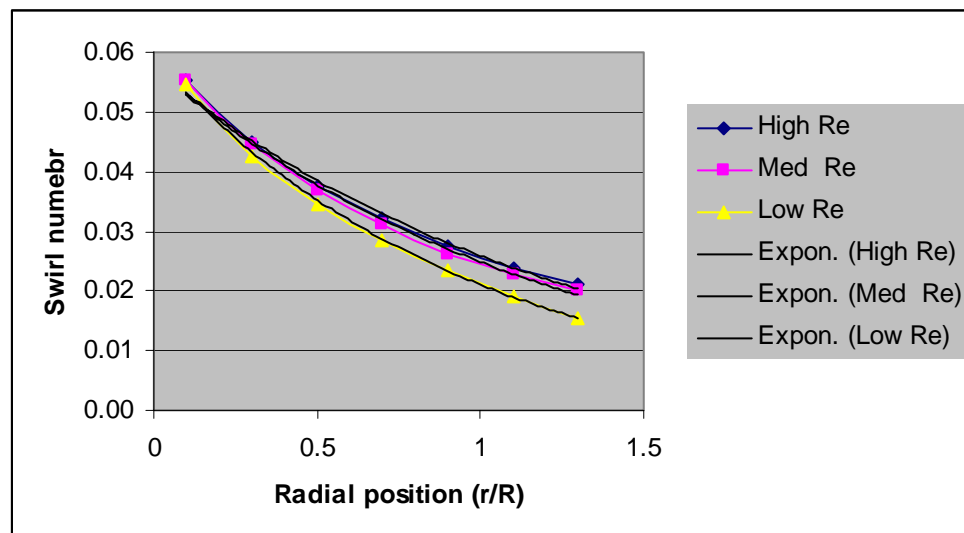


Figure 8.22: Trendline for estimating swirl decay rates

Reynolds number flow	Swirl decay equation	Decay rate
High	$S = 0.0575e^{-0.7985x}$	15.97
Medium	$S = 0.0575e^{-0.8390x}$	16.78
Low	$S = 0.0591e^{-1.0324x}$	20.65

Table 8.8: Swirl decay rates for the three Reynolds number flows

The swirl decay rate was calculated by dividing the exponential factor in the equation by the pipe diameter (0.05m). The swirl decay rates were in accordance with those resulting from the experiments. An analysis of the computed swirl decay rate values concluded that for air-only flows, the swirl decayed rapidly downstream of the swirl pipe and that the swirl decayed faster the lower the Reynolds number of the flow. This conclusion confirmed that from the experimental swirl decay rates carried out on air-only flows.

8.6 FURTHER STUDIES PERFORMED USING THE VALIDATED CFD MODELS

In this section, the validated CFD models are used to further investigate the effect of the swirl pipe on the flowfield. The effect of the swirl pipe on particulate flow was also inferred in this section from studies of particle trajectories modelled by a Lagrangian approach, 1-way coupled, within the validated CFD models. Firstly, the results of the high, medium and low Reynolds number flows variables from the CFD simulations with the control pipe and with the swirl pipe will be examined at more locations than used for validation purposes. A plane was created in the xz-axis (along the flow direction) to cross the rig model geometry vertically at the centre. Planes were also created in the yz-axis (perpendicular to the flow direction) as summarised in Table 8.9.

Distance from inlet (Pipe diameters) (m)		Reference location
0	0	inlet
6	0.3	start of developmental pipe
16	0.8	1/3 of developmental pipe
27	1.35	2/3 of developmental pipe
37	1.85	inlet of swirl/control pipe
40	2	1/3 of swirl/control pipe
42	2.1	mid of swirl/control pipe
44	2.2	2/3 of swirl/control pipe
46	2.3	start of visualisation pipe
48	2.4	2D downstream of swirl/control pipe
50	2.5	4D downstream of swirl/control pipe
52	2.6	6D downstream of swirl/control pipe
54	2.7	8D downstream of swirl/control pipe
56	2.8	10D downstream of swirl/control pipe
58	2.9	12D downstream of swirl/control pipe
60	3	14D downstream of swirl/control pipe
64	3.2	18D downstream of swirl/control pipe
65	3.25	19D downstream of swirl/control pipe
68	3.4	22D downstream of swirl/control pipe
70	3.5	24D downstream of swirl/control pipe
72	3.6	26D downstream of swirl/control pipe
75	3.75	29D downstream of swirl/control pipe

Table 8.9: Planes locations

8.6.1. Pressure variables

Static gauge pressure, dynamic pressure and total pressure were used to understand the flow behaviour within the part of the rig that was modelled. Static pressure corresponds to the fluid's weight when at rest while dynamic pressure corresponds to the movement of the fluid relative to the pipe. The static pressure and the dynamic pressure are added to give the total pressure.

The CFD results predict that the solids feeding device causes a significant drop in the static pressure of the system. This is accompanied by a simultaneous increase in dynamic pressure of the system. Both the decrease in the static pressure and the increase in dynamic pressure are directly proportional to the Reynolds number of the flow. These results confirm that the venturi section of the feeder is performing well. All three Reynolds number flows are also shown to have stabilised by the first third of the developmental pipe, i.e. after 10 pipe diameters post the exit of the feeder section. A fully developed flow may be assumed from this point onwards and therefore the flow going into the control or swirl pipe is fully developed for all three Reynolds number flows.

As was expected, the flows with the control pipe sections in place were undisturbed, with the dynamic pressure line being practically horizontal. The static pressure drop is also linear and proportional to the Reynolds number of the flow. On the other hand, the simulations with the swirl pipe section in place predict a decrease in dynamic pressure within the swirl pipe, before increasing again at the swirl pipe exit and within the visualisation pipe. The static pressure results predict a sudden drop when the flow exits the swirl pipe into the visualisation pipe. The drop in static pressure is again proportional to the Reynolds number of the flows. This is believed to be due to the flow hitting the pipe wall created because of the non-conformal geometry of the swirl and circular pipe sections.

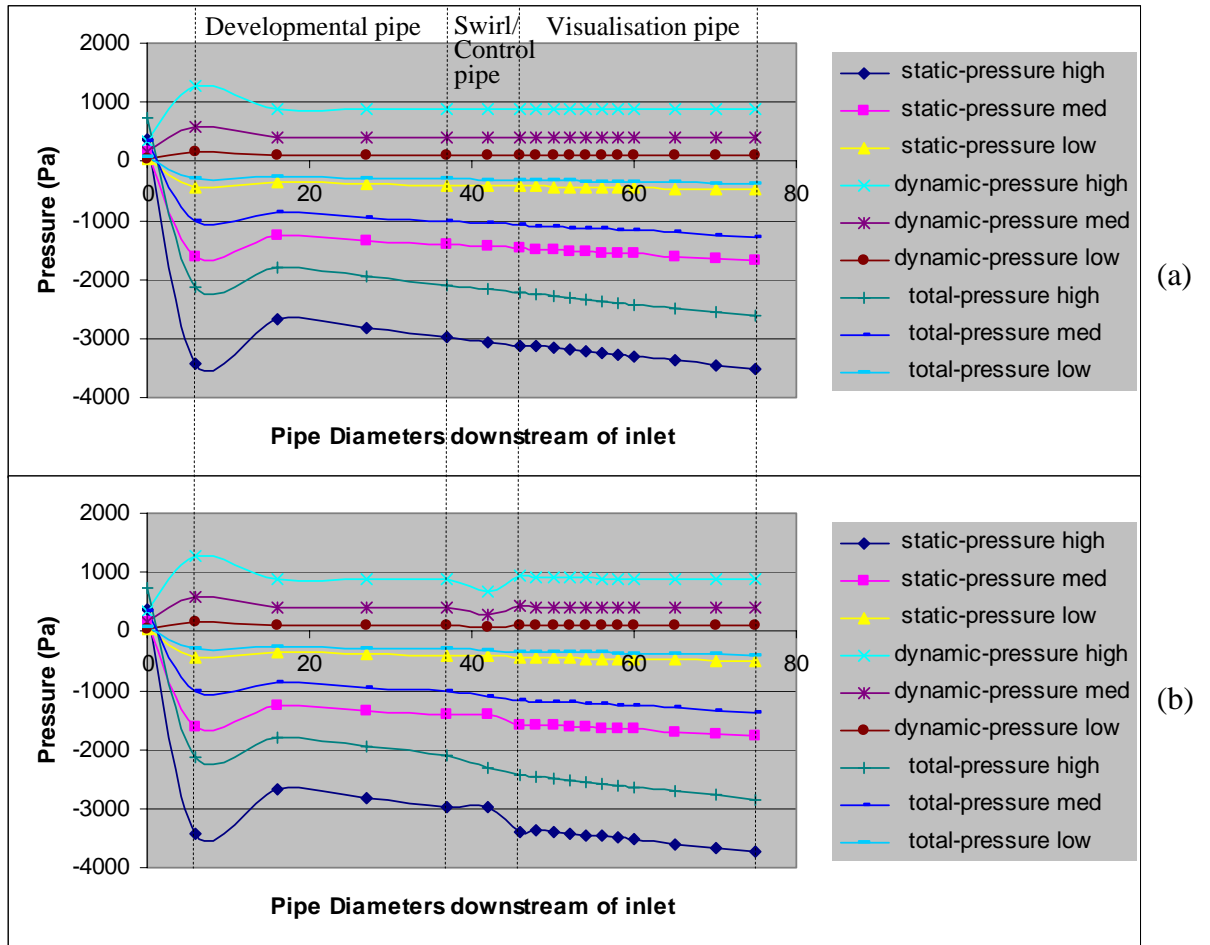


Figure 8.23: Computational pressure profile in horizontal section of rig model for (a) control pipe; (b) swirl pipe

Figure 8.23(a) and (b) show values that have been averaged over the area of the plane while variations of static and dynamic within the planes are shown in Figure 8.24 and Figure 8.25 for a better understanding of the behaviour of the flowfield.

Figure 8.24 confirms that the higher static pressure at the swirl pipe exit is due to the walls created because of the non-conformal geometry of the swirl and circular pipe sections, from the shape of the static pressure contours on the plane located at the swirl pipe exit. The contours also show that the static pressure distribution within any one plane perpendicular to the flow is higher at the walls than at the centre. This is accompanied by a higher dynamic pressure at the centre than at the walls, with the difference being the

greatest at the exit of the swirl pipe. Such a result was expected as the velocity at the walls was forced to zero by the non-slip wall boundary condition.

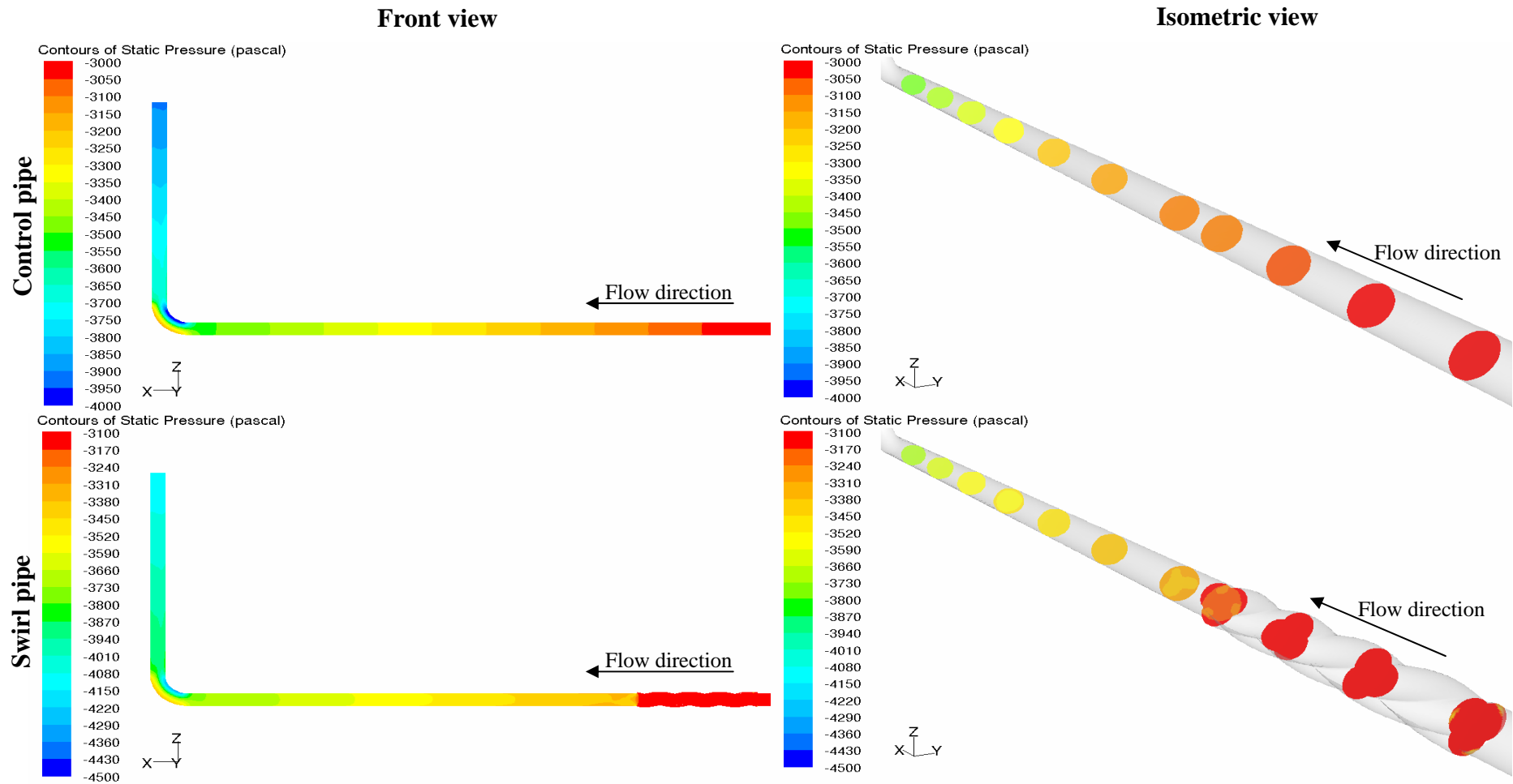


Figure 8.24: Static pressure distribution within model geometry for control and swirl pipe

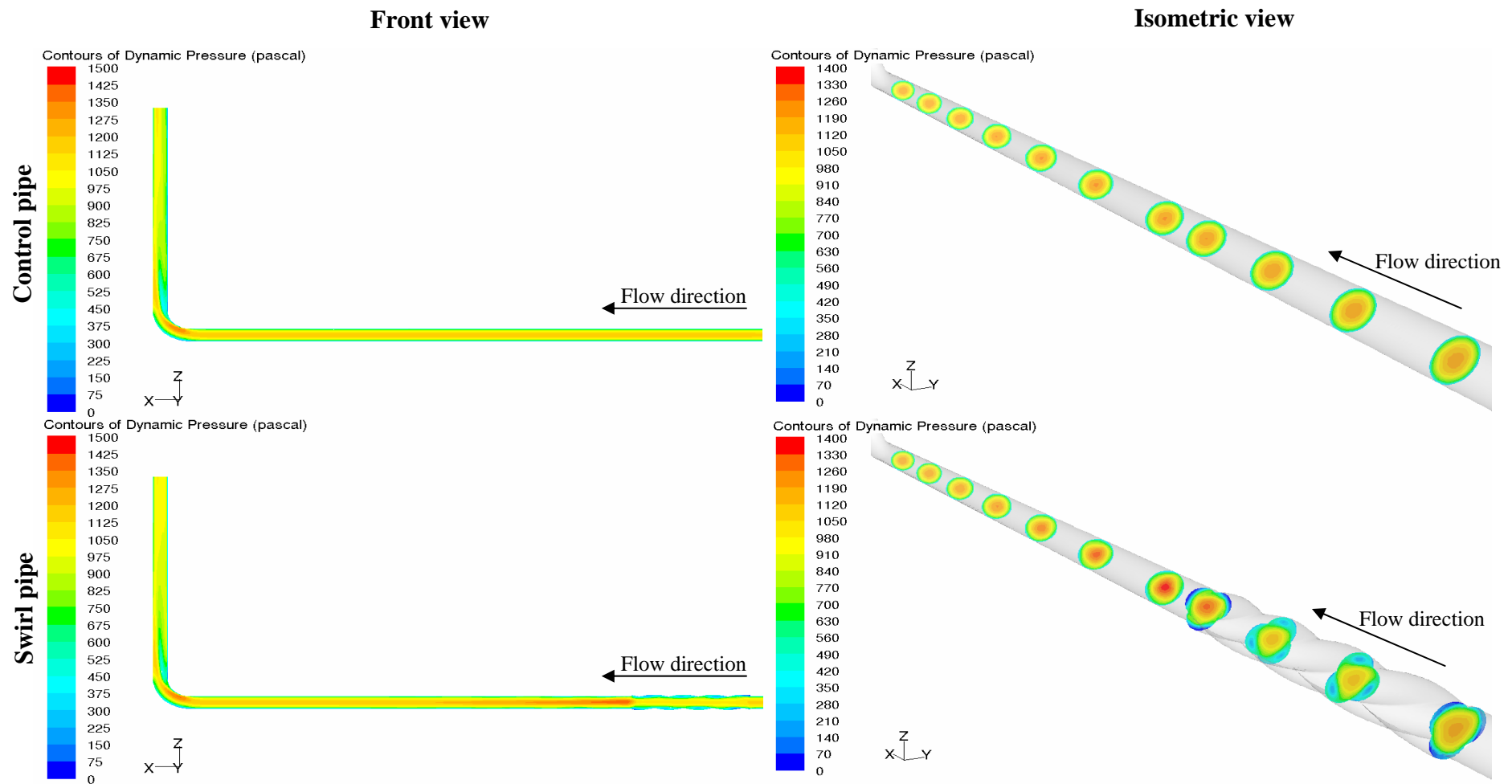


Figure 8.25: Dynamic pressure distribution within model geometry for control and swirl pipe

8.6.2. Air velocity variables

The plane averaged axial velocity values show that for both the control pipe and the swirl pipe simulations, the venturi section of the solids feeder increases the axial velocity (Figure 8.26). This then stabilises to a fully developed flow within the first third of the developmental pipe. The results show that for the control pipe simulations, there is no variation in the plane averaged axial velocity values, but that for the swirl pipe simulation, the plane averaged axial velocity value suddenly drops within the swirl pipe before regaining the pre-swirl axial momentum.

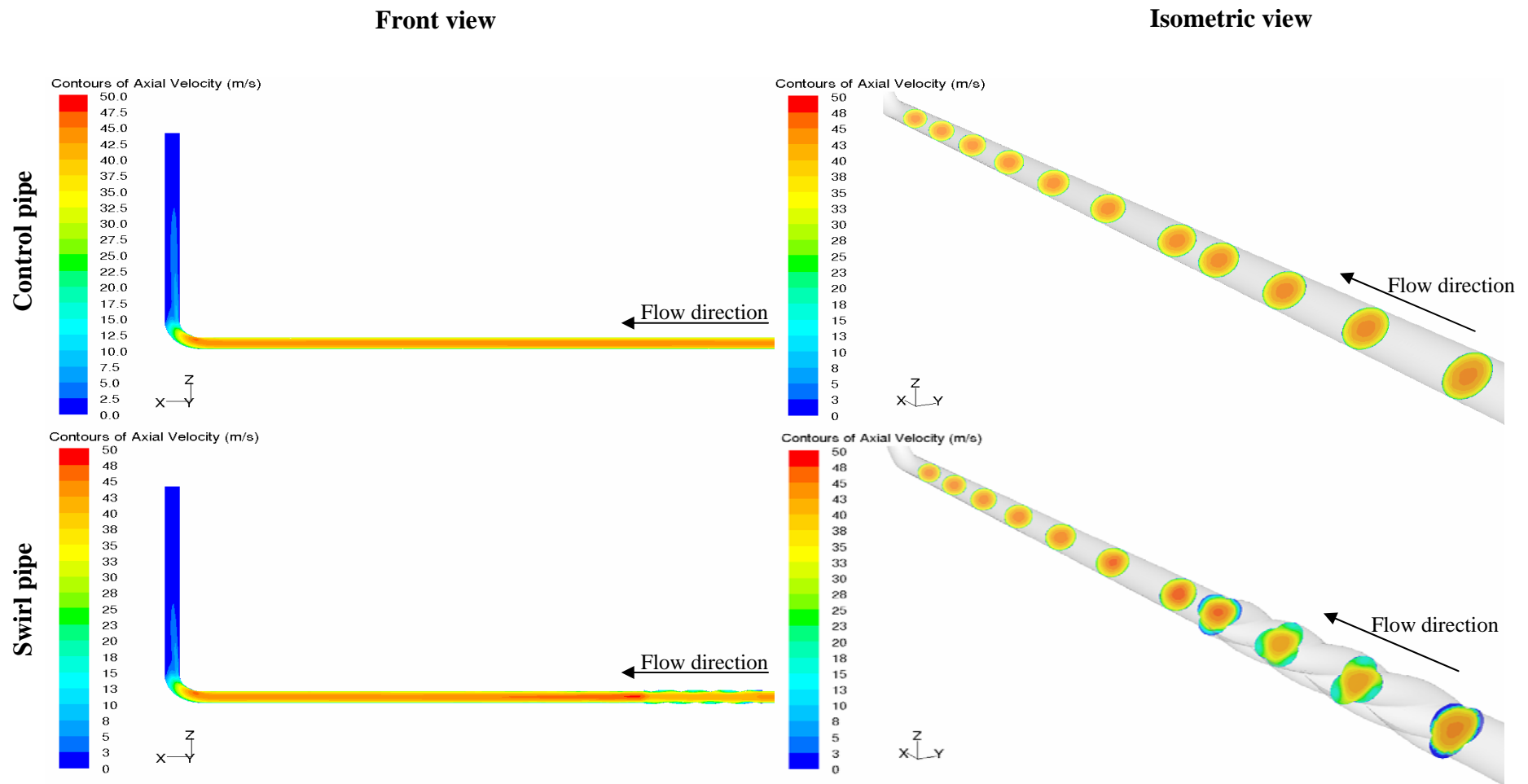


Figure 8.26: Axial air velocity distribution within model geometry for control and swirl pipe

Plane averaging the axial velocity values was believed to be misleading and hence the axial velocity values at the centreline points of these same planes were plotted (Figure 8.27). These show that for the first length of 37 pipe diameters, which corresponds to the location of the swirl pipe inlet, the axial velocity profile for the control simulation and the swirl pipe simulation were exactly the same. A drop in axial velocity is still observed within the swirl pipe, probably due to the sudden change in cross sectional area of the pipe. At and post the swirl pipe exit however, the axial velocity is higher than that of post the control pipe exit as well as pre-swirl pipe axial velocity until about 60 pipe diameters downstream of the inlet. Both the axial velocity drop within the swirl pipe and the axial velocity rise post the swirl pipe were directly proportional to the Reynolds number of the flow, with the low Reynolds flow for the swirl pipe simulation showing almost no axial velocity drop and rise when compared to the low Reynolds flow for the control pipe simulation.

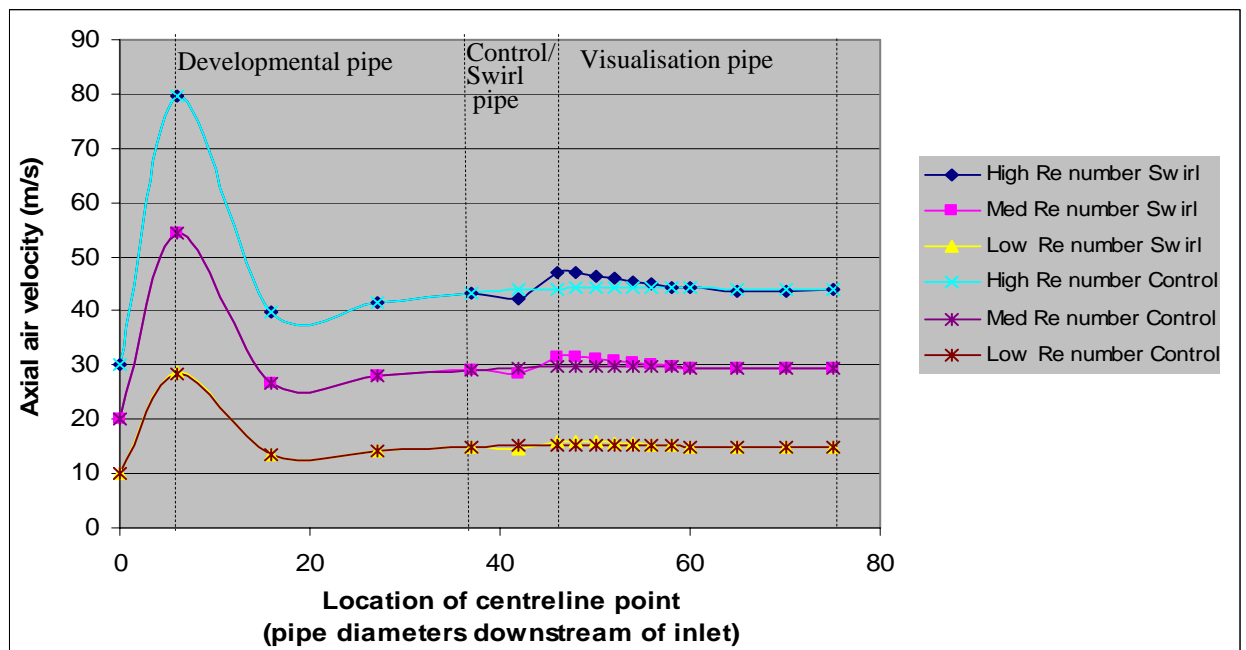


Figure 8.27: Axial air velocity profile within model geometry for control and swirl pipe

Tangential velocity was found to be non-existent in the horizontal section of the control rig model, while for the swirl pipe simulation, plane averaged tangential values were seen

to be non-existent prior to the swirl pipe, reaching a maximum within the swirl pipe section and gradually decreasing post the swirl pipe exit (Figure 8.28 and Figure 8.29).

The rise and fall of the plane averaged tangential values were directly proportional to the Reynolds number of the flow. The sudden rise in tangential velocity within the swirl pipe was found to correspond to the sudden fall in axial velocity within the swirl pipe (Figure 8.29). It can therefore be argued that the swirl pipe causes a redistribution of momentum from axial to tangential, thereby confirming that the swirl pipe imparts a swirl component to the flow.

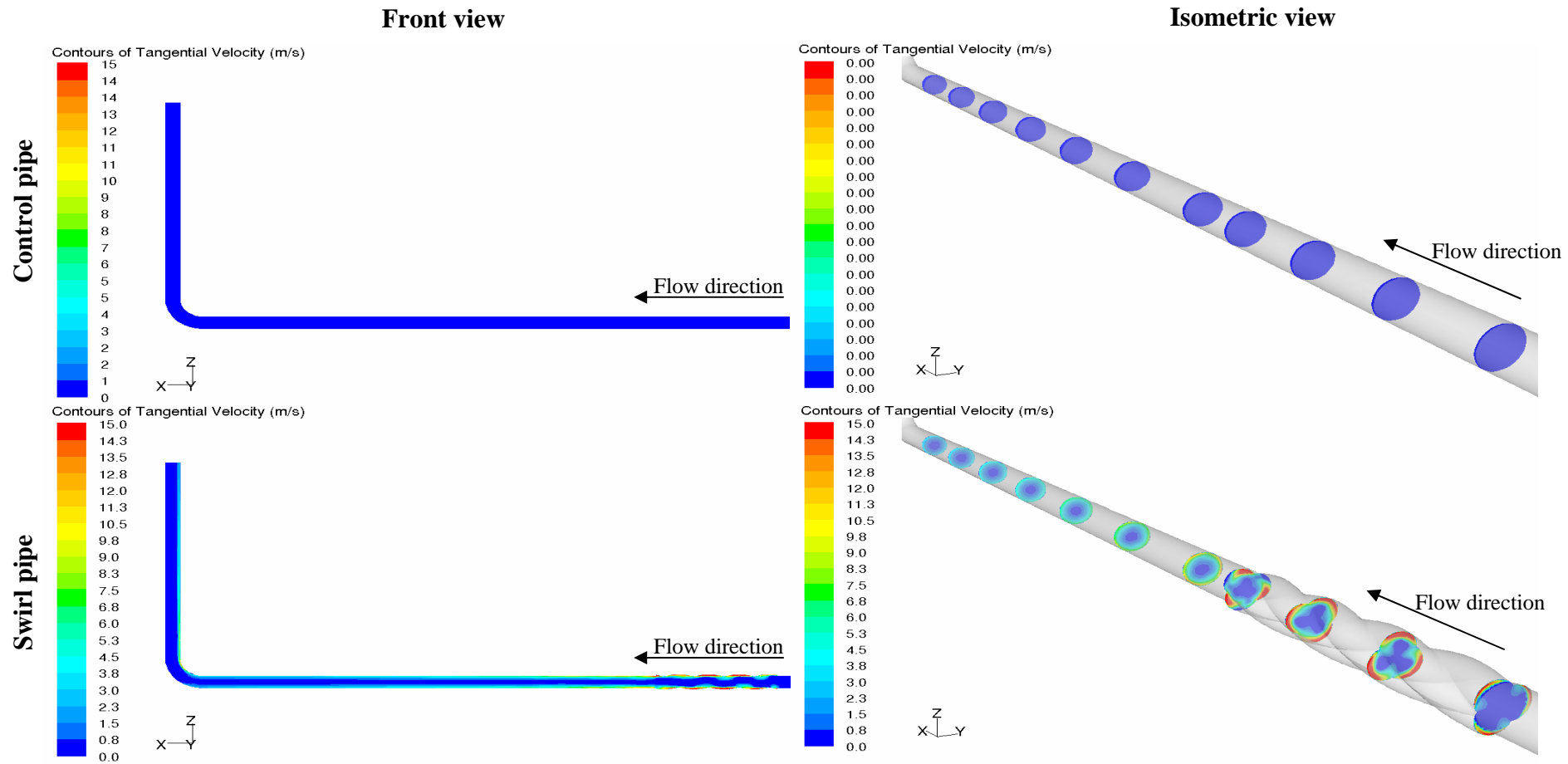


Figure 8.28: Tangential air velocity distribution within model geometry for control and swirl pipe

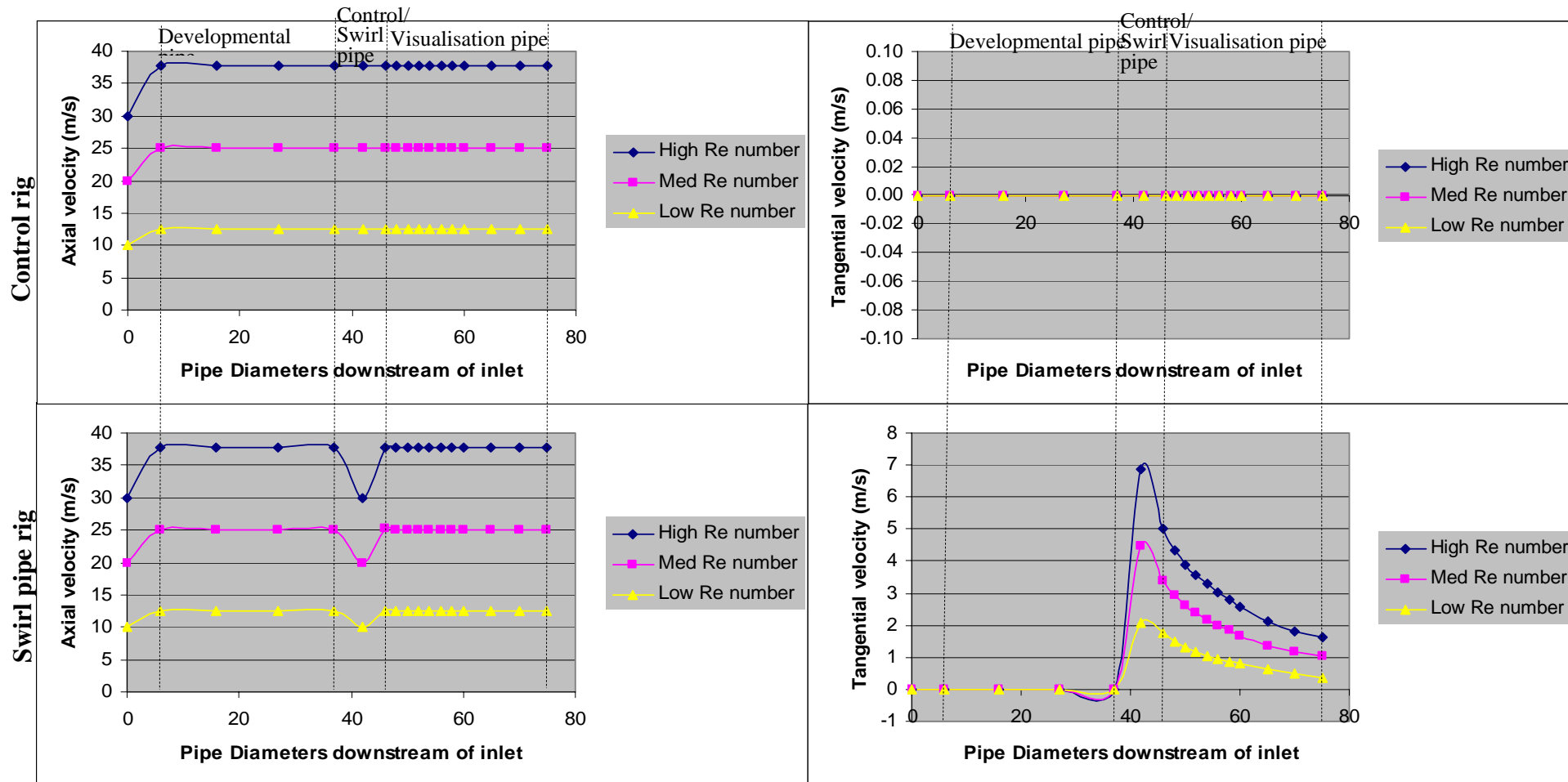


Figure 8.29: Axial and tangential air velocity profile within model geometry for control and swirl pipe for the three Reynolds number flows

8.6.3. Turbulence dissipation

Turbulence dissipation rates were found to be higher at the walls than at the centre of the circular and swirl pipe, in accordance to the log-wall region (Figure 8.30). In addition, within the swirl pipe, a core triangular region was observed with minimum turbulence dissipation rate. This area corresponded to the regions of high axial velocity. Away from the pipe centre, turbulence dissipation rate then increased in a region of the form of a triangular doughnut before again decreasing to a minimum in the lobed region of the swirl pipe. Turbulence dissipation rate was highest in the lobed regions at the swirl inlet and outlet (Figure 8.31). This trend was still visible at 2D downstream of the swirl pipe and gradually faded away. This high turbulence dissipation rate is believed to occur when the flow hits the interface wall was created due to the non-conformal geometries of the swirl and circular pipe.

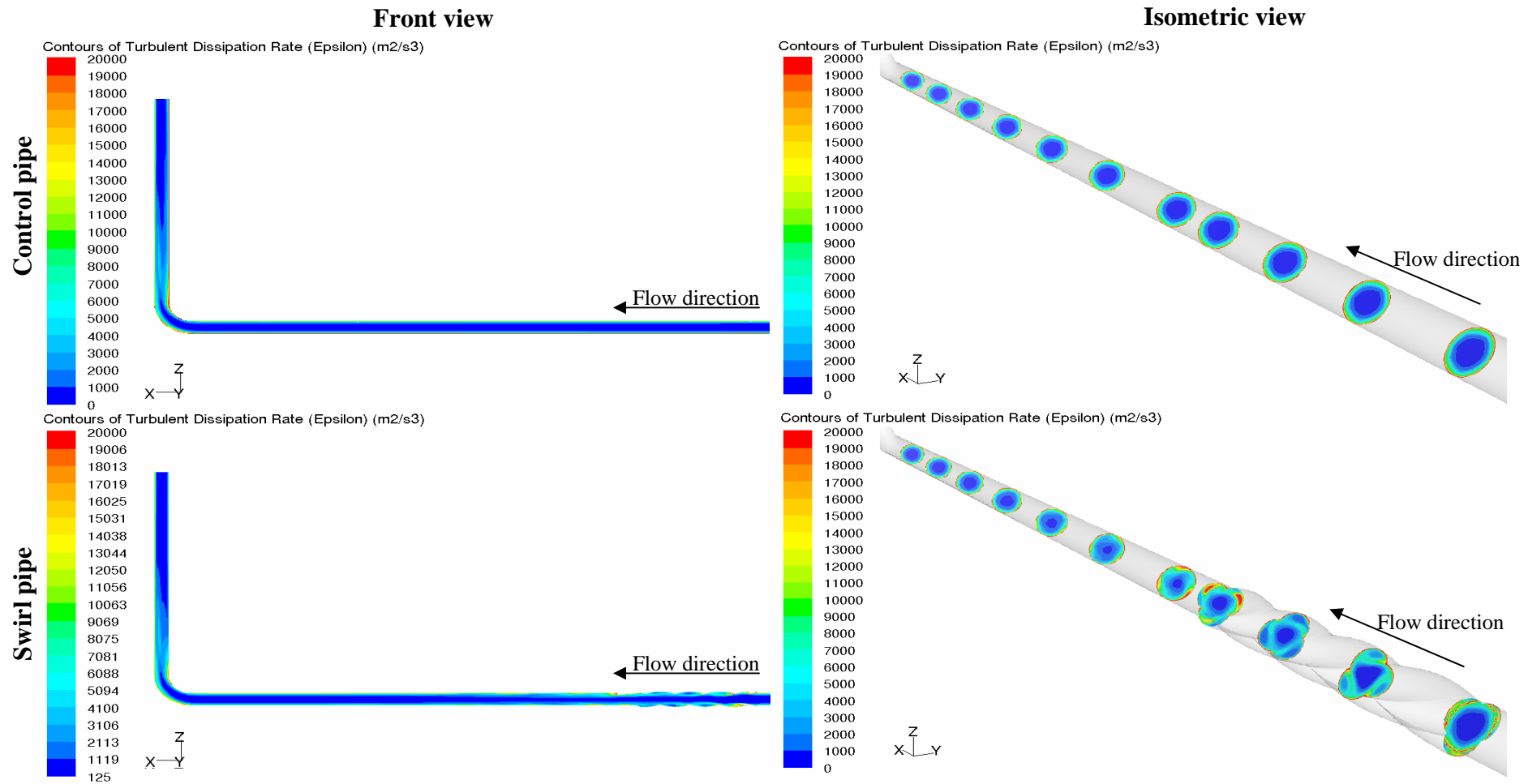


Figure 8.30: Turbulence dissipation rate distribution within model geometry for control and swirl pipe

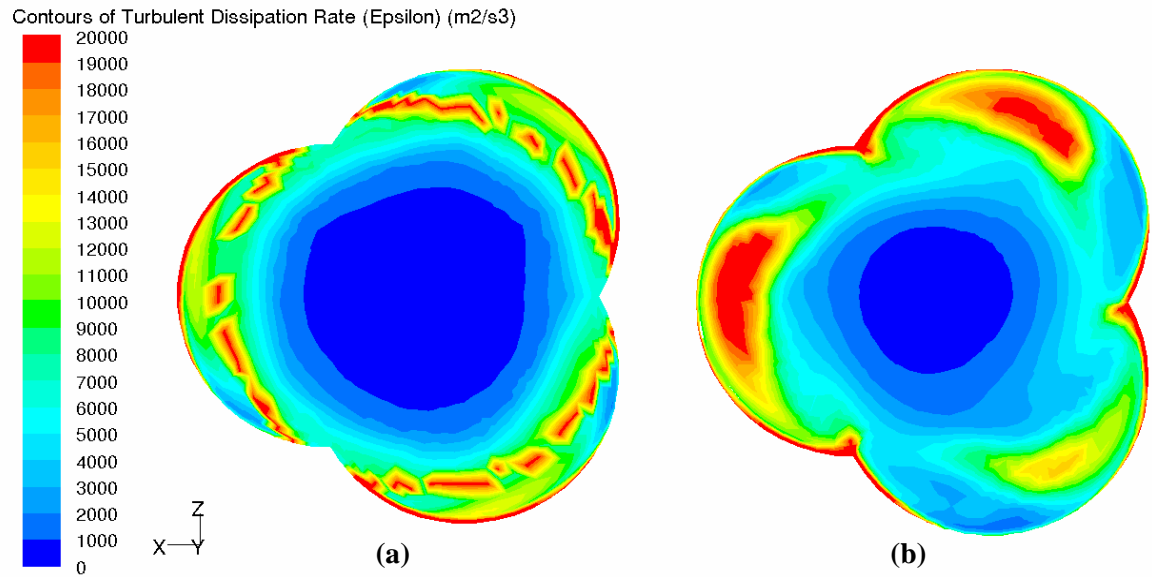


Figure 8.31: Turbulence dissipation rate distribution at (a) swirl pipe inlet plane and (b) swirl pipe outlet plane

The regions of high turbulence dissipation corresponded to those of high turbulence kinetic energy (Figure 8.32), which is the mean kinetic energy per unit mass associated with eddies and turbulent flow.

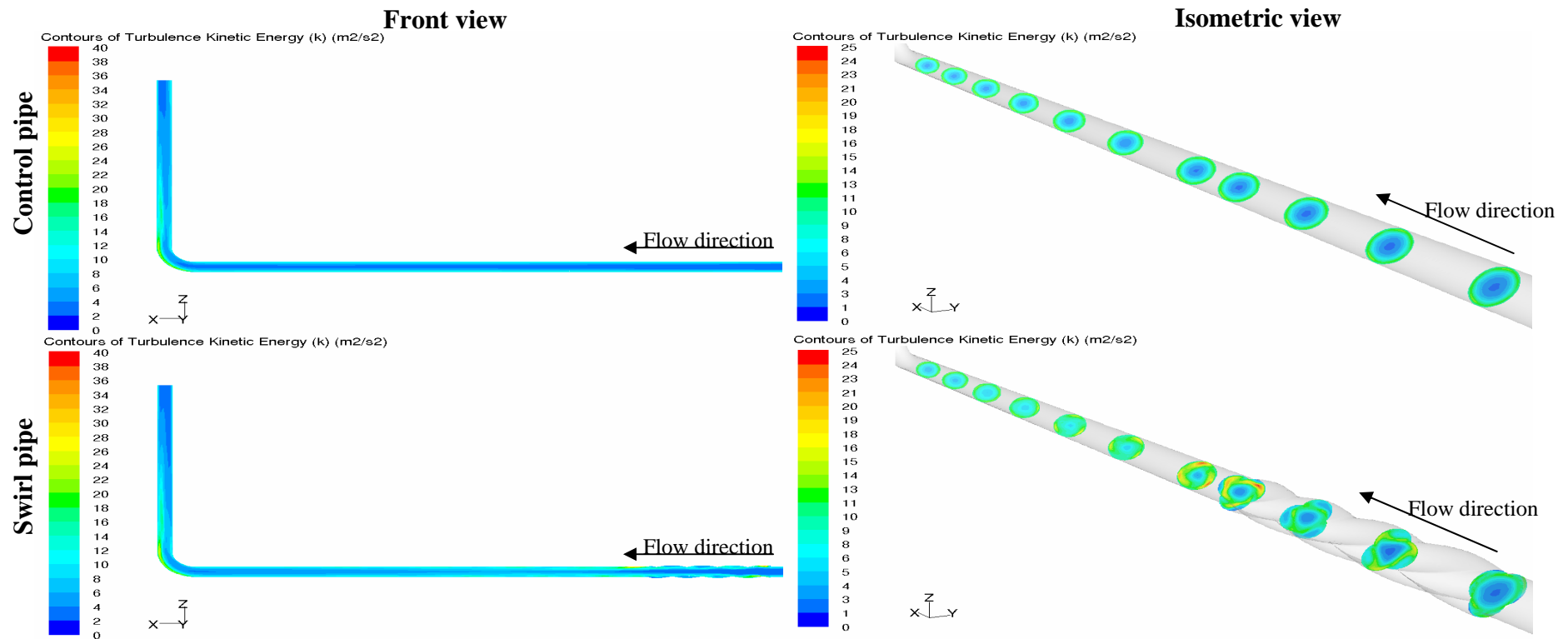


Figure 8.32: Turbulence kinetic energy distribution within model geometry for control and swirl pipe

8.6.4. Particles flow simulation

Particles trajectories can be predicted using the Lagrangian discrete phase model (DPM) supported by FLUENT version 6.2.16. The particles are simulated as a second phase consisting of spherical particles dispersed in the primary continuous phase of the flow field. This model follows the Euler-Lagrange approach, whereby the fluid phase is treated as a continuum to solve the time-averaged Navier-Stokes equations, while the dispersed phase is solved by tracking a large number of spherical particles through the calculated flow field.

A fundamental assumption made in this model is that the dispersed second phase occupies a low volume fraction, usually less than 10-12% that is typical of lean phase pneumatic conveying systems. The flow to be studied is the high Reynolds number flow with a particle seeding of 0.004kg/s. The resulting flow has a solids volume fraction of 0.08 and this model is therefore applicable. This sufficiently low particle concentration in turn enables the assumption that particle/particle interactions and the effect of the particle volume fraction on the gas flow are negligible. Since it is assumed that the presence of the solid phase does not affect the behaviour of the much more dominant fluid phase, one way-coupling can be considered. The behaviour of the injected particles in the turbulent flow is therefore carried out as a post-processing operation, whereby a converged solution for the air only flow within the model is used to construct a discrete phase model.

8.6.4.1 Equations of motion for particles

Initial input conditions such as the initial position, velocity and size of individual particles are used to initiate trajectory calculations. As the particle moves through the flow, the trajectory calculations are predicted by integrating the force balance on the particle. This force balance, shown in Equation 8.1, equates the particle inertia with the forces acting on the particle due to the local continuous phase conditions, such as hydrodynamic drag, gravity force, rotational force, shear forces, forces due to pressure gradient and the virtual mass force.

$$\frac{\partial u_p}{\partial t} = \underbrace{F_D(u - u_p)}_{\text{Drag force per unit particle mass}} + \underbrace{\frac{g(\rho_p - \rho)}{\rho_p}}_{\text{Gravity force}} + \underbrace{F}_{\text{Other forces such as virtual mass force (force required to accelerate the fluid surrounding the particles), pressure gradient in the fluid, forces on particles due to rotation of the frame of reference, lift forces due to shear, etc.}} \quad \text{Eq. (8.1)}$$

A stepwise integration method over discrete time steps is adopted to solve the particle trajectories.

8.6.4.2 Stochastic particle tracking in turbulent flow

The dispersion of particles due to turbulence in the fluid phase was predicted using the stochastic tracking model, whereby along the particle path the instantaneous fluid velocity, $\bar{u} + u'(t)$, for individual particles is used in the integration of the trajectory equations. This generates a sufficient number of representative particles (termed the “number of tries”) to account for the random effects of turbulence on the particle dispersion. The number of tries was specified as 20 for these simulation cases, causing each trajectory calculations to be performed with a new stochastic representation of the turbulent contributions to the trajectory equation.

Moreover, the Discrete Random Walk (DRW) model, or the “eddy lifetime” model, was implemented to simulate the interaction of a particle with a succession of discrete stylised fluid phase turbulent eddies.

An uncoupled (or 1-way coupling) approach was employed to describe the interaction between the two phases, whereby the discrete phase patterns are predicted based on a fixed continuous phase flow field. Hence the continuous phase always impacts the discrete phase, but the particles do not interact with the continuous phase. This was believed to be sufficient since the particles being simulated were small enough to be fully suspended in the flow and expected to faithfully follow the flow field. “Interaction with the continuous phase” option was enabled to make the discrete phase susceptible to the continuous phase. The particles were tracked and DPM sources were updated at intervals

of 25 iterations of the continuous phase. For steady-state simulations, like this one, a higher “number of continuous phase iterations per DPM iteration” increases the stability of the convergence, but requires more iteration to converge.

8.6.4.3 Boundary and initial conditions for the discrete phase

Inert particles were created to represent Fillite particles. An “inert” particle is a discrete phase element that obeys the force balance (Equation 8.2). The particles were defined by a density of 700 kg/m^3 and a Rosin-Rammler diameter distribution described by:

$$Y_d = e^{-\left(\frac{d}{d_e}\right)^n}$$

The Fillite particles distribution that was simulated was characterised by:

- Minimum diameter (the smallest diameter to be considered in the size distribution) = $0.494 \text{ } \mu\text{m}$
- Maximum diameter (the largest diameter to be considered in the size distribution) = $415.745 \text{ } \mu\text{m}$
- Mean diameter = $115 \text{ } \mu\text{m}$
- Spread parameter = 1.376

The particles were injected from a surface located at the venturi section of the feeder (3.64 pipe diameters downstream of the inlet), as shown in Figure 8.33. The initial conditions for the discrete phase are specified at the injection plane as follows:

- Velocities (u,v,w) of the particle = 0
- Mass flow rate of the particle stream that will follow the trajectory of the individual particle = 0.004 kg/s
- Particle injection is uniformly distributed on the injection surface, located at 3.66 pipe diameters from the air inlet plane

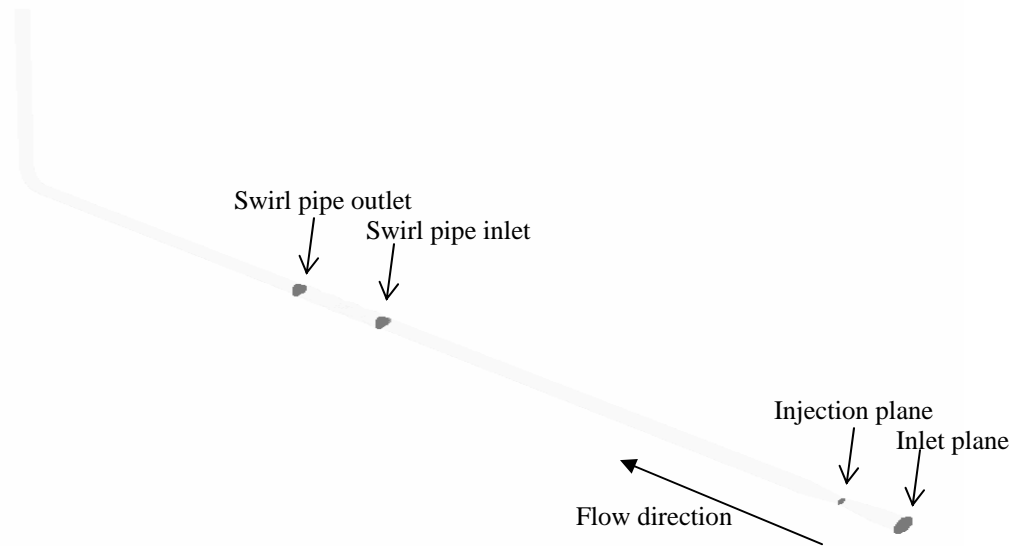


Figure 8.33: Location of injection plane in reference to rig inlet and swirl pipe inlet

These initial conditions provided the starting values for all of the dependent discrete phase variables that described the instantaneous conditions of an individual particle. These dependent variables were automatically updated according to the equations of motion (Equation 8.1) as the particle moves along its trajectory.

Boundary conditions for the models were set to determine the fate of the trajectory at that boundary. Upon hitting the wall, the fate of particles was assumed to rebound by applying the “reflect” boundary condition type at the walls. The change of momentum upon the collision is determined by the coefficient of restitution. The normal coefficient of restitution defines the amount of momentum in the direction normal to the wall that is retained by the particle after the collision with the boundary. Similarly, the tangential coefficient of restitution defines the amount of momentum in the direction tangential to the wall that is retained by the particle. Because a smooth Perspex or glass pipe was used in the experiments, a normal or tangential coefficient of restitution equal to 1.0 was applied, implying that the particle retains all of its normal or tangential momentum after the rebound (an elastic collision and all normal and tangential momentum are retained). The “escape” boundary condition type was automatically applied at the outflow boundary.

“Escape” reports the particle as having “escaped” when it encounters the boundary in question. Trajectory calculations are then terminated.

8.6.5. Particles flow simulation results

8.6.5.1 Pressure drop

The twisted 3-lobed geometry of the swirl pipe is a crucial feature to generate the secondary flow responsible for swirl flows, which has been shown cannot be generated by circular pipes. However, the 3-lobed cross-sectional geometry with twist of the swirl pipe has also been shown to cause more pressure loss than a circular pipe. This extra pressure drop is responsible for changing the axial momentum into the angular momentum and generating the swirl flow. The addition of particles into such a flow is therefore expected to produce even more pressure drop as more energy is required to convey the particles. This hypothesis is tested in the CFD simulation cases and the results for the high Reynolds number flow are shown in Figure 8.34.

It can be observed that air-only flow in the swirl pipe causes more pressure drop than air-only flow in the control circular pipe. The increased pressure drop is only visible from the exit of the swirl pipe into the circular visualisation pipe. When comparing the control pipe with air-only flow and air-particles flow, it can be observed that the addition of particles causes a high increase in pressure drop. This increase is more pronounced when the swirl pipe is in place. It can therefore be concluded that the addition of particles in an air-only flow causes pressure drop, but that a swirling particle flow causes higher levels of pressure drop.

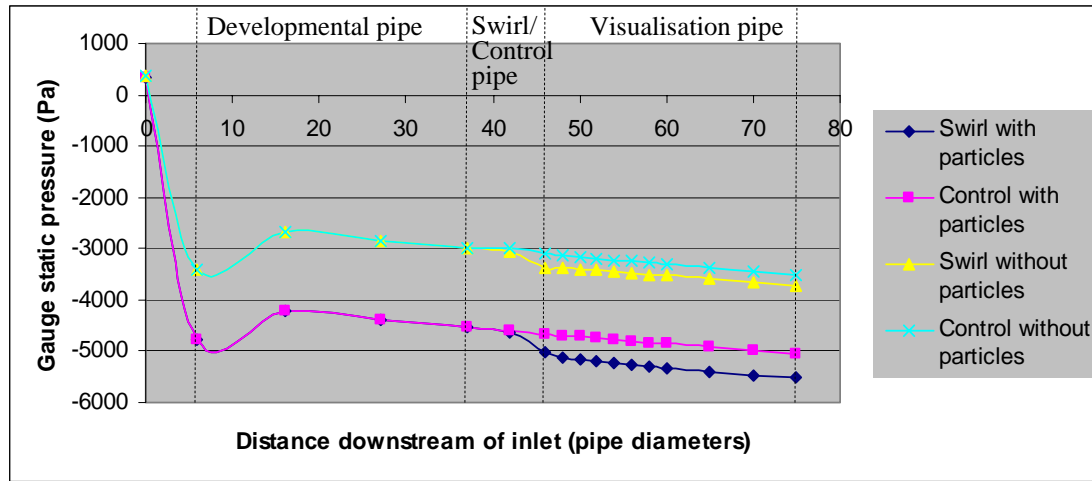


Figure 8.34: Pressure drop due to addition of particles

8.6.5.2 Particle tracks

To allow a better understanding of the kinetic behaviour of the particles in the swirl pipe, particle tracking was performed for the spherical particles in the solved flow domain. It was found that within the horizontal section of the control model, the particle tracks were practically straight, as shown in Figure 8.35. The simulation of particle flow within the swirl pipe model showed that the track followed by the particles could be broadly divided into two categories: swirling and straight. It was found that the trajectory followed by a particle was highly influenced by its location when it enters the swirl pipe. If it had a central core location, the particle seemed be unaffected by the swirl pipe and carried on a straight trajectory within and post the swirl pipe. On the other hand, if the particle entered the swirl pipe at the perimeter or in the lobed region, it was imparted with a swirling momentum within and post the swirl pipe. Within the swirl pipe itself, these particles tended to follow the helical paths defined by the cusps and ridges of the three lobe surfaces of the swirl pipe, as shown in Figure 8.35. This effect was still visible in the circular pipe section downstream of the swirl pipe. As a result of the high conveying air velocity at the centre of the pipe, the core particles travelled at higher velocities than the peripheral swirling particles, as shown in Figure 8.36. This result concurs with the description by Chiu and Seman (1971) of swirl flows in terms of primary and secondary flows, whereby the primary flow is parallel to the flow axis; the secondary flow is a

circulatory fluid motion about the axes parallel to the primary flow, hence the helical paths.

The trajectory of these particles showed that the pitch of the swirl imparted to them increased further away from the swirl pipe exit. This confirmed the earlier findings that the swirl decays with increasing distance from the swirl pipe exit. Unlike the experimental and computational results for the air-only flow within the rig, the particle flow simulation results showed that even at a distance of 30 pipe diameters, traces of the swirl component in the particle tracks were still present.

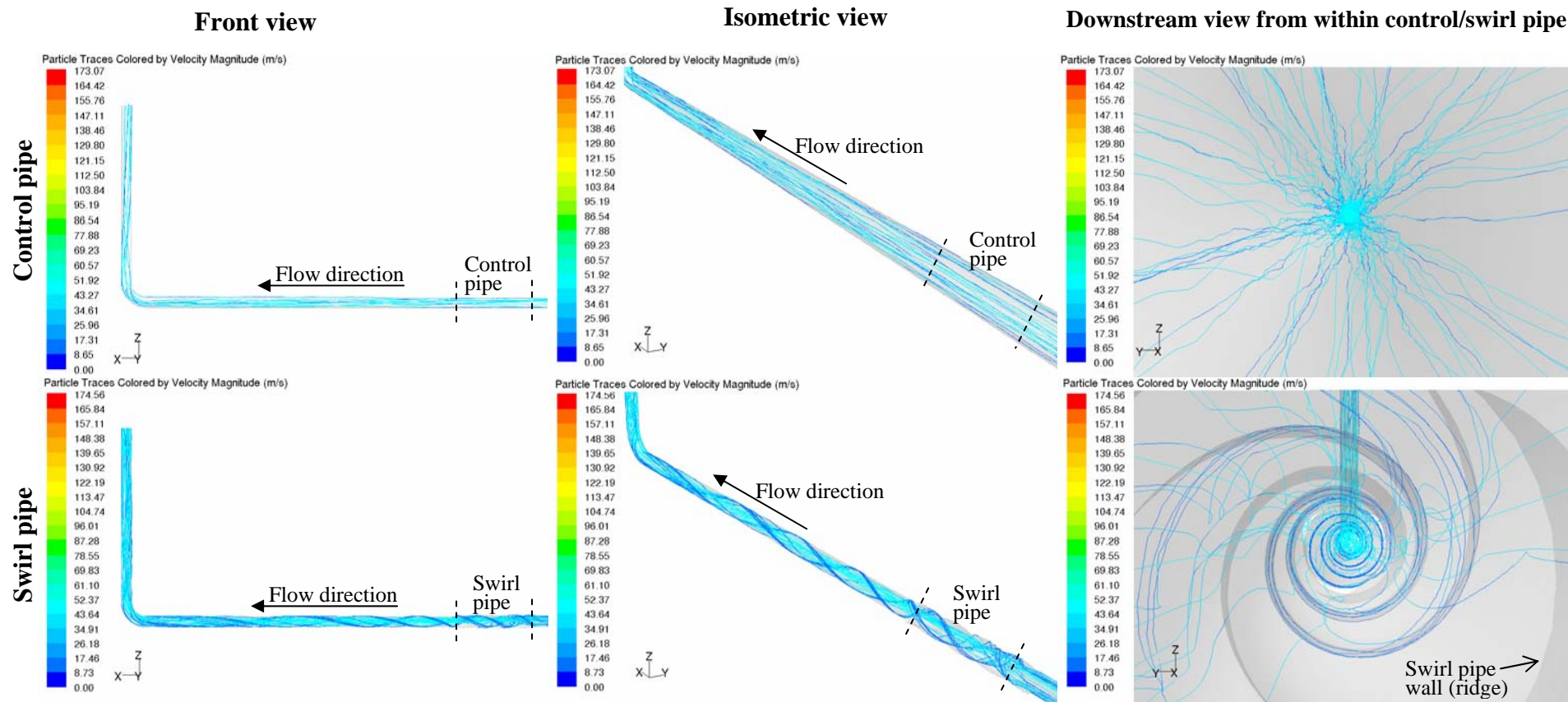


Figure 8.35: Particle tracks coloured by particles' velocity magnitude for high Reynolds flow in control and swirl pipe

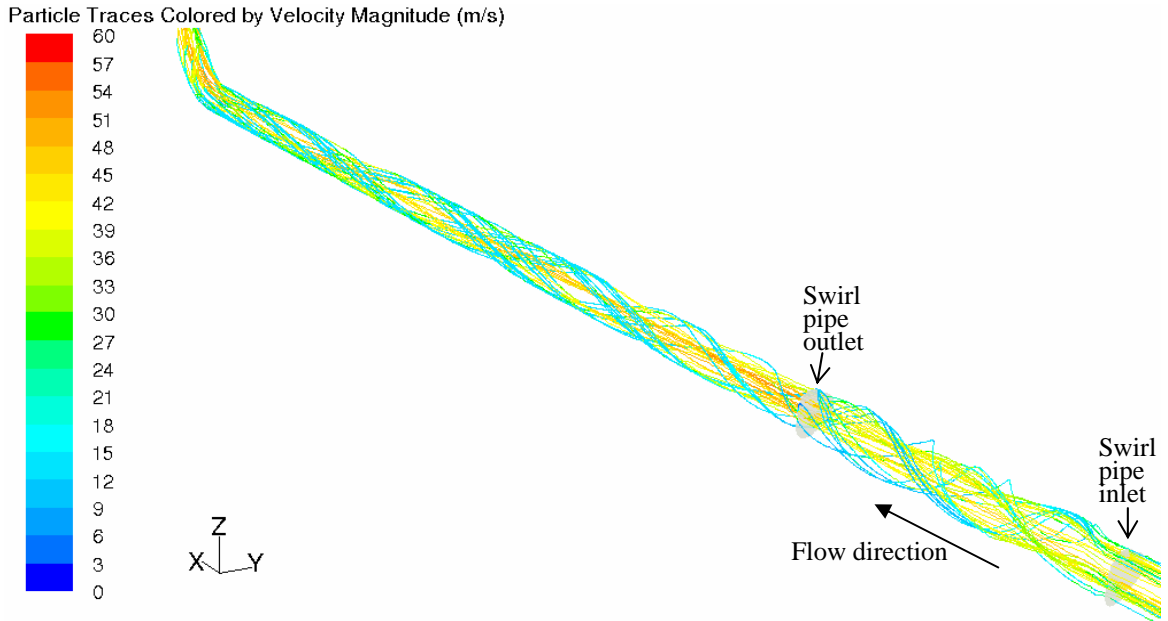


Figure 8.36: Particle tracks coloured by particle's velocity magnitude for high Reynolds flow in swirl pipe

Effect of particle diameter on particle tracks

How a particle responds to the rapid changes in the fluid motion surrounding it can be characterised by Stokes number. This was defined in Section 2.2, as the ratio of the aerodynamic response time of the particle to a characteristic time of the fluid motion, e.g. a nominal length, such as the pipe diameter, divided by the characteristic gas phase

velocity; $St = \frac{\tau_r}{\tau_f} = \frac{\rho_p d_p^2 U}{18 \mu_g D}$

Or the particle aerodynamic response time measured in terms of the eddy turnover time,

given by $\tau_n = \frac{\tau_r u_f^2 \rho_g}{\mu_g} = \frac{\rho_p d_p^2 u_f^2 \rho_g}{18 \mu_g^2}$ can also be used to the same purpose.

For any of the three Reynolds number flows considered, all the variables in the above two equations are constant, except for particle diameter, at any cross section of the flow in the streamwise direction. Since the simulated particles were not of a single diameter, but instead defined by a Rosin-Rammler distribution of diameters, with a minimum diameter

of $0.494\text{ }\mu\text{m}$ and a maximum diameter of $415.745\text{ }\mu\text{m}$, it can be expected that the different sized particles will respond differently to changes in the fluid motion surrounding them, as predicted by the particles' Stokes number and the particles' aerodynamic response time measured in terms of the eddy turnover time. Therefore the trajectory followed by a particle is expected to be highly influenced by its diameter.

In order to test this hypothesis, the particle tracks were coloured according to the diameter of the particle and were viewed from downstream as the particles entered the swirl pipe, within the swirl pipe, at the swirl pipe outlet and at various distances downstream of the swirl pipe into the circular visualisation pipe, as shown in Figure 8.37.

It was observed that the blue coloured tracks, of the smaller sized particles, follow small helical paths inside the first third of the swirl pipe. This is believed to be due to the presence of localised eddies formed because of the non-conformal cross-sectional geometry of the swirl and circular pipes, as shown in Figure 8.38. Since the particles are small enough ($St = 0.0003$), they are affected by these rapid changes in the fluid motion and hence the small helical paths. At two thirds through the swirl pipe the effects of these small localised vortices appear to have been overcome by the larger more powerful swirl due to the twisted 3-lobed geometry of the swirl pipe itself and the blue coloured tracks of the smaller sized particles acquire a general anticlockwise swirling motion, which they maintain at the swirl pipe exit and inside the visualisation pipe.

It is also observed that the blue coloured tracks of the smaller sized particles are primarily located on the outside periphery of the swirl pipe. This is due to the small particles being the most affected by centrifugal forces and being flung to the wall. The same reasoning would explain why the red coloured tracks of the largest sized particles are primarily located at the centre of the pipe. It appears that these particles are not affected by the swirl as their trajectories are almost straight. This would be explained by a higher Stokes number ($St = 225$) and hence the particles behave almost independently of the fluid motion.

Particle-wall collisions were observed to be significant inside the swirl pipe for the mid-size ranged particles. As can be seen from Figure 8.37, at 2.6 and 5.3 pipe diameters downstream of the swirl pipe inlet, the green and yellow coloured tracks of these mid-size ranged particles followed square helices as a result of particle-wall collisions with specified normal or tangential coefficients of restitution equal to 1.0. Particle-wall collisions were significantly less post the swirl pipe, into the visualisation pipe, where the particle tracks were smooth swirls in the same direction as the twists in the geometry of the swirl pipe.

The particles entering the swirl pipe inlet were observed to be concentrated in the upper left section of the swirl pipe. This is probably due to the high velocity in the pre-swirl developmental pipe, causing the particles to be fully suspended and concentrated in the top section of the pipe. However at the swirl pipe exit, it is observed that the particles are more uniformly distributed. This was attributed to the secondary circular flows. It can therefore be concluded that the swirl pipe results in effective mixing and redistribution of particles, making it particularly applicable as a pre-sampling device.

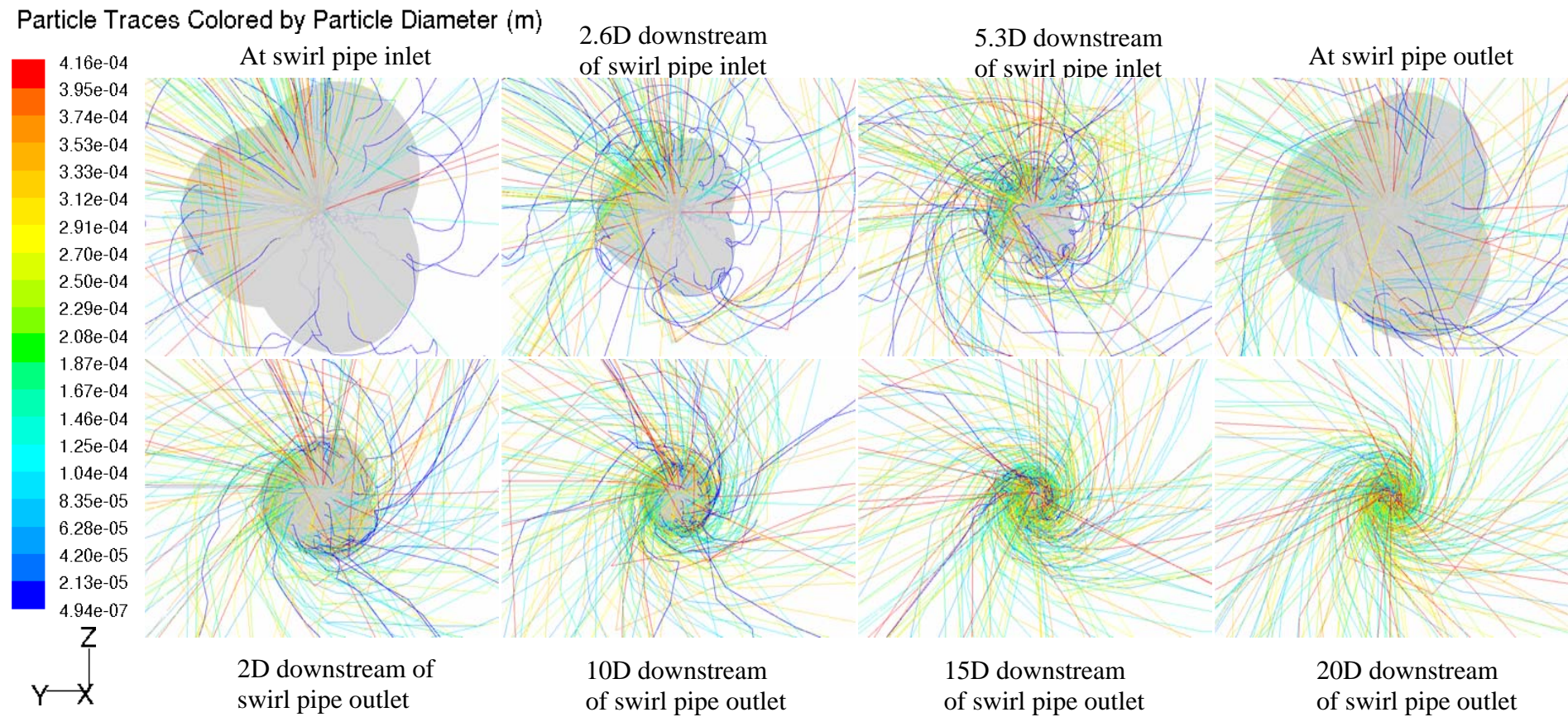


Figure 8.37: Particle tracks coloured by particle diameter for high Reynolds flow in swirl pipe

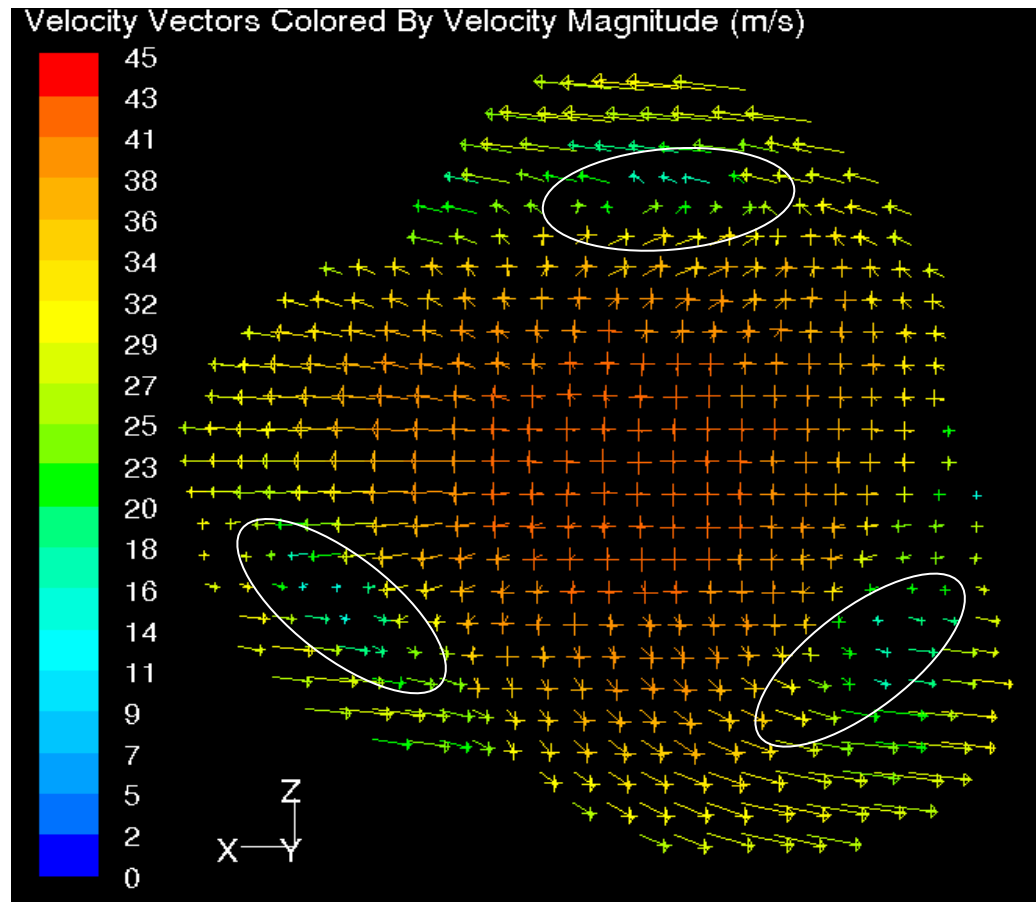


Figure 8.38: Velocity vectors showing localised eddies inside the swirl pipe (circled in white) due to the non-conformal cross-sectional geometries of the swirl and circular pipes

Effect of the conveying air velocity on particle tracks

In order to test the effect of the conveying air velocity on the particle trajectories, new simulation cases were run for the three Reynolds number flows but with the particle phase being characterised by a uniform diameter distribution of $115 \mu\text{m}$ (the mean diameter of the actual particle size distribution). Hence in these simulation cases, all the variables in the Stokes equations are constant, except for the mean conveying air velocity, U . The particle tracks are therefore expected to vary with the mean conveying air velocity and hence the Reynolds number of the flow.

The swirling effect was visible at all three Reynolds number flows, with low velocity particles travelling mostly on the outside edge of the pipe and the high velocity particles travelling mostly in the centre of the pipe. The velocity of the particles were directly

proportional to the Reynolds number of the flow. It was observed that prior to entering the swirl pipe, the particles of the high Reynolds number flow were the most segregated to the top section of the pipe, while this segregation effect was less pronounced for the low Reynolds number flow. The effective mixing and uniform redistribution of particles due to the swirl pipe was consequently better achieved for the low Reynolds number flow. Not much difference was observed in the pitch of the particle tracks for the three Reynolds number flows, possibly because the three conveying air velocities investigated were too close to each other.

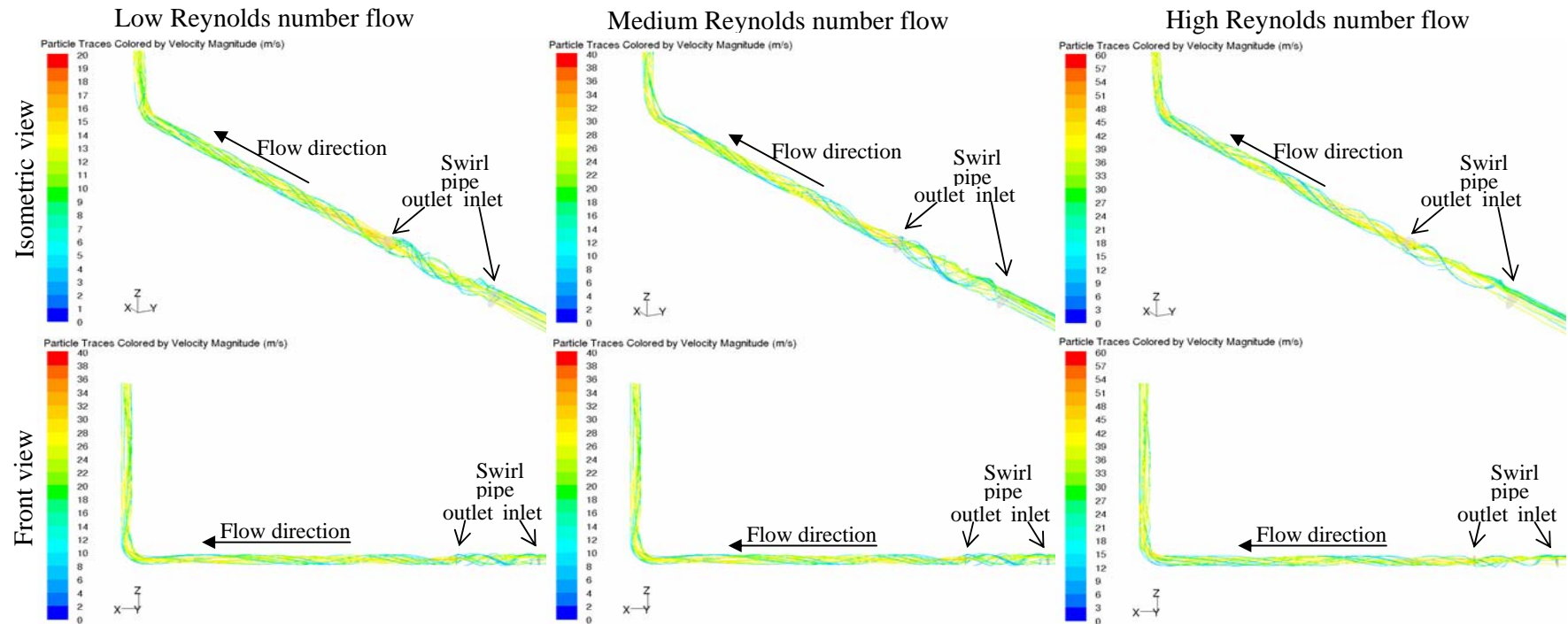


Figure 8.39: Particle tracks coloured by particles' velocity magnitude for low, medium and high Reynolds flow in swirl pipe

8.7 CONCLUSIONS

The first section of Chapter 8 was devoted to the validation of the CFD models of the pneumatic rig for testing the swirl pipe. Six simulation cases were run to account for the all three Reynolds number flows with either the swirl or the control pipe section.

The first validation parameter was the average static gauge pressure at the same plane locations at which static gauge pressure was measured during the experimental work. Velocity data obtained from the Laser Doppler Anemometry (LDA) experimental work as reported in Chapter 6 were used as additional validation parameters.

A maximum discrepancy of 20% existed in the pressure drop predictions and these were attributed to experimental shortcomings and assumptions made in the CFD models. The experimental shortcomings include the dampening effect by the water in the U-tube manometer reducing the sensitivity of the instrument, air leakages at the tappings/rubber tubing, rubber tubing/plastic connector and rubber tubing/manometer linkages. Fan fluctuations experienced during the experiments were not taken into account by the CFD models which assumed a steady flow. Moreover, the effects of the fan fluctuations were aggravated by the pressure measurements having been taken sequentially, while the predictions of the CFD model were based on a steady flow. All these would have contributed to the discrepancy between the measured and predicted results.

Good agreement in trend and accuracy was observed between the experimental and predicted axial velocities, with a maximum 7.5% difference between the sets of results. The computational results under predicted the tangential velocities by an average of 35%, when compared to experimental results. The difference is believed to be due to the steady state of the computational model compared to the fan fluctuations experienced during the experiments. Despite this, the computational w-velocity and tangential velocity profiles still followed the same trend as the experimental ones. Swirl intensity values were also overpredicted due to its strong dependency on tangential velocity. The swirl decay rates were in accordance with those resulting from the experiments.

Overall, the CFD models were successfully validated and employed to further our understanding of the geometrically induced swirl flow. The numerical solutions also confirmed, in agreement with the experimental observations that:

- a swirl flow is generated at the downstream end of the swirl pipe;
- the swirl pipe creates turbulence which imparts higher velocity to the flow - the core the axial velocity of the flow was increased up to about 14 pipe diameters downstream of the swirl pipe outlet;
- axial velocities were minimum at the pipe wall and maximum at the centre of the pipe. In contrast, tangential velocity is minimum at the centre of the pipe with a sudden increase in the region $0.25 < r/R < 0.88$, before decreasing to zero again at the pipe wall. The swirl pipe therefore causes a redistribution of momentum from axial to tangential, thereby confirming that the swirl pipe imparts a swirl component to the flow;
- the tangential velocity profile confirmed the swirl type characteristics to be that of wall jet swirls;
- the induced swirl decays with respect to increasing distance downstream and decreasing Reynolds number;
- pressure drop predictions confirmed that the transfer of axial to angular momentum was accompanied by a pressure drop proportional to the Reynolds number of the flow.

Moreover, the numerical static pressure results also showed a sudden drop when the flow exits the swirl pipe into the visualisation pipe. It was believed to be due to the flow hitting the pipe wall created due to the non-conformal geometry of the swirl and circular pipe sections. This was confirmed by the turbulence dissipation rate results being highest in the lobed regions at the swirl inlet and outlet. This high turbulence dissipation rate is believed to occur when the flow hits the interface wall. The regions of high turbulence dissipation corresponded to those of high turbulence kinetic energy, which is the mean kinetic energy per unit mass associated with eddies and turbulent flow. It was shown that the non-conformal geometries of the swirl and circular pipe cause localised eddies and therefore reduces the efficiency of the swirl pipe.

Particles trajectories were simulated by employing the Discrete Phase Model (DPM) supported by FLUENT version 6.2.16. The Euler-Lagrange approach to gas-solid flow modelling was employed, thereby assuming a low volume fraction of the solid particles and negligible particle/particle interactions. The dispersion of particles due to turbulence in the fluid phase was predicted using a stochastic tracking model along with the Discrete Random Walk (DRW) model. An uncoupled (or 1-way coupling) approach was employed to describe the interaction between the two phases. The particles were defined as inert particles and characterised by their density and a Rosin-Rammler diameter distribution. The particles were injected from a surface located at 3.64 pipe diameters downstream of the inlet. Elastic collisions were assumed at the walls. Six simulation cases were run to account for the all three Reynolds number flows with either the swirl or the control pipe section.

From these simulations, it was concluded that the addition of particles in an air-only flow causes pressure drop, but that a swirling particle flow causes higher levels of pressure drop. To allow a better understanding of the kinetic behaviour of the particles in the swirl pipe, particle tracking was performed for the spherical particles in the solved flow domain. The following conclusions were made:

- the track followed by the particles could be broadly divided into two categories: swirling and straight, concurring with the description by Chiu and Seman (1971) of swirl flows in terms of primary and secondary flows, whereby the primary flow is parallel to the flow axis; the secondary flow is a circulatory fluid motion about the axes parallel to the primary flow, hence the helical paths;
- the trajectory followed by a particle was highly influenced by its location when it enters the swirl pipe - if it had a central core location, the particle seemed be unaffected by the swirl pipe and carried on a straight trajectory within and post the swirl pipe; if the particle entered the swirl pipe at the perimeter or in the lobed region, it was imparted with a swirling momentum within and post the swirl pipe;
- within the swirl pipe itself, these particles tended to follow the helical paths defined by the cusps and ridges of the three lobe surfaces of the swirl pipe;

- the core particles travelled at higher velocities than the peripheral swirling particles as a result of the high conveying air velocity at the centre of the pipe;
- swirl induced to the particles' tracks also decay with increasing distance from the swirl pipe exit and decreasing Reynolds number of the conveying flow;
- the trajectory followed by a particle is highly influenced by its diameter – with the smaller sized particles being affected by localised eddies which are formed at the swirl pipe inlet and outlet because of the non-conformal cross-sectional geometry of the swirl and circular pipes. The smaller sized particles therefore follow small helical paths for a rough distance of three pipe diameters before being overcome by the larger more powerful swirl due to the twisted 3-lobed geometry of the swirl pipe itself and acquiring a general anticlockwise swirling motion. The smaller sized particles are also more inclined to have tangential velocity imparted to them and therefore their tracks are concentrated on the periphery of the pipes. On the other hand, the tracks of the larger sized particles are primarily located at the centre of the pipe since these particles are not affected by the swirl and their motion is almost independent of that of the fluid motion;
- particle-wall collisions were observed to be significant inside the swirl pipe for the mid-size ranged particles, but less so in the circular visualisation pipe, where their tracks were smooth anticlockwise swirls;
- secondary circular flows are responsible for mixing and distributing the particle concentration more uniformly throughout the pipe cross section.

This chapter was paramount to this research and to improving our understanding of geometrically induced swirl. It confirmed the empirical findings of Chapter 6 and enhanced on that knowledge. Insights into the development and eventual decay of the geometrically induced swirl flow by a twisted three-lobed helix pipe is presented as well as the influence of the swirl flow on particle trajectories. The aims and objectives of this study are therefore met. The ability of the swirl pipe to locally increase the flow velocity is confirmed. This conclusion endorses the claims made in Chapter 1 about the application of the swirl pipe in regions along pneumatic conveying lines where the conveying velocity needs to be increased in order to maintain a suspended flow of particles.

CHAPTER 9

CONCLUSIONS AND RECOMMENDATIONS FOR FUTURE WORK

This thesis sought to address the fundamentals of introducing geometrically induced swirl to pneumatic conveying, including a closer examination of the parameterisation of swirl, for keeping the particles in suspension in lean phase pneumatic conveying without escalating the costs associated with generating high conveying energy. It proposed the use of a twisted three-lobed helix pipe to address some of the localized drops in conveying velocity through harnessing the effects of centrifugal force and the secondary flows generated by the swirl pipe geometry. The findings from this study based on applying and testing of a geometrically induced swirl to pneumatic conveying are significant and encouraging, as will be justified in this chapter, and provide the needed insights to the literature.

This thesis also aimed to provide a better understanding of the fluid dynamics involved in swirl-flow pneumatic conveying and its resultant particle distributions. It addressed a void of research in the literature considering that prior research has investigated the use of swirl in hydraulic rather than pneumatic flows.

The methodology adopted for this research combined both experimental and computational approaches. The experiments involved pressure studies, high speed video recordings, velocity measurements from Particle Image Velocimetry (PIV) and Laser Doppler Anemometry (LDA). The experiments allowed a preliminary assessment and understanding of the geometrically induced swirl. It also enabled the collection of in-situ data, contributing to the repository of empirical data on swirl flow in the literature and providing validation parameters with which to compare the computational models. The computational approach involved computational fluid dynamics (CFD) modelling. Once validated, these models were used to further investigate the swirl flow in order to complement and supplement the empirical findings.

As the present study primarily focused on the experimental investigation of relationships between geometrically induced swirls and lean phase pneumatic conveying, an experimental rig was built. The rig was composed of:

- a conical inlet to monitor the airflow rate;
- a feeding device in the form of a gravity hopper fitted with a gate and used in conjunction with a venturi
- conveyed material in the form of hollow spherical silicate microspheres, commercially available under the trade name of Fillite
- pressure tappings at regular intervals to enable pressure monitoring
- Perspex pipes for the main part of the rig and fused silica glass was used for the visualisation and measurement section
- a cyclone to separate the solids from the airflow
- two 1800W centrifugal fans in series as the air mover

Three Reynolds number flows were identified at which to conduct the experiments and the same conditions were specified for the CFD models. These conditions are summarised in Table 9.1.

Flow	Reynolds number	Mean air velocity at inlet (m/s)	Inlet mass flowrate (kg/s)
Low	4.5×10^4	10	0.023
Medium	9.0×10^4	20	0.048
High	1.5×10^5	30	0.071

Table 9.1: Experimental and computational inlet flow conditions

Control experiments and simulations were also conducted at the same conditions but with a circular cross section pipe of the same length as the swirl pipe instead of the swirl pipe.

The flows were simulated using a commercial CFD software, FLUENT version 6.2.16, by employing the k- ϵ turbulence model to obtain a baseline solution which was refined

using the Reynolds Stress model. Standard wall function was implemented as the near wall treatment, the SIMPLE method was applied for the pressure-velocity coupling. Moreover, for convection terms, standard pressure discretisation scheme was employed and second-order central difference was used for viscous terms. Gravity and wall roughness were accounted for in relation to the fluid flow. Grid interfaces were applied at the intersection of the swirl and circular pipes due to their non-conformal boundaries. Particle trajectories were also simulated by employing the Lagrangian Discrete Phase Model (DPM). The stochastic dispersion of particles due to turbulence in the fluid phase was accounted for. The interaction between the fluid and particulate phase was modelled using a 1-way coupling approach. The particles were defined as inert particles, with a Rosin-Rammler diameter distribution and injected from a surface located at the venturi of the solids feeder section. Particle/wall collisions were modelled as being elastic.

9.1 CONCLUSIONS

The high speed camera experiments showed that the particles were fully suspended in the flow. It was concluded that the particles followed the more or less the same path as that of the airflow. The motion of the particles was hence inferred from that of the airflow for the PIV and LDA experiments due to the nature of these techniques.

Good agreement between predicted and experimental results was obtained for u , v , w velocity values at different locations post the swirl and control pipe. Despite the CFD model respectively under- and over-predicting tangential velocities and swirl intensity values, the CFD predictions still followed the same trend as the experimental results and the predicted swirl decay rates were in accordance with those resulting from the experiments. The models accurately predicted the trend of the gauge static pressure results when compared to experimental results, but slightly over predicted the values. Discrepancies between the empirical and computational results are believed to be due experimental shortcomings and simplifying assumptions made in the CFD simulations. The experimental shortcomings included a dampening effect by the water in the U-tube manometer reducing the sensitivity of the instrument, air leakages at the tappings/rubber tubing, rubber tubing/plastic connector and rubber tubing/manometer linkages, and finally to the steady state of the computational model compared to the

fan fluctuations experienced during the experiments. Errors and measurement uncertainties were found to be insignificant when compared to the actual values.

The findings of the experimental and computational work are summarised below:

- Visualisation experiments with the high speed camera, PIV and LDA measurements and numerical predictions all proved that the swirl pipe was effectively inducing swirl to the lean phase pneumatic flow. A decaying swirl pattern was formed in the same direction as the twists in the swirl pipe geometry, which is non-existent when the control pipe was used. The visualisation experiments also showed that the swirl patterns for a lean phase pneumatic flow were of the form of a ribbon effect, resulting in high and low regions of particle concentrations.
- Axial velocities were minimum at the pipe wall and maximum at the centre of the pipe. In contrast, tangential velocity is minimum at the centre of the pipe with a sudden increase in the region $0.25 < r/R < 0.88$, before decreasing to zero again at the pipe wall. The swirl pipe therefore causes the impartation of a tangential velocities, whereby adding an angular momentum to the flow, which appears as the swirl motion observed. These were confirmed both experimentally and computationally.
- The pressure experiments and predictions showed that the transfer of axial to angular energy was accompanied by a pressure drop proportional to the Reynolds number of the flow. It was also shown that the addition of particles in an air-only flow causes pressure drop, but that a swirling particle flow causes higher levels of pressure drop.
- The tangential velocity profiles from both the experimental and computational work allowed the swirl type to be characterised as wall jet swirls.
- Both the experimental and computational work confirmed that the swirl pipe creates turbulence which imparts an angular velocity to the flow. The swirl pipe was found to increase the core the axial velocity of the flow up to about 14 pipe diameters downstream of the swirl pipe outlet. The computational models suggested that this in turn affected the velocities of the suspended particles, with

the core particles travelling at higher velocities than the peripheral swirling particles.

- The degree of the swirl component at each location was quantified using the swirl numbering both the experimental and computational work. The geometrically induced swirl was found to decay with increasing distance downstream of the swirl pipe and inversely with the Reynolds number of the flow.
- The numerical static pressure results also showed a sudden drop when the flow exits the swirl pipe into the visualisation pipe. It was believed to be due to the flow hitting the pipe wall created due to the non-conformal geometry of the swirl and circular pipe sections. This was confirmed by the turbulence dissipation rate results being highest in the lobed regions at the swirl inlet and outlet. This high turbulence dissipation rate is believed to occur when the flow hits the interface wall. The regions of high turbulence dissipation corresponded to those of high turbulence kinetic energy, which is the mean kinetic energy per unit mass associated with eddies and turbulent flow. It was shown that the non-conformal geometries of the swirl and circular pipe cause localised eddies and therefore reduces the efficiency of the swirl pipe.
- As predicted by the numerical models, the tracks followed by the particles could be broadly divided into two categories: swirling and straight, whereby the primary flow is parallel to the flow axis and the secondary flow is a circulatory fluid motion about the axis of the primary flow.
- The trajectory followed by a particle was highly influenced by its location when it enters the swirl pipe - if it had a central core location, the particle seemed to be unaffected by the swirl pipe and carried on a straight trajectory within and post the swirl pipe; if the particle entered the swirl pipe at the perimeter or in the lobed region, it was imparted with a swirling momentum within and post the swirl pipe.
- The numerical models further suggested that within the swirl pipe itself, the internal surface of the swirl pipe greatly influence the trajectories of the particles, which tended to follow the helical paths defined by the cusps and ridges of the three lobe surfaces.

- The trajectory followed by a particle is highly influenced by its diameter - with the smaller sized particles being affected by localised vortices which are formed at the swirl pipe inlet and outlet because of the non-conformal cross-sectional geometry of the swirl and circular pipes. The smaller sized particles therefore follow small helical paths for a rough distance of three pipe diameters before being overcome by the larger more powerful swirl due to the twisted 3-lobed geometry of the swirl pipe itself and acquiring a general anticlockwise swirling motion. The smaller sized particles are also more affected by centrifugal forces and therefore their tracks are concentrated on the periphery of the pipes. On the other hand, the tracks of the larger sized particles are primarily located at the centre of the pipe since these particles are not affected by the swirl and their motion is almost independent of that of the fluid motion.
- From the computational models, particle-wall collisions were observed to be significant inside the swirl pipe for the mid-size ranged particles, but less so in the circular visualisation pipe, where their tracks were smooth anticlockwise swirls.
- Secondary circular flows were predicted to be responsible for mixing and distributing the particle concentration more uniformly throughout the pipe cross section by the computational models.

It was concluded that these effects were due to the presence of the swirl pipe as no such effects could be observed with the control pipe.

9.1.1 Contribution to knowledge

This section explicitly highlights how this work makes an original contribution to knowledge. Accordingly, the following eight points are offered as the principal contributions that have been made by this thesis:

- a thorough literature review of experimental and computational work carried out on lean phase pneumatic conveying
- experimental investigation of swirl-induction on a straight pipe section to better understand the influence of the swirl pipe on an airflow and therefore, by inference on lean gas-solid flows

- an extensive amount of experimental data and its use in validation of CFD predictions
- the application of CFD modelling techniques for swirl-inducing pipe flow and the validation of its predictions
- an improved understanding of the generation, development and eventual decay of the geometrically induced swirl by a twisted three-lobed helix pipe
- an improved understanding of the influence of the geometrically induced swirl on the particle distributions in swirl flow pneumatic conveying
- the identification of a novel approach to induce swirl to a pneumatic flow that is minimally intrusive to the flow and therefore does not obstruct the flow and cause any blockages
- the identification of a novel approach to locally increase the flow velocity in suspended flow pneumatic pipelines and prevent particle settlement

9.1.2 Possible application of swirl-induction

The main advantage of the swirl pipe highlighted by the present study was the increased conveying velocity just downstream of the swirl pipe, and the effective mixing and uniform distribution of the particle concentration across the pipe cross section. This therefore makes the swirl pipe particularly suited to:

- increasing conveying velocity at a local level in regions along pneumatic conveying lines where the conveying velocity needs to be increased in order to maintain a suspended flow of particles
- improving the efficiency of in-process sampling devices, for example for quality assurance purposes
- ensuring uniform reaction or heating due to increased fluid-particles interactions should swirling flow pneumatic conveying be used for an in-process application involving chemical reactions or heat transfer

- redistributing particles evenly across the pipe section after a bend and thereby reducing pipe wear, although this has to be confirmed by further work as recommended in Section 9.2.

9.2 RECOMMENDATIONS FOR FUTURE WORK

Knowledge about the behaviour of air flow and a lean particle phase subjected to geometrically induced swirl has been advanced by the present research. There are still many areas in which more work need to be carried out on to further advance this knowledge. This section details some recommendations for future research based on the research carried out in this thesis.

9.2.1 CFD modelling

With improvements in commercial CFD code and computing facilities, enhancements on the model used to simulate the multiphase system should be investigated. In particular, 2-way coupling of the particles and continuous phase should be included in the Discrete Phase Model. This is currently highly computationally expensive but worth investigating as Sommerfeld (1995, 1998) showed that even at mass loading as low as 0.1, particle-particle collisions have a strong influence on the profiles of the particle mass flux, particle velocities and the fluctuating motions of the particles.

Pipe bends are an integral part of pneumatic flow pipeline systems and it is well documented that solid particles impinging on the outer wall of the bend form a relatively dense phase structure called a “rope” as a result of the action of centripetal forces (Akili et al, 2001; Levy and Mason, 1998; McCluskey et al, 1989; Bilirgen and Levy, 2001; Huber and Sommerfeld, 1994). When the particles impinge on the outer bend wall, the roping mechanism has been shown to result in pipe erosive wear. Raylor (1998) demonstrated that the application of a swirl pipe before a horizontal to vertical 90° bend can distribute the particles more evenly throughout and post the bend and could reduce local wear. Ganeshalingham (2002) concurred and construed that the dispersion of solid particles in the bend was due to interaction of strong swirl-induction with secondary flows, centripetal action and gravitational forces. The combinations of these forces lifted the particles along the outside wall and dispersed then across the bend generally reducing the impact of particles on the outside wall of

the bend. This reduced collisions and/or friction between particles and pipe wall, dispersing the particles more uniformly across the bends.

From the work reported in this thesis, it is believed that the swirl pipe will have the similar positive effect in reducing wear in bends for pneumatic flows. A CFD erosion study on swirl pipe prior and post bends in pneumatic flows should be performed to confirm this. Pipeline erosion wear is potentially also significant within the swirl pipe itself, since it was shown that the particles tended to travel along the ridges of the three lobe surfaces of the swirl pipe and follow the helical paths defined by them. A CFD erosion study of the swirl pipe in a horizontal pipeline section should be performed to evaluate the balance between wear versus benefits of the swirl pipe.

Since it was shown that the swirl pipe did induce swirl in the air and particles flow, CFD should also be used to optimise the geometry of the swirl-inducing pipe design to minimise pressure loss while maximising the benefits of swirls. Several aspects of the optimisation such as number of lobes, pitch-to-diameter ratio, effective length and diameter of the swirl pipe and the influence of the conveying velocity need to be considered for the optimal swirl-inducing pipe design.

Non-dimensional number, swirl effectiveness, can be used as a measure parameter to determine the optimum performance of the swirl pipe. Swirl effectiveness includes both induced swirl and pressure loss for a swirl-inducing pipe can be defined as follows:

$$Swirl\ Effectiveness = \frac{Swirl\ Intensity}{Normalised\ Pressure\ Loss} = \frac{\left(\frac{\int_0^R uwr^2 dr}{R \int_0^R u^2 r dr} \right)}{\left(\frac{2\Delta P}{\rho u^2} \right)} \quad (9.1)$$

Ganeshalingham (2002) found that for hydraulic flows, increasing the number of lobes increased the number of helical channels that produced centrifugal forces in the flow

field and thus increased the swirling flow motions. However the greater number of lobes also increased the pressure loss due to the increased direct contact between the wall and the fluid. Hence Ganeshalingham (2002) found a twisted 2-lobed swirl pipe to be the most effective. This was however discarded due to its relatively narrow flow path, which was believed to be prone to blocking. It would be interesting to find out if this is also the case for pneumatic flows.

In optimising the swirl pipe for hydraulic flows, Ganeshalingham (2002) also tested different pitch lengths over a pipe length of 0.4m. The author found that lowering the pitch to diameter ratio increased the amount of swirl flow motion, because the tighter the twist, or lower the P/D ratio, the greater the change of axial momentum to the angular momentum thus resulting in higher tangential-velocity as well as swirl intensity. The downside was an accompanied increase in pressure loss across the pipe. It was hence concluded that for hydraulic flows, a pitch to diameter ratio of 4 (helix traversed through 720 degree of rotation) was the most effective. It is worth repeating the same computational optimisation procedure to see the effect of pitch to diameter ratio on swirl pipe for pneumatic flows.

As well as the pitch to diameter ratio of the swirl pipe, the effect of pipe diameter and flow velocity on the optimum pitch to diameter ratios needs investigating, even if Ganeshalingham (2002) found little or no influence for hydraulic flows.

Finally, the effective length of swirl pipe for pneumatic flows needs to be established. Ganeshalingham (2002) recommended that for hydraulic flows a 0.4m long 4-lobed pipe with a pitch-to-diameter ratio of 8 and a 0.6m long 3-lobed pipe with a pitch-to-diameter ratio of 6 were more efficient. It is very likely that these recommendations need to be modified for pneumatic flows considering the difference between the viscosity and density of air and water.

It was found that the sudden change in cross-section due to non-conformal geometries at the lobed swirl/circular pipe intersections caused increased pressure drop and turbulence dissipation. It is therefore recommended that transition entry and exit pipes be designed once an optimal swirl pipe has been designed for pneumatic flows.

Ariyaratne (2005) showed that for hydraulic flows, entry transition pipes increased

swirl generated at the exit of the swirl pipe and reduced pressure losses and that exit transition pipes reduced exit pressure losses and showed a very small increase in swirl generated, but reduced the initial swirl decay. Transition entry and exit pipes are believed to help increase swirl intensity while decreasing the pressure drop across the swirl section for pneumatic flows as well. Once designed with CFD codes, prototypes should also be produced for experimental assessment.

9.2.2 Experimental work

In this research, the swirl pipe was tested in a horizontal section. However the rig was designed in such a way as to also enable the testing of the swirl pipe in the following locations:

- Before a horizontal-to-vertical bend
- After a horizontal-to-vertical bend
- In a vertical section
- Before a vertical-to-horizontal bend
- After a vertical-to-horizontal bend

It is believed that these experimental studies should be carried out, especially before and after a bend.

As mentioned earlier, pipe bends suffer from pipe erosive wear. Moreover, pipe bends contribute to the system pressure drop and particle degradation, which according to Worster and Denny (1955) occurs approximately at a rate proportional to the cube of flow velocity and square root of the distance. It is believed that one of the practical implications of swirl-inducing pipes lies in enhancing the distribution of particles from ropes to a homogeneous distribution, thereby alleviating all of the above. These were proven for hydraulic flows by Raylor (1998) and Ganeshalingham (2002). The above suggested experimental studies would be useful to confirm whether the swirl pipe is as effective in reducing the system pressure drop, bend erosion wear and particle degradation in pneumatic flows as it was shown to be for hydraulic flows.

It would also be useful to know how the particles distribute themselves downstream of the swirl pipe. With the current rig layout and the Fillite particles used, the most cost effective method would be through the use of indirect measurement technique developed by Sommerfeld (1994). The author uses an experimental arrangement similar to this present study for the high speed video recordings with laser sheeting. Image analysis is performed to determine the intensity of the incident light for each pixel of the images taken by the CCD camera. The intensity of the scattered light is then related to the particle size, incident light and residence time of the particle within the light sheet, so that the light intensity of each pixel can in turn be related to particle mass concentration.

The present study provided a set of interesting finds and it is hoped that along with the future studies that have been suggested, this research provides the fundamentals for future research.

BIBLIOGRAPHY

Adeniji-Fashola, A. and Chen, C. P. 1990, "Modeling of confined turbulent fluid-particle flows using Eulerian and Lagrangian schemes", *International Journal of Heat and Mass Transfer*, vol. 33, pp. 691-701.

Akilli, H., Levy, E. K., and Sahin, B. 2001, "Gas-solid flow behaviour in a horizontal pipe after a 90o vertical-to-horizontal elbow", *Powder Technology*, vol. 116, pp. 43-52.

Al-Rafai, Tridimas, Y. D., and Wooley, N. H. A study of turbulent flows in pipe bends. *Proceedings of the Institution of Mechanical Engineers* 204, 399-408. 1990.

Alekseenko, V. and Okulov, V. L. 1996, "Swirl flow in technical applications (review)", *Thermophys.Aeromechan*, vol. 3, no. 2, pp. 97-128.

Alekseenko, S. V., Kuibin, P. A., Okulov, V. L., and Stork, S. I. 1999, "Helical vortices in swirl flow", *Journal of Fluid Mechanics*, vol. 382, pp. 195-243.

Algifri, A. H. and Bhardwaj, R. K. 1985, "Prediction of the heat transfer for decaying turbulent swirl flow in a tube", *Int.J.Heat Mass Transfer*, vol. 28, no. 9, pp. 1637-1643.

Algifri, A. H., Bhardwaj, R. K., and Rao, Y. V. N. 1988, "Turbulence measurements in decaying swirl flow in a pipe", *Applied Scientific Research (The Hague)*, vol. 45, no. 3, pp. 233-250.

American Institute of Aeronautics and Astronautics 1998, *AIAA guide for the verification and validation of computational fluid dynamics simulations* American Institute of Aeronautics and Astronautics, Reston, VA.

Anderson, J. D. 1995, *Computational fluid dynamics: the basics with applications* McGraw-Hill, New York.

Ariyaratne, C. 2005, *Design and optimisation of swirl pipes and transition geometries for slurry transport*, PhD thesis, University of Nottingham.

Backshall, R. G. and Landis, F. 1969, "The boundary-layer velocity distribution in turbulent swirling pipe flow", *Journal of Basic Engineering* pp. 728-733.

Baker D.W. and Sayre, C. L. 1974, "Decay of swirling turbulent flow of incompressible fluids in long pipes", R. B. Dowdell, ed., *Indus. Soc of America*, pp. 301-312.

Bali, T. 1998, "Modelling of heat transfer and fluid flow for decaying swirl flow in a circular pipe", *International Communications in Heat and Mass Transfer*, vol. 25, no. 3, pp. 349-358.

Bali, T. and Ayhan, T. 1999, "Experimental investigation of propeller type swirl generator for a circular pipe flow", *International Communications in Heat and Mass Transfer*, vol. 26, no. 1, pp. 13-22.

- Barth, W. 1956, "Design and layout of the cyclone separator on the basis of new investigations", *Brennst Waerme Kraft*, vol. 8, pp. 1-9.
- Batchelor, G. K. 2000, *An introduction to fluid dynamics* Cambridge University Press, Cambridge.
- Bell, T. A., Boxma, A., and Jacobs, J. B. 1996 "Proceedings of the 5th World Congress of Chemical ", pp. 238-243.
- Bilirgen, H., Levy, E. K., and Yilmaz, A. 1998, "Prediction of pneumatic conveying flow phenomena using commercial CFD software", *Powder Technology*, vol. 95, pp. 37-41.
- Bilirgen, H. and Levy, E. K. 1999, "Design of flow mixing devices for pneumatic conveying systems", *American Society of Mechanical Engineers, Pressure Vessels and Piping Division*, vol. 337, no. 2, pp. 261-270.
- Bilirgen, H. and Levy, E. K. 2001, "Mixing and dispersion of particle ropes in lean phase pneumatic conveying", *Powder Technology*, vol. 119, no. 2-3, pp. 134-152.
- Bridle, I. and Woodhead, S.R. 2002, "Particle degradation in pneumatic conveyors: Use of data from a pilot-sized test facility to predict degradation in an industrial conveyor", *Proceedings of the Institution of Mechanical Engineers, Part E: Journal of Process Mechanical Engineering*, v 216, n 2, pp. 65-71.
- British Standard, E. S. B. 1997, *Fans for general purposes Part 1: Performance testing using standardized airways* BS 848-1.
- Brown, G. J., Reilly, D., and Mills, D. 1996, "Development of an ultrasonic tomography system for application in pneumatic conveying", *Measurement Science and Technology*, vol. 7, pp. 396-405.
- Burnett, A. J. 1993, "Wear in pneumatic conveying pipelines - A review of past and present work", *Powder Handling and Processing*, vol. 5, no. 2, pp. 123-128.
- Burnett, A. J., Pittman, A. N., and Bradley, M. S. A. 1998 "Observations on and the modelling of erosive wear of a long-radius pneumatic conveyor bend", 5th edn., pp. 369-379.
- Burnett, A. J. 2001, "Wear in pneumatic conveying pipelines- A review of past and present work", *Powder Handling and Processing*, vol. 5, no. 2, pp. 123-128.
- Busch, D. 2003, *Digital photography solutions* Muska and Lipman Pub, Indianapolis.
- Cao, J. and Ahmadi, G. 1995, "Gas-particle two-phase turbulent flow in a vertical duct", *International Journal of Multiphase Flow*, vol. 21, no. 6, pp. 1203-1228.
- Cartaxo, S. J. M. and Rocha, S. C. S. 2001, "Object oriented simulation of the fluid dynamics of gas-solid flow", *Powder Technology*, vol. 117, pp. 177-188.

- Chang, F. and Dhir, V. K. 1995, "Mechanisms of heat transfer enhancement and slow decay of swirl in tubes using tangential injection", *International Journal of Heat and Fluid Flow*, vol. 16, no. 2, pp. 78-87.
- Chen, T. and Zhou, L. 1997, "Numerical simulation of the behaviour of swirling gas-particle flows with different swirl numbers", *ISMNP*, vol. 2, pp. 52-27.
- Cheremisinoff, P. N. and Young, R. A. 2006, "Advancements in air pollution control", *Pollution Engineering*, vol. 7, no. 5, pp. 30-93.
- Chiu, C. L. and Seman, J. J. 1971, "Head loss in spiral solid-liquid flow in pipes," in *Advances in Solid-Liquid Flow in Pipes and Its Applications*, 1 edn, Zandi I., ed., Pergamon Press Inc, Oxford, pp. 227-236.
- Copestake, S. 2001, *Paintshop Pro 7 in easy steps*. Computer Step.
- Crowe, C. T. 1982, "Review - Numerical models for dilute gas-particle flows", *Journal of Fluids Engineering*, vol. 104, pp. 297-303.
- Crowe, C. T. 1982, "Numerical models for dilute gas-particle flows", *Journal of Fluids Engineering*, vol. 104, pp. 297-303.
- Crowe, C. T., Gore, R. A., and Troutt, T. R. 1985, "Particle dispersion by coherent structures in free shear flows", *Particulate Science And Technology*, vol. 3, pp. 149-158.
- Crowe, C. T. 1986, "Two-fluid v/s trajectory models; range of applicability", *American Society of Mechanical Engineers, Fluids Engineering Division*, vol. 35, pp. 91-95.
- Crowe, C. T. 1992, "Basic research needs in fluid-solid multiphase flows", *Proceedings of the Fluids Engineering Conference*, Los Angeles, CA, USA, vol. 134, pp. 51-52.
- Crowe, C. T., Johnson, R., Prosperetti, A., Sommerfeld, M., and Tsuji, Y. 1996, "Numerical methods for multiphase flows", San Diego, CA, USA, p. 1.
- Crowe, C. T., Troutt, T. R., and Chung, J. N. 1996, "Numerical models for two-phase turbulent flows", *Annual Review Fluid Mechanics*, vol. 28, pp. 11-43.
- Crowe, C. T. 1997, "Recent advances in modelling of turbulent gas particle flows", *Proceedings of the 1997 International Symposium on Multiphase Fluid, Non-Newtonian Fluid and Physico-Chemical Fluid Flows, ISMNP'97*, Beijing, China, p. 1.
- Crowe, C. T., Sommerfeld, M., and Tsuji, Y. 1998, *Multiphase flows with droplets and particles* CRC Press.
- Crowe, C. T., Troutt, T. R., and Chung, J. N. 2002, "Numerical models for two-phase turbulent flows", *Annual Review of Fluid.Mech.*, vol. 28, pp. 11-43.
- Dantec Dynamics. Principles of PIV.
<http://www.dantecdynamics.com/piv/Princip/Index.html> . 2006.

Dantec Dynamics. Principles of LDA.

<http://www.dantecdynamics.com/lda/Princip/Index.html> . 2006.

Davis, J. C. 1986, *Statistics and data analysis in geology*, second edn, John Wiley and Sons, New York.

Deloughry, R., Pickup, E., and Ponnappalli, P. 2001, "Closed loop control of a pneumatic conveying system using tomographic imaging", *Journal of Electronic Imaging*, vol. 10, no. 3, pp. 653-660.

Deng, T., Chaudhry, A.R., Patel, M., Hutchings, I., Bradley, M.S.A. 2005, " Effect of particle concentration on erosion rate of mild steel bends in a pneumatic conveyor" *Wear*, vol. 258, no. 1-4, pp. 480-487.

Durrani, T. S. and Clive, A. G. 1977, *Laser systems in flow measurement* Plenum Press, London.

Durst, F., Melling, A., and Whitelaw, J. H. 1981, *Principles and practice of laser-doppler anemometry*, 2 edn, Academic Press, London.

Durst, F., Milojevic, D., and Schonung, B. 1984, "Eulerian and Lagrangian predictions of particulate two-phase flows: a numerical study", *Applied Mathematical Modelling*, vol. 8, pp. 101-115.

Dyakowski, T., Jeanmeure, L. F. C., and Jaworski, A. J. 2000, "Application of electrical tomography for gas-solids and liquid-solids flows - a review", *Powder Technology*, vol. 112, pp. 174-192.

Eastman Kodak Company, M. A. S. D. 1998, *Kodak Motion Corder SR Ultra user's manual* Kodak, California.

Elghobashi, S. and Truesdell, G. C. 1993, "Two-way interaction between homogeneous turbulence and dispersed solid particles. I. Turbulence modification", *Physics of Fluids A: Fluid Dynamics*, vol. 5, no. 7, p. 1790.

Elghobashi, S. 1994, "On predicting particle-laden turbulent flows", *Applied Scientific Research (Hague)*, vol. 52, pp. 309-329.

Fluent Incorporated 2003, *GAMBIT (v2.1.6) User's Guide Manual* Fluent Incorporated, 10 Cavendish Court, Lebanon, New Hampshire, 03766, USA.

Fluent Incorporated 2004, *FLUENT (v6.2.16) User's Guide Manual* 10 Cavendish Court, Lebanon, New Hampshire, 03766, USA.

Ganeshalingam, J. 2002, *Swirl induction for improved solid-liquid flow in pipes*, PhD thesis, University of Nottingham.

Gibson, M. and Younis, B. A. 1986, "Calculation of swirling jets with a Reynolds stress closure", *Physics of fluids*, vol. 29, no. 1, pp. 38-48.

- Goldstein, R. J. 1996, *Fluid mechanics measurements*, 2 edn, Taylor and Francis, Washington DC.
- Gore, R. A. and Crowe, C. T. 1989, "Effect of particle size on modulating turbulent intensity", *International Journal of Multiphase Flow*, vol. 15, no. 2, pp. 279-285.
- Gore, R. A. and Crowe, C. T. 1989, "Effect of particle size on modulating turbulent intensity: influence of radial location", *American Society of Mechanical Engineers, Fluids Engineering Division*, vol. 80, pp. 31-35.
- Gore, R. A. and Crowe, C. T. 1990, "Turbulence in slurry pipe flow", *ASME Fluids Engineering Div.* Toronto, Ont, Can, vol. 98, pp. 175-178.
- Gore, R. A. and Crowe, C. T. 1991, "Modulation of turbulence by a dispersed phase", *Journal of Fluids Engineering*, vol. 113, no. 2, pp. 304-307.
- Grace, J. and Taghipour, F. Verification and validation of CFD models and dynamic similarity for fluidized beds. *Powder Technology* 139, 99-110. 2004.
- Gupta, A. K., Lilley, D. G., and Syred, N. 1984, *Swirl flows* Tunbridge Wells.
- Hauptman, P., Hoppe, N., and Puttmer, A. 2002, "Application of ultrasonic sensors in the process industry- a review article", *Measurement Science and Technology*, vol. 13, pp. 73-83.
- Hay, W. and West, P. D. 1975, "Heat transfer in free swirling flow in a pipe", *Journal of Heat Transfer, Transactions ASME*, vol. 97, no. 3, pp. 411-416.
- Herbreteau, C. and Bouard, R. 2000, "Experimental study of parameters which influence the energy minimum in horizontal gas-solid conveying", *Powder Technology*, vol. 112, pp. 213-220.
- Hilbert, J. D. Jr. 1984, "Splitting of pneumatic conveying pipelines", *Bulk Solids Handling*, vol. 4, no. 1, pp. 189-192.
- Hirai, S., Takagi, T., Tanaka, K., and Kida, K. 1987, "Effect of swirl on the turbulent transport of momentum in a concentric annulus with a rotating inner cylinder", *Trans.JSME*, vol. 53, p. 432.
- Hirai, S., Takagi, T., and Matsumoto, M. 1998, "Prediction of the laminarization phenomena in turbulent swirling flows", *ASME Journal of Fluids Engineering*, vol. 110, p. 424.
- Hong, J., Shen, Y., and Tomita, Y. 1995, "Phase diagrams in dense phase pneumatic transport", *Powder Technology*, vol. 84, pp. 213-219.
- Huber, N. and Sommerfeld, M. 1994, "Characterisation of the cross-sectional particle concentration distribution in pneumatic conveying systems", *Powder Technology*, vol. 79, pp. 191-210.

Huber, N. and Sommerfeld, M. 1998, "Modelling and numerical calculation of dilute-phase pneumatic conveying in pipe systems", *Powder Technology*, vol. 98, pp. 90-101.

Huber, N. S. and Sommerfeld, M. 1999, "Experimental analysis and modelling of particle-wall collisions", *International Journal of Multiphase Flow*, vol. 25, pp. 1457-1489.

Hussainov, M., Kartushinsky, A., Rudi, U., Shcheglov, I., Kohnen, G., and Sommerfeld, M. 2000, "Experimental investigation of turbulence modulation by solid particles in a grid-generated vertical flow", *International Journal of Heat and Fluid Flow*, vol. 21, no. 3, pp. 365-373.

Hyder, L. M., Bradley, M. S. A., Reed, A. R., and Hettiaratchi, K. 2000, "An investigation into the effect of particle size on straight-pipe pressure gradients in lean-phase conveying", *Powder Technology*, vol. 112, pp. 235-243.

Jama, G. A., Klinzing, G. E., and Rizk, F. 1999, "Analysis of unstable behavior of pneumatic conveying systems", *Particulate Science And Technology*, vol. 17, pp. 43-68.

Jaworski, A. J. and Dyakowski, T. 2001, "Application of electrical capacitance tomography for measurement of gas-solids flow characteristics in a pneumatic conveying system", *Measurement Science and Technology*, vol. 12, pp. 1109-1119.

Jones, M.G. and Williams, K.C. 2003, "Solids Friction Factors for Fluidized Dense-Phase Conveying", *Particulate Science and Technology*, vol. 21, pp. 45-56.

Jones, T. F. 1993, *Improved slurry presentation for measurement, control and optimisation: In-situ diagnostic methods*. ECSC Coal RTD Programme.

Kalman, H. 1999, "Attrition control by pneumatic conveying", *Powder Technology*, vol. 104, pp. 214-220.

Kalman, H. 2000, "Attrition of powders and granules at various bends during pneumatic conveying", *Powder Technology*, vol. 112, pp. 244-250.

Kenning, V. and Crowe, C. T. 1994, "Effect of solids concentration on self-induced turbulence", *American Society of Mechanical Engineers*, vol. 189, pp. 71-74.

Kenning, V. M. and Crowe, C. T. 1997, "On the effect of particles on carrier phase turbulence in gas-particle flows", *International Journal of Multiphase Flow*, vol. 23, no. 2, pp. 403-408.

Khodadadi, J. M. and Vlachos, N. S. 1990, "Effects of turbulence model constants on computation of confined swirling flows", *AIAA Journal*, vol. 28, no. 4, pp. 750-752.

Kitoh, O. 1991, "Experimental study of turbulent swirling flow in a straight pipe", *Journal of Fluid Mechanics*, vol. 225, pp. 445-479.

Kline, S. J., Reynolds, W. C., Schraub, F. A., and Runstadler, P. W. 1967, "The structure of turbulent boundary layers", *Journal of Fluid Mechanics*, vol. 30, pp. 741-773.

- Kobayashi T. and Yoda M. 1987, "Modified k -e model for turbulent swirling flow in a straight pipe", *JSME International Journal, Series 2: Fluids Engineering, Heat Transfer, Power Combustion, Thermophysical Properties*, vol. 259, no. 30, pp. 66-71.
- Kreith, F. and Sonju, O. K. 1965, "The decay of a turbulent swirl in a pipe", *Journal of Fluid Mechanics*, vol. 22, pp. 257-271.
- Kussin, J. and Sommerfeld, M. 2002, "Experimental studies on particle behaviour and turbulence modification in horizontal channel flow with different wall roughness". *Experiments in Fluids* 33, pp.143-159.
- Lain, S. and Sommerfeld, M. 2003, "Turbulence modulation in dispersed two-phase flow laden with solids from a Lagrangian perspective", *International Journal of Heat and Fluid Flow*, vol. 24, no. 4, pp. 616-625.
- Lapple, C. E. 1951, "Processes use many collector types", *Chemical Engineering*, vol. 58, pp. 144-151.
- Launder, B. E. and Spalding, D. B. 1972, *Lectures in mathematical models of turbulence* Academic Press, London, England.
- Launder, B. E. and Spalding, D. B. 1974, "The Numerical Computation of Turbulent Flows", *Comp.Meth.Appl.Mech.Eng.*, vol. 3, pp. 269-289.
- Leith 1979, *Handbook of Environmental Engineering* Humana Press, New Jersey.
- Levy, A. and Mason, D. J. 1998, "The effect of a bend on the particle cross-section concentration and segregation in pneumatic conveying systems", *Powder Technology*, vol. 98, no. 2, pp. 95-103.
- Levy, A. and Mason, D. J. 1998, "Numerical investigation of the effect of bend radius on gas-solids flow in pneumatic conveying systems", *Powder Handling and Processing*, vol. 10, no. 3, pp. 249-253.
- Levy, A. and Mason, D. J. 2000, "Two-layer model for non-suspension gas-solids flow in pipes", *Powder Technology*, vol. 112, no.3, pp. 256-262.
- Levy, A. 2000, "Two-fluid approach for plug flow simulations in horizontal pneumatic conveying", *Powder Technology*, vol. 112, n 3, pp. 263-272.
- Levy, A. and Borde, I. 2001, "Two-fluid model for pneumatic drying of particulate materials", *Drying Technology*, vol. 19, no. 8, pp. 1773-1788.
- Levy, A. and Mason, D. J. 2001, "Two-layer model for non-suspension gas-solids flow in pipes", *Powder Technology*, vol. 112, no. 3, pp. 256-262.
- Li, H. and Tomita, Y. 1996, "An experimental study of swirling flow pneumatic conveying system in a horizontal pipeline", *ASME Journal of Fluids Engineering*, vol. 118, pp. 526-530.

- Li, H. and Tomita, Y. 1998 "Numerical simulation of swirling gas-solid flow in a vertical pipeline". *Proceedings of the 1998 ASME Fluids Engineering Division Summer Meeting*.
- Li, H. and Tomita, Y. 2000, "Particle velocity and concentration characteristics in a horizontal dilute swirling flow pneumatic conveying", *Powder Technology*, vol. 107, pp. 144-152.
- Li, H. and Tomita, Y. 2000, "A numerical simulation of swirling flow pneumatic conveying in a horizontal pipeline", *Particulate Science And Technology*, vol. 18, no. 4, pp. 275-291.
- Li.H., Nozaki, T., and Nakahori, K. 1999 "An experimental study on a horizontal swirling flow pneumatic conveying with a curve pipe", *Proceedings of the FEDSM*,
- Louge, M. Y., Mastorakos, E., and Jenkins, J. T. 1991, "The role of particle collisions in pneumatic transport", *Journal of Fluid Mechanics*, vol. 231, pp. 345-359.
- Lun, C. K. K. 2000, "Numerical simulation of dilute turbulent gas-solid flows", *International Journal of Multiphase Flow*, vol. 26, no. 10, pp. 1707-1736.
- Marcus, R. D. 1984, "Minimum energy pneumatic conveying 1 - Dilute phase", *Journal of Pipelines*, vol. 4, pp. 113-121.
- Marjanovic, P., Levy, A., and Mason, D. J. 1999, "An investigation of the flow structure through abrupt enlargement of circular pipe", *Powder Technology*, vol. 104, pp. 296-303.
- Martemianov, S. and Okulov, V. L. 2004, "On heat transfer enhancement in swirl pipe flows", *International Journal of Heat and Mass Transfer*, vol. 47, no. 10-11, pp. 2379-2393.
- Mason, D. J., Marjanovic, P., and Levy, A. 1998, "Simulation system for pneumatic conveying systems", *Powder Technology*, vol. 95, no. 1, pp. 7-14.
- Mason, D. J. and Levy, A. 1998, "Comparison of one-dimensional and three-dimensional models for the simulation of gas-solids transport systems", *Applied Mathematical Modelling*, vol. 22, no. 7, pp. 517-532.
- Mason, D. J., Levy, A., and Marjanovic, P. 1998, "Influence of bends on the performance of pneumatic conveying systems", *Advanced Powder Technology*, vol. 9, no. 3, pp. 197-206.
- Mason, D. and Li, J. 2000, "A novel experimental technique for the investigation of gas-solids flow in pipes", *Powder Technology*, vol. 112, pp. 203-212.
- McCluskey, D. R., Easson, W. J., Greated, C. A., and Glass, D. H. 1989, "The use of Particle Image Velocimetry to study roping in pneumatic conveyance", *Particle and Particle Systems Characterization*, vol. 6, pp. 129-132.

- McKee, S. L., Williams, R. A., Dyakowski, T., BELL, T. A., and Allen, T. 1993, "Industrial application of electrical tomography to conveying processes", *Chemical Engineering Research and Design*, vol. 71, pp. 347-349.
- McKee, S. L., Dyakowski, T., Williams, R. A., BELL, T. A., and Allen, T. 1995, "Solids flow imaging and attrition studies in a pneumatic conveyor", *Powder Technology*, vol. 82, pp. 105-113.
- Mills, D. 2004, *Pneumatic conveying design guide*, 2 edn, Elsevier Butterworth-Heinemann, Oxford.
- Miyazaki, K., Chen, G., Yamamoto, F., and Horii, K. 1999, "An investigation into sand transportation with spiral air flow".
- Murakhtina, T. and Okulov, V. L. 2000, "Changes in topology and symmetry of vorticity field during the turbulent vortex breakdown", *Tech.Phys.Lett.*, vol. 26, no. 10, pp. 798-800.
- Najafi, A. F., Saidi, M. H., Sadeghipour, M. S., and Souhar, M. 2005, "Numerical analysis of turbulent swirling decay pipe flow", *International Communications in Heat and Mass Transfer*, vol. 32, pp. 627-638.
- Narezhnyi, E. G. and Sudarev, B. V. 1975, "Calculation of the temperature of flame tubes of gas turbine combustion chambers with three-tier swirlers", *Heat Transfer-Soviet Res.*, vol. 6, pp. 23-27.
- Nejad A.S., Vanka S.P., Favaloro S.C., Samimy M., and Langenfeld C. 1989, "Appclation of laser velocimetry for characterization of confined swirling flow", *Journal of Engineering for Gas Turbines and Power*, vol. 111, pp. 36-45.
- Nishibori, K., Koji, K., Mitsukiyo, M., and Takeshi M. 1987, "Effect of inlet swirl on the turbulent flow in an axially rotating pipe.", *Trans.JSME*, vol. 53, pp. 1150-1158.
- Okulov, V. L. 1996, "The transition from the right helical symmetry to the left symmetry during vortex breakdown.", *Tech.Phys.Lett.*, vol. 22, no. 10, pp. 798-800.
- Osborne, W. C. 1977, *Fans*, 2 edn, Pergamon, Oxford.
- Pacific Pneumatics Inc. A Short History of Pneumatic Conveying .
<http://www.pacpneu.com/page14.html> . 2005.
- Pan, R. 1999, "Material properties and flow modes in pneumatic conveying", *Powder Technology*, vol. 104, pp. 157-163.
- Papadopoulos, D. G., Teo, C. S., Ghadiri, M., and BELL, T. A. 1998, "World Congress on Particle Technology", p. 156.
- Parchen R.R. and Steenbergen W. 1998, "An experimental and numerical study of turbulent swirling pipe flows", *Journal of Fluids Engineering*, vol. 120, pp. 54-61.

- Portela, L. M., Cota, P., and Oliemans, R. V. A. 2002, "Numerical study of the near-wall behaviour of particles in turbulent pipe flows", *Powder Technology*, vol. 125, pp. 149-157.
- Raffel, M. and Willert, C. E. K. J. 1998, *Particle image velocimetry : a practical guide* Springer, Berlin.
- Raylor, B. 1998, *Pipe design for improved distribution and improved wear*, PhD thesis, University of Nottingham.
- Reynolds, A. J. 1974, *Turbulent flows in engineering* Wiley, London.
- Roache, P. J. 1998, *Verification and validation in computational science and engineering* Hermosa publishers, Albuquerque, N.M.
- Robinson, P. A., Cusworth, R. A., and Sislian, J. P. 1986, *Laser Doppler velocimetry measurements in coaxial, co- and counter-swirling, isothermal jets*, University of Toronto. Institute for Aerospace Studies, Toronto, 308.
- Rocklage-Marliani G., Schmidts M., and Ram V.I.V. 2003, "Three-dimensional Laser-Doppler Velocimeter Measurements in Swirling Turbulent Pipe Flow", *Flow Turbulence and Combustion*, vol. 70, pp. 43-67.
- Roco, M. C. 1993, *Particulate two-phase flow* Butterworth-Heinemann, Boston.
- Rodi, W. 1975, "Note on the empirical constant in the kolmogorov-prandtl eddy-viscosity expression", *Journal of Fluids Engineering*, vol. 97, no. 3, pp. 386-389.
- Schallert, R. and Levy, E. K. 2000, "Effect of a combination of two elbows on particle roping in pneumatic conveying", *Powder Technology*, vol. 107, pp. 226-233.
- Schlichting, H. and Gersten, K. 2000, *Boundary-layer theory*, 8th rev. and enl. ed. edn, Springer, Berlin.
- Schott Glass, B. D. Schott Glas Borofloat catalogue. 2006. Germany.
- Shaw, C. T. 1995, *Using computational fluid dynamics* Prentice Hall, New York.
- Shimada, K. and Ishihara, T. 2002, "Application of a modified k-epsilon model to the prediction of aerodynamic characteristics of rectangular cross-section cylinders", *Journal of Fluids and Structures*, vol. 16, no. 4, pp. 465-485.
- Sislian, J. P. and Cusworth, R. A. 1984, *Laser Doppler velocimetry measurements of mean velocity and turbulent stress tensor components in a free isothermal swirling jet*, University of Toronto. Institute for Aerospace Studies, Ontario, 281.
- Sommerfeld, M. 1990, "Particle dispersion in turbulent flow. The effect of particle size distribution", *Particle and Particle Systems Characterization*, vol. 7, no. 4, pp. 209-220.

- Sommerfeld, M. 1990, "Numerical simulation of the particles dispersion in turbulent flow. The importance of lift forces and particle/wall collision models", *American Society of Mechanical Engineers, Fluids Engineering Division*, vol. 91, pp. 11-18.
- Sommerfeld, M. and Qiu, H.-H. 1991, "Detailed measurements in a swirling particulate two-phase flow by a phase-doppler anemometer", *International Journal of Heat and Fluid Flow*, vol. 12, no. 1, pp. 20-28.
- Sommerfeld, M. 1992, "Modelling of particle-wall collisions in confined gas-particle flows", *International Journal of Multiphase Flow*, vol. 18, no. 6, pp. 905-926.
- Sommerfeld, M., Ando, A., and Wennerberg, D. 1992, "Swirling, particle-laden flows through a pipe expansion", *Journal of Fluids Engineering*, vol. 114, no. 4, pp. 648-656.
- Sommerfeld, M. and Qiu, H.-H. 1993, "Characterization of particle-laden, confined swirling flows by phase-doppler anemometry and numerical calculation", *International Journal of Multiphase Flow*, vol. 19, no. 6, pp. 1093-1127.
- Sommerfeld, M. 1994, "Importance of detailed measurements for the validation of numerical models and methods for dispersed two-phase flows", *American Society of Mechanical Engineers*, vol. 180, pp. 1-14.
- Sommerfeld, M. 1995, "Importance of inter-particle collisions in horizontal gas-solid channel flows", *Proceedings of the 1995 ASME/JSME Fluids Engineering and Laser Anemometry Conference and Exhibition*, Hilton Head, SC, USA, vol. 228, pp. 335-345.
- Sommerfeld, M. 1998, "Modelling and numerical calculation of turbulent gas-solids flows with the Euler-Lagrangian approach", *KONA*, vol. 16, pp. 194-204.
- Sommerfeld, M. and Huber, N. 1999, "Experimental analysis and modelling of particle-wall collisions", *International Journal of Multiphase Flow*, vol. 25, no. 6, pp. 1457-1489.
- Sommerfeld, M. 2001, "Validation of a stochastic Lagrangian modelling approach for inter-particle collisions in homogeneous isotropic turbulence", *International Journal of Multiphase Flow*, vol. 27, no. 10, pp. 1829-1858.
- Sommerfeld, M. 2002, "Kinetic simulations for analysing the wall collision process of non-spherical particles", *Proceedings of the 2002 ASME Joint U.S.-European Fluids Engineering Conference*, Montreal, Que., United States, vol. 257, pp. 539-547.
- Sommerfeld, M. 2003, "Analysis of collision effects for turbulent gas-particle flow in a horizontal channel: Part I. Particle transport", *International Journal of Multiphase Flow*, vol. 29, no. 4, pp. 675-699.
- Sommerfeld, M. and Kussin, J. 2003, "Analysis of collision effects for turbulent gas-particle flow in a horizontal channel. Part II. Integral properties and validation", *International Journal of Multiphase Flow*, vol. 29, no. 4, pp. 701-718.
- Sommerfeld, M. and Ho, C. A. 2003, "Numerical calculation of particle transport in turbulent wall bounded flows", *Powder Technology*, vol. 131, pp. 1-6.

- Sommerfeld, M. and Kussin, J. 2004, "Wall roughness effects on pneumatic conveying of spherical particles in a narrow horizontal channel", *Powder Technology*, vol. 142, pp. 180-192.
- Spall, R. E. and Ashby, B. M. 2000, *ASME Journal of Fluids Engineering*, vol. 122, p. 179.
- Spanner, E. F. 1945, *Improvements in tubes for heat exchanger apparatus*, GB569000 (patent).
- Speziale, C., Sarkar, S., and Gatski, T. B. 1991, "Modelling the pressure-strain correlation of turbulence. An invariant dynamical systems approach", *Journal of Fluid Mechanics*, vol. 227, pp. 245-272.
- Speziale, C. G., Younis, B. A., and Berger, S. A. 2000, "Analysis and modelling of turbulent flow in an axially rotating pipe", *Journal of Fluid Mechanics*, vol. 407, no. 1, pp. 1-26.
- Stairmand, C. J. 1951, "The design and performance of cyclone separators", *Trans.IChemE*, vol. 29, p. 356.
- Steenbergen, W. and Voskamp, J. 1998, "Rate of decay of swirl in turbulent pipe flow", *Flow Measurement and Instrumentation*, vol. 9, no. 2, pp. 67-78.
- Stock, D. E. 1996, "Particle dispersion in flowing gases - 1994 freeman scholar lecture", *Journal of Fluids Engineering*, vol. 118, pp. 4-17.
- Taneda, S. 1956, "Experimental investigation of the wake behind a sphere at low Reynolds numbers", *J.Phys.Soc.Jpn*, vol. 11, pp. 1104-1108.
- Tashiro, H. and Tomita, Y. 1990, "Numerical simulation of a gas solid two-phase flow (A method of dealing with the collision between particles in a horizontal pipe)", *Transactions of the Japan Society of Mechanical Engineers*, vol. 56, no. 256, pp. 1615-1618.
- Tashiro, H., Peng, X., and Tomita, Y. 1997, "Numerical prediction of saltation velocity for gas-solid two-phase flow in a horizontal pipe", *Powder Technology*, vol. 91, pp. 141-146.
- Tennekes, H. and Lumley, J. L. 1972, *A first course in turbulence* M.I.T. Press, Cambridge, Mass.
- Tonkin, R. J. J. 2004, *Swirling pipeflow of non-Newtonian and particle-laden fluids*, PhD thesis, University of Nottingham.
- Triesch, O. and Bohnet, M. 2001, "Measurement and CFD prediction of velocity and concentration profiles in a decelerated gas-solids flow", *Powder Technology*, vol. 115, pp. 101-113.

- Versteeg, H. K. and Malalasekera, W. 1995, *An Introduction to computational fluid dynamics: the finite volume method* Longman Scientific and Technical, Harlow.
- White, F. 1994, *Fluid mechanics*, 4th edn, McGraw-Hill, Boston, Mass.
- Wolfstein, M. 1969, "The velocity and temperature distribution in one-dimensional flow with turbulence augmentation and pressure gradient", *Int.J.Heat Mass Transfer*, vol. 12, no. 3, pp. 301-318.
- Worster, R. C. and Denny, D. F. 1955, "Hydraulic transport of solid material in pipes", *Proc.Inst.Mech.Eng*, vol. 169, pp. 563-583.
- Yakhot, V. and Orszag, S. A. 1986, "Renormalization group analysis of turbulence. I. Basic theory", *Journal of Scientific Computing*, vol. 1, no. 1, pp. 3-51.
- Yan, Y. and Byrne, B. 1997, "Measurement of solids deposition in pneumatic conveying", *Powder Technology*, vol. 91, pp. 131-139.
- Yeh, Y. and Cummins, H. Z. 1964, "Localised flow measurement with an He-Ne laser spectrometer", *Applied Physics Letters*, vol. 4, p. 176.
- Yilmaz, A., Levy, E. K., and Bilirgen, H. 1996, "Effect of an elbow on flow characteristics in lean phase pneumatic conveying, fluidisation and fluid-particle systems", *AIChE Annual Meeting*, pp. 98-102.
- Yilmaz, A. and Levy, E. K. 2001, "Formation and dispersion of ropes in pneumatic conveying", *Powder Technology*, vol. 114, pp. 168-185.
- Young, J. and Leeming, A. 1997, "A theory of particle deposition in turbulent pipe flow", *Journal of Fluid Mechanics*, vol. 340, pp. 139-159.
- Yu, S. C. M. and Kitoh, O. 1994, "General formulation for the decay of swirling motion along a straight pipe", *International Communications in Heat and Mass Transfer*, vol. 21, no. 5, pp. 719-728.
- Zaherzadeh, N. H. and Jagadish, B. S. 1975, *International Journal of Heat and Mass Transfer*, vol. 8, p. 941.
- Zhang, Y. and Reese, J. M. 2001, "Particle-gas turbulence interactions in a kinetic theory approach to granular flows", *International Journal of Multiphase Flow*, vol. 27, no. 11, pp. 1945-1964.
- Zhou, L. X., Chen, T., Xu, Y., Ma, Z. H., and Guo, Y. C. 1998, "Strongly swirling gas-particle flows and coal combustion in a cyclone combustor", *Symposium (International) on Combustion*, vol. 2, pp. 3119-3126.
- Zhou, L. X. and Li, Y. 2000, "Simulation of swirling gas-particle flows using a DSM-PDF two-phase turbulence model", *Powder Technology*, vol. 113, pp. 70-79.

Zhou, L. X., Li, Y., Chen, T., and Xu, Y. 2000, "Studies on the effect of swirl numbers on strongly swirling turbulent gas-particle flows using a phase-Doppler particle anemometer", *Powder Technology*, vol. 112, no. 1, pp. 79-86.

Zhou, L. and Chen, T. 2001, "Simulation of swirling gas-particle flows using USM and k - ϵ - k_p two-phase turbulence models", *Powder Technology*, vol. 114, p. 1.

Zhou, L. X., Xu, Y., and Li, Y. 2001, "Simulation of swirling gas-particle flows using an improved second-order moment two-phase turbulence model", *Powder Technology*, vol. 116, pp. 178-189.

Zhou, L. X. and Gu, H. X. 2002, "Simulation of swirling gas-particle flows using a non-linear k - ϵ - k_p two-phase turbulence model", *Powder Technology*, vol. 128, pp. 47-55.

Ziskind, G. and Gutfinger, C. 2002, "Shear and gravity effects on particle motion in turbulent boundary layers", *Powder Technology*, vol. 125, pp. 140-148.

APPENDIX A1

DIMENSIONS OF INLET FLANGE

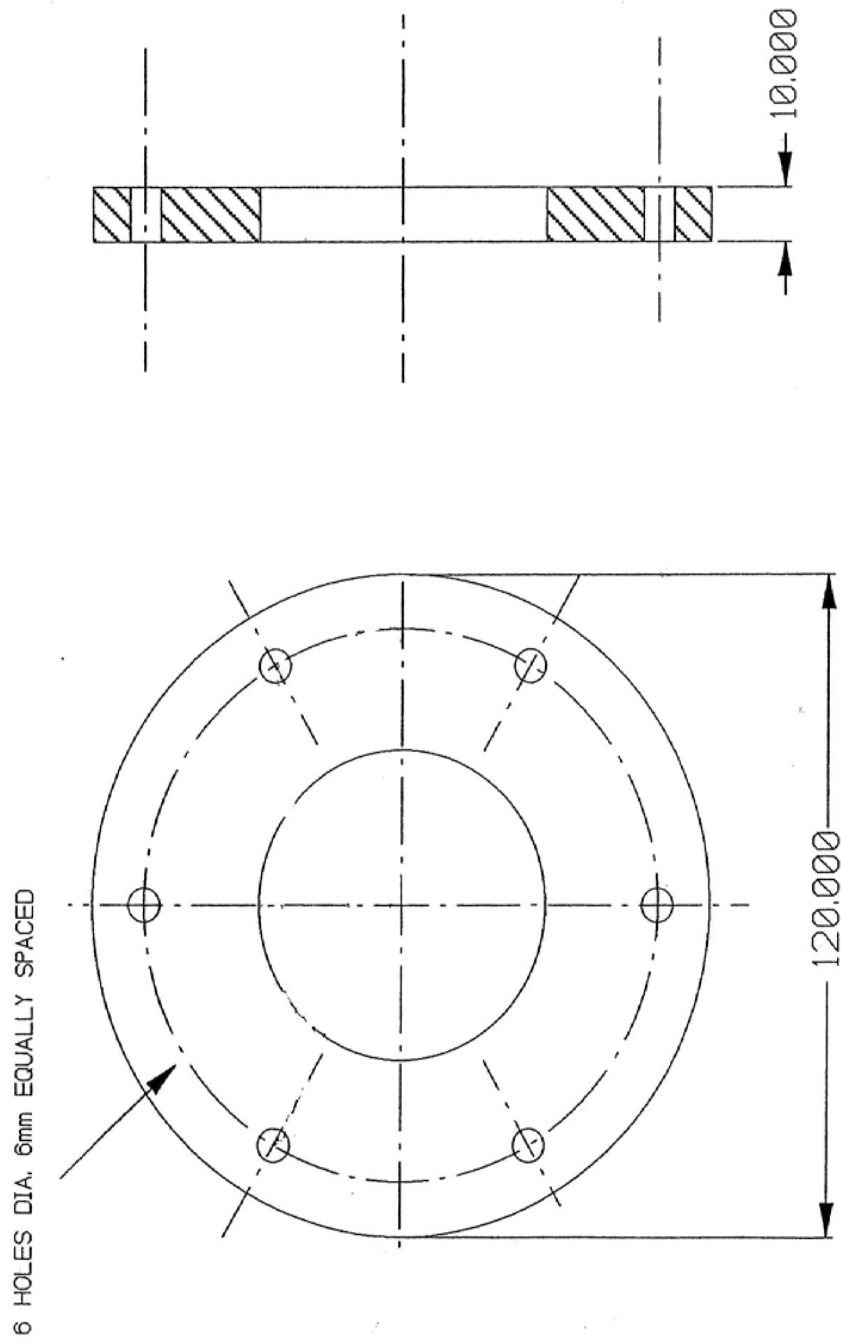


Figure A.1: Dimensions of inlet flange

APPENDIX A2

DIMENSIONS OF OUTLET FLANGE

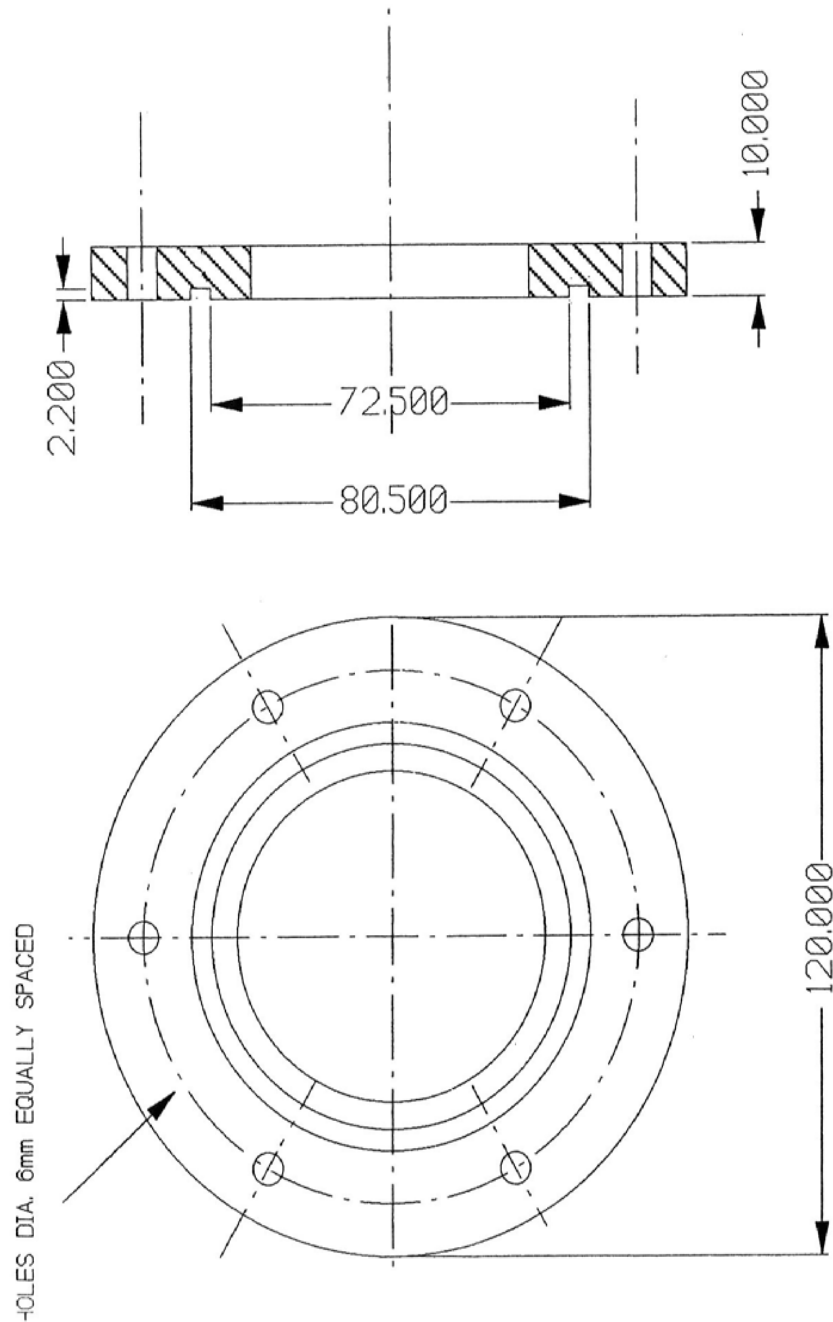


Figure A.2: Dimensions of outlet flange

APPENDIX B

HIGH SPEED CAMERA RECORDINGS

- File 1: White light recording at 500 frames per second (fps) at 15^0 to control pipe, showing 0-10D
- File 2: White light recording at 500 frames per second (fps) at 15^0 to helix pipe, showing 0-10D
- File 3(a-f): Laser light recording at 250 frames per second (fps) at 2D, 3D, 4D, 5D, 8D and 10D downstream of control pipe respectively
- File 4(a-f): Laser light recording at 250 frames per second (fps) at 2D, 3D, 4D, 5D, 8D and 10D downstream of helix pipe respectively

APPENDIX C

BASIC PRINCIPLES OF PIV METHODS

The application of PIV techniques works on the principle that the fluid of interest is seeded with tracer particles which are illuminated in the target area of interest for the study by a sheet of laser light. A charged couple device (CCD) camera then records the instantaneous positions of these particles, a short time interval between each light pulse captures separate image frames. The system then determines the velocity field from a pair of sequential images of the particles which move a measurable distance under the influence of the suspension flowfield for this given period of time. Equation 6.2, is the differential approximation to the definition of velocity, and forms the basis of PIV measurement techniques (Raffel et al., 1998).

$$velocity = \frac{displacement}{time}$$

An accurate measure of the displacement - and thus also the velocity - is achieved by performing a sub-pixel interpolation. This procedure involves dividing the images into small subsections called interrogation areas. The local displacement vector for the images of the tracer particles between the first and second illumination is determined for each interrogation area by means of performing statistical (auto and cross correlation) methods. It is assumed that all particles in one interrogation area have moved homogeneously between the two illuminations. The correlation produces a signal peak, identifying the common particle displacement. A velocity vector map over the whole target area is obtained by repeating the cross-correlation for each interrogation area over the two image frames captured by the CCD camera. A schematic diagram illustrating the process is shown in Figure C.. The components needed for PIV include:

- a flow seeding mechanism
- an illumination source and optical system to illuminate the test section
- digital imagers for capturing the flow field
- a system for image processing, particle identification, particle tracking, and vector field cleaning.

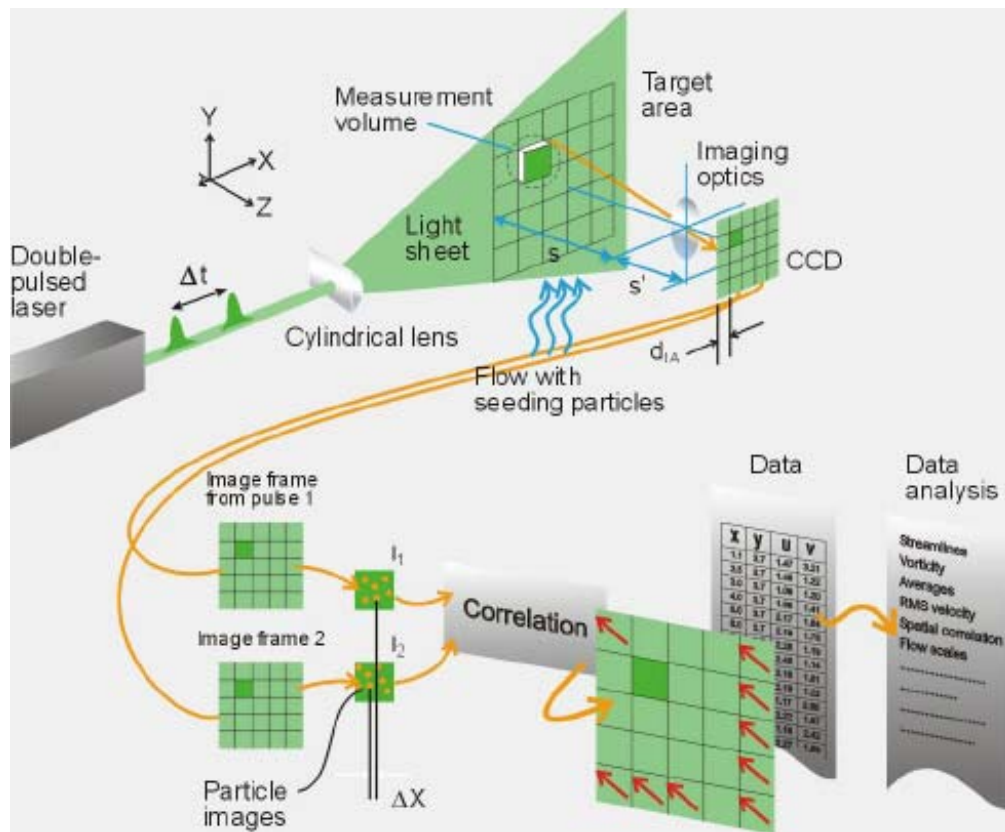


Figure C.1: Schematic diagram illustrating the components involved in performing PIV analysis of a flow process (from DANTEC Dynamics)

PIV limitations and sources of error

PIV techniques measure the velocity of the fluid element indirectly by means of measurement of the velocity of tracer particles added to the flow. It is hence required to check whether the tracer particles faithfully follow the motion of the fluid. It is observed that small particles tend to follow the flow streamlines more closely. This is however in contradiction with the need for large enough particles because of their better light scattering efficiency. A compromise needs to be found. The tracer particles are also required to be homogeneously distributed in the flow. A medium density seeding of about five to six particles per interrogation area is desired for high quality PIV recordings to obtain optimal evaluation. Finally, the interrogation area needs to be sufficiently small so that velocity gradients have no significant influence on the results.

APPENDIX C

BASIC PRINCIPLES OF LDA METHODS

In an LDA system, the fluid velocity at a point is generated by sensing the Doppler frequency shift of laser light scattered by the moving seeded particles within the flow. In order to enable this, a basic LDA configuration needs to be consisted of (Durst, 1981):

- a continuous wave laser,
- transmitting optics, including a beam splitter and a focusing sending lens,
- receiving optics, comprising a focussing receiving lens, an interference filter and a photodetector,
- a signal conditioner and a signal processor.

Traverse systems can also be used to facilitate the moving of the optics head to different measurement locations precisely. Similarly, angular encoders can be used to rotate the optics head with precision. A schematic diagram illustrating the process is shown in Figure D..

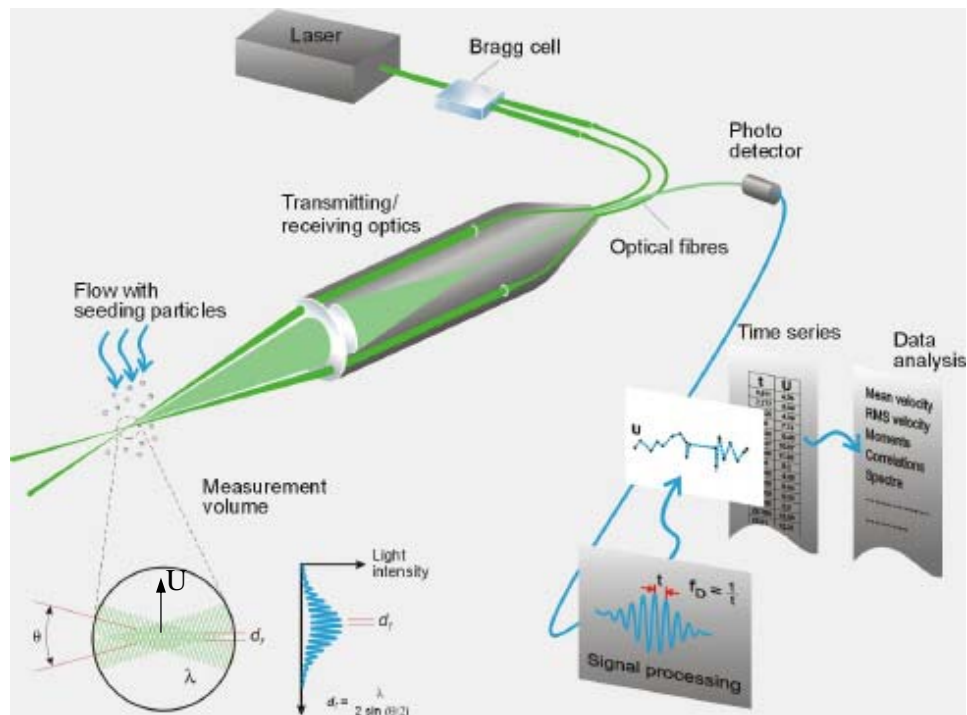


Figure D.1: A single-component dual-beam LDA system in backward scatter model (from <http://www.dantcdynamics.com/Lda/Princip/Index.html>)

A brief explanation of the basic principles behind how a laser Doppler anemometer works is given below in terms of the fringe model. An alternative explanation in terms of the heterodyne model also exists in the literature (see Durst (1981) for a thorough explanation of this model).

"One-component dual-beam system" is the most common type of LDA system used. As the name suggests, it only measures one specific velocity component (the U component in the diagram) from the use of two laser beams of equal intensity. The beams are generated from a single laser using a beam splitter, known commonly as the Bragg cell, which is a glass crystal with a vibrating piezo crystal attached. The vibration generates acoustical waves that act like an optical grid. The two laser beams of equal intensity coming out of the Bragg cell are focused into optical fibres bringing them to a probe, where they are focussed by a lens, called the sending lens. The lens also changes the direction of the beams causing them to intersect at a region on which they are focussed.

Velocity measurements are made within this focus region, which is not a single point in space, but a volume due to the wave properties of the light. It is usually referred to as the measurement volume. Its size and position is determined by the wavelength of the laser light, the diameter and the separation of the incoming beams and the focal length of the lens.

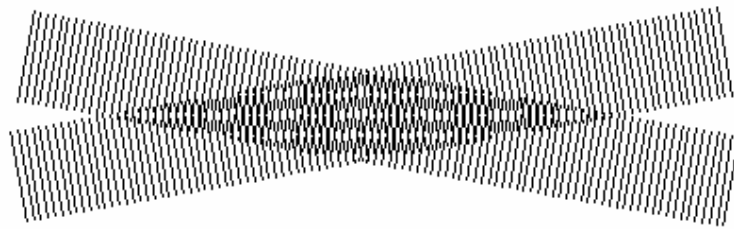


Figure D.2: Detail of the measurement volume showing the formation of fringes. Lines represent the peaks of the light

Laser light is monochromatic (i.e. of one frequency and wavelength) and coherent (all adjacent and successive waves are in phase). So when they intersect in the measurement volume, the two coherent laser beams form interference fringes, parallel planes of high light intensity. The fringes are either dark or bright, corresponding to regions where the amplitude of the laser beams respectively cancel or reinforce each

other based upon their relative phases. As can be seen in Figure D., the bright and dark fringes formed are in lines parallel to the bisector of the beams. A measurement is made when a tracer particle, seeded into the flow, passes through these fringes and scatters the light back to the laser optics head.

In the so-called backscatter mode, the receiving optics and photo detector are placed on the same side of the flow as the transmitting optics, so that they can be integrated into a single unit, thereby greatly reducing alignment difficulties.

The intensity of this scattered light will vary periodically as the particle passes through the alternating dark and bright fringes in this volume, i.e. the laser light is Doppler shifted. The frequency of the Doppler shift, f_D , will depend upon the spacing of the fringes and the particle velocity perpendicular to the bisector of the two laser beams.

To detect the Doppler shift frequency, the light scattered by the particle is collected by a second lens, the receiving lens, and is focussed onto a photodetector. An interference filter is mounted before the photodetector to filter out unrequired wavelengths so as to remove noise from ambient light and from other wavelengths before they reach the photodetector. This is usually a photomultiplier, which amplifies and converts the light intensity fluctuations into fluctuations in a voltage signal, which is usually referred to as the Doppler signal, and which is sinusoidal with a Gaussian envelope due to the intensity profile of the laser beams.

The electronic signal given out by the photodetector contains periods of silence randomly interspersed with bursts of signal. These correspond respectively to the absence and presence of particles in the measurement volume. The overall bell shape of the burst is a consequence of the intersecting laser beams producing a measurement volume that is stronger at its centre than at their edges. Hence as the particles travels from one edge of the measurement volume, through the centre, to the other edge, the signal fluctuation goes from weak to stronger and then decays again. Signal processors use digital technology such as burst-detection circuits to analyse each burst and extract the frequency and thus velocity at that instant. The signals are then digitised and analysed, often by frequency analysis using the robust Fast Fourier Transform (FFT) algorithm.

The signal processor then works out the velocity of the tracer particle from the fringe spacing and the Doppler frequency data. The fringe spacing, d_f provides information about the distance travelled by the particle and the Doppler frequency f_D provides information about the time: $t = 1/f_D$ and therefore the velocity of the tracer particles is given by $U = d_f * f_D$. This velocity is a nearly instantaneous velocity measurement, corresponding to that of the particle averaged over the time required for it to traverse the measurement volume.

Most modern LDA systems use a preshift feature, created by the Bragg cell, to overcome the problem of directional ambiguity, whereby two particles moving in opposite directions in the measurement volume at the same speed will give identical signals. Also a stationary particle produces no signal without the preshift. The latter is effectively an enforced slight shift in the frequency of one of the laser beams. This causes the fringes in the measurement volume to move at a constant. Stationary particles exposed to these moving fringes thus produce signals of constant frequency, equivalent to that of the shift. Particles moving with velocities U_{pos} and U_{neg} will generate signal frequencies f_{pos} and f_{neg} , respectively. The frequency difference is still determined by the LDA equation. The directional ambiguity is thus removed.

The one-component dual-beam system described above can be easily extended by using two or three one-component systems, aligned so that their measurement volumes overlap in order to simultaneously measure two or three velocity components. Single systems using three or more beams intersecting at a point can also be used to measure multiple components as shown in Figure D..

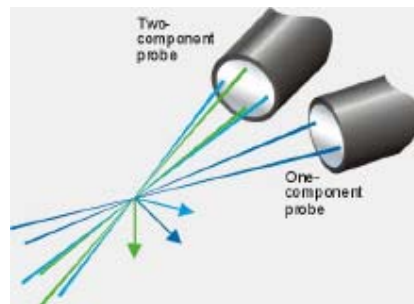


Figure D.3: Optics for measuring three velocity components (from <http://www.dantecdynamics.com/lda/Princip/Index.html>)

6.6.2.1 LDA limitations and sources of error

LDA cannot be operated without tracer seeding particles. Liquids often contain sufficient natural seeding, whereas gases must be seeded in most cases. The particle material can be solid (powder) or liquid (droplets).

Since the velocity of the flow is not measured directly, but inferred from that of the seeding particles, it is important that these particles be small enough to accurately follow all the movements of the flow, so that the measured velocity of the particles is equivalent to that of the flow. Yet the particles should be large enough to scatter sufficient light to obtain a good signal-to-noise ratio at the photo-detector output (Durst, 1981). Stokes number, as defined in equation 2.2, can be used to find the maximum particle diameter that is able to respond to the flow velocity fluctuations and closely follow the flow. Typically a seeding particle ranging between 1 μm and 10 μm in diameter is used.

The concentration of seeding also plays another factor to be considered, as in theory, the higher the concentration, the higher its influence on the flow field. However in practice, it is of accepted practice to assume that even in well seeded flows, the particles only form only a minuscule fraction of the volume of the fluid and therefore have no significant effect upon the flow (Durst, 1981).

Another problem associated with the presence of particles in the flow is the loss of coherence in the laser beams due to the diffraction of the light waves around the tracer particles. This leads to increased noise levels of the Doppler signal. Since the application of LDA would be impossible without the presence of tracer particles, care is taken not to heavily seed the flow. This is to ensure a low probability of there being more than one tracer particle present in the measurement. This prevents the Doppler signals interfering with each other, leading to a degradation of the signal quality from noise and loss of coherence of the laser beams. Another way round this problem is to ensure that the measurement volume is small.

Since transparency is a prerequisite for the application of LDA, it has to be ensured that the mixture is optically transparent. Another limitation of the LDA system is the fact that the sampling of the velocity data is random, i.e. the time between two successive samples is variable as the velocity information is discontinuous since it is

only available when a particle travels through the measurement region. This random sampling of data creates a bias as when the flow velocity is high, more particles will pass through the volume in a given time than when it is low (Durst, 1981). This over predicts the mean flow velocity if the individual velocity samples are simply averaged. This is commonly called the particle averaging bias and tends to be largest when measuring poorly seeded air flows and/or reversing flows in which the velocity can instantaneously be very small. Ways around this limitation is currently a topic of debate in the research community.

The amount of noise that accompanies the typically small Doppler signal is another major limitation, as the noise will affect the velocity estimates. The cross correlation technique has been developed for processing randomly sampled LDA data. It also explicitly attempts to eliminate the noise from turbulence power spectra.

If the measurement volume is in a region where a velocity gradient exists, such as in a boundary layer, successive particles passing through the measurement volume may have different velocities by virtue of their different positions in the gradient.

Therefore, even if the flow is completely steady, the LDA will measure a velocity fluctuation. This error is referred to as velocity gradient broadening as it tends to increase the measured variance of the velocity samples and it may be corrected simply by subtracting the extra variance from the measured value (Durst, 1981).

The same applies for finite transit time broadening error. Durst (1981) explains the error to originate from deducing a frequency from a limited number of cycles when processing a signal burst, whereby the fewer the number of fringes, the less cycles and thus the larger the potential error. Differing errors on successive bursts from particles travelling at the same speed therefore give the impression of a velocity fluctuation when there is none.

APPENDIX E

The following paper was written as part of the literature review process for the current research project. It was accepted for publication in Chemical Engineering and Processing in April 2003. The full paper can be found on the attached CD, in the folder named Appendix E.



Available online at www.sciencedirect.com



Chemical Engineering and Processing 43 (2004) 677–691



www.elsevier.com/locate/cep

Characterisation of the cross sectional particle concentration distribution in horizontal dilute flow conveying—a review

S. Fokeer^{a,*}, S. Kingman^a, I. Lowndes^a, A. Reynolds^b

^a School of Chemical, Environmental and Mining Engineering, University of Nottingham, Nottingham NG7 2RD, UK

^b Silsoe Research Institute, Wrest Park, Silsoe, Bedford MK45 4HS, UK

Received 15 April 2003; received in revised form 16 April 2003; accepted 16 April 2003

Abstract

This paper presents a review and analysis of the results of recent research that has been carried out on horizontal pneumatic conveying of materials in the dilute phase. An introduction to dilute phase pneumatic conveying is given. Many in-process applications require a detailed knowledge of the cross-sectional particle concentration distribution and an insight into the research carried out in that field is reviewed. Tomography and computational fluid dynamics (CFD) modelling have been identified as the available tools for achieving the aims of such a study and an overview of each is presented. Recent research has concentrated on identifying the optimum operating conditions to increase the energy efficiency of the systems and reducing pipe wear. A developing research area has been the modelling of particle behaviour within pipe systems, especially after bends. Gravitational settling in horizontal pipes, inertial behaviour in pipe bends and branches, turbulent dispersion, turbophoresis and transverse lift forces induced by particle rotation were reported to be the effects governing particle motion that ought to be accounted for by a dilute gas-particle flow model. Particle size, solids loading ratio, pipe material and bend characteristics were identified to be the controllable parameters that determine cross-sectional particle concentration distribution. The effect of secondary turbulent flows and lift forces are enhanced by wall roughness and particle-wall interactions. A new technique of swirling flow pneumatic conveying (SFPC) has been recently applied. However, numerical modelling of such flows is still at an early stage because the mutual coupling between the two phases is not well understood. The physical understanding and modelling of the cross sectional distribution of particles in dilute SFPC has been identified as a challenging area for future research.

© 2003 Published by Elsevier Science B.V.

Keywords: Dilute phase pneumatic conveying; Cross-sectional particle concentration distribution; Dilute swirling flow pneumatic conveying; Tomography; Particle dispersion models

1. Introduction

Pneumatic conveying is a method of transportation of bulk products in a pipeline using a gas stream. Bulk solid materials have been conveyed pneumatically on an industrial scale ever since the early twentieth century [1]. The sizes of particles that can be pneumatically conveyed vary widely from 10 of μm to 10 of cm. The process is applicable to many solid particulate materials. Because of this versatility, the applications of pneumatic conveying extend across the breadth of the process industries including chemical, pharmaceutical, food, mineral processing, steel, plastic, rubber and electric

power generation. Such a diverse application has attracted much research into the processes involved to support the development and optimisation of pneumatic conveying systems. However, an understanding of the cross-sectional distribution is essential to any of these developments and improvements. It is particularly important should the in-process application involve heat transfer, mass transfer, reactions and comminution. Consequently, this review paper summarises the work carried out in the particle cross sectional distribution of horizontal dilute phase pneumatic conveying systems.

Pneumatic conveying may be broadly divided into two broad categories: dilute (or lean) phase and dense phase conveying, depending on the applications. Dilute phase conveying is frequently the most cost-effective solution for the transport of flour, sugar, starches, chemicals, granular and palletised products. Under dilute flow conditions the solid

* Corresponding author. Tel.: +44-115-951-4672;

fax: +44-115-951-4115.

E-mail address: enxsf1@nottingham.ac.uk (S. Fokeer).